

ELECTRONIC AND VIBRATIONAL DYNAMICS OF HEME MODEL
COMPOUNDS-AN ULTRAFAST SPECTROSCOPIC STUDY

By

JAGANNADHA REDDY CHALLA

Submitted in partial fulfillment of the requirements

For the degree of Doctor of Philosophy

Dissertation Advisor: Dr. M. Cather Simpson

Department of Chemistry

CASE WESTERN RESERVE UNIVERSITY

AUGUST, 2007

CASE WESTERN RESERVE UNIVERSITY
SCHOOL OF GRADUATE STUDIES

We hereby approve the dissertation of

candidate for the Ph.D. degree *.

(signed) _____

(chair of the committee)

(date) _____

*We also certify that written approval has been obtained for any proprietary material contained therein.

Dedicated

to

My loving uncle Subba Reddy

TABLE OF CONTENTS

TABLE OF CONTENTS	i
LIST OF TABLES	v
LIST OF FIGURES	viii
LIST OF ABBREVIATIONS	xxiii
ACKNOWLEDGEMENTS	xxv
ABSTRACT	xxvi
CHAPTER 1. INTRODUCTION	1
1.1 Heme proteins and biological significance	1
1.2 Heme model compounds	4
1.3 Electronic dynamics	10
1.4 Vibrational dynamics	15
1.5 Objectives	19
1.6 References	21
CHAPTER 2. EXPERIMENTAL METHODS AND INSTRUMENTATION	30
2.1 Introduction	30
2.2 Transient absorption spectroscopy	32
2.3 Time resolved resonance Raman spectroscopy (TR³S)	33
2.4 Generation and amplification of ultrashort pulses	36

2.5 Pulse duration measurement of ultrashort pulses	38
2.6 CLARK MXR INC. CPA-1000 fs laser system	39
2.7 Single color pump-probe setup	42
2.8 Quantronix Integra fs laser system	46
Wavelength tunability	48
Fs visible and IR OPA	49
Ps visible OPA	53
CHAPTER 3. THE ELECTRONIC AND VIBRATIONAL DYNAMICS OF	
Fe^{II}OEP-2MeIm IN CH₂Cl₂	67
3.1 Introduction	67
3.2 Materials and methods	70
3.3 Results	73
3.4 Discussion	87
3. 5 Conclusions	96
3.6 References	97
CHAPTER 4. THE ELECTRONIC AND VIBRATIONAL DYNAMICS OF	
Fe^{II}OEP-(Im)₂ in CH₂Cl₂	104
4.1 Introduction	104
4.2 Materials and methods	107
4.3 Results	110

4.4 Discussion	120
4.5 Conclusions	125
4.6 References	126
CHAPTER 5. THE ELECTRONIC DYNAMICS of Fe^{II}OEP-2MeIm and	
Fe^{II}OEP-(Im)₂ in CH₂Cl₂ UPON Q-BAND EXCITATION	133
5.1 Introduction	133
5.2 Materials and methods	136
5.3 Results and discussion	138
5.4 Conclusions	146
5.5 References	147
CHAPTER 6. EFFECT OF METHYL GROUPS ON THE VIBRATIONAL	
DYNAMICS OF PARA-NITROANILINE	149
6.1 Introduction	149
6.2 Materials and methods	157
6.3 Results	159
NNDMPNA	163
2-MPNA	166
2, 6-DMPNA	170

6.4 Discussion	173
6.5 Conclusions	178
6.6 References	179
APPENDIX	187
BIBLIOGRAPHY	194

LIST OF TABLES

Table 2-1	Summary of the fs UV-visible OPA output wavelengths and their energies. I: idler, S: signal, SHI: second harmonic of idler, SHS: second harmonic of signal, FHI: fourth harmonic of idler, FHS: fourth harmonic of signal, SHSFI: second harmonic of SFI, SHSFS: second harmonic of SFS, 2B: Type I BBO crystal, 3B: Type II BBO crystal, 5B: Type I BBO crystal, 6B: Type I BBO crystal, H: horizontal, V: vertical. -----	52
Table 2-2	Summary of the fs IR OPA output wavelengths and their energies. I: idler, S: signal, NDF: nonlinear difference frequency, 8B: Type I AgGaS ₂ crystal, 9: Type I GaSe crystal, H: horizontal, V: vertical. -----	53
Table 2-3	Summary of the ps UV-vis OPA TWNB output energies. S: signal, SHS: second harmonic of signal, H: horizontal, V: vertical. -----	54
Table 3-1	Vibrational Dynamics in Photoexcited FeOEP-2MeIm. ^a Determined from simulations of the kinetic traces in Figure 3-3 using the fit decay life time, a pump/probe relative flux of 0.4 and convolution with a 600 fs Gaussian function. ^b From fitting only the decay portions of the kinetic traces in Figure 3-3. ^c From fitting only the bleach recovery portions of the kinetic traces in Figure 3-5. -----	79
Table 3-2	Kinetic Analysis for TA experimental Data and Simulations. ^a $r^2 >$	

	0.99 for all fits except the last three experimental ones, which were 0.987, 0.979, 0.966. -----	82
Table 3-3	Parameters used in TA simulations. ^a See text for details of the equations used to simulate the TA data. ^b The $\bar{\nu}(0)$ values for S_0^* are red-shifted 300 cm^{-1} relative to the values for the thermal S_0 ground state spectrum. The $\omega(0)$ values for S_0^* are $1.2 \times$ the values for S_0 . -----	85
Table 4-1	Exponential Fit parameters to Experimental TA Measurements of $\text{Fe}^{\text{II}}\text{OEP}-(\text{Im})_2$ in CH_2Cl_2 using Soret band pump white light continuum probe. R^2 values in order from top: 0.99, 0.99, 0.99, 0.96, 0.97, 0.98, 0.99, 0.99, 0.98, 0.98, 0.95, 0.95, 0.94, 0.98, 0.96, 0.97, 0.93, and 0.94. -----	114
Table 5-1	Exponential Fits to Experimental TA Measurements of $\text{Fe}^{\text{II}}\text{OEP}-2\text{MeIm}$ in CH_2Cl_2 following excitation at 541 nm. -----	141
Table 5-2	Exponential Fits to Experimental TA Measurements of $\text{Fe}^{\text{II}}\text{OEP}-(\text{Im})_2$ in CH_2Cl_2 following excitation at 541 nm. -----	145
Table 6-1	Selected experimental and calculated vibrational frequencies (in cm^{-1}). ^a Experimental data in DMSO obtained with 403 nm (PNA), 403.5 nm (NNDMPNA), 410.5 nm (2-MPNA), 410.35 nm (2, 6-DMPNA). ^b Scaling factor 0.98; ^c Assignment and Mode descriptions according to Varsanyi ⁴⁵ and Kozich et al ^{15, 41} . -----	162
Table 6-2	Effect of methyl group substitution on the vibrational energy relaxation lifetimes of PNA ^a . ^a Lifetimes obtained by plotting the	

transient integrated or average peak intensity as a function of time delay. ^bLifetimes of PNA obtained from Gunaratne et al. *ChemPhysChem* 2005, 6, 1157-63. ----- 175

Table 6-3 Effect of methyl group substitution on the vibrational energy relaxation lifetimes of PNA^a.^aLifetimes obtained using change in vibrational frequency as a function of the time delay. ^bLifetimes of PNA obtained from Gunaratne et al. *ChemPhysChem* 2005, 6, 1157-63. ----- 175

LIST OF FIGURES

Figure 1-1	The chemical structure of Fe protoporphyrin IX also known as protoheme. -----	1
Figure 1-2	The chemical structure of the heme prosthetic group present in deoxy form of the Mb. -----	3
Figure 1-3	Edge on view of the heme group present in Hb and Mb. The porphyrin macrocycle is domed in five-coordinate form and changes to planar upon O ₂ binding with simultaneous change from high to low spin state. -----	3
Figure 1-4	The chemical structure of 2-methyl imidazole complex of iron octaethyl porphyrin [Fe ^{II} OEP-2MeIm]. It is a five-coordinate high-spin heme. -----	5
Figure 1-5	The chemical structure of bis-imidazole complex of iron octaethylporphyrin [Fe ^{II} OEP-(Im) ₂] It is a six-coordinate, low-spin heme. -----	6
Figure 1-6	The UV-vis absorption spectrum of Fe ^{II} OEP-2MeIm in CH ₂ Cl ₂ . The Q-band is an order of magnitude weaker than B band. -----	7
Figure 1-7	The UV-vis absorption spectrum of [Fe ^{II} OEP-(Im) ₂] in CH ₂ Cl ₂ . The six-coordinate, low-spin ferrous compound has two band on the Q band region corresponding to Q ₀₀ and Q ₀₁ . -----	8
Figure 1-8	The Stokes resonance Raman spectrum of Fe ^{II} OEP-2MeIm in CH ₂ Cl ₂ obtained with 413 nm excitation. -----	9

Figure 1-9	The Stokes resonance Raman spectrum of Fe ^{II} OEP-(Im) ₂ in CH ₂ Cl ₂ obtained with 410 nm excitation. -----	9
Figure 1-10	Parallel and sequential intermediate excited electronic state decay models of Petrich et al. and Franzen et al. representing the electronic relaxation dynamics of both ligated and unligated heme proteins as well that of an iron PPIX. -----	13
Figure 1-11	Vibrationally hot ground electronic state models of Kholodenko et al and Ye et al. representing the electronic and ground state vibrational relaxation of heme proteins. -----	14
Figure 1-12	General experimental scheme representing the monitoring of intramolecular vibrational energy redistribution (IVR) and intermolecular vibrational energy relaxation (VER) using Raman scattering following IR or UV-vis excitation. -----	16
Figure 2-1	General Pump-Probe scheme in time-resolved spectroscopy. -----	30
Figure 2-2	Energy level diagrams for Stokes and anti-Stokes Raman scattering. -----	34
Figure 2-3	Principle of chirped pulse amplification. The femtosecond seed pulse is stretched in time prior to amplification and compressed back to its near original duration subsequent to amplification. -----	37
Figure 2-4	The schematic layout of the various components of Clark-MXR Inc. CPA-1000 fs laser system. -----	39
Figure 2-5	The second harmonic spectrum of the CPA-1000 output after frequency doubling in a 30 mm long KDP crystal. The nonlinear	

Gaussian and Lorentzian peak fits together with the corresponding bandwidths are shown. The spectral shape deviates from Gaussian and has a Lorentzian line shape. ----- 42

Figure 2-6 Single color pump-probe setup for time resolved resonance Raman spectroscopy. SHG: second harmonic generation, KDP: Potassium dihydrogen phosphate crystal, BS: beam splitter, M1 to M7: Mirrors, I1 and I2: apertures, ND1 and ND2: neutral density filters, PR: polarization rotator, L1 and L2: +750 mm fused silica lenses, CL: collecting lens, FL: focusing lens, HNF: holographic notch filter, PS: polarization scrambler, CCD: charge coupled device camera. ----- 43

Figure 2-7 Pulse characteristics of the CPA-1000 system. Frequency resolved optical gating (FROG) analysis of (A1) 800 nm CPA-1000 output using second harmonic generation in 100 μm Type I BBO crystal (B1) spectrally narrowed 400 nm output after KDP using third harmonic generation with 800 nm in 100 μm Type II BBO crystal. (A2) Auto-correlation trace of 800 nm beam (B2) Cross-correlation trace of 400 nm beam with the residual 800 nm beam (A3) Energy spectrum of the autocorrelation signal (B3) Energy spectrum of the cross correlation signal. ----- 45

Figure 2-8 The schematic layout of the various components inside the Quantronix Integra I-3.5 femtosecond laser system. ----- 46

Figure 2-9 Schematic representation of the Integra output energy distribution

for various wavelength conversion modules. BS1: beam splitter (35:65), BS2: beam splitter (50:50), BS3: beam splitter (35:65), CM1 and CM2: collimating mirrors, DEM: dielectric mirror, FROG: frequency resolved optical gating device, KDP: Potassium dihydrogen phosphate crystal, M1 to M7: Mirrors, OPA: optical parametric amplifier, TOPAS: travelling wave optical parametric amplifier of superfluorescence, W1 and W2: wedges. ----- 48

Figure 2-10 Experimental setup for the two color time resolved resonance Raman spectroscopy using two independently tunable pump and probe pulses. BS: beam splitter, M1 to M7: Mirrors, I1 and I2: apertures, ND1 and ND2: neutral density filters, PR: polarization rotator, L1 and L2: +750 mm fused silica lenses, CL: collecting lens, FL: focusing lens, HNF: holographic notch filter, PS: polarization scrambler, CCD: charge coupled device camera. ----- 55

Figure 2-11 FROG analysis of the pump (550 nm) and probe (490 nm) pulses from the fs UV-vis TOPAS and ps UV-vis TWNB respectively. Sum frequency generation in a Type II BBO crystal provides the cross correlation signal of the pump and probe pulses. The 2D correlation and the corresponding cross correlation trace at the peak 280 nm are shown. The cross correlation width is 0.88 ± 0.02 ps. ----- 56

Figure 2-12 Experimental setup for the two color time resolved resonance Raman spectroscopy using a tunable pump pulse from fs UV-vis

OPA and a fixed probe pulse at 402 nm. BS: beam splitter, KDP: potassium dihydrogen phosphate, DEM: dielectric mirror, T1: lens telescope, M1 to M7: mirrors, I1 and I2: apertures, ND1 and ND2: neutral density filters, PR: polarization rotator, L1 and L2: +750 mm fused silica lenses, CL: collecting lens, FL: focusing lens, HNF: holographic notch filter, PS: polarization scrambler, CCD: charge coupled device camera. ----- 58

Figure 2-13 Nonresonant coherent anti-Stokes Raman signal observed at -1390 cm^{-1} in the time resolved anti-Stokes Raman spectrum of DMSO using 425.70 nm pump and 401.78 nm probe pulses at zero time delay. The pump probe spectrum at the zero time delay and the corresponding pump only and probe only spectra are also shown. The solvent band of DMSO at 676 cm^{-1} seen in both probe only and pump-probe spectrum completely disappears in the transient spectrum. ----- 59

Figure 2-14 Evolution of the nonresonant coherent signal in DMSO as a function of the time delay between the pump (425.70 nm) and probe (401.78 nm) pulses. The full width at half maximum is about 200 to 300fs. ----- 60

Figure 3-1 UV-visible absorption spectrum of $\text{Fe}^{\text{II}}\text{OEP-2meIm}$ in CH_2Cl_2 . The intense band centered at 424 nm is the Soret or B band. The band centered at 543 nm is the Q-band and is an order of magnitude weaker than the B band. Gaussian fits of the B band

- line shape are also included. ----- 73
- Figure 3-2** Time resolved anti-Stokes resonance Raman spectra of Fe^{II}OEP-2MeIm in CH₂Cl₂ using 413 nm pump and 413 nm probe at the indicated time delays. The energies of the pump and probe pulses are 5.5 and 2.5 uJ respectively. Transients are obtained by subtracting the reference spectra at $\Delta t = -25$ ps. The upper trace is a steady state Stokes resonance Raman spectrum obtained at the probe wavelength of 413 nm. ----- 74
- Figure 3-3** Vibrational mode decay kinetics on the ground electronic state of Fe^{II}OEP-2MeIm using TRARRS. The rise times are estimated to be ~ 750 fs. Experimental kinetic traces were formed by averaging the three peak intensities for each band and then averaging these across the multiple data sets. No further processing was done. Squares are ν_2 , circles are ν_4 and the triangles are ν_5 . ----- 76
- Figure 3-4** Time resolved Stokes resonance Raman spectra of Fe^{II}OEP-2MeIm in CH₂Cl₂ using 410 nm pump and 410 nm probe. Transients are obtained by subtracting the reference spectra at $\Delta t = 64$ ps. ----- 77
- Figure 3-5** Vibrational mode population recovery kinetics on the ground electronic state of Fe^{II}OEP-2MeIm using time-resolved Stokes resonance Raman spectroscopy. All the five observed vibrational modes recover with an average time constant of 2.1 ± 0.2 ps. ----- 78

Figure 3-6 Transient absorption experimental data and simulations for Fe^{II}OEP-2meIm in CH₂Cl₂. Pump=402 nm, Probe=white light continuum generated in CaF₂ (360-700 nm) and the instrument response is 110 fs. OD of the sample is less than 1.0 at 402 nm. Panel (A) shows the fast dynamics associated with the first 2.0 ps and panel (B) shows the slower dynamics on the 25 ps time scale. The large dip in the spectrum is a laser line artifact at the pump wavelength of 402 nm (thin black line). ----- 80

Figure 3-7 (A) Kinetic traces from the experimental transient absorption data at the indicated probe wavelengths using 402 nm pump. (B) Kinetic traces obtained from the simulated transient absorptions [look in the figure 3-8, Tables 3-2 and 3-3 legends for simulation parameters]. ----- 81

Figure 3-8 Transient absorption data (filled circles) and simulations (lines) for Fe^{II}OEP-2MeIm in CH₂Cl₂ using the vibrationally hot ground electronic state model. Pump = 402 nm, Probe = white light continuum (360-750 nm). The large dip in the spectra is a laser line artifact from the experiment (thin black line). Left panels are the first 2 ps (panel A) and 25 ps (panel B) with simulations using the parameters [S₂: τ = 10 fs, S₁: τ = 800 fs and S₀^{*}: t(v) = 10 ps, t(ω) = 8 ps and the absorption of S₀^{*} was modeled as red-shifted by 300 cm⁻¹ and broadened by 20 % relative to S₀]. Right panels are the first 2 ps (panel C) and 25 ps (panel D) with simulations

using the parameters from reference 30 [S_1 : $\tau = 50$ fs and S_0^* : $t(v) = 4$ ps, $t(\omega) = 400$ fs and the absorption of S_0^* was modeled as red-shifted by 200 cm^{-1} and broadened by 150 % relative to S_0]. ----- 86

Figure 3-9 Simplified picture representing the events that follow electronic excitation in the Soret band of model heme $\text{Fe}^{\text{II}}\text{OEP-2MeIm}$ in CH_2Cl_2 , derived from the complimentary TA, simulations and TRARRS studies. ----- 88

Figure 4-1 UV-vis absorption spectrum of $\text{Fe}^{\text{II}}\text{OEP-(Im)}_2$ in CH_2Cl_2 . ----- 110

Figure 4-2 Femtosecond UV-vis transient absorption spectra of $\text{Fe}^{\text{II}}\text{OEP-(Im)}_2$ in CH_2Cl_2 using 402 nm excitation and broad-band white light continuum probe (360-700 nm). The instrument response is 110 fs. The optical density of the sample at excitation wavelength of 402 nm is ~ 0.5 per mm. Left panel shows the fast dynamics within the first 2 ps and right panel shows the slower dynamics up to 1.2 ns. ----- 111

Figure 4-3 Chirp corrected kinetic traces of the TA signal of $\text{Fe}^{\text{II}}\text{OEP-(Im)}_2$ in CH_2Cl_2 at the indicated wavelengths. Pump=402 nm, Probe=white light continuum. Instrument response=110 fs. ----- 113

Figure 4-4 Time evolution of the integrated transient band intensity of $\text{Fe}^{\text{II}}\text{OEP-(Im)}_2$ in CH_2Cl_2 . Left panel shows the rise and decay of the transient Soret band. The fast component contributes to 59%. Right panel shows the decay of the transient Q-band. Residual transient absorption is evident in both the traces even after 100 ps.

Figure 4-5 Time evolution of the integrated transient band intensity of $\text{Fe}^{\text{II}}\text{OEP}-(\text{Im})_2$ in CH_2Cl_2 . Left panel shows the bi-exponential recovery of the transient Q_1 band bleach centered at 519 nm. The fast component contributes to 65% of the decay. Right panel shows the recovery of the transient Q_2 band. Residual bleach is present even after 100 ps. -----

116

Figure 4-6 Spectral evolution of the transient spectra of $\text{Fe}^{\text{II}}\text{OEP}-(\text{Im})_2$ in CH_2Cl_2 . Left panel (top) shows the peak positions of the two Q-band bleaches and the Q-band transient absorption as a function of time delay. Right panel (top) shows the kinetic trace of the transient Q-band and the corresponding bi-exponential fit. The fast component contributes to 90%. Left panel (bottom) shows the spectral widths of the two Q-band bleaches and the Q-band transient absorption as a function of time delay. Right panel (top) shows the kinetic trace of the transient Q-band spectral width and the corresponding exponential fit. The peak position evolution has a fast component of about 600 fs and a slower component of about 12 ps. The spectral narrowing has a time constant of about 4.5 ps. -

117

Figure 4-7 Time resolved Stokes resonance Raman spectra of $\text{Fe}^{\text{II}}\text{OEP}-(\text{Im})_2$ in CH_2Cl_2 using 410 nm pump and 410 nm probe. Transients are obtained by subtracting the reference spectra at $\Delta t=64$ ps. -----

118

Figure 4-8	Vibrational mode population recovery kinetics on the ground electronic state of Fe ^{II} OEP-(Im) ₂ using time-resolved Stokes resonance Raman spectroscopy. Pump=Probe=410 nm. -----	119
Figure 5-1	A representative set of Transient absorption experimental data showing the fast dynamics associated with the first 2.0 ps for Fe ^{II} OEP-2MeIm in CH ₂ Cl ₂ . Pump=541 nm, Probe=white light continuum generated in CaF ₂ , Instrument response=300 fs. -----	139
Figure 5-2	A representative set of transient absorption experimental data showing the slow dynamics from 2 to 40 ps for Fe ^{II} OEP-2MeIm in CH ₂ Cl ₂ . Pump=541 nm, Probe=white light continuum generated in CaF ₂ , Instrument response=300 fs. -----	140
Figure 5-3	Kinetic traces of the transient absorption data for Fe ^{II} OEP-2MeIm in CH ₂ Cl ₂ at the wavelengths indicated and the associated exponential fits. -----	141
Figure 5-4	A representative set of transient absorption experimental data showing the fast dynamics associated with the first 2.7 ps for Fe ^{II} OEP-(Im) ₂ in CH ₂ Cl ₂ . Pump=541 nm, Probe=white light continuum generated in CaF ₂ , Instrument response=300 fs. -----	142
Figure 5-5	Transient absorption experimental data showing the slow dynamics from 2.7 ps to 2.0 ns for Fe ^{II} OEP-(Im) ₂ in CH ₂ Cl ₂ . Pump=541 nm, Probe=white light continuum generated in CaF ₂ , Instrument response=300 fs. -----	143
Figure 5-6	Kinetic traces of the transient absorption data for Fe ^{II} OEP-(Im) ₂ in	

	CH ₂ Cl ₂ at the wavelengths indicated and the associated exponential fits. -----	144
Figure 6-1	The events following photoexcitation of PNA forming the charge transfer excited electronic state. Figure based on the results of Kovalenko et al. PNA undergoes rapid internal conversion to the ground state or intersystem crossing to the lowest triplet state. The branching ratio and the individual relaxation rates are strongly dependent on the solvent polarity.	152
Figure 6-2	The chemical structures of 4-nitroaniline (PNA) and its methyl derivatives 2-methyl-4-nitroaniline (2-MPNA), 2, 6-dimethyl-4-nitroaniline (2, 6-DMPNA) and N, N-dimethyl-4-nitroaniline (NNDMPNA). -----	156
Figure 6-3	UV-visible absorption spectra of 4-nitroaniline, 2-methyl-4-nitroaniline, 2, 6-dimethyl-4-nitroaniline and N, N-dimethyl-4-nitroaniline dissolved in dimethylsulfoxide. -----	160
Figure 6-4	Stokes Resonance Raman spectra 4-nitroaniline, 2-methyl-4-nitroaniline , 2, 6-dimethyl-4-nitroaniline and N, N-dimethyl-4-nitroaniline in DMSO, obtained with 403, 410.5, 410.35 and 403.5 nm excitation respectively, normalized to the intense NO ₂ symmetric stretching vibration at about 1310 cm ⁻¹ . The DMSO solvent bands are marked with *. -----	161
Figure 6-5	Representative set of time-resolved anti-Stokes resonance Raman spectra of NNDMPNA in DMSO obtained using pump and probe	

beams at 403.5 nm. Transient spectra were generated by subtracting the pump-probe spectrum at $\Delta t = -103$ ps from the pump-probe spectra at each time delay. The background in the transient Raman spectra was removed using Origin 7.5 TM baseline routine. -----

164

Figure 6-6 Kinetic analysis of time-resolved anti-Stokes resonance Raman spectra of NNDMPNA dissolved in DMSO. Squares and circles represent the experimental integrated intensity, triangles represent the average peak intensity at -1495 cm^{-1} and lines represent the exponential curve-fits at positive time delay. The decay only portion of the 1495 cm^{-1} band is fit using $A_1 \exp^{-t/\tau_1}$; the rise and decay kinetics of 1310 and 855 cm^{-1} bands are fit using $A_1 \exp^{-t/\tau_1} + A_2 \exp^{-t/\tau_2}$. -----

165

Figure 6-7 Kinetic analysis of the peak position shifts of anti-Stokes Raman transients subsequent to photoexcitation at 403.5 nm of NNDMPNA in DMSO. Peak positions were determined by nonlinear fitting of the transients with Lorentzian peak shapes. The lines represent the exponential fits to the peak-position data at positive time delay. The 855 cm^{-1} band is fit using a function of the form $y=y_0+ A_1 \exp^{-t/\tau_1}+ A_2 \exp^{-t/\tau_2}$; $y_0=-853.82\pm 0.28\text{ cm}^{-1}$. The 1310 cm^{-1} band is fit using a function of the form $y=y_0+ A_1 \exp^{-t/\tau_1}$; $y_0=-1311.85\pm 0.67\text{ cm}^{-1}$. The value of y_0 corresponds to the equilibrium vibrational frequency of the corresponding mode. -----

166

Figure 6-8 Representative set of time-resolved anti-Stokes resonance Raman spectra of 2-MPNA in DMSO obtained using pump and probe beams at 410.5 nm. Transient spectra were generated by subtracting the pump-probe spectrum at $\Delta t = 60$ ps from the pump-probe spectra at each time delay. The background in the transient Raman spectra was removed using Origin 7.5 TM baseline routine. ----- 167

Figure 6-9 Kinetic analysis of the transient anti-Stokes Raman mode of 2-MPNA in DMSO at 1307 cm^{-1} . Circles represent the experimental integrated intensity, squares represent the central peak position and lines represent the exponential curve-fits at positive time delay. The rise and decay kinetics of 1310 cm^{-1} band intensity is fit using $A_1 \exp^{-t/\tau_1} + A_2 \exp^{-t/\tau_2}$. The peak position shift is fit using a function of the form $y = y_0 + A_1 \exp^{-t/\tau_1}$; $y_0 = -1307.04 \pm 0.66\text{ cm}^{-1}$. The value of y_0 corresponds to the equilibrium vibrational frequency of the corresponding mode. ----- 168

Figure 6-10 Kinetic analysis of time-resolved anti-Stokes resonance Raman spectra of 2-MPNA dissolved in DMSO. Symbols represent the average peak intensity of the individual vibrational modes seen in the transient spectra and lines represent the exponential curve-fits at positive time delay. The average peak intensity at 1303 cm^{-1} was obtained by averaging the intensity at 1301, 1302, 1303, 1304 and 1305 cm^{-1} . The average intensity of other modes was also

obtained similarly. The rise and decay kinetics at average peak positions of 1303, 933, 815 and 768 cm^{-1} are fit using a biexponential function of the form $A_1 \exp^{-t/\tau_1} + A_2 \exp^{-t/\tau_2}$. ----- 169

Figure 6-11 Representative set of time-resolved anti-Stokes resonance Raman spectra of 2, 6-DMPNA in DMSO obtained using pump and probe beams at 410.35 nm. Transient spectra were generated by subtracting the pump-probe spectrum at $\Delta t = 64$ ps from the pump-probe spectra at each time delay. The background in the transient Raman spectra was removed using Origin 7.5 TM baseline routine. ----- 170

Figure 6-12 Kinetic analysis of the transient anti-Stokes Raman mode of 2, 6-DMPNA in DMSO at 1307 cm^{-1} . Symbols represent the experimental integrated intensity and central peak position and lines represent the corresponding exponential curve-fits at positive time delay. The rise and decay kinetics of 1310 cm^{-1} band intensity is fit using $A_1 \exp^{-t/\tau_1} + A_2 \exp^{-t/\tau_2}$. The peak position shift is fit using a function of the form $y = y_0 + A_1 \exp^{-t/\tau_1}$; $y_0 = -1305.73 \pm 0.65$ cm^{-1} . The value of y_0 corresponds to the equilibrium vibrational frequency of the corresponding mode. ----- 171

Figure 6-13 Kinetic analysis of time-resolved anti-Stokes resonance Raman spectra of 2-MPNA dissolved in DMSO. Symbols represent the average peak intensity of the individual vibrational modes seen in the transient spectra and lines represent the exponential curve-fits

at positive time delay. The average peak intensity at 1476 cm^{-1} was obtained by averaging the intensity at 1474, 1475, 1476, 1477 and 1478 cm^{-1} . The average intensity of other modes was also obtained in the same way. The rise and decay kinetics at average peak positions of 1476, 1297, 945 and 809 cm^{-1} are fit using a bi-exponential function of the form $A_1 \exp^{-t/\tau_1} + A_2 \exp^{-t/\tau_2}$. ----- 172

LIST OF ABBREVIATIONS

BBO	Beta Barium Borate
BS	Beam Splitter
CCD	Charge Coupled Device
CL	Collimating Lens
CM	Collimating Mirror
CPA	Chirped Pulse Amplification
DMSO	Dimethyl Sulfoxide
FHI	Fourth Harmonic of Idler
FHS	Fourth Harmonic of Signal
FL	Focusing Lens
FROG	Frequency Resolved Optical Gating
Fs	Femtosecond
HNF	Holographic Notch Filter
I	Idler
KDP	Potassium Dihydrogen Phosphate
MPA	Multi Pass Amplifier
ND	Neutral Density
OD	Optical Density
OPA	Optical Parametric Amplifier
OPG	Optical Parametric Generation
PR	Polarization Rotator
PS	Polarization Scrambler
Ps	Picosecond

PSU	Pulse Synchronization Unit
PTT	Photothermal therapy
RGA	Regenerative Amplifier
S	Signal
SFI	Sum Frequency of Idler
SFS	Sum Frequency with Signal
SH(SFI)	Second harmonic of SFI
SH(SFS)	Second Harmonic of SFS
SHG	Second Harmonic Generation
SHI	Second Harmonic of Idler
SHS	Second Harmonic of Signal
TA	Transient Absorption
TBP	Time Bandwidth Product
TCU	Temperature Control Unit
TOPAS	Travelling wave Optical Parametric Amplifier of Superfluorescence
TRRRS	Time-Resolved Resonance Raman Spectroscopy
TRARRS	Time-Resolved anti-Stokes Resonance Raman Spectroscopy

ACKNOWLEDGEMENTS

There are so many people that I wish to thank who contributed directly or indirectly to this work. First of all, I would like to thank my thesis advisor, Dr. Simpson. This work would not have been possible without her enthusiastic supervision, critical thinking and enough pushing. Thanks to my committee members Dr. Dunbar, Dr. Protasiewicz and Dr. Paul Carey and I am grateful to Dr. Kenneth Singer of Physics department at Case for taking time off his busy schedule to be on the committee.

I am grateful to Dr. Michael Rogers at Bowling Green State University, for kindly letting us use their transient absorption facilities of the BGSU Center for Photochemical Sciences. I am also thankful to Dr. Terry Gustafson, for kindly letting us use the transient absorption facilities at the Ohio State University Center for Chemical and Biophysical Dynamics and Dr. Huo-Lei Peng for helping me set up the experiments.

I wish to thank our group members Tissa, Peng, Stephen, John, Ashley, Alex, Miles and Chantia. I was fortunate to work with Dr. Tissa Gunaratne on the time-resolved experiments and I am forever thankful to him for all the things that I learnt about lasers, nonlinear optics and time-resolved experimental methods. The help of the generous staff at Chemistry department is much appreciated.

I would like thank all my friends at Case for making my graduate years filled with unforgettable memories. And, finally I would like to thank my family, especially my mom and my loving wife Latha without whose unconditional love, never ending patience, and sacrifices I will be not be where I am right now.

Jagannadha Reddy Challa, Cleveland, May 2007

Electronic and Vibrational Dynamics of Heme Model Compounds

-An Ultrafast Spectroscopic Study

Abstract

By

JAGANNADHA REDDY CHALLA

The ultrafast electronic and vibrational dynamics of a model five-coordinate, high-spin heme Fe^{II}OEP-2MeIm, following excitation in the Soret band, have been studied in a coordinated fashion using ultrafast transient absorption, time-resolved Stokes and anti-Stokes resonance Raman spectroscopies. Electronic excitation on the blue side of the Soret band region led to sub-100 fs S₂→S₁, followed by 800 fs nonradiative decay to a vibrationally hot, nonthermal ground state species S₀^{*}. S₀^{*} then evolved to the thermally equilibrated ground state species S₀ on ~ 10 ps timescale. The initial accepting modes during the S₁→S₀ internal conversion underwent rapid vibrational relaxation evidenced by 1-3 ps decay of transient anti-Stokes signals. Comparison to other studies in heme proteins where the initial excited electronic state was prepared by ligand photolysis led to insight into the state dependence of vibrational dynamics in hemes.

The ultrafast dynamics of a six-coordinate low-spin heme Fe^{II}OEP-(Im)₂ were studied following photolysis of one of the imidazole ligands upon electronic excitation.

No detectable vibrationally hot six-coordinate ground state heme is observed, indicating the intrinsic quantum yield of the photolysis to be close to unity. The intramolecular vibrational relaxation is the major contribution to the photoproduct cooling on the order of 0.6 to 4.5 ps time scale. The intermolecular vibrational cooling has a lifetime of approximately 10 ps. On average 75% of the photolysed ligand geminately recombines on the time scale of 10-20 ps strongly overlapping with the vibrational cooling dynamics. Complimentary time resolved Stokes resonance Raman experiments support these observations as well.

The effect of methyl groups on the vibrational relaxation processes of para-nitroaniline (PNA) was studied. Minimal impact upon electronic dynamics, significant impact upon vibrational dynamics was observed in 2-methyl, 2, 6-dimethyl and N, N-dimethyl PNA compounds. NO₂ group wagging overtone ($\sim 1495\text{ cm}^{-1}$) acts as the coupling and primary accepting mode during internal conversion in all four compounds. N-methyl substitution increases vibrational cooling lifetimes, phenyl ring substitution populates two new low frequency ring vibrations not present in PNA or N, N-dimethyl PNA. Anti-Stokes intensity decay and peak-shift evolution yield different lifetimes. Off-diagonal anharmonic coupling to populated low frequency motions of the phenyl are likely to be important.

CHAPTER 1

INTRODUCTION

1.1 HEME PROTEINS AND BIOLOGICAL SIGNIFICANCE

Heme proteins are a class of biological molecules that serve in several different functions. Myoglobin (Mb) and hemoglobin (Hb) are respiratory proteins that serve as oxygen storage and transport agents respectively in vertebrate systems. The cytochrome b's and c's serve as one electron transfer agents. Cytochrome P 450 and peroxidases are involved in irreversible covalent transformation of substrates. The metal cofactor of all these proteins is based upon protoporphyrin IX.

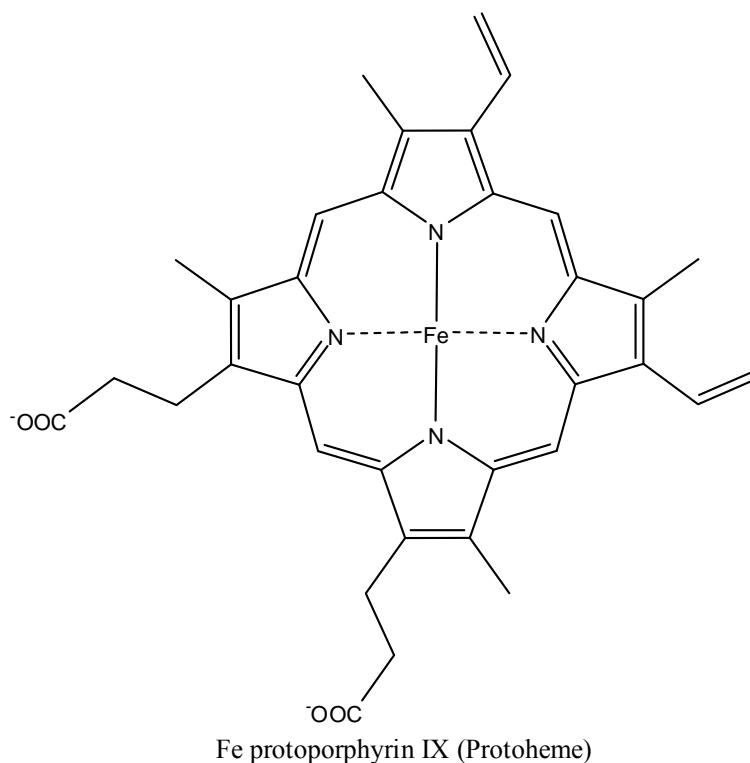


Figure 1 - 1 The chemical structure of Fe protoporphyrin IX also known as protoheme.

Hemoglobin and Myoglobin:

Hemoglobin¹⁻³ serves as O₂ transport agent in vertebrates. In mammals, hemoglobin is a hetero tetramer with each of the four subunits having a Protoporphyrin IX (PPIX) prosthetic group also known as protoheme that can bind a single O₂ molecule. The PPIX is covalently bound to each of the protein subunits via the imidazole ring of a histidine protein residue. Dioxygen can bind to the sixth coordination site of the Fe atom completing its octahedral coordination. The Fe atom can be Fe²⁺ or Fe³⁺ state and the ferri hemoglobin with a Fe³⁺ cannot bind O₂. In adult humans the most common type of hemoglobin, known as hemoglobin A, is a tetramer of two α and two β chains each of 141 and 146 amino acid residues respectively. The binding of oxygen to hemoglobin was shown to be cooperative and allosterically controlled. The cooperative binding nature of the hemoglobin results in rapid, complete binding in the regions of high O₂ concentration and rapid, complete release in regions of low O₂ concentration. The quaternary structure of hemoglobin with four O₂ molecules bound to the four subunits is known as the Relaxed or R form and the structure of the deoxy form with no bound O₂ molecules is known as the tense or T form.

Myoglobin is a heme protein that serves as oxygen carrying pigment of muscle tissues. The crystal structure of the Myoglobin was solved by John Kendrew in 1958^{4,5}. It is an unusual protein that is made up of almost exclusively α helices with no β sheets. Unlike hemoglobin, myoglobin is monomer of 16700 daltons molecular weight with no cooperative binding of O₂. A protoheme group of heme type b similar in the case of hemoglobin is responsible for oxygen binding.

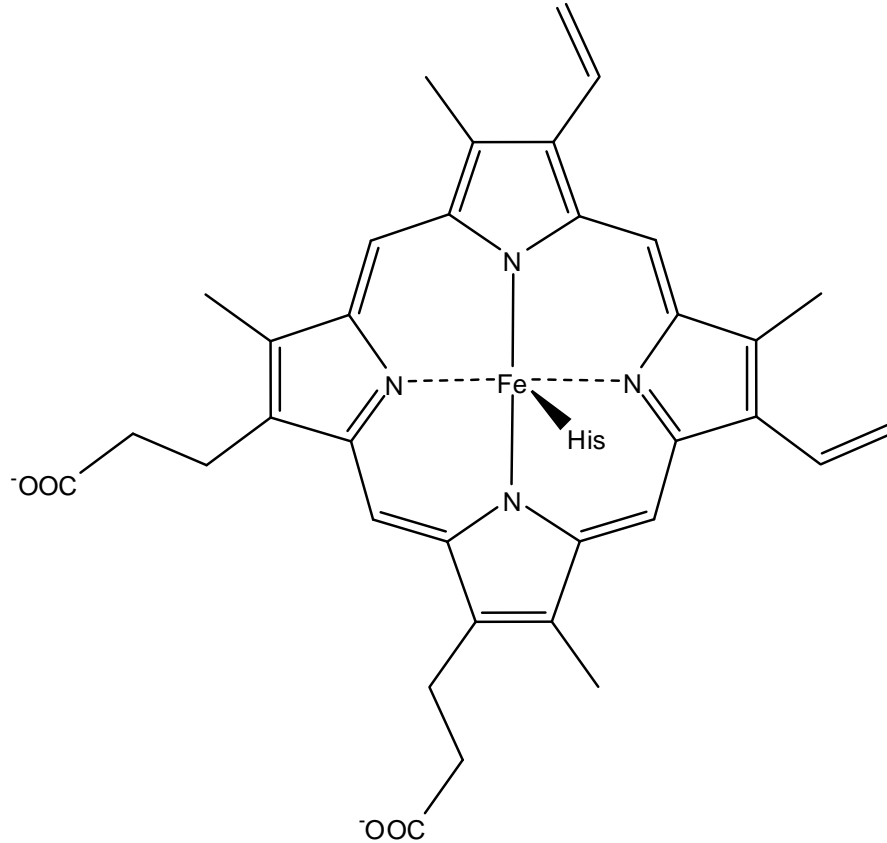
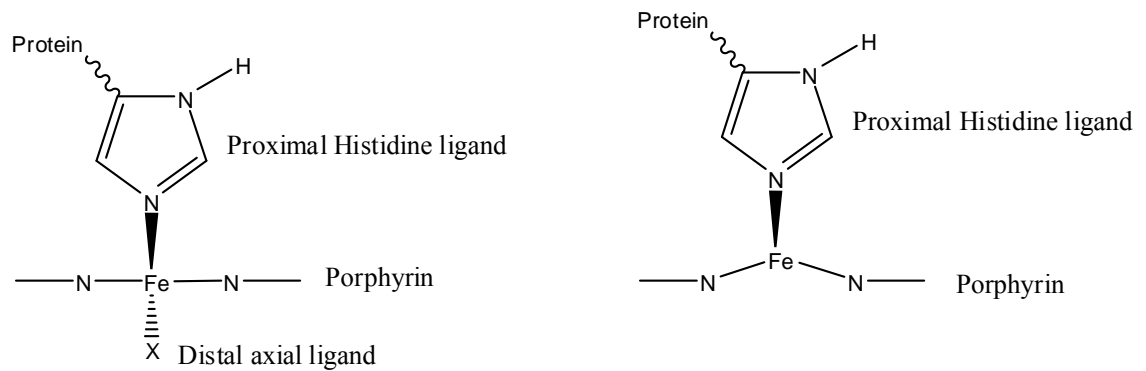


Figure 1 - 2 The chemical structure of the heme prosthetic group present in deoxy form of the Mb.



Six-coordinate, in-plane, low-spin Fe(II)

Five-coordinate, domed, high-spin Fe(II)

Figure 1 - 3 Edge on view of the heme group present in Hb and Mb. The porphyrin macrocycle is domed in five-coordinate form and changes to planar upon O₂ binding with simultaneous change from high to low spin state.

Cytochrome c:

Cytochrome c⁶⁻⁸ is a small (12500 Daltons), soluble protein in the inner membrane of mitochondria that is used to shuttle electrons from the Cytochrome bc₁ complex to cytochrome oxidase. Unlike hemoglobin and myoglobin it is six coordinated and does not bind O₂. The heme prosthetic group is of type c and is covalently bound to the protein via thioether bridges between two cysteine residues and the two peripheral vinyl groups. It is also coordinated to the protein via a histidine and a methionine in the axial positions.

1.2 HEME MODEL COMPOUNDS

The two heme model compounds studied in this work are based on iron octaethyl porphyrin that has ethyl groups in all the β peripheral substituent positions of the protoheme structure in Figure 1. 2-methyl imidazole group in the fifth-coordination site of the iron atom with the iron atom being in the ferrous Fe^{II} state mimics the active site of the monomeric heme protein myoglobin (Mb). This model compound without the protection offered by the globular protein in Mb towards oxidation is not stable in the presence of O₂. The compound thus needs to be kept in a deoxygenated environment for the iron atom to be in Fe^{II} state. The steric bulkiness of the 2-methyl imidazole ring because of the methyl group in the second position makes the iron porphyrin domed towards the ligand just like in the case of Mb and coordination by another 2-methyl imidazole ligand in the sixth coordination is hindered. This is five-coordinate, high-spin, Fe (II) octaethyl porphyrin 2-methylimidazole [Fe^{II}OEP-2MeIm] complex.

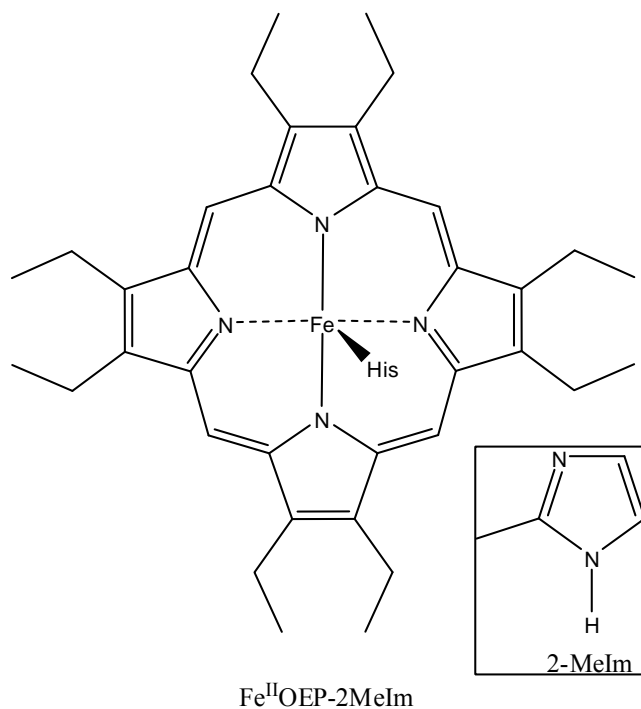


Figure 1 - 4 The chemical structure of 2-methyl imidazole complex of iron octaethyl porphyrin [Fe^{II}OEP-2MeIm]. It is a five-coordinate high-spin heme.

The crystal structure of this model compound has been determined very recently⁹. The 2-methyl imidazole ligand is found to be disordered having a major (75%) and a minor orientation with a small dihedral angle of 6.6° between the two orientations. However, the major orientation dominates the structural features of the molecule. The molecule has an expanded porphyrinate core (2.049 Å core radius), large equatorial Fe-N bond distances (2.077 Å) and a significant out of plane displacement of the iron atom. The overall structure of the molecule is domed with a displacement of Fe atom by 0.34 Å from the plane defined by the four porphyrin nitrogens and by 0.46 Å from the 24-atom mean plane of the porphyrin core corresponding to a doming of 0.12 Å. Bulky 2-methyl imidazole leads to an off-axis tilt of the iron-imidazole bond from the heme normal by an angle of 6.9° and a rotation of the 2-MeIm ligand to maximize the distance between the ligand and the porphyrin core atoms.

The second model compound has an imidazole ligand that can bind to both the fifth and sixth coordination sites of the Fe atom of iron octaethylporphyrin leading to a six-coordinate, low-spin Fe^{II} octaethyl porphyrin bis-imidazole [$\text{Fe}^{\text{II}}\text{OEP}-(\text{Im})_2$] complex. The iron atom is in the plane of porphyrin similar to the case of Mb bound to a diatomic ligand. This compound is also unstable in the presence of oxygen leading to rapid oxidation of Fe^{II} to Fe^{III} .

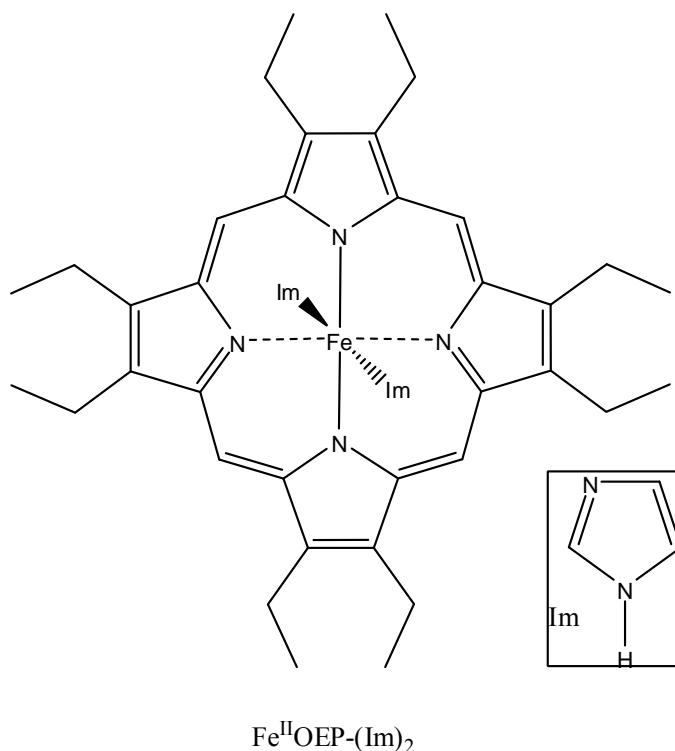


Figure 1 - 5 The chemical structure of bis-imidazole complex of iron octaethylporphyrin [$\text{Fe}^{\text{II}}\text{OEP}-(\text{Im})_2$] It is a six-coordinate, low-spin ferrous heme.

The UV-vis absorption spectrum of the five-coordinate, high-spin heme model compound $\text{Fe}^{\text{II}}\text{OEP}-2\text{MeIm}$ in dichloromethane is shown in Figure 1-6. The most intense feature centered at 424 nm is the Soret (or B) band. The band centered at 543 nm is the Q-band and is an order of magnitude weaker than the Soret band. The

corresponding absorption maxima for Human adult deoxy hemoglobin are 428 and 554 nm respectively¹⁰.

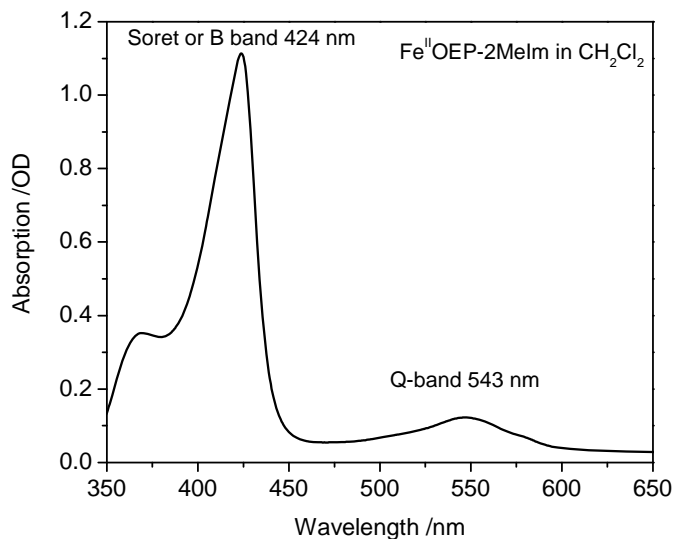


Figure 1 - 6 The UV-vis absorption spectrum of Fe^{II}OEP-2MeIm in CH₂Cl₂. The Q-band is an order of magnitude weaker than B band.

The UV-vis absorption spectrum of the six-coordinate, low-spin heme model compound Fe^{II}OEP-(Im)₂ in dichloromethane is shown in Figure 1-7. The most intense feature is the Soret (or B) band, which has a maximum at 412 nm. The two bands in the low energy region at 519 and 548 nm are due to Q-band and are an order of magnitude weaker than the Soret band. The corresponding absorption maxima of carbonmonoxy hemoglobin are 420, 538 and 570 nm respectively¹⁰. The corresponding absorption maxima of ferrous horse heart cytochrome c are 415, 521 and 550 nm respectively. It is interesting to note that the absorption maxima of the six-coordinate model compound are very close to those of reduced cytochrome c.

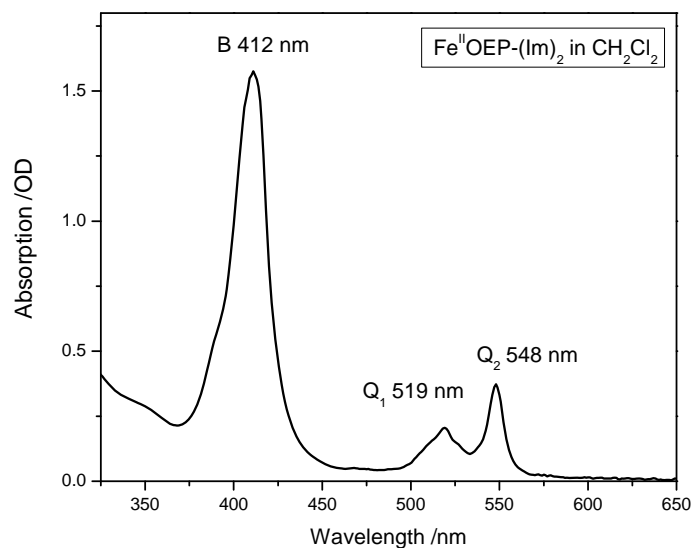


Figure 1 - 7 The UV-vis absorption spectrum of $[\text{Fe}^{\text{II}}\text{OEP}(\text{Im})_2]$ in CH_2Cl_2 . The six-coordinate, low-spin ferrous compound has two bands in the Q band region corresponding to Q_{00} and Q_{01} .

The Stokes resonance Raman spectra of $\text{Fe}^{\text{II}}\text{OEP}-2\text{MeIm}$ and $\text{Fe}^{\text{II}}\text{OEP}(\text{Im})_2$ in CH_2Cl_2 are presented in Figures 1-8 and 1-9 respectively. The bands are assigned^{11, 12} as follows: ν_2 , an A_{1g} in-phase $\text{C}_\beta\text{-C}_\beta$ stretch; ν_3 , an A_{1g} $\text{C}_\alpha\text{-C}_m$ stretch; ν_4 , an A_{1g} symmetric pyrrole half-ring stretch; ν_5 , an A_{1g} $\text{C}_\beta\text{-C}_{\text{ethyl}}$ stretch; ν_6 , an A_{1g} pyrrole breathing; ν_7 , an A_{1g} symmetric pyrrole deformation and ν_{CH} , an A_{1g} symmetric CH_2 twist of the ethyl peripheral substituents. The high frequency ν_2 and ν_3 modes more sensitive to core size, ligation state and spin state are shifted to higher frequencies in going from five-coordinate, high-spin, domed heme to six-coordinate, low-spin, planar heme. The π electron density sensitive mode ν_4 position did not change.

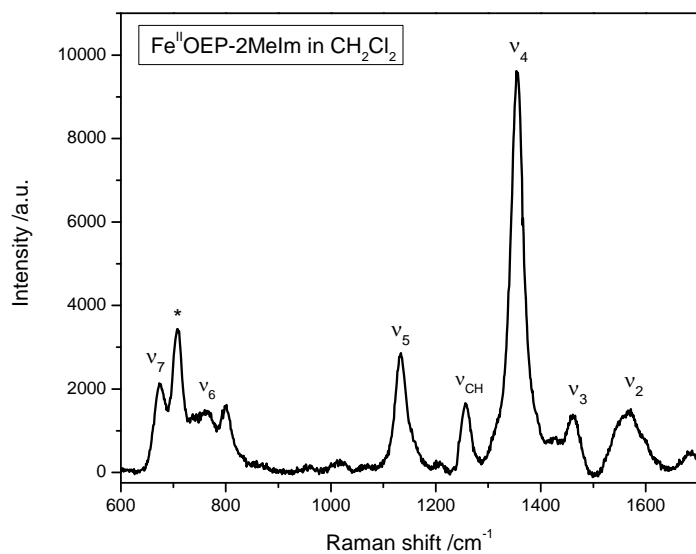


Figure 1 - 8 The Stokes resonance Raman spectrum of Fe^{II}OEP-2MeIm in CH₂Cl₂ obtained with 413 nm excitation.

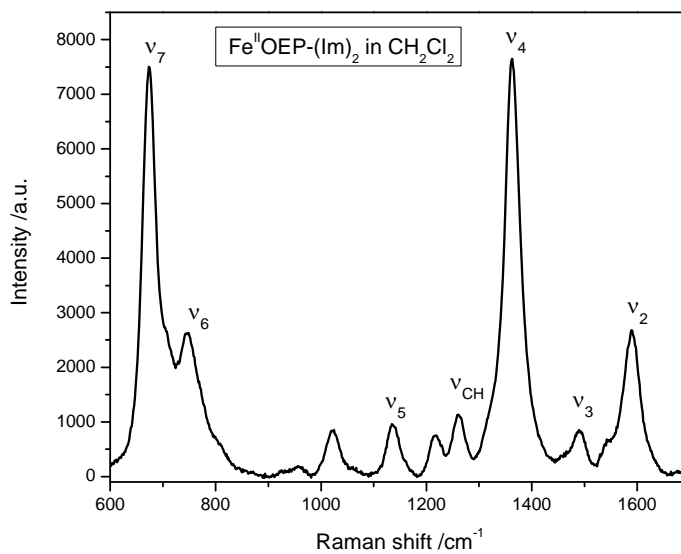


Figure 1 - 9 The Stokes resonance Raman spectrum of Fe^{II}OEP-(Im)₂ in CH₂Cl₂ obtained with 410 nm excitation.

1.3 ELECTRONIC DYNAMICS

The heme group of the respiratory proteins hemoglobin and myoglobin can also reversibly bind diatomic ligands like CO and NO in addition to O₂. In the bound state the iron atom is in the plane of the porphyrin macrocycle and has a low-spin (S=0) state. In the unligated state, the iron atom is displaced from the porphyrin plane by $\sim 0.3 \text{ \AA}$ towards the proximal histidine and has high-spin (S=2) state. Another interesting property of the hemes bound to diatomic ligands is that the ligand can be photolysed on the ultrafast time scale which then recombines at a later time to reform the bound heme. Even though these heme proteins are not directly involved in any photochemical transformations, the biological function of hemoglobin and myoglobin can be optically triggered using a short light pulse and the associated structural changes in the heme group as well as the surrounding protein can be studied by creating a situation similar to oxygen uptake and release.

In order to briefly explain the events associated with the photolysis in heme proteins, part of the light energy will be consumed in breaking the iron to ligand bond and the energy in excess of that required for photolysis is shared between the unligated heme and ligand. The events following photolysis include ligand escape, electronic and vibrational relaxation of the unligated heme, Fe atom out of plane motion and spin state change, ligand rebinding and the associated protein structural and conformational relaxation. The usefulness of the transient spectral changes occurring as a result of these events in elucidating the protein structure function relationships has led to an enormous amount of theoretical and experimental studies of these heme proteins.

Early flash photolysis studies¹³⁻¹⁵ on heme proteins focused on measuring the dissociation quantum yields for each of the ligands and showed that the measured quantum yields for diatomic ligand photolysis varied in the order of $\text{CO} > \text{O}_2 > \text{NO}$. Various reasons for this discriminatory nature of hemoglobin and myoglobin towards binding of O_2 over CO leading to difference in quantum yields have been proposed by different research groups such as different ligand dependent energy barriers for rebinding¹⁶, the formation of non-reactive states¹⁷, formation of short lived intermediate states¹⁸, different spin-orbit effects¹⁹, thermal barriers to rebinding evidenced by equal rates of combination of O_2 and CO at low temperature studies, fast recombination of O_2 and NO compared to CO ²⁰, with the primary assumption of an intrinsic quantum yield of 1 for all the ligands.

With rapid growth in ultrafast laser technology at about the same time, the early μs to ps flash photolysis studies evolved into the fs time-resolution pump-probe experiments. One of the initial studies by Martin et al.²¹ in 1983 using 250 fs pulses indicated the photolysis to occur within the pulse duration giving rise to a high-spin in plane iron heme that relaxed to a high-spin domed configuration within 350 fs which in turn decayed to non-reactive states with a life time of 3.5 ps . The pioneering work of molecular dynamics simulation studies by Henry et al^{22, 23} predicted photolysis lifetimes of 50-150 fs and non exponential cooling life times of 1-4 ps (50%), 20 to 40 ps (50%) and sub ns ligand recombination life times.

A number of ultrafast spectroscopy experiments have been reported. Despite several years of active research by various groups, the heme electronic dynamics has not yet converged to single model and various reports in the literature lead to the following

two models. 1. Intermediate excited electronic state model 2. Vibrationally hot ground electronic state model.

Intermediate excited electronic state model:

Petrich et al.²⁰ in 1988 gave a detailed description of the electronic dynamics of the heme proteins unligated and ligated with diatomic ligands CO, NO and O₂ as well as that of a protoheme ligated with CO and NO in the absence of the protein. Single wavelength kinetics were measured following photo excitation in the Q-band (S₁). Photolysis was reported to occur in all the compounds with or without the presence of protein in less than 50 fs leading to the formation of two intermediate electronic states Hb_I* and Hb_{II}* each having a lifetime of 300 fs and 2.5 ps (3.2 ps in case of deoxy Mb) respectively. The absorption maxima for these two intermediate electronic states were assigned to 470 and 455 nm based on kinetic evidence, but no spectral information of the two states has been reported by them or by anyone in the following years.

This parallel intermediate electronic state decay model was modified 13 years later by Franzen et al.²⁴ to sequential relaxation pathway (Q₁-Hb_I*-Hb_{II}*-Hb) through the same intermediate electronic states. Again, both the ligated and unligated heme proteins are studied following electronic excitation in the Q-band (S₁). The intermediate electronic state Hb_I* was proposed to form via ultrafast iron-to-porphyrin ring charge transfer and then Hb_{II}* due to porphyrin ring-to-iron back charge transfer process. The absorption maxima were assigned at 450 and 478 nm respectively for Hb_I* and Hb_{II}* again based on kinetic evidence. Both these studies and the interpretations are based on single wavelength kinetics or global fitting of the kinetics at several wavelengths and ignored

the effect of absorption spectral evolution such as narrowing and blue-shifting as the molecule vibrationally cools to return to thermal equilibrium.

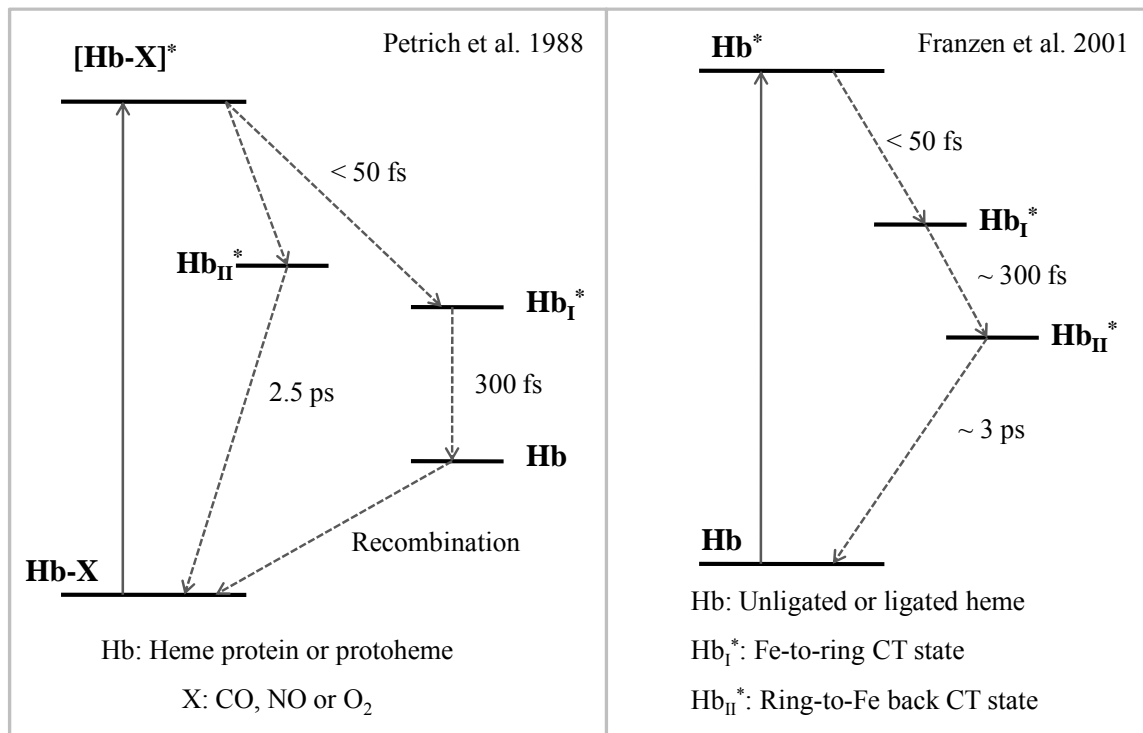


Figure 1 - 10 Parallel and sequential intermediate excited electronic state decay models of Petrich et al.²⁰ and Franzen et al.²⁴ representing the electronic relaxation dynamics of both ligated and unligated heme proteins as well that of an iron PPIX.

Vibrationally hot ground electronic state model:

Exactly a year before the above study by Franzen et al.²⁴ was published; Kholodenko et al.²⁵ reported transient absorption study of deoxy Mb in the Q-band and band III (a weak absorption band centered at 630 nm) regions using Soret band excitation (S₂). Two electronic relaxation processes, one less than 100 fs and another of a few 100 fs were reported and based on the anisotropy decay values, it was concluded that there were no electronic relaxation components present after ~ 600fs, in contrast to the predictions

by Petrich and Franzen et al. The transient spectral features were successfully simulated to represent the difference spectra of vibrationally hot and cold ground state Mb molecules and the ground state vibrational relaxation was shown to be bi-exponential involving a major fast (1.5 to 4 ps) and a minor slow (~ 15 ps) component.

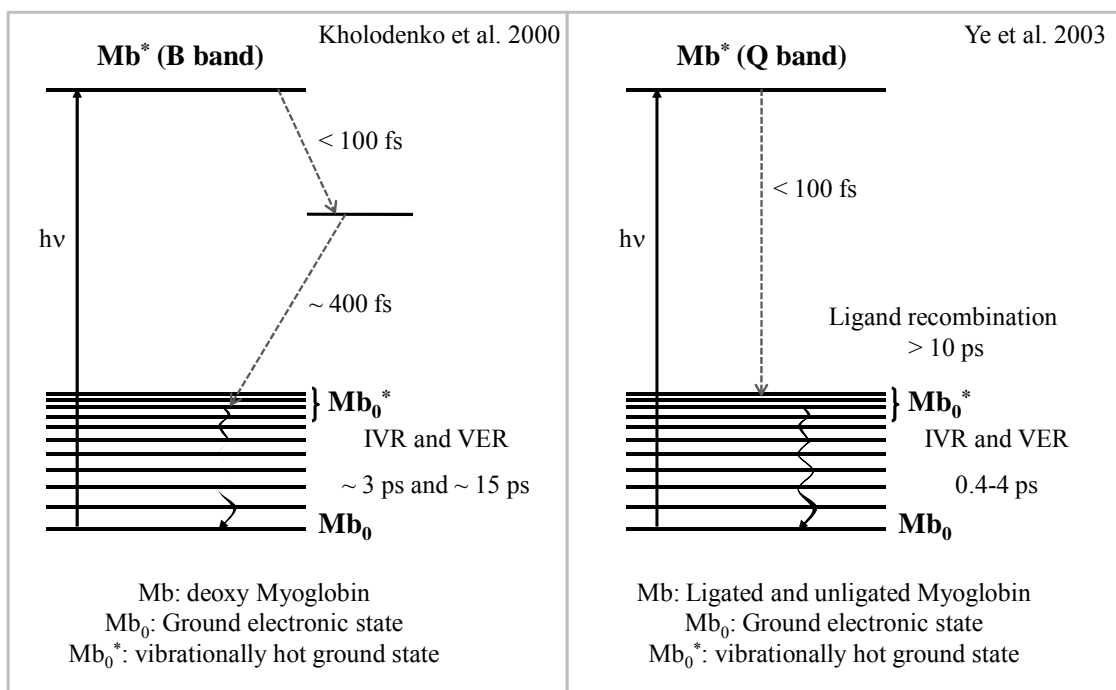


Figure 1 - 11 Vibrationally hot ground electronic state models of Kholodenko et al.²⁵ and Ye et al.²⁶ representing the electronic and ground state vibrational relaxation of heme proteins.

More recent studies by Ye et al.^{26, 27} in 2002 and 2003 confirmed this vibrationally hot ground electronic state model using Q-band excitation experiments of both ligated (MbCO, MbNO and met Mb) and ligand free deoxy Mb. The electronic relaxation of the S_2 state is not present in these studies and the vibrationally hot ground electronic state of the five-coordinate heme was found to form in less than 100 fs and the vibrational cooling features were successfully simulated by using lifetimes of 0.4 and 4 ps for transient spectral narrowing and blue-shifting respectively. The transient features

were shown to be corresponding to the difference of hot and cold ground state absorption spectra that spectrally narrow and blue-shift as the hot ground electronic state cools vibrationally. Temperature dependent absorption spectral studies of heme proteins by Cupane et al.²⁸ in 1988 have reported the similar behavior of narrowing and blue-shifting as the temperature is decreased.

1.4 VIBRATIONAL DYNAMICS

The flow of vibrational energy in condensed phase molecules is a fundamental physical process that is not yet well-understood. Following population of a vibrational mode either by direct IR excitation or via nonradiative decay from an excited electronic state, the excess energy in the molecular system can be redistributed intramolecularly to other vibrational modes of the same molecule (IVR) or via intermolecular vibrational energy relaxation (VER) to the solvent/bath degrees of freedom. The time scales of IVR and VER depend on the specific molecular system being studied and in condensed phase on the solvent properties as well. However, sometimes the solvent might not affect the dynamics at all as reported in few molecular systems by Brooks H Pate and coworkers²⁹.

One can experimentally monitor these relaxation processes by preparing a specific excited vibrational state via infrared excitation or an initial vibrational energy distribution via nonradiative decay from an excited electronic state following UV-vis excitation and following the evolution of it via IR absorption³⁰⁻³⁶ or Raman scattering³⁶⁻⁴⁰. The IR pump-probe as well as the IR pump-Raman probe methods are successfully applied to several small to medium size polyatomic molecules. But in case of large polyatomic molecules as the number of vibrational modes increase with the number of atoms, it

resonance Raman spectroscopy the ideal probe of the relaxation of this excess vibrational energy. Moreover the anti-Stokes resonance Raman scattering occurs only from population in the excited vibrational levels where as the Stokes Raman scattering can occur from both ground and excited vibrational populations. Thus time-resolved anti-Stokes resonance Raman scattering has been the most used technique in studying the heme protein vibrational dynamics and a few transient IR studies monitoring the Fe-CO and free CO vibrational frequencies during the photolysis of MbCO⁴² and transient grating studies measuring the solvent response are also reported^{43, 44}.

Before presenting various important research contributions in elucidating the heme vibrational dynamics, it is important to point out that the iron histidine bond is orthogonal to the heme porphyrin plane and hence is also orthogonal to the porphyrin in-plane vibrations that are well-coupled to the heme group π - π^* electronic excitation. This makes the vibrational energy decay through the axial histidine ligand to the protein highly improbable and the main relaxation pathway of heme cooling will be through the peripheral side chains and in particular through the isopropionate and water interactions as pointed out in these studies^{45, 46}.

However a low-frequency vibrational mode at about 216-220 cm^{-1} corresponding to the Fe-His stretch was found to exhibit resonance enhancement and is one of the most focused Raman bands of Hb and Mb⁴⁷. This is primarily because the iron-histidine bond is the only covalent linkage between the heme cofactor and the protein. This band which is absent in Mb-CO, appears following the photolysis of the ligand corresponding to the iron out-of-plane displacement caused by ligand dissociation.

Initial time-resolved resonance Raman studies measured the Stokes resonance Raman scattering with 435 nm pulses, following photolysis of HbCO by 575 nm pulses giving a vibrational cooling life time of less than 10 ps for the ν_4 band⁴⁸. Single pulse transient resonance Raman methods with laser pulses longer than the relaxation events were used to create the steady state populations within the pulse duration⁴⁹⁻⁵³. The ratio of the anti-Stokes and Stokes resonance Raman scattering intensities corrected to first order for reabsorption and Raman cross-section differences as a function of the laser flux, showed the presence of non-equilibrium Boltzmann population distributions at early times^{53, 54}.

The time resolved Stokes and anti-Stokes resonance Raman spectra of deoxy Hb by Lingle et al. in 1991 with 8 ps pulses reported negative Stokes and positive anti-Stokes transients for several porphyrin in-plane and peripheral group vibrational modes that decayed with a time constant of 2-5 ps and the process is assigned to vibrational cooling^{55, 56}. Detailed time resolved Stokes and anti-Stokes resonance Raman spectral analysis of MbCO following the photolysis of CO ligand reported by Mizutani et al.^{57, 58} gave lifetimes of 1.9 ± 0.6 ps (93%) and 16 ± 9 ps (7%) for the ν_4 band using 435 nm probing and a life time of 1.1 ± 0.6 ps using 442 nm probing based on transient anti-Stokes resonance Raman intensity decay. Cooling life times of 3.0 ± 1.0 ps and 25 ± 14 ps were predicted based on the decay of Boltzmann temperature values obtained from the ratio of anti-Stokes to Stokes intensity. Lifetimes of 7.5 ± 1.5 ps (60%) and ~ 20 ps (40%) were predicted from the time resolved IR studies monitoring the heating of the surrounding solvent. The difference in lifetimes of heme cooling and water heating was attributed to

the presence of two different decay channels involving classical diffusion process and collective motions of the protein.

1.5 OBJECTIVES

The initial vibrational energy relaxation dynamics study of the five-coordinate high-spin heme model compound $\text{Fe}^{\text{II}}\text{OEP-2MeIm}$ was done by Loparo et al.⁵⁴ using single pulse transient resonance Raman spectroscopy with ~ 10 ns pulses of 436 nm light. This simple transient Raman method provided valuable qualitative information about the picosecond relaxation processes occurring within the ns pulse duration such as the formation of preferential mode-specific non-equilibrium vibrational energy distributions in the ground state vibrational modes following the excited electronic state decay. Upon comparison to the similar studies in deoxyHb and 2MeIm bound protoheme, it was pointed out that the observed dynamics are metallo-porphyrin or heme group specific and the role of protein in the heme group relaxation events is very subtle.

So the main objectives of this work are:

1. To extend important work of Loparo et al to time-resolved spectroscopy domain in order to obtain quantitative information about the observed mode-specific vibrational dynamics of $\text{Fe}^{\text{II}}\text{OEP-2MeIm}$.
2. To derive direct comparisons between the dynamics of vastly studied heme proteins Hb and Mb and that of the simple model compound $\text{Fe}^{\text{II}}\text{OEP-2MeIm}$ that has entirely different peripheral substituents and no globular protein.

3. To study the photolysis of an imidazole ligand from $\text{Fe}^{\text{II}}\text{OEP}(\text{Im})_2$ in comparison to that of diatomic ligands in bound heme proteins such as MbCO, MbNO, MbO₂ or HbCO, HbNO and HbO₂.

4. To look for any changes in the vibrational dynamics of the model compounds as a function of the way the initial excited electronic state is prepared i.e. Q-band excitation versus B-band excitation and photolysis versus direct nonradiative decay.

5. To obtain relationships between the structure and energy relaxation mechanisms.

A close examination of all the time-resolved experiments done in heme proteins reveals that most of them involve electronic excitation to the Q-band except a very few that used Soret band excitation. Some of the studies used ligated hemes and others used deoxy like unligated hemes. The working hypothesis behind these studies is that the initial distribution of excess vibrational energy deposited in the ground electronic state from a photoexcited (or intermediate excited) electronic state, and the subsequent redistribution and relaxation dynamics, depend strongly upon (1) the total amount of excitation energy in the system (2) the nature of the electronic excited state that couples to the ground state in the IC process, and (3) the intrinsic coupling of each mode to other molecular and solvent degrees of freedom. In practice, then, there is no single lifetime for a given vibrational mode.

As a part of investigating how structure affects the vibrational dynamics, work was done on simpler compounds to start with, such as an important push-pull molecule para-nitroaniline⁵⁹. The vibrational dynamics of this compound as well as the effect of methyl group substitution on the amino group versus phenyl ring on the observed dynamics of

para-nitroaniline were studied. The vibrational dynamics of 2-methyl-4-nitroaniline, 2, 6-dimethyl-4-nitroaniline and N, N-dimethyl-4-nitroaniline in comparison to that of 4-nitroaniline were investigated using time-resolved resonance Raman spectroscopy.

1.6 REFERENCES

1. Fermi, G.; Perutz, M. F.; Shulman, R. G., Iron distances in hemoglobin: comparison of x-ray crystallographic and extended x-ray absorption fine structure studies. *Proceedings of the National Academy of Sciences of the United States of America* **1987**, 84, (17), 6167-8.
2. Perutz, M. F.; Fermi, G.; Luisi, B.; Shaanan, B.; Liddington, R. C., Stereochemistry of cooperative mechanisms in hemoglobin. *Accounts of Chemical Research* **1987**, 20, (9), 309-21.
3. Bettati, S.; Mozzarelli, A.; Perutz, M. F., Allosteric mechanism of haemoglobin: rupture of salt-bridges raises the oxygen affinity of the T-structure. *Journal of molecular biology* **1998**, 281, (4), 581-5.
4. Bluhm, M. M.; Bodo, G.; Dintzis, H. M.; Kendrew, J. C., The crystal structure of myoglobin. IV. A Fourier projection of sperm-whale myoglobin by the method of isomorphous replacement. *Proc. Roy. Soc. (London)* **1958**, A246, 369-89.
5. Kendrew, J. C.; Bodo, G.; Dintzis, H. M.; Parrish, R. G.; Wyckoff, H.; Phillips, D. C., A three-dimensional model of the myoglobin molecule obtained by x-ray analysis. *Nature* **1958**, 181, (4610), 662-6.
6. Lange, C.; Hunte, C., Crystal structure of the yeast cytochrome bc₁ complex with its bound substrate cytochrome c. *Proceedings of the National Academy of Sciences of the United States of America* **2002**, 99, (5), 2800-2805.

7. Takano, T.; Dickerson, R. E., Conformation change of cytochrome c. I. Ferrocycytochrome c structure refined at 1.5 Å resolution. *Journal of Molecular Biology* **1981**, 153, (1), 79-94.
8. Swanson, R.; Trus, B. L.; Mandel, N.; Mandel, G.; Kallai, O. B.; Dickerson, R. E., Tuna cytochrome c at 2.0 Å resolution. I. Ferricytochrome structure analysis. *Journal of Biological Chemistry* **1977**, 252, (2), 759-75.
9. Hu, C.; An, J.; Noll Bruce, C.; Schulz Charles, E.; Scheidt, W. R., Electronic configuration of high-spin imidazole-ligated iron(II) octaethylporphyrinates. *Inorganic chemistry* **2006**, 45, (10), 4177-85.
10. Zijlstra, W. G.; Buursma, A.; Meeuwse-van der Roest, W. P., Absorption spectra of human fetal and adult oxyhemoglobin, de-oxyhemoglobin, carboxyhemoglobin, and methemoglobin. *Clinical chemistry* **1991**, 37, (9), 1633-8.
11. Tsai, H.-H.; Simpson, M. C., Isolated Impact of Ruffling on the Vibrational Spectrum of Ni Porphyrins. Diagnosing Out-of-Plane Distortions. *Journal of Physical Chemistry A* **2004**, 108, (7), 1224-1232.
12. Li, X. Y.; Czernuszewicz, R. S.; Kincaid, J. R.; Stein, P.; Spiro, T. G., Consistent porphyrin force field. 2. Nickel octaethylporphyrin skeletal and substituent mode assignments from nitrogen-15, meso-d4, and methylene-d16 Raman and infrared isotope shifts. *Journal of Physical Chemistry* **1990**, 94, (1), 47-61.
13. Bucher, T.; Kaspers, J., Photochemical cleavage of carbon monoxide-myoglobin by ultraviolet radiation (activity of the protein component of the pigment for absorbed quanta). *Biochimica et Biophysica Acta* **1947**, 1, 21-34.

14. Gibson, Q. H.; Ainsworth, S., Photosensitivity of hem compounds. *Nature (London, United Kingdom)* **1957**, 180, 1416-17.
15. Brunori, M.; Giacometti, G. M., Photochemistry of hemoproteins. *Methods in Enzymology* **1981**, 76, (Hemoglobins), 582-95.
16. Austin, R. H.; Beeson, K. W.; Eisenstein, L.; Frauenfelder, H.; Gunsalus, I. C., Dynamics of ligand binding to myoglobin. *Biochemistry* **1975**, 14, (24), 5355-73.
17. Chernoff, D. A.; Hochstrasser, R. M.; Steele, A. W., Geminate recombination of oxygen and hemoglobin. *Proceedings of the National Academy of Sciences of the United States of America* **1980**, 77, (10), 5606-10.
18. Reynolds, A. H.; Rand, S. D.; Rentzepis, P. M., Mechanisms for excited state relaxation and dissociation of oxymyoglobin and carboxymyoglobin. *Proceedings of the National Academy of Sciences of the United States of America* **1981**, 78, (4), 2292-6.
19. Cornelius, P. A.; Hochstrasser, R. M.; Steele, A. W., Ultrafast relaxation in picosecond photolysis of nitrosylhemoglobin. *Journal of Molecular Biology* **1983**, 163, (1), 119-28.
20. Petrich, J. W.; Poyart, C.; Martin, J. L., Photophysics and reactivity of heme proteins: a femtosecond absorption study of hemoglobin, myoglobin, and protoheme. *Biochemistry* **1988**, 27, (11), 4049-60.
21. Martin, J. L.; Migus, A.; Poyart, C.; Lecarpentier, Y.; Astier, R.; Antonetti, A., Femtosecond photolysis of carbon monoxide-ligated protoheme and hemoproteins: appearance of deoxy species with a 350-fsec time constant. *Proceedings of the National Academy of Sciences of the United States of America* **1983**, 80, (1), 173-7.

22. Henry, E. R.; Levitt, M.; Eaton, W. A., Molecular dynamics simulation of photodissociation of carbon monoxide from hemoglobin. *Proceedings of the National Academy of Sciences of the United States of America* **1985**, 82, (7), 2034-8.
23. Henry, E. R.; Eaton, W. A.; Hochstrasser, R. M., Molecular dynamics simulations of cooling in laser-excited heme proteins. *Proceedings of the National Academy of Sciences of the United States of America* **1986**, 83, (23), 8982-6.
24. Franzen, S.; Kiger, L.; Poyart, C.; Martin, J.-L., Heme photolysis occurs by ultrafast excited state metal-to-ring charge transfer. *Biophysical Journal* **2001**, 80, (5), 2372-2385.
25. Kholodenko, Y.; Volk, M.; Gooding, E.; Hochstrasser, R. M., Energy dissipation and relaxation processes in deoxy myoglobin after photoexcitation in the Soret region. *Chemical Physics* **2000**, 259, (1), 71-87.
26. Ye, X.; Demidov, A.; Rosca, F.; Wang, W.; Kumar, A.; Ionascu, D.; Zhu, L.; Barrick, D.; Wharton, D.; Champion, P. M., Investigations of Heme Protein Absorption Line Shapes, Vibrational Relaxation, and Resonance Raman Scattering on Ultrafast Time Scales. *Journal of Physical Chemistry A* **2003**, 107, (40), 8156-8165.
27. Ye, X.; Demidov, A.; Champion, P. M., Measurements of the Photodissociation Quantum Yields of MbNO and MbO₂ and the Vibrational Relaxation of the Six-Coordinate Heme Species. *Journal of the American Chemical Society* **2002**, 124, (20), 5914-5924.
28. Cupane, A.; Leone, M.; Vitano, E.; Cordone, L., Structural and dynamic properties of the heme pocket in myoglobin probed by optical spectroscopy. *Biopolymers* **1988**, 27, (12), 1977-97.

29. Lehmann, K. K.; Pate, B. H.; Scoles, G. In *Intramolecular vibrational energy relaxation (IVR) in large molecules: homogeneous IVR lifetimes and the mechanism of energy relaxation*, 1992; 1992; pp 53-65.
30. Hamm, P.; Wiemann, S.; Zurek, M.; Zinth, W., Highly sensitive multichannel spectrometer for subpicosecond spectroscopy in the mid-infrared. *Optics Letters* **1994**, 19, (20), 1642-4.
31. Hamm, P.; Lim, M.; Hochstrasser, R. M., Vibrational energy relaxation of the cyanide ion in water. *Journal of Chemical Physics* **1997**, 107, (24), 10523-10531.
32. Hamm, P.; Ohline, S. M.; Zinth, W., Vibrational cooling after ultrafast photoisomerization of azobenzene measured by femtosecond infrared spectroscopy. *Journal of Chemical Physics* **1997**, 106, (2), 519-529.
33. Lian, T.; Locke, B.; Kholodenko, Y.; Hochstrasser, R. M., Energy Flow from Solute to Solvent Probed by Femtosecond IR Spectroscopy: Malachite Green and Heme Protein Solutions. *Journal of Physical Chemistry* **1994**, 98, (45), 11648-56.
34. Okamoto, H.; Tasumi, M., Picosecond transient infrared spectroscopy of electronically excited 4-dimethylamino-4'-nitrostilbene in the fingerprint region (1640-940 cm⁻¹). *Chemical Physics Letters* **1996**, 256, (4,5), 502-508.
35. Okamoto, H., High-sensitivity measurement of ultrafast transient infrared spectra based on optically heterodyned detection of absorption anisotropy. *Chemical Physics Letters* **1998**, 283, (1,2), 33-38.
36. Kozich, V.; Dreyer, J.; Ashihara, S.; Werncke, W.; Elsaesser, T., Mode-selective O-H stretching relaxation in a hydrogen bond studied by ultrafast vibrational spectroscopy. *Journal of Chemical Physics* **2006**, 125, (7), 074504/1-074504/9.

37. Wang, Z.; Pang, Y.; Dlott, D. D., The vibrational Stokes shift of water (HOD in D₂O). *Journal of Chemical Physics* **2004**, 120, (18), 8345-8348.
38. Lawrence, C. P.; Skinner, J. L., Vibrational spectroscopy of HOD in liquid D₂O. VI. Intramolecular and intermolecular vibrational energy flow. *Journal of Chemical Physics* **2003**, 119, (3), 1623-1633.
39. Tokmakoff, A.; Sauter, B.; Kwok, A. S.; Fayer, M. D., Phonon-induced scattering between vibrations and multiphoton vibrational up-pumping in liquid solution. *Chemical Physics Letters* **1994**, 221, (5-6), 412-18.
40. Wang, Z.; Pang, Y.; Dlott Dana, D., The vibrational Stokes shift of water (HOD in D₂O). *J Chem Phys FIELD Full Journal Title: The Journal of chemical physics* **2004**, 120, (18), 8345-8.
41. Champion, P. M.; Lange, R., On the quantitation of light emission from cytochrome c in the low quantum yield limit. *Journal of Chemical Physics* **1980**, 73, (12), 5947-57.
42. Causgrove, T. P.; Dyer, R. B., Picosecond structural dynamics of myoglobin following photolysis of carbon monoxide. *Journal of Physical Chemistry* **1996**, 100, (8), 3273-7.
43. Ogilvie, J. P.; Plazanet, M.; Dadusc, G.; Miller, R. J. D., Dynamics of Ligand Escape in Myoglobin: Q-Band Transient Absorption and Four-Wave Mixing Studies. *Journal of Physical Chemistry B* **2002**, 106, (40), 10460-10467.
44. Goodno, G. D.; Miller, R. J. D., Femtosecond Heterodyne-Detected Four-Wave-Mixing Studies of Deterministic Protein Motions. 1. Theory and Experimental Technique

of Diffractive Optics-Based Spectroscopy. *Journal of Physical Chemistry A* **1999**, 103, (49), 10619-10629.

45. Bu, L.; Straub, J. E., Vibrational energy relaxation of "tailored" hemes in myoglobin following ligand photolysis supports energy funneling mechanism of heme "cooling". *Journal of Physical Chemistry B* **2003**, 107, (38), 10634-10639.

46. Sagnella, D. E.; Straub, J. E., Directed Energy "Funneling" Mechanism for Heme Cooling Following Ligand Photolysis or Direct Excitation in Solvated Carbonmonoxy Myoglobin. *Journal of Physical Chemistry B* **2001**, 105, (29), 7057-7063.

47. Nagai, K.; Kitagawa, T., Differences in iron(II)-Ne(His-F8) stretching frequencies between deoxyhemoglobins in the two alternative quaternary structures. *Proceedings of the National Academy of Sciences of the United States of America* **1980**, 77, (4), 2033-7.

48. Petrich, J. W.; Martin, J. L.; Houde, D.; Poyart, C.; Orszag, A., Time-resolved Raman spectroscopy with subpicosecond resolution: vibrational cooling and delocalization of strain energy in photodissociated (carbonmonoxy)hemoglobin. *Biochemistry* **1987**, 26, (24), 7914-23.

49. Alden, R. G.; Chavez, M. D.; Ondrias, M. R.; Courtney, S. H.; Friedman, J. M., Direct measurement of vibrational temperatures in photoexcited deoxyhemoglobin on picosecond time scales. *Journal of the American Chemical Society* **1990**, 112, (8), 3241-2.

50. Alden, R. G.; Ondrias, M. R.; Courtney, S.; Findsen, E. W.; Friedman, J. M., Power-induced broadening of transient resonance Raman spectra of deoxyhemoglobin. *Journal of Physical Chemistry* **1990**, 94, (1), 85-90.

51. Alden, R. G.; Schneebeck, M. C.; Ondrias, M. R.; Courtney, S. H.; Friedman, J. M., Mode-specific relaxation dynamics of photoexcited iron(II) protoporphyrin IX in hemoglobin. *Journal of Raman Spectroscopy* **1992**, 23, (10), 569-74.
52. Li, P.; Sage, J. T.; Champion, P. M., Probing picosecond processes with nanosecond lasers: electronic and vibrational relaxation dynamics of heme proteins. *Journal of Chemical Physics* **1992**, 97, (5), 3214-27.
53. Schneebeck, M. C.; Vigil, L. E.; Ondrias, M. R., Mode-selective energy localization during photoexcitation of deoxyhemoglobin and heme model complexes. *Chemical Physics Letters* **1993**, 215, (1-3), 251-6.
54. Loparo, J. J.; Cheatum, C. M.; Ondrias, M. R.; Simpson, M. C., Transient Raman observations of heme vibrational dynamics in five-coordinate iron porphyrins. *Chemical Physics* **2003**, 286, (2-3), 353-374.
55. Lingle, R., Jr.; Xu, X.; Zhu, H.; Yu, S. C.; Hopkins, J. B., Picosecond Raman study of energy flow in a photoexcited heme protein. *Journal of Physical Chemistry* **1991**, 95, (23), 9320-31.
56. Lingle, R., Jr.; Xu, X.; Zhu, H.; Yu, S. C.; Hopkins, J. B.; Straub, K. D., Direct observation of hot vibrations in photoexcited deoxyhemoglobin using picosecond Raman spectroscopy. *Journal of the American Chemical Society* **1991**, 113, (10), 3992-4.
57. Mizutani, Y.; Kitagawa, T., Direct observation of cooling of heme upon photodissociation of carbonmonoxy myoglobin. *Science (Washington, D. C.)* **1997**, 278, (5337), 443-446.
58. Mizutani, Y.; Kitagawa, T., Ultrafast dynamics of myoglobin probed by time-resolved resonance Raman spectroscopy. *Chemical Record* **2001**, 1, (3), 258-275.

59. Gunaratne, T.; Challa, J. R.; Simpson, M. C., Energy flow in push-pull chromophores: vibrational dynamics in para-nitroaniline. *ChemPhysChem* **2005**, 6, (6), 1157-1163.

CHAPTER 2

EXPERIMENTAL METHODS AND INSTRUMENTATION

2.1 INTRODUCTION.

The pump-probe technique¹ is the most widely used among the various ultrafast spectroscopic tools. It requires two synchronized laser pulses of duration usually shorter than the dynamic event being studied and of appropriate wavelength. Typically, a higher energy laser pulse, called the pump, is used to initiate some process of interest like a chemical reaction in a sample of molecules. Another lower energy laser pulse, called the probe, is used to study the dynamic changes occurring in the sample as a function of time with the help of a spectroscopic technique such as absorption, transmission, emission or scattering. The delay between the arrival times of the pump and probe pulses at the sample is controlled, by making one of the beams travel a fixed optical path and the second beam go through a variable path length delay stage.

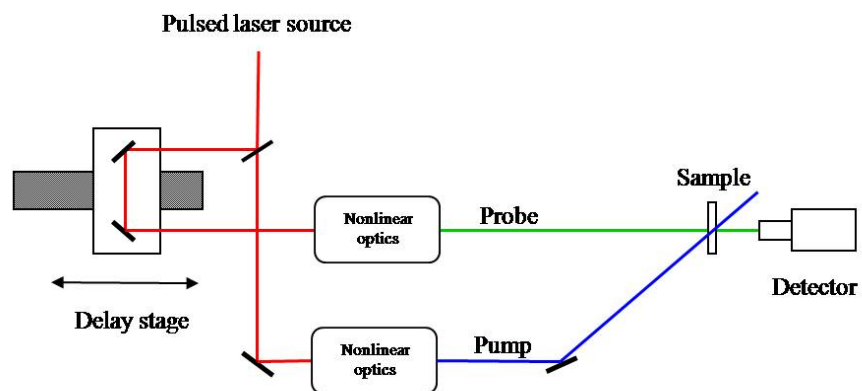


Figure 2 - 1 General Pump-Probe scheme in time-resolved spectroscopy.

The delay stage consists of a retro reflector mounted on a computer controlled linear translation stage with micrometer precision. Since the speed of light is finite and the two pulses are in synchrony, an optical path length difference of 1 μm between the two beams corresponds to a time delay of 3.336 fs (fs = 10^{-15} s) between the pump and probe pulses. Upon interaction with the sample, the changes in a spectroscopic property of the probe with and without the presence of pump beam are detected. The detected signal provides spectroscopic information about the transient species and the change in signal as a function of time delay gives the kinetic information. UV-visible absorption and resonance Raman scattering are the two spectroscopic techniques of our choice for probing the vibrational dynamics subsequent to photo excitation in heme systems.

The aim is to investigate the vibrational dynamics in hemes and other push-pull chromophore systems. So the protocol is to prepare an initial vibrational excited state or nonthermal vibrational energy distribution and follow the evolution of it in time^{2, 3}. IR pump/probe^{4,12}, also known as IR transient absorption and IR pump/Raman probe^{4, 10, 13-20} are the two most important pump-probe methods successfully applied in the literature by various groups. An indirect approach will be to start with a nonthermal vibrational energy distribution created from an excited electronic state decay and follow the evolution of it with a Raman probe. This is done using time resolved resonance Raman spectroscopy and has been extensively applied to several biologically important systems that respond to visible light of the electromagnetic spectrum such as retinal²¹⁻²³, and beta-carotene²⁴. UV-visible transient absorption spectroscopy coupled with time resolved resonance Raman spectroscopy can provide the most valuable information regarding the photochemical and photophysical properties of any photoactive molecule.

2.2 TRANSIENT ABSORPTION SPECTROSCOPY

Time evolution of excited electronic species or the chemical products following photo-excitation of a sample can be studied using transient absorption spectroscopy²⁵. Usually a pump beam in the UV-vis wavelength region is passed through a chopper set to half the frequency of repetition rate (500 Hz) of the laser to get subsequent pump-on and pump-off conditions in the sample. Then a white light continuum probe pulse^{26, 27} passed through the excited region of the sample is dispersed with a monochromator and detected with a CCD camera or a photomultiplier tube coupled with a lock-in amplifier. The ratio of the intensity of the transmitted probe beam as a function of wavelength with the pump-on and pump-off conditions is used to get a transient absorption spectrum according to the following relation.

$$\Delta A = -\log \left[\frac{I_{t, \text{pump-on}}}{I_{t, \text{pump-off}}} \right]$$

Following photo excitation by the pump, the probe pulses can be absorbed or amplified (stimulated emission). The high flux pump beam causes bleaching of the ground state absorption due to depletion of the ground state population. With the pump on condition, the probe beam appears to be transmitting more. Stimulated emission or fluorescence from the excited electronic state is also possible, in which case the probe beam appears to be transmitting more. The excited state or the transient species itself can absorb, in which case the probe beam seems to be transmitting less. So, the main features in a transient absorption spectrum are bleaching, stimulated emission and transient or excited electronic state absorption. Bleaching signals appear as negative absorption peaks at wavelengths corresponding to the ground state absorption peaks and report the loss and recovery of population from the ground electronic state. Stimulated emission from the

excited electronic states also appears as negative absorption, but usually red-shifted from the ground state absorption peaks and report the excited state decay. Transient absorption signals appear as standard positive absorption peaks which are due to absorption of the transient species being formed or the absorption of the excited electronic state to higher states. Often the individual spectral features are overlapped with one another as the underlying vibrational progressions make them broad. Nonlinear curve fitting analysis is performed to separate the overlapping transient absorption peaks and extract useful information. The transient absorption signal at any given wavelength as a function of the time delay between the pump and probe pulses gives the kinetic information.

2.3 TIME RESOLVED RESONANCE RAMAN SPECTROSCOPY (TRRRS)

When electromagnetic radiation passes through matter, most of the radiation continues in the original direction while part of it gets absorbed, but a small fraction of light is also scattered in other directions. Majority of the scattered light has the same wavelength as incident wavelength and is known as Rayleigh scattering. Light that is scattered at wavelengths shifted from the incident wavelength is known as Raman scattering²⁸. Raman scattering can occur with a change in vibrational, rotational or electronic energy of a molecule, but we are primarily concerned with the vibrational Raman scattering. Raman scattered light occurs at wavelengths that are shifted from the incident light by energies of molecular vibrations. Raman spectroscopy is the measurement of wavelength and intensity of such inelastic scattered light from molecules and is presented as intensity versus Ramanshift plots; here Raman shift is the energy

difference between the incident photon and the scattered photon expressed in the units of cm^{-1} .

There are two types of Raman scattering, namely Stokes and anti-Stokes Raman scattering. Radiation scattering to the lower energy side of the exciting line is called Stokes Raman scattering, while the radiation scattering to the higher energy side of the exciting laser is called anti-stokes Raman scattering. A photon of energy $h\nu$ upon interaction with a molecule in a vibrational state (ground state or excited state) transfers part of its energy to the molecule and the scattered photon will have a reduced energy of $h\nu-h\nu_v$. This leads to Stokes Raman scattering. Similarly a molecule which is already in an excited vibrational state can transfer part of its energy to the incident photon and the scattered photon will have an increased energy of $h\nu+h\nu_v$. This leads to anti-Stokes Raman scattering.

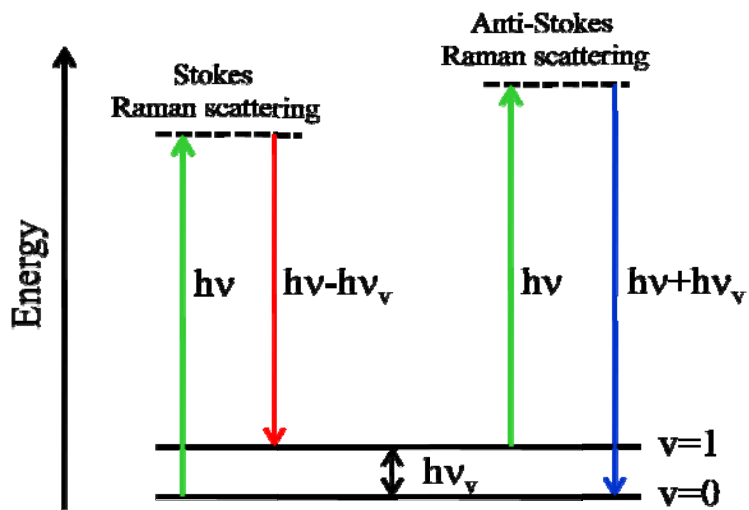


Figure 2 - 2 Energy level diagrams for Stokes and anti-Stokes Raman scattering.

Anti-Stokes Raman scattering occurs only from molecules in the excited vibrational levels whereas the Stokes Raman scattering occurs from molecules both in the

ground and excited vibrational states. Anti-Stokes lines will be weaker than the Stokes lines in a Raman spectrum, since the excited vibrational level population will be lower than that of a ground vibrational level at any given temperature. In spite of the weak intensity, anti-Stokes Raman scattering provides a useful probe of the vibrational dynamics in time-resolved spectroscopy since the origin of it is only from excited vibrational populations.

Intensity of the Raman scattered light can be significantly enhanced by tuning the excitation wavelength closer to an allowed electronic transition of the sample. This is known as resonance Raman Effect. Resonance Raman spectroscopy is very useful in studying the active sites of biological proteins, since the signal from only a specific part of the protein can be enhanced by carefully selecting the excitation wavelength²⁹. The intensity of the Raman scattered light also depends upon the concentration of sample, power of the incident beam, the temperature and the polarizability of the molecule.

In a time-resolved Raman experiment, usually the anti-Stokes Raman scattering of the probe beam with and without the presence of the pump beam is measured to get a pump-probe spectrum and a probe only spectrum respectively. The anti Stokes Raman spectrum with only the pump beam is also measured. Subtracting the pump only and probe only spectra from the pump-probe spectrum gives a transient Raman spectrum. By varying the time delay between the pump and probe beams a series of transient Raman spectra are obtained. The excited vibrational dynamics information is obtained by plotting the integrated peak intensity, peak position and width of the various vibrational modes visible in the transient spectra as a function of the time delay between the pump

and probe beams. The Stokes Raman scattering can also be measured in the same fashion to obtain recovery time scales of the ground state population.

2.4 GENERATION AND AMPLIFICATION OF ULTRASHORT PULSES

Time resolved experiments to monitor the formation of transient species with high temporal resolution require the use of ultrafast lasers with high enough energy per pulse. So a brief understanding of the generation and amplification of ultrashort pulses is essential for anyone working in the area of time-resolved spectroscopy. The development of ultrafast laser technology and its applications^{1, 30-37} have been extensively discussed in the literature. Since the advent of self mode-locking in Titanium doped Sapphire (Ti:Sapphire) laser material³⁸, the ultrafast laser technology has been greatly commercialized and most of the research laboratories still use Ti:Sapphire based femtosecond lasers. The broad gain bandwidth of Ti:Sapphire, its high thermal conductivity and high energy density threshold makes it a very good energy storage medium for lasers³⁹ and is used to produce pulses as short as 5 fs in duration. But the peak energies per pulse can still be too low to be useful in photophysics and photochemistry. For example a pulsed light beam with 100 mW average power and a repetition rate of 100 MHz, typical of the mode-locked oscillators, has only 1nJ energy per pulse. So the nJ energy level femtosecond pulses from a mode-locked Ti:Sapphire laser need to be amplified to mJ energy level to put them to use. But a 100 fs pulse train with 1 mJ energy per pulse focused to a 100 μm spot, typical of the beam size in most regenerative amplifiers, will have a peak intensity of 10^{12} W/cm^2 , three orders of magnitude greater than the damage threshold of most optical materials. So a direct

amplification of the femtosecond beam leads to very high peak intensities in the gain medium resulting in nonlinear effects that will deteriorate the beam quality and eventually destroy the crystal. This problem is usually overcome by using chirped pulse amplification instead.

Chirped Pulse Amplification

The technique of chirped pulse amplification⁴⁰⁻⁴³ was introduced by Prof. Mourou and his coworkers at the University of Rochester in the mid 1980s. Ti:Sapphire as a laser gain medium had not been introduced at that time and dyes like Rhodamine 6G were the main amplifier media. The principle of CPA is illustrated in the Figure 2-3.

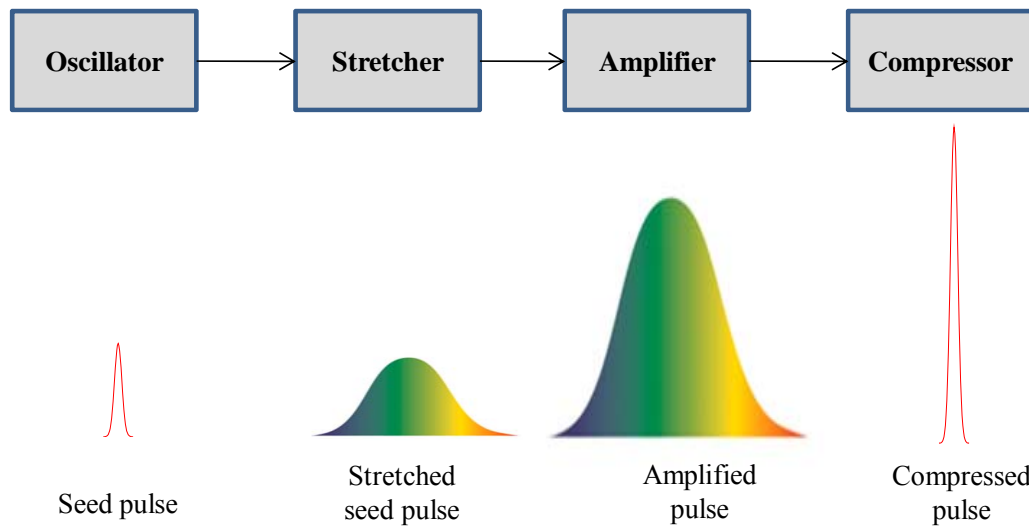


Figure 2 - 3 Principle of chirped pulse amplification. The femtosecond seed pulse is stretched in time prior to amplification and compressed back to its near original duration subsequent to amplification.

The basic idea is to stretch the pulse duration before amplification, thus significantly reducing its peak intensity. This low intensity optical pulse is then amplified, with a chance of significantly reduced gain damage⁴¹. Following amplification, the pulse is recompressed to its near original duration with high energy

value per pulse. The essential criterion for obtaining a cleaner pulse with near initial pulse duration is a matched Stretcher – Compressor pair. This is done using a stretcher design proposed by Martinez⁴⁴ and the compressor design proposed by Treacy⁴⁵.

2.5 PULSE DURATION MEASUREMENT OF ULTRASHORT PULSES

To measure a fast event, a detector with a faster response is needed. Since the detectors with response times faster than ultrafast pulse durations are very limited, usually an alternative method known as the ‘autocorrelation’ is used to measure the pulse duration. The ultrafast beam is split into two parts, a variable time delay is introduced between them and they are mixed in an instantaneously responding medium such as a nonlinear crystal to generate a pulsed light signal of doubled frequency. The intensity of the signal is given by

$$I_{sig}(t, \tau) \propto I_1(t) * I_2(t - \tau)$$

Where, t is time, τ is time delay between the two pulses, I_1 is the intensity of the first pulse and I_2 is the intensity of the second time-delayed pulse. Since the detectors are usually too slow to resolve this signal in time, the average intensity is measured using a photodiode and is known as the intensity autocorrelation. The intensity autocorrelation is given by

$$I_{sig}^{avg}(\tau) = \int_{-\infty}^{\infty} I_1(t) * I_2(t - \tau) dt$$

The intensity autocorrelation does not give any information about the signal spectral distribution and phase. The photodiode can be replaced by a grating monochromator coupled with a CCD camera in order to measure the signal spectrum

versus time delay. This provides both the time resolution and frequency resolution and is famously known as frequency resolved optical gating or simply FROG^{46, 47}. Another simplified version of the FROG designed by Rick Trebino and coworkers is also widely used in several research laboratories. This design uses a simple Fresnel biprism that eliminates the beam splitter, optical delay stage and the beam pointing optics. A thick nonlinear crystal is used to simultaneously perform the role of a thin nonlinear crystal and spectrometer commonly used in FROG schemes. And hence this is named Grating Eliminated No-nonsense Observation of Ultrafast Incident Laser Light E-fields or simply GRENOUILLE^{48, 49}. Since there is no moving optics involved in this scheme, a single shot auto-correlation with both intensity and phase information can be obtained.

2.6 CLARK-MXR INC. CPA-1000 FEMTOSECOND LASER SYSTEM

The femtosecond laser in our lab is a commercial Clark – MXR Inc. CPA – 1000 system capable of producing 100 fs pulses of 800 nm light with 1mJ energy at variable repetition rate, though we usually run it at 1 kHz.

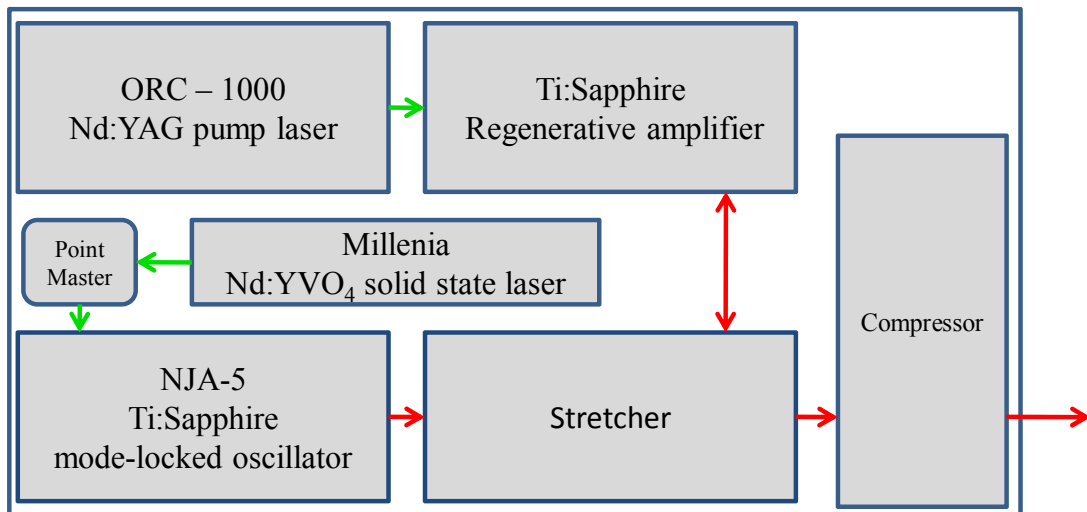


Figure 2 - 4 The schematic layout of the various components of Clark-MXR Inc. CPA-1000 fs laser system.

The essential components of this laser system are 1. Millenia pump laser (Spectra Physics Inc.) 2. Mode-locked Ti:Sapphire oscillator (NJA-5, Clark MXR Inc.) 3. Pulse Stretcher 4. Q-switched intra-cavity doubled Nd:YAG pump laser (ORC-1000, Clark-MXR Inc.) 5. Ti:Sapphire based Regenerative amplifier and 6. Pulse compressor. This one also works based on the principle of Chirped pulse amplification.

Millenia is a diode pumped, intra-cavity frequency-doubled Nd: YVO₄ continuous wave (CW) laser that can produce up to 5.5 W of 532 nm light. The oscillator is pumped by Millenia CW laser output at 4.0 W, with active pointing stability (Point Master, Clark-MXR Inc.). The oscillator can be mode-locked to produce a train of femtosecond pulses (~100-150 fs) at 97 MHz repetition rate with 800 nm center wavelength and 300 mW average power. The center wavelength is also tunable in a small range from 780-836 nm without significantly affecting the pulse characteristics. Thus the oscillator is the most important part of the CPA-1000 system responsible for the generation of seed femtosecond pulses which are then amplified within the rest of the system. These 100 fs pulses are stretched out to roughly 300 ps in duration in the stretcher. A tiny fraction of the oscillator output is sent to a Pockels cell driver unit (DT-105, Clark-MXR Inc.) through a photodiode, which provides a trigger for synchronous firing of ORC-1000 Nd:YAG laser. The photodiode output is also used to monitor the mode-locked pulses and the stability of mode-locking on a daily basis.

The stretched seed pulses are then injected into the regenerative – amplifier with the help of a time-gated polarization rotation device (Pockels cell), the timing of which is controlled by the Delay 1 setting of the DT-105 unit. The regenerative amplifier by itself is a lasing cavity with Ti:Sapphire gain medium pumped at 1 kHz by a Q-switched, intra

cavity frequency-doubled Nd:YAG laser with 8 W average power at center wavelength 532 nm and ~ 150 ns pulse duration. The seed beam, carefully overlapped with the amplifier cavity mode travels back and forth between the cavity end mirrors through the Ti:Sapphire crystal and gets amplified. The amplified seed pulse at the peak of its waveform is ejected out of the amplifier cavity, also known as cavity dumping, with the help of another time-gated polarization rotation, the timing of which is controlled by the Delay 2 setting of the DT-105 unit. A tiny fraction of the amplified output is sent to a photodiode for monitoring the waveform of the amplified seed pulse. The amplified pulses are then sent into the compressor which recompresses the pulse width back to its near original duration. The final output of the amplified pulse is ~ 0.8 mJ across the 785-840 nm tunability range with 100-150 fs pulse duration and 1 kHz repetition rate.

Wavelength tunability

The simplest approach to generate visible light from the ~ 800 nm output of the CPA1000 system is frequency doubling in a nonlinear crystal. The inherent tunability in the output of CPA1000 results in visible light tunable from 392 to 420 nm. Unlike UV-vis absorption spectra which are very broad, typical bandwidths of a vibrational mode correspond to only a few tens of wavenumbers. In order to be able to use this visible output to study the vibrational dynamics, the spectral width of these pulses need to be smaller than 30 cm^{-1} . At the same time the pulses need to be short enough to monitor the quickly evolving dynamics with high temporal resolution. For a transform limited Gaussian pulse, this corresponds to a temporal width of 0.49 ps or higher. Narrow band width pulses are needed for better spectral resolution and the shortest pulses are required

for a better temporal resolution. This was achieved by using a 30 mm long Potassium dihydrogen phosphate (KDP) crystal for frequency doubling.

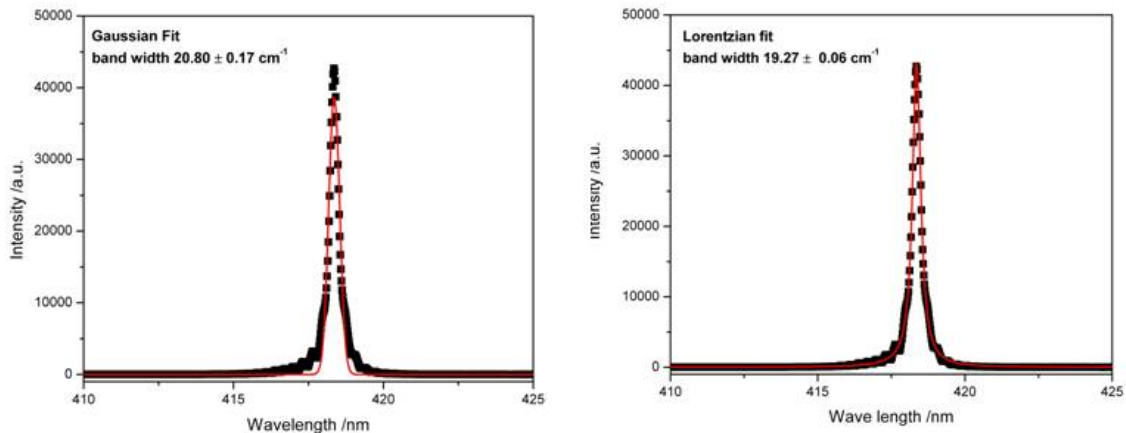


Figure 2 - 5 The second harmonic spectrum of the CPA-1000 output after frequency doubling in a 30 mm long KDP crystal. The nonlinear Gaussian and Lorentzian peak fits together with the corresponding bandwidths are shown. The spectral shape deviates from Gaussian and has a Lorentzian line shape.

This novel method produces relatively clean $17\text{-}25 \text{ cm}^{-1}$ bandwidth visible pulses while still maintaining the sub-picosecond time resolution. The spectral shape deviates from Gaussian after passing through the long crystal and appears more like a Lorentzian as shown in the Figure 2-5.

2.7 SINGLE COLOR PUMP-PROBE SETUP FOR TRRRS:

Frequency-doubling of approximately 300 mW of the CPA-1000 output (785-840 nm) in a 30 mm long KDP crystal is used to produce 60-70 uJ per pulse energy at 392-413 nm. This corresponds to a second harmonic conversion efficiency of 20-25 %. A dielectric mirror with high reflectance in the 400 nm region is used to separate the residual 800 nm light. A 50-50 beam splitter generates pump and probe beams of the

second harmonic light, which are attenuated to 5.5 and 2.5 $\mu\text{J}/\text{pulse}$ respectively using neutral density filters. The probe beam after passing through a computer controlled, calibrated translation stage (MM3000, Newport Inc.) is overlapped with the pump beam at the sample in a near collinear geometry ($\sim 5^\circ$). Both the pump and probe beams are focused to a spot size of less than 1 mm using 750 mm fused silica lenses. The relative polarization of the pump beam with respect to that of the probe beam is kept at magic angle (54.7°) by using a polarization rotator to avoid any contributions from the orientational dynamics in the kinetic information being measured.

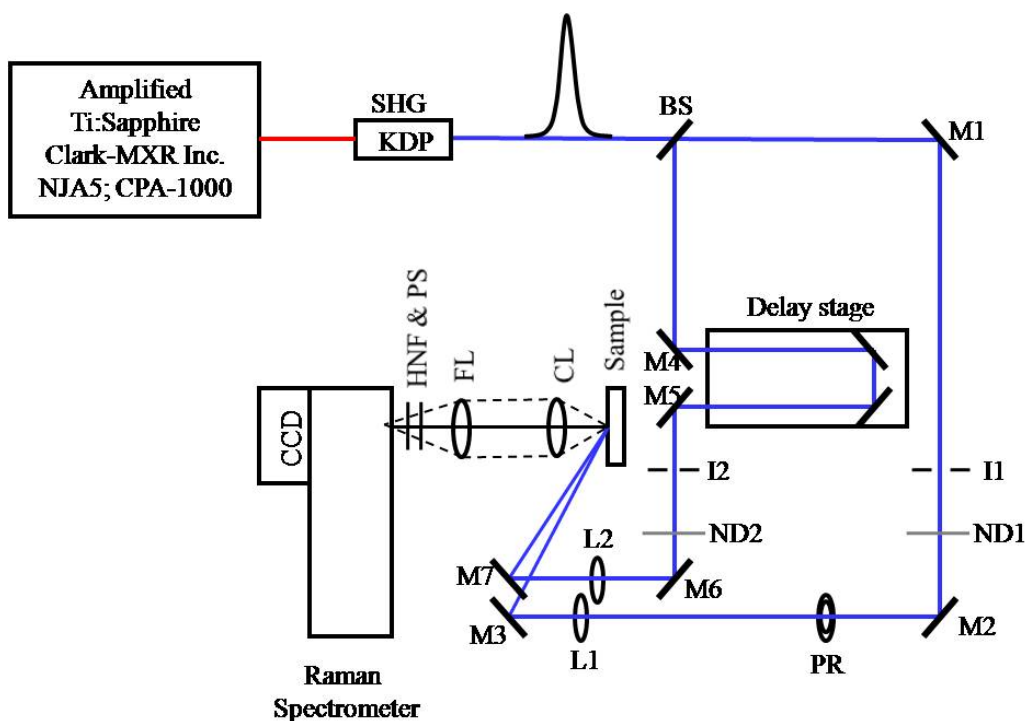


Figure 2 - 6 Single color pump-probe setup for time resolved resonance Raman spectroscopy. SHG: second harmonic generation, KDP: Potassium dihydrogen phosphate crystal, BS: beam splitter, M1 to M7: Mirrors, I1 and I2: apertures, ND1 and ND2: neutral density filters, PR: polarization rotator, L1 and L2: +750 mm fused silica lenses, CL: collecting lens, FL: focusing lens, HNF: holographic notch filter, PS: polarization scrambler, CCD: charge coupled device camera.

The sample is circulated through a 1 mm quartz flow cell using Teflon tubing so that a fresh volume of the sample is available for each pulse. Raman spectra are collected

in a 135° back-scattering geometry using a matched focusing and collecting lens pair. Rayleigh scattering is rejected using an angle-tuned holographic super notch filter (Kaiser Optics Inc.) appropriate for the laser wavelength. A polarization scrambler is used to remove any polarization contributions in the scattered light. The Raman scattering is dispersed with a 0.5 m imaging spectrograph (Chromex 500 IS) and recorded with a thermoelectrically cooled, back-illuminated CCD camera (DU-420 BV, Andor) or liquid nitrogen cooled, back-illuminated CCD camera (Photometrics).

Determining the temporal overlap point of the pump and probe (time-zero) and temporal correlation function of the two beams was not straight forward. Appropriate nonlinear materials were not readily available for wavelengths around 400 nm and the pulses were too long to use coherent behavior. A two step procedure was employed. First, Time-zero was estimated by mixing the 800 nm beams along the pump and probe beams and doubling them in a 100 μm Type I BBO crystal ($\theta=44.3^\circ$, $\phi=90^\circ$) at the sample position. Second, the residual 800 nm pulses along the pump beam are mixed with the probe beam at the sample position in a 100 μm Type II BBO crystal ($\theta=55.5^\circ$, $\phi=0^\circ$). This gave us the time-zero and temporal profile of the pulses used for the Raman studies which are shown in Fig 2-7.

Since both the pulses have the same wavelength in this kind of setup, their identities as pump and probe depend only on which one arrives first at the sample. Thus when the pump and probe pulses have the same flux, the magnitude of the change in Raman intensity for a given vibrational mode induced by the pump and measured by the probe will be symmetric about the zero-time delay. This was illustrated using the transient anti-Stokes Raman intensity of the phenyl breathing mode at 867 cm^{-1} of *para*-

nitroaniline in DMSO as a function of the time delay and hence is routinely used in our laboratory for establishing the zero-time delay of single color TRRRS experiments with wavelengths around 400 nm.

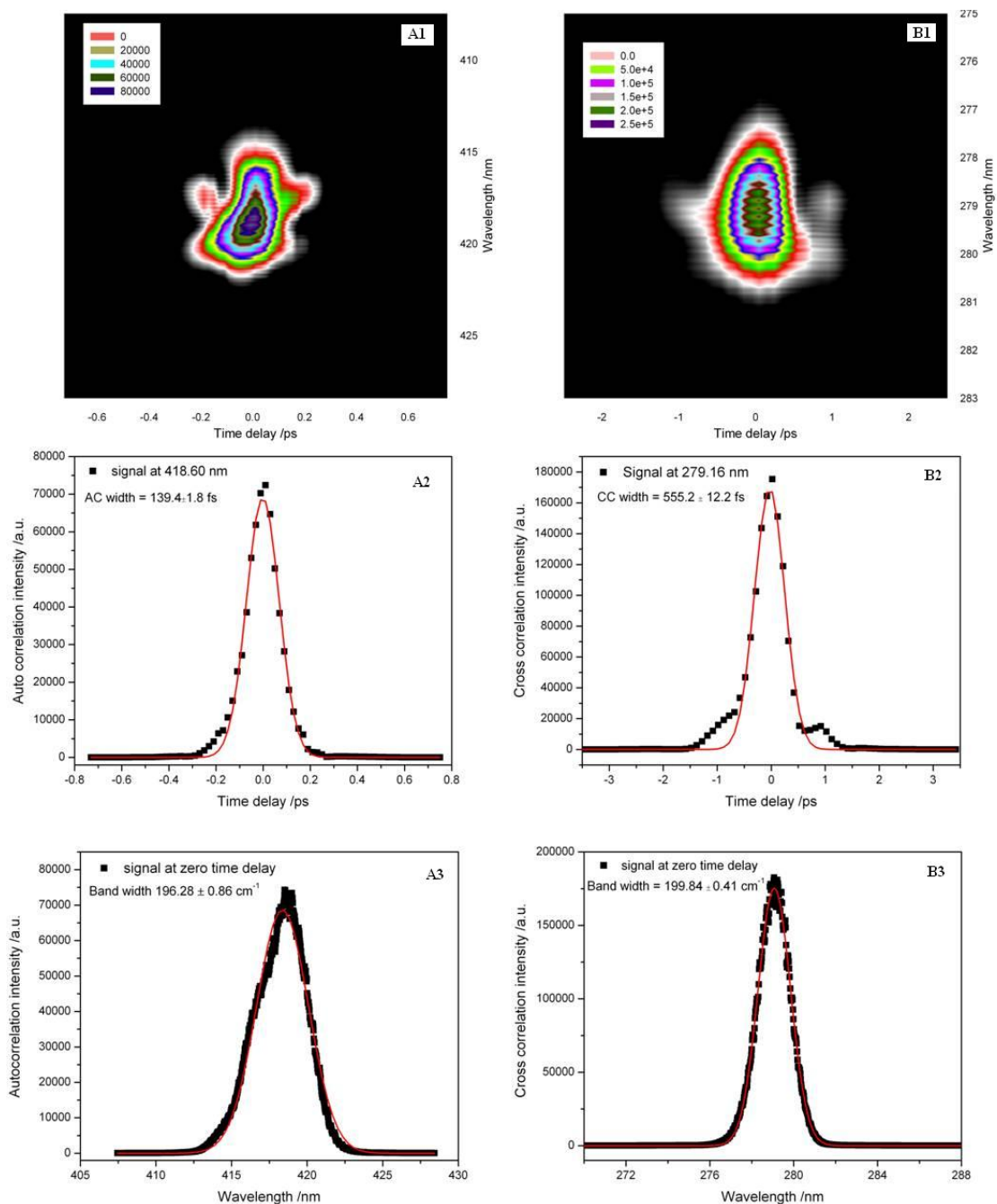


Figure 2 - 7 Pulse characteristics of the CPA-1000 system. Frequency resolved optical gating (FROG) analysis of (A1) 800 nm CPA-1000 output using second harmonic generation in 100 μm Type I BBO

crystal (B1) spectrally narrowed 400 nm output after KDP using third harmonic generation with 800 nm in 100 μm Type II BBO crystal. (A2) Auto-correlation trace of 800 nm beam (B2) Cross-correlation trace of 400 nm beam with the residual 800 nm beam (A3) Energy spectrum of the autocorrelation signal (B3) Energy spectrum of the cross correlation signal.

2.6 QUANTRONIX INTEGRA FEMTOSECOND LASER SYSTEM

A more recent addition to our lab facilities is a compact, single box integrated turn-key operated femtosecond laser Integra-i-3.5 from Quantronix. It is a femtosecond pulse regenerative and multi pass amplifier system with maximum pulse energy up to 3.5 mJ at center wavelength of 800 nm. The main components of the Integra are femtosecond fiber oscillator (Femtolite FX-10, IMRA), stretcher, the pump laser (FALCON-527, Quantronix), regenerative amplifier (RGA), multipass amplifier (MPA), compressor, pulse synchronization unit (PSU-100) and a temperature control unit (TCU-100).

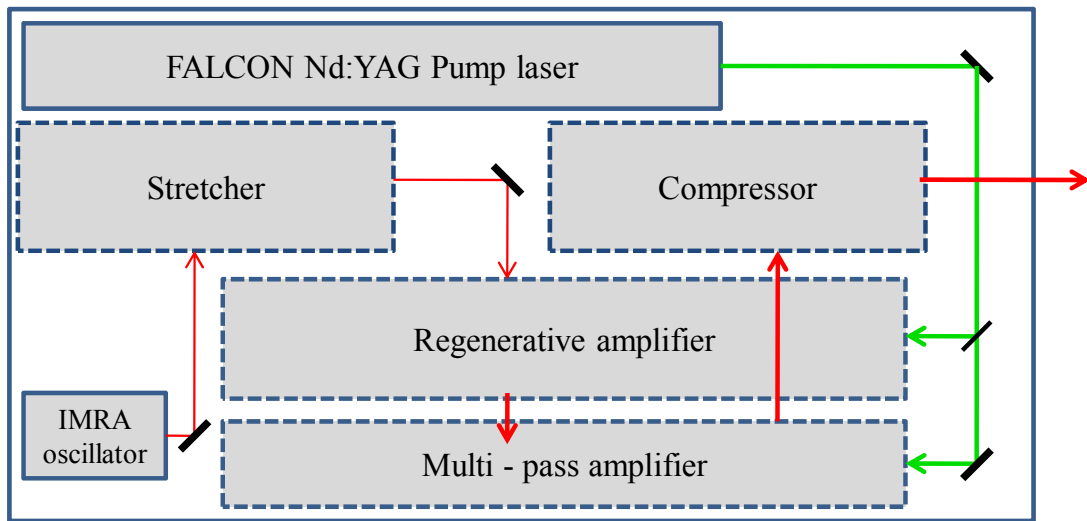


Figure 2 - 8 Schematic layout of the various components inside the Quantronix Integra I-3.5 femtosecond laser system.

It also works based on the same principle of CPA, though the fundamental difference between the Clark CPA-1000 and Quantronix Integra lies in the oscillator and amplifier. The mode-locked Ti:Sapphire oscillator is replaced by a very compact rare earth metal doped fiber oscillator (Femtolute FX-10, IMRA) that puts out 110 fs pulses at 50 MHz repetition rate and with more than 10 mW average power at the center wavelength 800 nm. A tiny fraction of the oscillator output is sent to a Pockels cell driver unit (PSU-100, Quantronix) through a photodiode which is used to produce 1 kHz trigger for the pump laser and synchronization of the oscillator and pump pulse trains. The regenerative amplifier is pumped by part of the energy from the frequency-doubled Nd:YLF laser (FALCON527-25-M, Quantronix) Q-switched at 1 kHz centered at 527 nm wavelength.

The pulse stretcher is similar. The stretched seed pulses are then injected into the regenerative amplifier cavity with the help of a time-gated polarization rotation device such as Pockels cell and a thin film polarizer, the timing of which is controlled by the Delay A setting of the PSU-100. A tiny fraction of the regenerative amplifier output is sent to an oscilloscope through a photodiode for monitoring purposes. The amplified seed pulse at the peak of amplification is dumped out of the regenerative amplifier cavity by another time-gated polarization rotation using the Delay B setting of the PSU-100 unit. The average power at this point is roughly 850 to 900 mW. The RGA output is then sent to a multipass amplifier, a 2 pass amplification stage for further amplification. The average power after the MPA can go up to 5.2 W.

The output from the MPA is sent to a pulse compressor through another Pockels cell, controlled by the Delay C setting of the PSU-100 unit for better contrast ratio. The

compressor uses a pair of gratings perfectly parallel to each other and is used to compress the pulse duration back to its near original pulse width. One of the gratings is mounted on a linear translation stage, which can be used to optimize the pulse compression. The total energy loss in the compressor is roughly about 30 %, and hence the typical output of the Integra system is a 3.5 mJ energy per pulse, ~ 100 fs pulse train at 1 kHz with 804 nm center wavelength.

Wavelength tunability:

The femtosecond output of the Integra laser at 804 nm can be converted into pulsed light of other wavelengths using various nonlinear frequency conversion processes, the simplest of which is frequency doubling in a nonlinear crystal such as KDP. The output of the Integra is converted into other wavelengths continuously tunable from 240 nm in UV to 24.0 μm in the IR with the help of commercial optical parametric amplifiers (OPA) from Light Conversion.

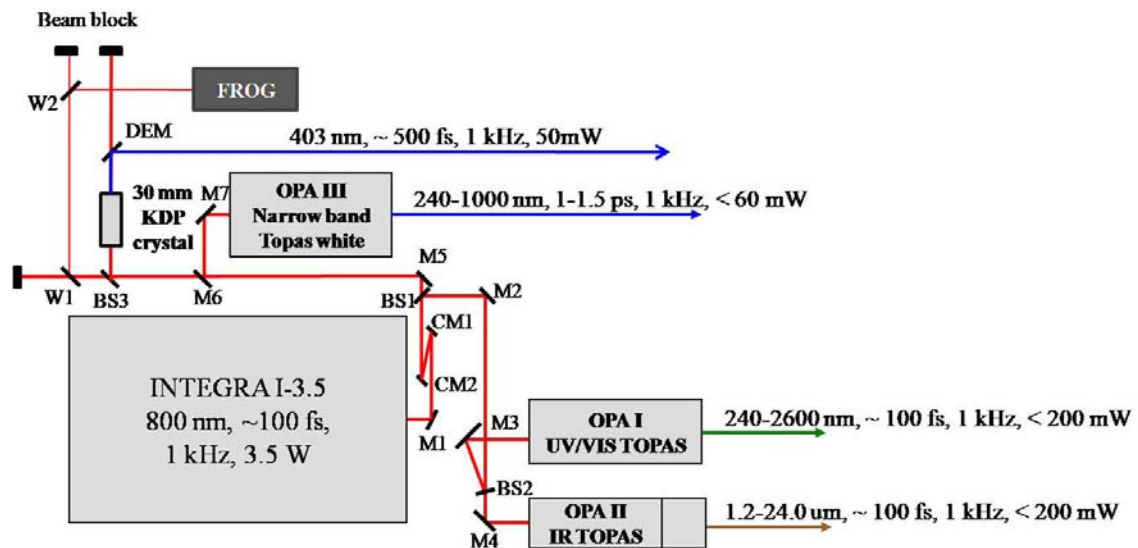


Figure 2 - 9 Schematic representation of the Integra output energy distribution for various wavelength conversion modules. BS1: beam splitter (35:65), BS2: beam splitter (50:50), BS3: beam splitter (35:65), CM1 and CM2: collimating mirrors, DEM: dielectric mirror, FROG: frequency

resolved optical gating device, KDP: Potassium dihydrogen phosphate crystal, M1 to M7: Mirrors, OPA: optical parametric amplifier, TOPAS: travelling wave optical parametric amplifier of superfluorescence, W1 and W2: wedges.

The Integra beam is collimated and beam diameter is reduced to 5.0 mm using a mirror telescope consisting of CM1 and CM2. Then the output is split into three different parts each of 1 mJ in energy with the help of two beam splitters, BS1 (0.35:0.65) and BS2 (0.5:0.5) and were being used to pump three different OPA's from Light Conversion. There is also a provision for bypassing the pump beam to OPA III by removing mirror M6, which is then split into two parts by using a beam splitter BS3 (0.35:0.65). One is used to monitor the pulse duration with a frequency resolved optical gating (FROG) device from Swamp Optics and the other is used to produce second harmonic output at 403 nm with 30 mm long KDP crystal.

Femtosecond visible and infrared optical parametric amplifiers:

OPA1 (fs visible) and OPA II (fs infrared) are similar to each other. Both work based on the optical parametric down conversion of 800 nm light in a travelling wave optical parametric amplifier of superfluorescence (TOPAS) module. Optical parametric down conversion is a 2nd order nonlinear process in which a single light wave of frequency ω_3 upon interaction with a non-centrosymmetric crystal produces two light waves of frequencies ω_1 and ω_2 . The phase matching condition requires that $n_3\omega_3 = n_1\omega_1 + n_2\omega_2$, where n_1 , n_2 and n_3 are the refractive indices of the crystal at frequencies ω_1 , ω_2 and ω_3 respectively. By varying the crystal indices which in turn can be changed merely by changing the crystal orientation towards the incident beam, one can generate a continuously tunable output at ω_1 and ω_2 . The output beam with higher frequency is called signal and the one with lower frequency is called idler. The maximum

possible frequency of the signal is given by, $\omega_s = \omega_{\text{pump}} - \omega_{\text{abs}}$, where ω_{abs} corresponds to the IR absorption edge of the nonlinear crystal. For example for a beta-BaB₃O₄ (BBO) crystal, the IR absorption edge corresponds to 3300 cm⁻¹. So the highest signal frequency obtainable with 800 nm pump corresponds to 1050 nm.

TOPAS has a single optical parametric generation (OPG) stage and 4 optical parametric amplification stages arranged in a single type II phase matched BBO crystal. In type I phase matching, the degree of nonlinearity is high but no degeneracy exists between the signal and idler. Moreover the polarizations of signal and idler are parallel to each other and orthogonal to that of the input beam. In Type II phase matching, even though the degree of nonlinearity is relatively low, degeneracy exists and the polarizations of the signal and idler are orthogonal to each other. It offers an advantage of being able to separate the signal and idler using polarizers inspite of them having the same frequency at degeneracy.

The pump beam is split into 3 parts. One is used to generate broad-band superfluorescence (parametric signal) during its first pass through the BBO crystal. The OPG signal undergoes four more passes through the same BBO crystal for amplification. The preamplifiers (2nd, 3rd and 4th passes) shape the signal acting as small amplifying aperture in the far field of the seed beam. The parametric signal after the third pass is diffracted off of a grating and overlapped with the second part of the pump beam spatially and temporally in the crystal. The preamplified signal after the fourth pass is reflected off of a metallic mirror and overlapped with the bulk of the remaining pump beam spatially and temporally in the crystal for final amplification. So a standard TOPAS with type II BBO crystal pumped by 800 nm ~100 fs output of an amplified Ti:Sapphire

laser, produces signal (1.1 to 1.6 μm) and idler (1.6 to 2.6 μm) beams with beam divergence close to diffraction limit and time bandwidth product well below unity. The presence of three different wavelengths (signal, idler and residual pump at 800 nm) at the output of TOPAS, presents various possibilities in terms of wavelength tunability.

OPA I has two computer controlled rotation stages, called mixer 1 and mixer 2, mounted with nonlinear crystals attached to the output aperture of the TOPAS in a series fashion. Mixer 1 has a Type I BBO crystal ($\theta=23^\circ$) and a type II BBO crystal ($\theta = 30^\circ$). The Type I BBO crystal is used for the second harmonic generation of signal (SHS) and idler (SHI). Since the signal has vertical polarization, the crystal is rotated in the horizontal plane for efficient SHS. Instead, the crystal is rotated in the vertical plane for efficient SHI since the idler has horizontal polarization. The same crystal is also used for generating the sum frequency of the idler (SFI) with the residual pump, the crystal rotation being in the vertical plane. The type II BBO crystal is used for generating the sum frequency of signal (SFS) with the residual pump and the crystal is rotated in the vertical plane. There is a dielectric mirror installed before the output aperture of TOPAS that can block 800 nm pump light and transmit the signal and idler beams and this mirror can be easily flipped in and out of the beam path by rotating a knob. The mirror is closed to block the pump while using the second harmonics and the mirror is opened for using sum frequency mixing.

Mixer 2 is used to generate the second harmonics of the output of Mixer 1. It has two different Type I BBO crystals, one with $\theta = 35^\circ$ and the other with $\theta = 48^\circ$. The BBO crystal with $\theta = 35^\circ$ is used for generating the second harmonic of both SHI and SHS.

The BBO crystal with $\theta = 48^\circ$ is used for generating the second harmonic of both SFI and SFS.

	Wavelength range (nm)		Mixer crystals		Mixer rotation axis		Output polarization	Output power (mW)
I	1596	2619	-	-	-	-	H	
S	1160	1620	-	-	-	-	V	
SHI	800	1180	2B	-	H	-	V	10-115
SHS	580	810	2B	-	V	-	H	20-165
SFI	535	605	2B	-	H	-	V	75-110
SFS	480	537	3B	-	H	-	V	135-220
FHI	400	500	2B	5B	H	V	H	10-45
FHS	290	405	2B	5B	V	H	V	20-60
SHSFI	268	302	2B	6B	H	V	H	7-15
SHSFS	240	268	3B	6B	H	V	H	15-40

Table 2 - 1 Summary of the fs UV-visible OPA output wavelengths and their energies. I: idler, S: signal, SHI: second harmonic of idler, SHS: second harmonic of signal, FHI: fourth harmonic of idler, FHS: fourth harmonic of signal, SHSFI: second harmonic of SFI, SHSFS: second harmonic of SFS, 2B: Type I BBO crystal, 3B: Type II BBO crystal, 5B: Type I BBO crystal, 6B: Type I BBO crystal, H: horizontal, V: vertical.

OPA II can be used to extend the wavelength tuning range to infrared. It has a noncollinear difference frequency generator module fixed at the output of TOPAS module. The signal and idler waves of the TOPAS output are separated using a dichroic beam splitter and mixed using another dichroic beam splitter in nonlinear crystals AgGaS₂ and GaSe of type I phase matching to generate difference frequency in the range 2.6 to 24.0 μm . The difference frequency pulse wavelength tuning is done by rotating the crystal in the vertical plane and also by changing the angle between the signal and idler beams. The conversion efficiency is optimized by controlling the time delay between the interacting beams. The dichroic beam splitter that directs the signal and idler beams onto the crystal and the nonlinear crystals are mounted on computer controlled rotation stages.

	Wavelength range (nm)		Mixer crystals		Mixer rotation axis		Output polarization	Output power (mW)
	I	S	8B	9	H	V		
I	1596	2672	-	-	-	-	H	
S	1150	1620	-	-	-	-	V	
NDF1	2600	13000	8B	-	H	-	H	3-20
NDF2	3500	24000	9	-	H	-	H	1-18

Table 2 - 2 Summary of the fs IR OPA output wavelengths and their energies. I: idler, S: signal, NDF: nonlinear difference frequency, 8B: Type I AgGaS₂ crystal, 9: Type I GaSe crystal, H: horizontal, V: vertical.

Ps visible optical parametric amplifier:

OPA III is a narrow-band width parametric amplifier of white light, called as Topas White-NB (TWNB), custom designed for our Raman experiments by Light Conversion. The main components are white light continuum generator, second harmonic generator, two-stage pump pulse generator, white-light monochromator, non-collinear parametric amplifier and signal collimator. About 1 mJ energy of the Integra output at 800 nm is sent to the TWNB. A tiny fraction (~ 2%) of the 800 nm fundamental is used to generate white light continuum pulse in a sapphire plate. The rest of the 800 nm input is frequency doubled in a 0.5 mm thick Type I BBO crystal ($\theta=29^\circ$, $\phi=90^\circ$) to generate second harmonic pump at 400 nm. The two-stage pump pulse generator uses a sequence of prisms to provide the necessary pump pulse duration for the parametric amplification narrowing the frequency bandwidth of the second harmonic by a factor of 3 to 5 compared to 800 nm fundamental band width. A 20:80 beam splitter splits the pump beam into two parts which pump the 1st and 2nd stages of the parametric amplifier.

The white light is dispersed off of a diffraction grating in vertical plane so that only 5-10 cm⁻¹ bandwidth overlaps with the first stage pump beam. The 1st stage pump beam acts as a slit for this monochromator. The non-collinear parametric amplifier

employs a two stage amplification of the white light seed in a single BBO crystal of Type I phase matching. The white light seed from the monochromator is overlapped spatially and temporally in the crystal to give preamplified signal of wavelength tunable from 480 to 1000 nm by varying the grating angle of the white light monochromator. The conversion efficiency is optimized by the nonlinear crystal rotation and the temporal overlap of the beams in the first pass. The preamplified signal is boosted in power in the 2nd pass by overlapping with the rest of the pump spatially and temporally. The most important criterion for efficient amplification of white light in the TWNB system is that the pump beams in the two stages should be exactly parallel to each other so that the phase matching angle is the same both stages of amplification. The signal after the parametric amplifier is collimated using a cylindrical mirror telescope.

OPA III has a computer controlled second harmonic generation stage fixed at the output aperture of the TWNB module for extending the wavelength tunability to UV region up to 240 nm. A 2.5 mm thick Type I BBO crystal is used for doubling the 480-540 nm signal of the TWNB and a 3 mm thick Type I BBO crystal is used for doubling the 540-1000 nm signal. The OPA III output energies and the polarizations are listed in Table 2-3.

	Wavelength range (nm)		Mixer crystals	Mixer rotation axis	Output polarization	Output power (mW)
S	480	1000	-	-	H	20-60 mW
SHS	240	270	2.5 mm BBO (Type I, $\theta=50^\circ$)	H	V	8-15 mW
SHS	270	478	3 mm BBO (Type I, $\theta=35^\circ$)	H	V	4-10 mW

Table 2 - 3 Summary of the ps UV-vis OPA TWNB output energies. S: signal, SHS: second harmonic of signal, H: horizontal, V: vertical.

Two color pump probe setup for TRRRS:

The experimental setup and detection scheme for the two-color TRRRS is exactly the same as the one described for the single color TRRRS experiments.

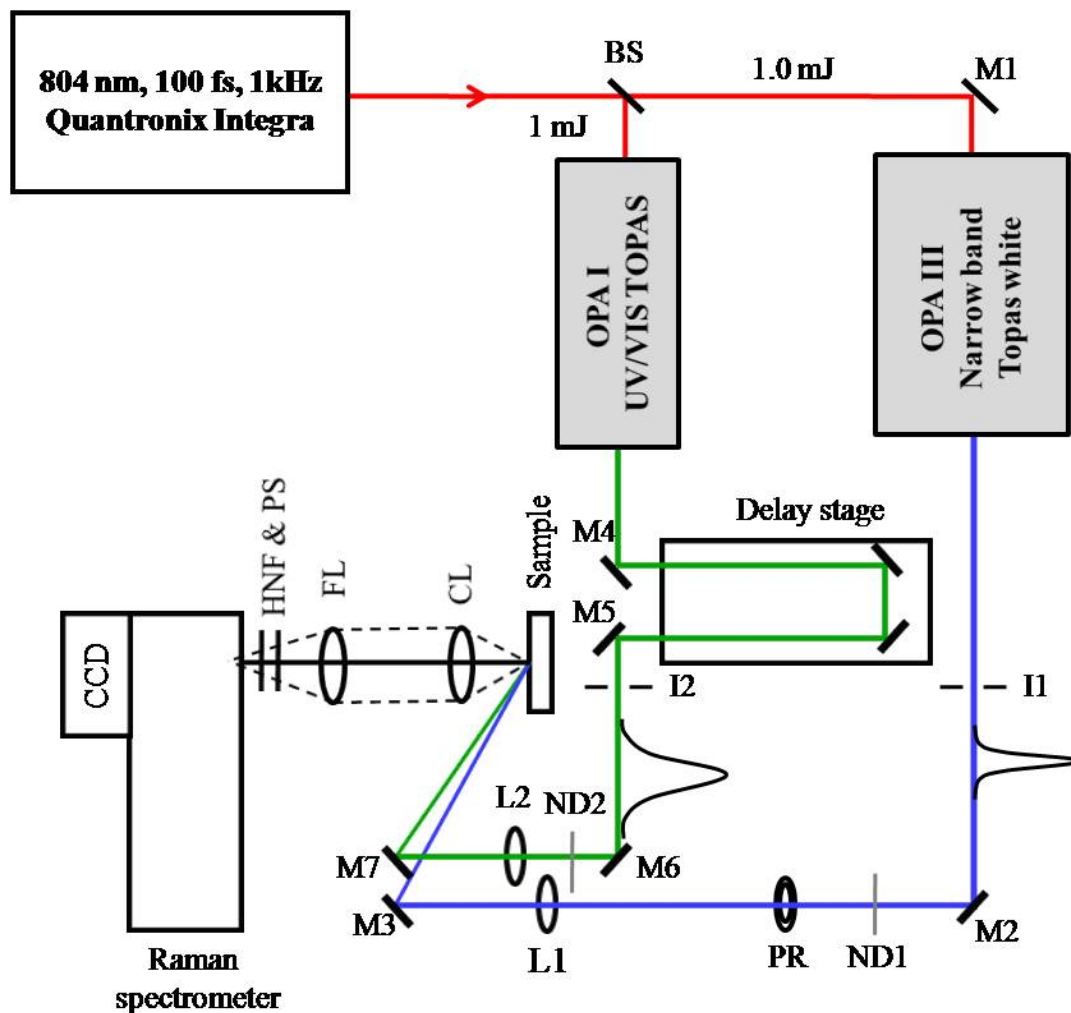


Figure 2 - 10 Experimental setup for the two color time resolved resonance Raman spectroscopy using two independently tunable pump and probe pulses. BS: beam splitter, M1 to M7: Mirrors, I1 and I2: apertures, ND1 and ND2: neutral density filters, PR: polarization rotator, L1 and L2: +750 mm fused silica lenses, CL: collecting lens, FL: focusing lens, HNF: holographic notch filter, PS: polarization scrambler, CCD: charge coupled device camera.

A short broad band UV-visible pulse from the fs UV-vis TOPAS is used as pump and a relatively long narrow band UV-visible pulse from the ps UV-vis TOPAS is used to probe the Raman scattering of the system under study. Now both the pump and probe

pulses are independently tunable in the entire visible range and up to 240 nm in the ultraviolet region making it applicable to most of the photoactive compound. And also the detection efficiency of the weak anti-Stokes Raman signal has been significantly enhanced by using a thermoelectrically cooled electron multiplying charge coupled device (EMCCD) camera (Newton DU971 BV, Andor Corp.).

The zero-time delay of the two pulses is determined by measuring the cross-correlation of the pump and probe pulses in a 100 μm Type II BBO crystal placed at the position of the sample by generating the sum frequency. The sum frequency generation is done in a background free noncollinear arrangement and the sum frequency signal is measured using a fiber optic coupled spectrometer (S2000, Ocean optics). The intensity of the sum frequency signal as a function of time delay and wavelength and the corresponding cross correlation trace is shown in Figure 2-11.

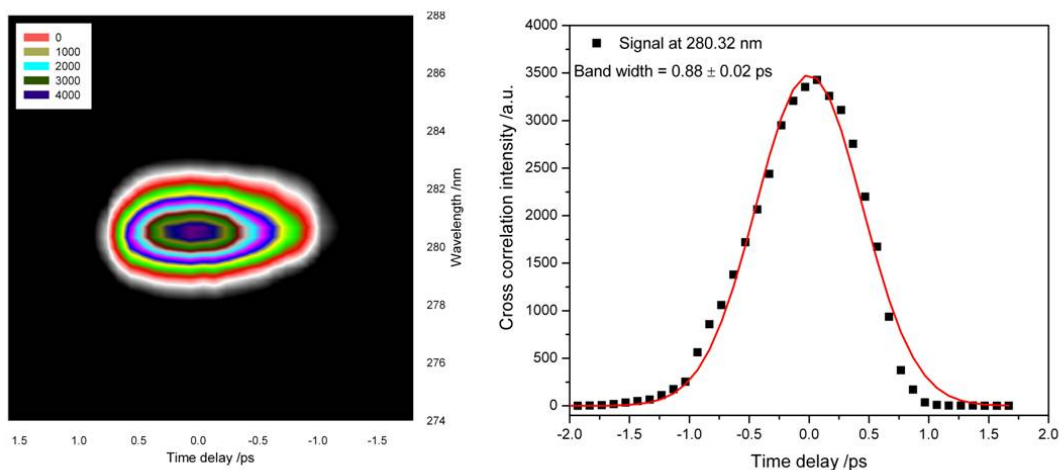


Figure 2 - 11 FROG analysis of the pump (550 nm) and probe (490 nm) pulses from the fs UV-vis TOPAS and ps UV-vis TWNB respectively. Sum frequency generation in a Type II BBO crystal provides the cross correlation signal of the pump and probe pulses. The 2D correlation and the corresponding cross correlation trace at the peak 280 nm are shown. The cross correlation width is 0.88 ± 0.02 ps.

As mentioned in the Table 2-3, the output energy of TWNB in the wavelength region of 350-450 nm is only about 4-8 μJ per pulse. So the probe beam in this region after going through various optical elements like a few mirrors and a lens on its way to the sample suffers significant losses in energy and hence is found not efficient for obtaining a decent anti-Stokes Raman signal. So the TWNB is certainly limited in this wavelength region for Raman experiments and hence we used frequency-doubling of the 800 nm output of Integra in 30 mm long KDP crystal as an alternative for generating a probe wavelength at 400 nm.

The experimental setup remains the same, except that the 800 nm pump beam to TWNB is bypassed and $\sim 300 \mu\text{J}$ energy is sent to a 30 mm long KDP crystal. This generated 402 nm pulses of 50 μJ energy and 25-35 cm^{-1} frequency band width. The second harmonic output at 402 nm is separated from the residual 800 nm using a harmonic separator and a bandpass filter. A lens telescope is added in the beam path to collimate the beam.

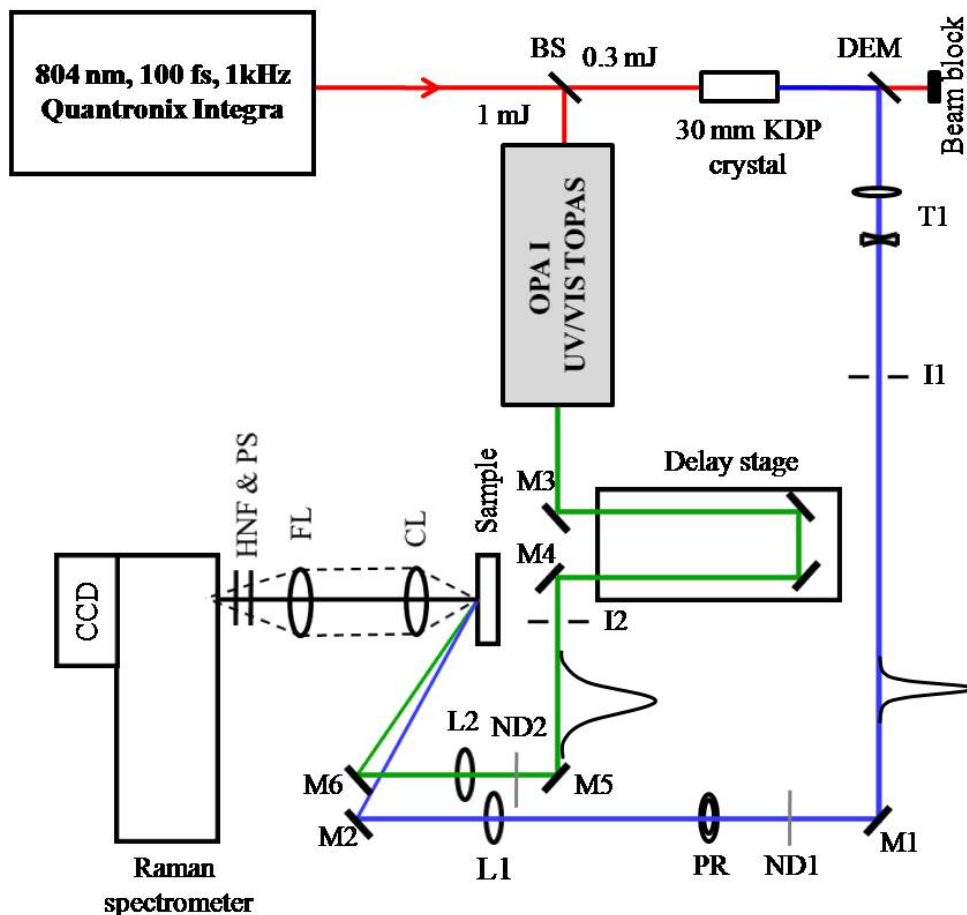


Figure 2 - 12 Experimental setup for the two color time resolved resonance Raman spectroscopy using a tunable pump pulse from fs UV-vis OPA and a fixed probe pulse at 402 nm. BS: beam splitter, KDP: potassium dihydrogen phosphate, DEM: dielectric mirror, T1: lens telescope, M1 to M7: mirrors, I1 and I2: apertures, ND1 and ND2: neutral density filters, PR: polarization rotator, L1 and L2: +750 mm fused silica lenses, CL: collecting lens, FL: focusing lens, HNF: holographic notch filter, PS: polarization scrambler, CCD: charge coupled device camera.

The zero time delay for this two-color pump probe experimental setup and the instrument response is determined with the help of a nonresonant coherent anti-Stokes Raman signal being generated at the difference frequency of the pump and probe pulse wavelengths. The approximate zero time is determined initially by generating second harmonic of the residual 800 nm output along the pump and probe arms in a BBO crystal at the sample. Then the crystal is replaced with dimethylsulfoxide solvent and the

transient anti-Stokes Raman signal is measured as function of time delay with pump wavelength close to 402 nm (probe wavelength). At exact zero time delay of the pump and probe pulses, an intense coherent anti-Stokes Raman signal is observed at the Raman shift corresponding to the frequency difference of the pump and probe wavelengths in cm^{-1} . The evolution of this coherent signal as a function of the time delay also provides the instrument response function. The coherent signal measured in DMSO with 425.70 nm pump and 401.78 nm probe pulses at zero time delay is shown in Figure 2-13.

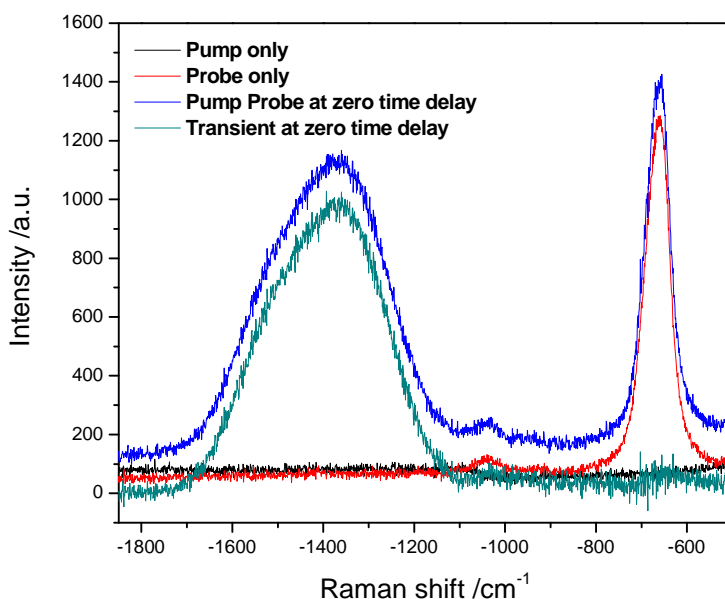


Figure 2 - 13 Nonresonant coherent anti-Stokes Raman signal observed at -1390 cm^{-1} in the time resolved anti-Stokes Raman spectrum of DMSO using 425.70 nm pump and 401.78 nm probe pulses at zero time delay. The pump probe spectrum at the zero time delay and the corresponding pump only and probe only spectra are also shown. The solvent band of DMSO at 676 cm^{-1} seen in both probe only and pump-probe spectrum completely disappears in the transient spectrum.

The pump only and the probe only spectra are subtracted from the pump-probe anti-Stokes Raman spectrum at zero time delay to get the transient Raman signal. The solvent band at 676 cm^{-1} completely disappears in the transient spectrum and a very

strong coherent signal is seen at 1390 cm^{-1} corresponding to the frequency difference of the pump and probe pulses. By tuning the pump wavelength to 416.47 nm and 420.88 nm , the coherent signal moves to 884 cm^{-1} and 1100 cm^{-1} respectively. The intensity of the signal is optimized by adjusting the spatial overlap of the pump and probe beams inside the sample.

The evolution of the signal intensity as a function of the time delay also provides the instrument response function. The transient signal obtained with DMSO using 425.70 nm pump and 401.78 nm probe is fit with Gaussian peak functions and the integrated peak intensity is plotted as a function of time delay and is shown in the Figure 2-14. It has a sharp rise followed by an exponential decay. The full width at half maximum is less than 300 fs .

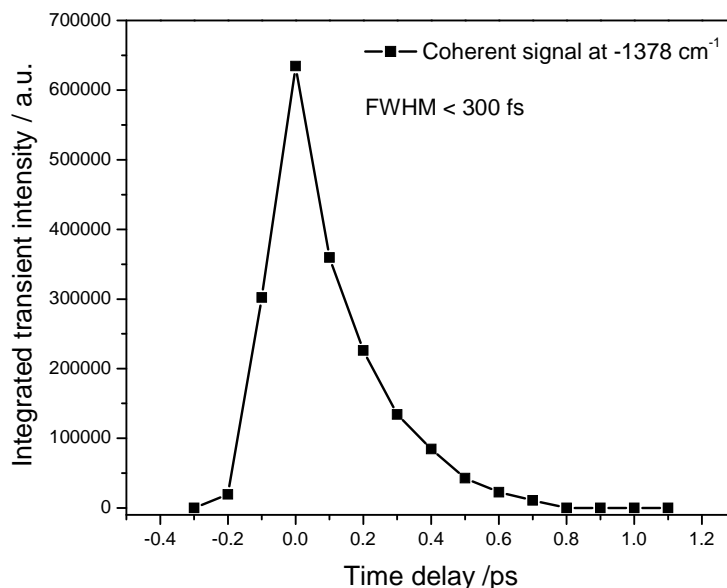


Figure 2 - 14 Evolution of the nonresonant coherent signal in DMSO as a function of the time delay between the pump (425.70 nm) and probe (401.78 nm) pulses. The full width at half maximum is about 200 to 300fs .

The presence of the coherent signal even with solutes like *para*-nitroaniline and N, N-dimethyl *para*-nitroaniline and 2, 6-dichloro *para*-nitroaniline present in DMSO is observed and hence provides a very useful tool in determining the zero time delay and optimizing the spatial overlap of the pump and probe beams in the sample.

References:

1. Reid, G. D.; Wynne, K., Ultrafast laser technology and spectroscopy. *Encyclopedia of Analytical Chemistry* **2000**, 13644-13670.
2. Assmann, J.; Kling, M.; Abel, B., Watching photoinduced chemistry and molecular energy flow in solution in real time. *Angewandte Chemie, International Edition* **2003**, 42, (20), 2226-2246.
3. Cho, M., Ultrafast vibrational spectroscopy in condensed phases. *PhysChemComm* **2002**, 40-58.
4. Laubereau, A.; Kaiser, W., Vibrational dynamics of liquids and solids investigated by picosecond light pulses. *Reviews of Modern Physics* **1978**, 50, (3), 607-65.
5. Heilweil, E. J.; Casassa, M. P.; Cavanagh, R. R.; Stephenson, J. C., Population lifetimes of hydroxyl($\nu = 1$) and hydroxyl-d($\nu = 1$) stretching vibrations of alcohols and silanols in dilute solution. *Journal of Chemical Physics* **1986**, 85, (9), 5004-18.
6. Graener, H.; Seifert, G., Vibrational and orientational relaxation of monomeric water molecules in liquids. *Journal of Chemical Physics* **1993**, 98, (1), 36-45.
7. Bakker, H. J., Effect of intermolecular interactions on vibrational-energy transfer in the liquid phase. *Journal of Chemical Physics* **1993**, 98, (11), 8496-506.

8. Tokmakoff, A.; Urdahl, R. S.; Zimdars, D.; Francis, R. S.; Kwok, A. S.; Fayer, M. D., Vibrational spectral diffusion and population dynamics in a glass-forming liquid: variable bandwidth picosecond infrared spectroscopy. *Journal of Chemical Physics* **1995**, 102, (10), 3919-31.
9. Hamm, P.; Lim, M.; Hochstrasser, R. M., Vibrational energy relaxation of the cyanide ion in water. *Journal of Chemical Physics* **1997**, 107, (24), 10523-10531.
10. Kozich, V.; Dreyer, J.; Ashihara, S.; Werncke, W.; Elsaesser, T., Mode-selective O-H stretching relaxation in a hydrogen bond studied by ultrafast vibrational spectroscopy. *Journal of Chemical Physics* **2006**, 125, (7), 074504/1-074504/9.
11. Lenchenkov, V.; She, C.; Lian, T., Vibrational Relaxation of CN Stretch of Pseudo-Halide Anions (OCN⁻, SCN⁻, and SeCN⁻) in Polar Solvents. *Journal of Physical Chemistry B* **2006**, 110, (40), 19990-19997.
12. Owrutsky, J. C.; Li, M.; Locke, B.; Hochstrasser, R. M., Vibrational Relaxation of the CO Stretch Vibration in Hemoglobin-CO, Myoglobin-CO, and Protoheme-CO. *Journal of Physical Chemistry* **1995**, 99, (13), 4842-6.
13. Graener, H.; Laubereau, A., New results on vibrational population decay in simple liquids. *Applied Physics B: Photophysics and Laser Chemistry* **1982**, B29, (3), 213-18.
14. Zinth, W.; Kolmeder, C.; Benna, B.; Irgens-Defregger, A.; Fischer, S. F.; Kaiser, W., Fast and exceptionally slow vibrational energy transfer in acetylene and phenylacetylene in solution. *Journal of Chemical Physics* **1983**, 78, (6, Pt. 2), 3916-21.

15. Tokmakoff, A.; Sauter, B.; Kwok, A. S.; Fayer, M. D., Phonon-induced scattering between vibrations and multiphoton vibrational up-pumping in liquid solution. *Chemical Physics Letters* **1994**, 221, (5-6), 412-18.
16. Deak, J. C.; Iwaki, L. K.; Dlott, D. D., Vibrational energy redistribution in polyatomic liquids: ultrafast IR-Raman spectroscopy of acetonitrile. *Journal of Physical Chemistry A* **1998**, 102, (42), 8193-8201.
17. Deak, J. C.; Iwaki, L. K.; Dlott, D. D., Vibrational Energy Redistribution in Polyatomic Liquids: Ultrafast IR-Raman Spectroscopy of Nitromethane. *Journal of Physical Chemistry A* **1999**, 103, (8), 971-979.
18. Deak, J. C.; Iwaki, L. K.; Rhea, S. T.; Dlott, D. D., Ultrafast infrared-Raman studies of vibrational energy redistribution in polyatomic liquids. *Journal of Raman Spectroscopy* **2000**, 31, (4), 263-274.
19. Deak, J. C.; Pang, Y.; Sechler, T. D.; Wang, Z.; Dlott, D. D., Vibrational Energy Transfer Across a Reverse Micelle Surfactant Layer. *Science (Washington, DC, United States)* **2004**, 306, (5695), 473-476.
20. Dlott, D. D., Vibrational energy redistribution in polyatomic liquids: 3D infrared-Raman spectroscopy. *Chemical Physics* **2001**, 266, (2-3), 149-166.
21. Shimojima, A.; Tahara, T., Picosecond Time-Resolved Resonance Raman Study of the Photoisomerization of Retinal. *Journal of Physical Chemistry B* **2000**, 104, (39), 9288-9300.
22. McCamant, D. W.; Kukura, P.; Yoon, S.; Mathies, R. A., Femtosecond broadband stimulated Raman spectroscopy: Apparatus and methods. *Review of Scientific Instruments* **2004**, 75, (11), 4971-4980.

23. Wilbrandt, R.; Jensen, N. H., Time-resolved resonance Raman spectroscopy: the triplet state of all-trans-retinal. *Journal of the American Chemical Society* **1981**, 103, (5), 1036-41.
24. Wylie, I. W.; Koningstein, J. A., Photoisomerization and time-resolved Raman studies of 15-15'-cis-b-carotene and 15-15'-trans-b-carotene. *Journal of Physical Chemistry* **1984**, 88, (14), 2950-3.
25. Foggi, P.; Bussotti, L.; Neuwahl, F. V. R., Photophysical and photochemical applications of femtosecond time-resolved transient absorption spectroscopy. *International Journal of Photoenergy* **2001**, 3, (2), 103-109.
26. Alfano, R. R., The super continuum laser source. **1989**.
27. Zeylikovich, I.; Alfano, R. R., Coherence properties of the supercontinuum source. *Applied Physics B: Lasers and Optics* **2003**, 77, (2-3), 265-268.
28. Raman, C. V.; Krishnan, K. S., A new type of secondary radiation. *Nature (London, United Kingdom)* **1928**, 121, 501-2.
29. Schweitzer-Stenner, R., Structure and dynamics of biomolecules probed by Raman spectroscopy. *Journal of Raman Spectroscopy* **2005**, 36, (4), 276-278.
30. Backus, S.; Durfee, C. G., III; Murnane, M. M.; Kapteyn, H. C., High power ultrafast lasers. *Review of Scientific Instruments* **1998**, 69, (3), 1207-1223.
31. Bhattacharjee, Y., Measuring the immeasurable. *Nature (London, United Kingdom)* **2001**, 412, (6846), 474-476.
32. Bloembergen, N., From nanosecond to femtosecond science. *Reviews of Modern Physics* **1999**, 71, (2), S283-S287.

33. Cheriaux, G.; Chambaret, J.-P., Ultra-short high-intensity laser pulse generation and amplification. *Measurement Science and Technology* **2001**, 12, (11), 1769-1776.
34. Keller, U., Recent developments in compact ultrafast lasers. *Nature (London, United Kingdom)* **2003**, 424, (6950), 831-838.
35. Mourou, G., The ultrahigh-peak-power laser. Present and future. *Applied Physics B: Lasers and Optics* **1997**, 65, (2), 205-211.
36. Zewail, A. H., Femtochemistry. Past, present, and future. *Pure and Applied Chemistry* **2000**, 72, (12), 2219-2231.
37. Zewail, A. H., Femtochemistry: Atomic-Scale Dynamics of the Chemical Bond. *Journal of Physical Chemistry A* **2000**, 104, (24), 5660-5694.
38. Spence, D. E.; Kean, P. N.; Sibbett, W., 60-Femtosecond pulse generation from a self-mode-locked titanium-doped sapphire laser. *Optics Letters* **1991**, 16, (1), 42-4.
39. Moulton, P. F., Spectroscopic and laser characteristics of titanium-doped aluminum oxide. *Journal of the Optical Society of America B: Optical Physics* **1986**, 3, (1), 125-33.
40. Strickland, D.; Mourou, G., Compression of amplified chirped optical pulses. *Optics Communications* **1985**, 55, (6), 447-9.
41. Maine, P.; Strickland, D.; Bado, P.; Pessot, M.; Mourou, G., Generation of ultrahigh peak power pulses by chirped pulse amplification. *IEEE Journal of Quantum Electronics* **1988**, QE-24, (2), 398-403.
42. Pessot, M.; Maine, P.; Mourou, G., 1000 Times expansion/compression of optical pulses for chirped pulse amplification. *Optics Communications* **1987**, 62, (6), 419-21.

43. Pessot, M.; Squier, J.; Mourou, G.; Harter, D. J., Chirped-pulse amplification of 100-fsec pulses. *Optics Letters* **1989**, 14, (15), 797-9.
44. Martinez, O. E., *IEEE Journal of Quantum Electronics* **1987**, QE-23, (1), 59-64.
45. Treacy, E. B., Optical pulse compression with diffraction gratings. *IEEE Journal of Quantum Electronics* **1969**, QE-5, 454-58.
46. Trebino, R.; DeLong, K. W.; Fittinghoff, D. N.; Sweetser, J. N.; Krumbugel, M. A.; Richman, B. A.; Kane, D. J., Measuring ultrashort laser pulses in the time-frequency domain using frequency-resolved optical gating. *Review of Scientific Instruments* **1997**, 68, (9), 3277-3295.
47. Trebino, R.; Kane, D. J., Using phase retrieval to measure the intensity and phase of ultrashort pulses: frequency-resolved optical gating. *Journal of Optical Society of America A* **1993**, 10, (5), 1101-1110.
48. Trebino, R.; Editor, *Frequency-Resolved Optical Gating: The Measurement of Ultrashort Laser Pulses*. **2002**; p 456 pp.
49. Trebino, R.; O'Shea, P.; Kimmel, M.; Gu, X., Measuring ultrashort laser pulses just got a lot easier! *Optics & Photonics News* **2001**, 12, (6), 22-25.

CHAPTER 3

THE ELECTRONIC AND VIBRATIONAL DYNAMICS OF

Fe^{II}OEP-2MeIm IN CH₂Cl₂

3.1 INTRODUCTION

Heme proteins such as myoglobin and hemoglobin can reversibly bind diatomic oxygen and serve as the oxygen storage and transporting agents in mammals. The central ferrous iron atom of the protoheme prosthetic group is responsible for the reversible binding of diatomic O₂, while the oxidation of Fe (II) to Fe (III) is inhibited by the protection afforded by the surrounding protein. The heme group is covalently linked to the protein via a single covalent bond to the imidazole side chain of a histidine protein residue and is embedded in a hydrophobic protein cavity. The heme proteins can also bind other diatomic ligands like CO and NO. The axial ligands were shown to be conveniently photodissociated by visible light at the same time resulting in a deligated heme with excess energy, in order to study the protein structural changes associated with ligand binding and release and correlate it to the function of heme proteins.

Even small energy inputs in biological molecules give rise to highly directed processes leading to highly correlated huge structural changes in the protein according to its function¹⁻³. So the relaxation mechanisms, the energy flow path ways and the associated life times involved in the heme group deactivation following photolysis of bound hemes as well as direct photoexcitation of the unligated hemes such as deoxy Mb and deoxy Hb and protoheme based model compounds in the absence of protein have

been the subject of numerous theoretical⁴⁻¹¹ and experimental studies using Raman spectroscopy¹²⁻²⁴, transient visible spectroscopy²⁵⁻³⁰, transient IR spectroscopy³¹⁻³³ and transient grating spectroscopy¹ to list a few. Despite active research in the last 20 years by several research groups, electronic and vibrational dynamics of hemes have not yet converged to single model. It is generally accepted that the ground electronic state is repopulated within about 5 ps of initial excitation, whether the pump laser is tuned to the Soret band (S_2) or the Q-band (S_1), and whether ligand photolysis is involved or not. However, broad consensus is still lacking for a model that describes how this rapid IC back to the ground state occurs.

We apply time resolved anti-Stokes resonance Raman spectroscopy (TRARRS) method here to study the energy relaxation dynamics of a simple heme model compound Fe^{II}OEP-2MeIm in the absence of protein or photolysis using Soret band electronic excitation. The crystal structure of this model compound has been determined recently³⁴. The 2-methyl imidazole ligand is found to be disordered having a major (75%) and a minor orientation with a small dihedral angle of 6.6° between the two orientations. However, the major orientation dominates the structural features of the molecule. The molecule has an expanded porphyrinate core (2.049 Å core radius), large equatorial Fe-N bond distances (2.077 Å) and a significant out of plane displacement of the iron atom. The overall structure of the molecule is domed with a displacement of Fe atom by 0.34 Å from the plane defined by the four porphyrin nitrogens and by 0.46 Å from the 24-atom mean plane of the porphyrin core towards the ligand corresponding to a doming of 0.12 Å. Bulky 2-methyl imidazole leads to an off-axis tilt of the iron-imidazole bond

from the heme normal by an angle of 6.9° and a rotation of the 2-MeIm ligand to maximize the distance between the ligand and the porphyrin core atoms.

The first vibrational energy relaxation dynamics study of this five-coordinate high-spin heme model compound was done by Loparo et al. using single pulse transient resonance Raman spectroscopy with ~ 10 ns pulses of 436 nm light²³. This simple transient Raman method provided valuable qualitative information about the picosecond relaxation processes occurring within the ns pulse duration such as the formation of preferential mode-specific non-equilibrium vibrational energy distributions in the ground state vibrational modes following the excited electronic state decay. Upon comparison to the similar studies in deoxyHb and 2MeIm bound protoheme^{14, 15, 18, 35, 36}, it was pointed out that the observed dynamics are metallo-porphyrin or heme group specific and the role of protein in the heme group relaxation events is very subtle.

The vibrational dynamics study of Fe^{II}OEP-2MeIm by Loparo et al. has been extended here to time-resolved spectroscopy domain in order to get quantitative information about the individual vibrational modes involved in the mode-specific relaxation on the ground state electronic state. The system was both excited and probed in the Soret π - π^* (S_2) transition in a one-color configuration. In order to tease out the electronic and vibrational contributions to the observed dynamics, parallel ultrafast, time-resolved UV/Vis pump – Stokes resonance Raman probe (TR³S) and ultrafast transient absorption (TA) spectroscopy were employed in the Soret region of the UV/Vis spectrum as well. The results are compared to analogous findings from the more complex ligand photolysis dynamics from the standpoint of the effect of state preparation upon IC and the subsequent vibrational dynamics.

3.2 MATERIALS AND METHODS

Iron^{II} octaethyl porphyrin 2-methyl imidazole (Fe^{II}OEP-2MeIm) was prepared using a reported two phase method²³ as follows. All solutions were degassed several times and kept under a slight overpressure of N₂(g). 2-methyl imidazole (2MeIm; Aldrich) was recrystallized at least twice from benzene. Fe^{III}OEP (Porphyrin Products; no further purification) was dissolved in CH₂Cl₂ (Fisher; spectroscopic grade) to 0.5-1.0 mM. 10 mL of this solution was added to an equal volume of CH₂Cl₂ saturated with 2MeIm. 10 mL of 1.0 M Na₂S₂O₄ in deionized, distilled water and saturated with 2MeIm was added to the Fe^{III}OEP / 2MeIm solution under nitrogen pressure using an air-tight syringe (Hamilton). The solution was thoroughly agitated to generate Fe^{II}OEP-2MeIm. The top (aqueous) layer with excess ligand and reducing agent acts as a protective barrier towards oxygen diffusion into the MP-containing layer below, and enhances the redox stability of the sample.

The details of the laser system used for time-resolved resonance Raman studies has been described elsewhere³⁷. Briefly, the output of a Ti:Sapphire based regenerative amplifier (785-835 nm, 120 fs, 650±50 μJ/pulse, 1 kHz; Clark MXR, Inc.) was frequency doubled in a long (30 mm) KDP crystal to produce 410 or 413 nm pulses (17-25 cm⁻¹ FWHM, 500-800 fs, 60-70 μJ/pulse). A 50-50 beam splitter generated pump and probe beams, which were attenuated to 5.5 and 2.5 μJ/pulse, respectively, using neutral density filters. The probe beam, after passing through a motorized, calibrated translational stage (MM3000; Newport Inc.), was overlapped with the pump beam at the sample in a near collinear (~5°) geometry with a spot size of ~2 mm at the sample. The sample was circulated through a 1 mm quartz flow cell using Teflon tubing and an over pressure of

N₂ (g). Extreme care was taken to flow only the porphyrin containing organic layer. Even a few drops of the aqueous layer containing the reducing agent that enter the flow cell results in huge increase of the scattering background.

Raman spectra were collected in a $\sim 135^\circ$ back-scattering geometry. Rayleigh scattering was rejected with an angle tuned super notch filter (center $\lambda = 415$ nm, Kaiser, Inc.). The Raman scattering was dispersed with a 0.5 meter imaging spectrograph (500 is, Chromex Inc.) and recorded with a thermoelectrically cooled, back-illuminated CCD camera (DU420 BV, Andor). Typical accumulation times were 20 s for Stokes spectra and 60 s for anti-Stokes spectra. A reference spectrum at $\Delta t = 64$ ps was collected for each set of four Stokes Raman spectra, and at $\Delta t = -25$ ps for each set of three anti-Stokes Raman spectra. Spectra were collected in random order of the time delay positions, and the complete dynamics were measured multiple times.

The data was processed using Origin 7.5TM software. Transient spectra were obtained by subtracting the reference spectra from the corresponding set of pump-probe spectra after removing the artifacts due to cosmic radiation in all the Raman spectra. The background was then manually subtracted using the baseline subtraction (Origin 7.5TM) routine to generate transient spectra. The kinetic traces are obtained from the peak intensities of the transient Raman spectra. Limited smoothing is done by averaging three intensities at the peak position. The decay portions of the kinetic traces are fit with single exponentials.

The femtosecond transient absorption experiments were performed at the Ohio Laboratory for Kinetic Spectrometry at Bowling Green State University. The details of

the laser system and the experimental setup have been described in detail elsewhere³⁸. Briefly, the output (800 nm, 100 fs and 1 kHz) from a Spectra-Physics Hurricane was used to generate pump pulses at 400 nm and white light continuum probe pulses (3 mm CaF₂ plate, 360-750 nm). The pump was chopped at 100 Hz, focused to ~2 mm at the sample, and overlapped with the probe in near collinear geometry (~ 5°) with polarizations at magic angle. Signals were collected by a 400 μm optical fiber coupled to a CCD spectrograph (Ocean Optics, PC 2000). The instrument response was 110 fs. The optical chopper, delay stage and the CCD spectrograph were controlled by LabView (National Instruments, Inc.) programs written by Ultrafast Systems, LLC. The sample was circulated under Ar gas pressure through a 1 mm flow cell using a micropump. The concentration of the sample for the transient absorption experiments was approximately 0.15 mM so that the optical density of the sample is less than 1.0 at excitation wavelength of 402 nm. The final transient spectra are an average of three complete cycles scanning the entire set of time delay positions.

The continuum probe exhibited some chirp, with the red edge reaching the sample later than the blue. This chirp was corrected by fitting data at thirteen wavelengths to an empirical function ($y = A_2 + (A_1 - A_2)/(1 - \lambda/\lambda_0)^P$) chosen for goodness of fit across the experimentally measured range. $A_1 = 0.43774$; $A_2 = 1.15446$; $\lambda_0 = 393.93747$; $P = 7.65254$; rms deviation from the experimental values = 0.05. The (chirp-corrected) $\Delta t = 0$ at 426 nm was used for plotting the transients in the Soret band region. The $\Delta t = 0$ is chirp-corrected using this function for all of the kinetic traces analyzed and shown.

3.3 RESULTS

The UV-vis absorption spectrum of the five-coordinate, high-spin heme model compound $\text{Fe}^{\text{II}}\text{OEP-2MeIm}$ in dichloromethane is shown in figure 3-1. The most intense feature centered at 424 nm is the Soret (or B) band. The band centered at 543 nm is the Q-band and is an order of magnitude weaker than the Soret band.

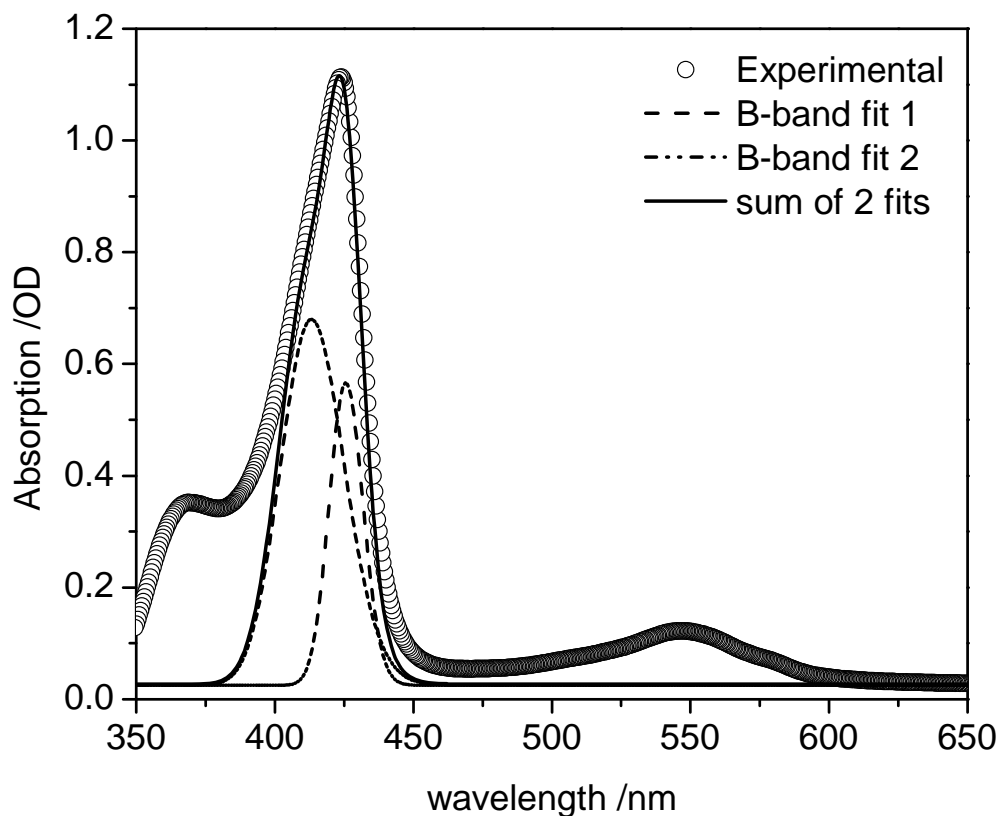


Figure 3 - 1 UV-visible absorption spectrum of $\text{Fe}^{\text{II}}\text{OEP-2meIm}$ in CH_2Cl_2 . The intense band centered at 424 nm is the Soret or B band. The band centered at 543 nm is the Q-band and is an order of magnitude weaker than the B band. Gaussian fits of the B band line shape are also included.

Excitation of the heme leads to rapid increase in the anti-Stokes intensities of several vibrational modes. Figure 3-2 shows a representative set of transient anti-Stokes Raman spectra generated by exciting the molecule on the blue side of the Soret transition ($\lambda_{\text{pump}} = 413 \text{ nm}$), and then probing at the same wavelength as a function of time delay.

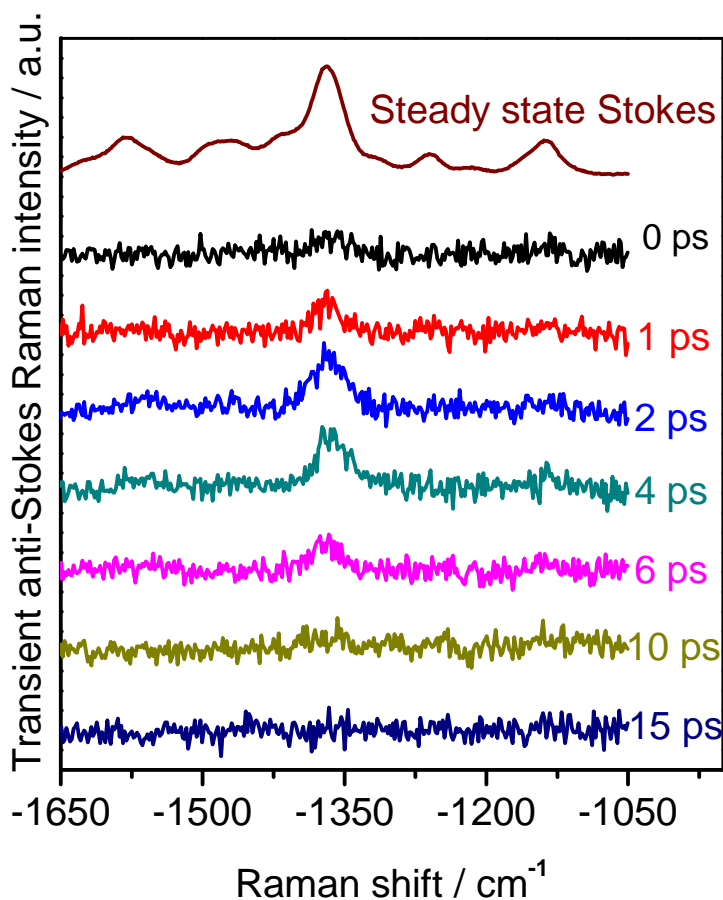


Figure 3 - 2 Time resolved anti-Stokes resonance Raman spectra of Fe^{II}OEP-2MeIm in CH₂Cl₂ using 413 nm pump and 413 nm probe at the indicated time delays. The energies of the pump and probe pulses are 5.5 and 2.5 μJ respectively. Transients are obtained by subtracting the reference spectra at $\Delta t = -25 \text{ ps}$. The upper trace is a steady state Stokes resonance Raman spectrum obtained at the probe wavelength of 413 nm.

The most intense transient feature appears at 1360 cm^{-1} , and is assigned to ν_4 , a symmetric (A_{1g}) pyrrole breathing motion. This transition is the most intense in the Stokes spectrum as well. Two other peaks are weaker, but apparent. These bands at 1565 cm^{-1} and 1135 cm^{-1} also grow in rapidly, and decay completely by about $\Delta t = 10\text{ ps}$. The weak transient feature at 1565 cm^{-1} has been assigned to ν_2 , an A_{1g} in-phase C_β - C_β stretch³⁹. The 1135 cm^{-1} band is most likely ν_5 , a C_β -substituent mode⁴⁰. CO photolysis experiments^{19,20} place ν_5 at 1112 cm^{-1} . However, analysis of resonance Raman spectra of NiOEP⁴⁰ assign a weak band at 1139 cm^{-1} to this motion.

Figure 3-3 shows a kinetic analysis of the peak heights of the three bands discussed. Several observations can be made from these data. All three traces exhibit intensity well before $\Delta t = 0$. This is a consequence of the one-color, two pulse method employed in these studies, and is used to help evaluate the temporal characteristics of the incident pulse. Since both pulses have same wavelength of 413 nm in this setup, their identities as pump and probe depend only on which one arrives first at the sample. So either can act as a pump or probe and the magnitude of change in Raman intensity for a given vibrational mode induced by the pump and measured by the probe will be symmetric about time zero. Nominally, this means that the signals will be symmetric about a minimum at $\Delta t = 0$. However, since the two beams impose different fluxes on the sample, the negative Δt changes are less intense than their positive counterparts. The ratio between the intensities of the 'probe' and 'pump' beams is about 0.4, so the dip position is shifted to slightly negative time delay. This method was already illustrated by us in these previous publications^{37,41}.

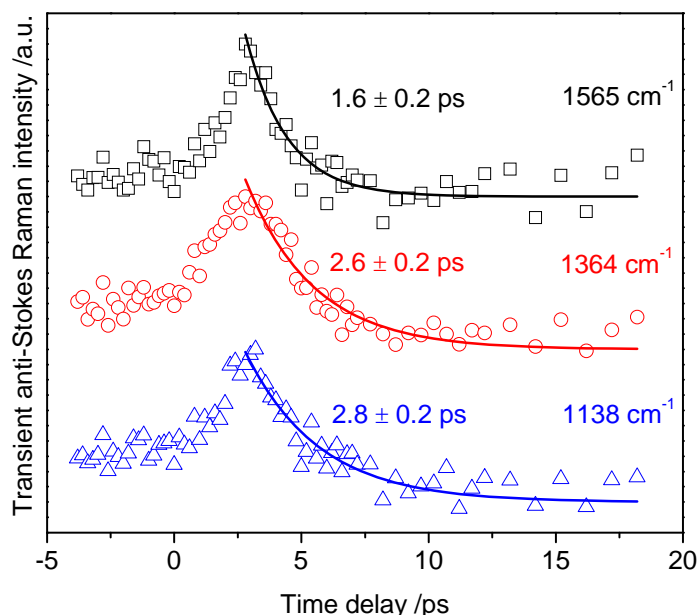


Figure 3 - 3 Vibrational mode decay kinetics on the ground electronic state of Fe^{II}OEP-2MeIm using TRARRS. Experimental kinetic traces were formed by averaging the three peak intensities for each band and then averaging these across the multiple data sets. No further processing was done. Squares are ν_2 , circles are ν_4 and the triangles are ν_5 . The rise times are estimated to be ~ 750 fs.

The decay portions of these traces were fit with single exponentials. The ν_4 and ν_5 bands decay with very similar kinetics, with 2.6 ± 0.2 and 2.8 ± 0.2 ps time constants, respectively. The ν_2 transient decays significantly more rapidly ($\tau = 1.6 \pm 0.2$ ps). The rises of the three bands have been estimated by simulating the data with the symmetric kinetics, weighted by 0.4 at negative time and convolved with a Gaussian pulse (FWHM = 600 fs). ν_5 , simulated with a 750 fs rise and 2.56 ps decay time fits the kinetic trace very well. Similar simulations for ν_4 and the ν_2 peaks gave rise times of 750 and 650 fs, respectively.

Complementary ultrafast time resolved Stokes resonance Raman spectra of Fe^{II}OEP-2MeIm in CH₂Cl₂ obtained with 410 nm excitation and probing are shown in Figure 4. The bleaching of the Stokes intensities at early times is apparent. As with the TRARRS spectra, bleach can be seen well before time zero as a consequence of the one-color, two pulse method employed.

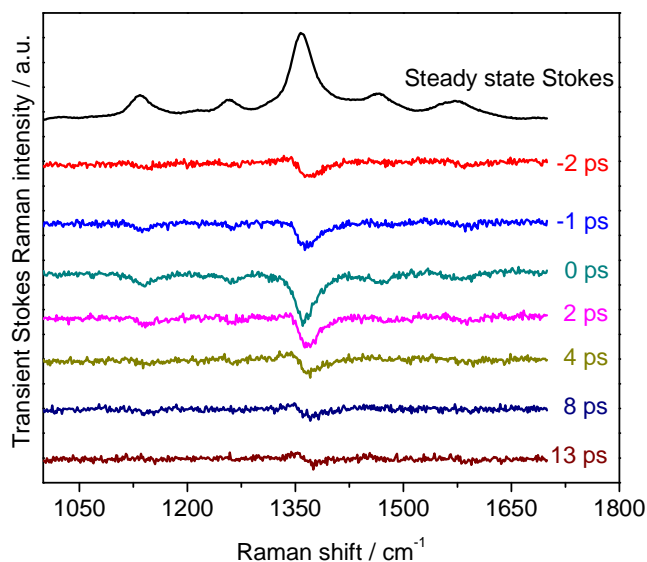


Figure 3 - 4 Time resolved Stokes resonance Raman spectra of Fe^{II}OEP-2MeIm in CH₂Cl₂ using 410 nm pump and 410 nm probe. Transients are obtained by subtracting the reference spectra at $\Delta t=64$ ps

The ν_4 (1362 cm⁻¹) band, strongest of the TRARR transient peaks, suffers the most loss of Stokes scattering intensity. Four other features are prominent, though weaker. The band at 1140 cm⁻¹ assigned to ν_5 an A_{1g} (C _{β} -C_{ethyl}) symmetric stretch appears in the ultrafast anti-Stokes spectra as well. The ν_2 mode (1580 cm⁻¹) also shows dynamics in both the Stokes and anti-Stokes spectra. The transients at 1260 cm⁻¹ and

1470 cm^{-1} do not have counterparts visible in the TRARR spectra. They are assigned to ν_{CH} , a symmetric CH_2 twist of the ethyl peripheral substituents, and ν_3 , an A_{1g} ($\text{C}_\alpha\text{-C}_\beta$) symmetric stretching motion.

Figure 3-5 shows kinetic traces of the Stokes TRRR intensities of the vibrational modes ν_2 , ν_3 , ν_4 , ν_{CH} and ν_5 at 1583 cm^{-1} , 1471 cm^{-1} , 1360 cm^{-1} and 1140 cm^{-1} respectively. Single exponential fits of the bleach recovery are shown as well (Table 3-1). The bleach recovery signals exhibit similar kinetics. On average, they recover with a time constant of 2.1 ± 0.2 ps.

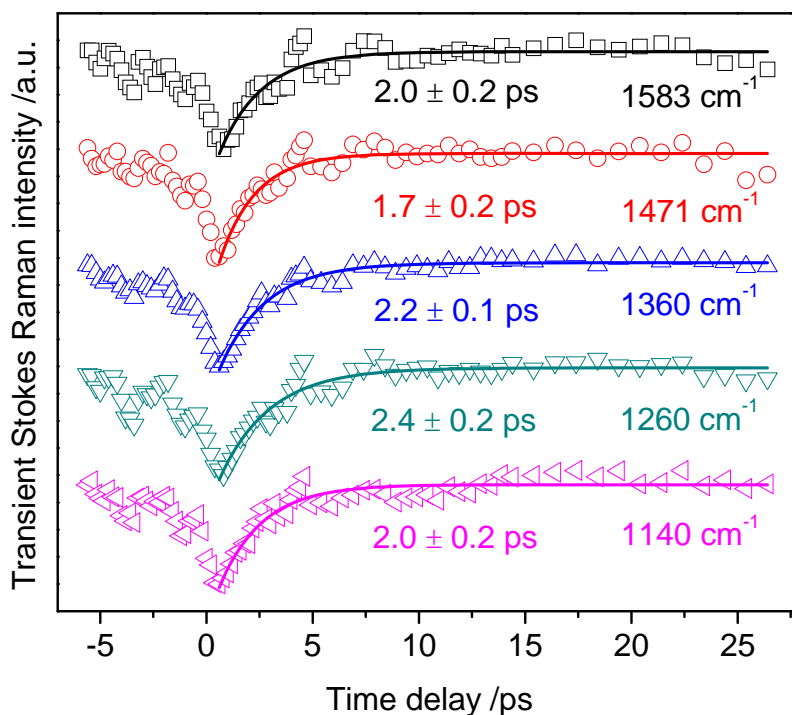


Figure 3 - 5 Vibrational mode population recovery kinetics on the ground electronic state of $\text{Fe}^{\text{II}}\text{OEP-2MeIm}$ using time-resolved Stokes resonance Raman spectroscopy. All the five observed vibrational modes recover with an average time constant of 2.1 ± 0.2 ps.

	Anti-Stokes (TRARRS)			Stokes (TR ³ S)	
Vibrational	Position /	^a $\tau_{\text{RISE}} / \text{ps}$	^b $\tau_{\text{DECAY}} / \text{ps}$	Position /	^c $\tau_{\text{BLEACH}} / \text{ps}$
v ₂	1565	0.65	1.6 ± 0.2	1580	2.0 ± 0.2
v ₃	--	--	--	1470	1.7 ± 0.2
v ₄	1360	0.75	2.6 ± 0.2	1362	2.2 ± 0.1
v _{CH}	--	--	--	1260	2.4 ± 0.2
v ₅	1135	0.75	2.8 ± 0.2	1140	2.0 ± 0.2

Table 3 - 1 Vibrational Dynamics in Photoexcited FeOEP-2MeIm. ^aDetermined from simulations of the kinetic traces in Figure 3-3 using the fit decay life time, a pump/probe relative flux of 0.4 and convolution with a 600 fs Gaussian function. ^bFrom fitting only the decay portions of the kinetic traces in Figure 3-3. ^cFrom fitting only the bleach recovery portions of the kinetic traces in Figure 3-5.

Ultrafast TA spectroscopy with excitation on the blue side of the Soret band ($\lambda_{\text{pump}} = 402 \text{ nm}$; 110 fs instrument response) was performed to evaluate the behavior of the UV/Vis absorption spectrum during the same time frame as the TR³ and TRARR experiments. Figure 3-6 shows the evolution of the transient spectra in the Soret region to the red of the excitation pulse. Within the instrument response, Soret-band bleach that corresponds to ground electronic state depletion appears instantly. A broad, red-shifted transient absorption band rapidly blue-shifts and narrows until about $\Delta t = 2.5 \text{ ps}$ (Figure 3-6A). After that, a steady decrease in intensity and continued blue-shift is

observed (Figure 3-6B). The dynamics on the red side of the Soret are complete by $\Delta t = 30$ ps.

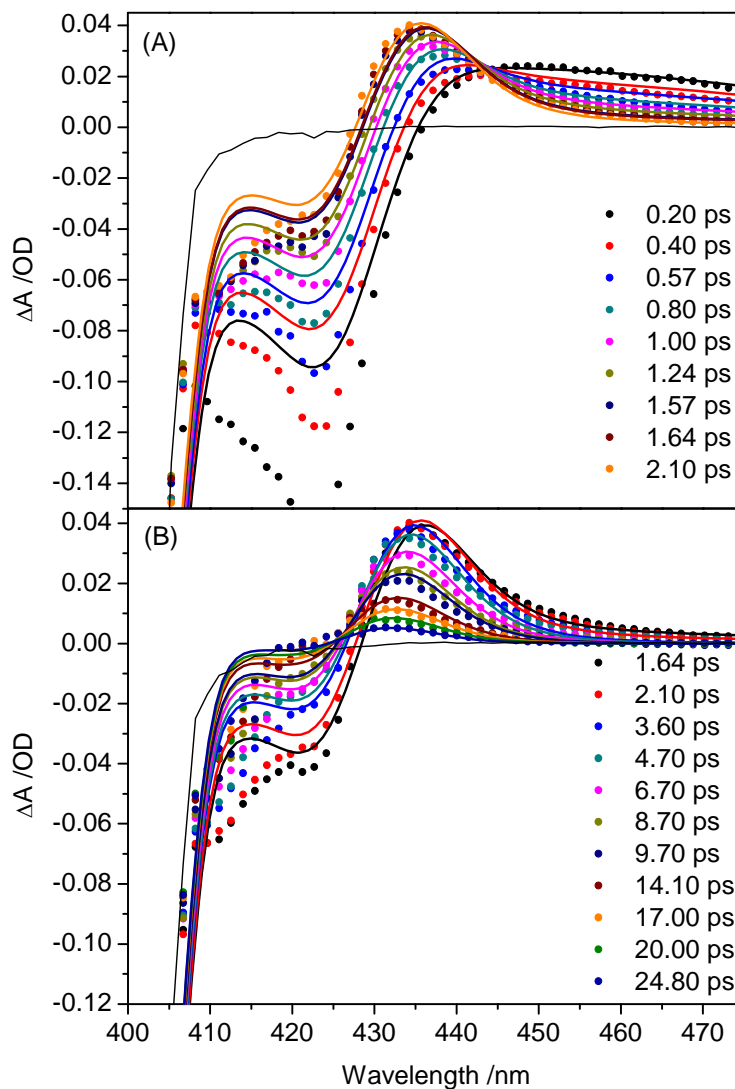


Figure 3 - 6 Transient absorption experimental data and simulations for $\text{Fe}^{\text{II}}\text{OEP-2meIm}$ in CH_2Cl_2 . Pump=402 nm, Probe=white light continuum generated in CaF_2 (360-700 nm) and the instrument response is 110 fs. OD of the sample is less than 1.0 at 402 nm. Panel (A) shows the fast dynamics associated with the first 2.0 ps and panel (B) shows the slower dynamics on the 25 ps time scale. The large dip in the spectrum is a laser line artifact at the pump wavelength of 402 nm (thin black line).

Kinetic traces at several wavelengths presented in Figure 3-7 show that evolution of the UV/Vis absorption is quite complicated. The traces can be fit with exponential functions (Table 3-2); resulting time constants that vary with wavelength. For example, from 430 nm to 480 nm the t_3 decay lifetime shortens monotonically from 12.1 ± 0.5 ps to 2.4 ± 0.3 ps. This sort of behavior is the hallmark blue-shifting and/or narrowing of the underlying absorption bands that occurs on the time scale of the population changes.

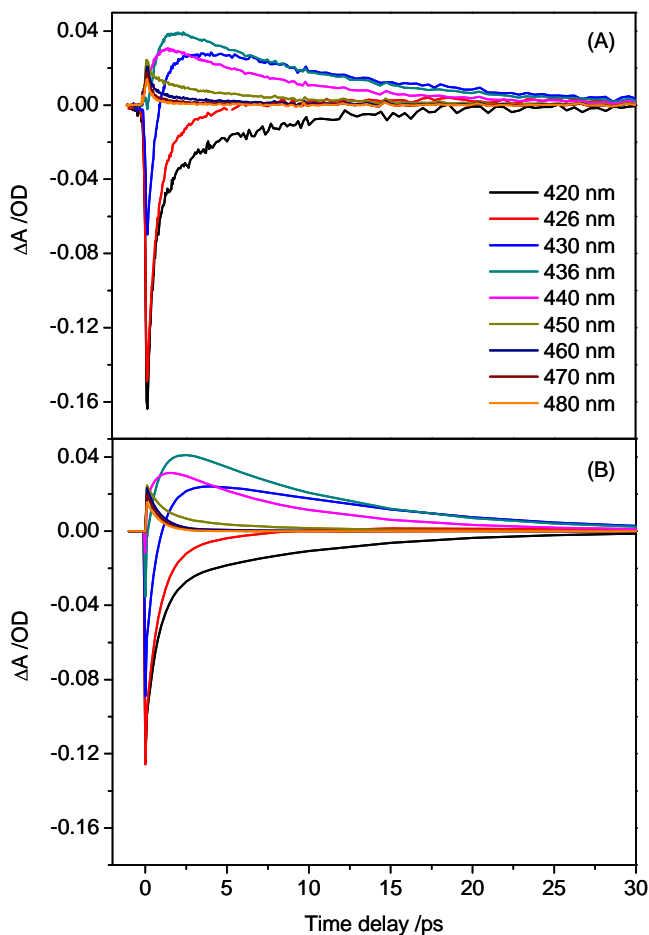


Figure 3 - 7 (A) Kinetic traces from the experimental transient absorption data at the indicated probe wavelengths using 402 nm pump. (B) Kinetic traces obtained from the simulated transient absorptions [look in the Figure 3-8, Tables 3-2 and 3-3 legends for simulation parameters]

Exponential Fit to Experimental TA Measurements^a

$\lambda(\text{nm})$	$A_1 (\%), t_1 (\text{fs})$	$A_2 (\%), t_2 (\text{ps})$	$A_3 (\%), t_3 (\text{ps})$	$A_4 (\%), t_4 (\text{fs})$
420	-90, 433±9	-10, 5.4±0.1		
426	-90, 511±33	-10, 1.6±0.2		
430	-66, 615±26	-11, 2.5±0.8	23, 12.1±0.5	
436	-57, 627±8		43, 9.9±0.1	
440	-43, 568±15		57, 8.3±0.1	
450			48, 6.7±0.1	52, 361±18
460			21, 4.8±0.2	79, 312±11
470			13, 3.1±0.2	87, 244±9
480			11, 2.4±0.3	89, 245±12

Exponential Fit to Simulated TA^a

$\lambda(\text{nm})$	$A_1 (\%), t_1 (\text{fs})$	$A_2 (\%), t_2 (\text{ps})$	$A_3 (\%), t_3 (\text{ps})$	$A_4 (\%), t_4 (\text{fs})$
420	-70, 661±46	-30, 8.2±0.9		
426	-22, 88±20	-78, 1.1±0.1		
430	-15, 38±10	-63, 0.9±0.1	22, 13.7±0.5	
436	-60, 557±58		40, 11.1±1.2	
440	-56, 158±23		44, 10.0±1.0	
450			31, 6.1±0.01	69, 932±9
460			5, 5.1±0.1	95, 818±1
470			1, 4.1±0.1	99, 805±0
480			0.2, 2.9±0.4	99.8, 800±0

Table 3 - 2 Kinetic Analysis for TA experimental Data and Simulations.

^a $r^2 > 0.99$ for all fits except the last three experimental ones, which were 0.987, 0.979, 0.966.

Simulations of the Transient Absorption Dynamics.

Simulations of the TA results were performed using a three-electronic state model ($S_2 \rightarrow S_1 \rightarrow S_0^* \rightarrow S_0$). In this model, S_2 and S_1 were treated as the Soret and Q-band excited electronic states, respectively. S_0^* represents vibrationally excited, ground state species newly created by IC from S_1 . The lineshapes (width, peak position) of both S_1 and S_0^* were allowed to evolve in time; the S_2 and S_0 lineshapes were static. The S_0 and S_0^* lineshapes were derived from non-linear least squares fitting of the experimental UV/Vis spectrum as shown in Figure 3-1.

Straightforward kinetic equations for the populations of S_2 , S_1 and S_0^* can be written:

$$S_2(t) = S_2(0)e^{-t/\tau_2} \quad (3-1a)$$

$$S_1(t) = S_2(0) \frac{\tau_1}{\tau_2 - \tau_1} (e^{-t/\tau_2} - e^{-t/\tau_1}) \quad (3-1b)$$

$$S_0^*(t) = S_2(0) \left\{ \frac{\tau_1 (1 - e^{-t/\tau_1}) - \tau_2 (1 - e^{-t/\tau_2})}{\tau_1 - \tau_2} \right\} \quad (3-1c)$$

where τ_2 and τ_1 are the lifetimes of the S_2 and S_1 states, respectively, and $S_2(0)$ is the fraction of molecules initially excited from S_0 by the incident light pulse, which is treated as a delta function here. The line shapes associated with these populations are given by single Gaussian functions for S_2 and S_1 of the form

$$G_2 = \frac{A_2}{\omega_2 \sqrt{\pi/2}} e^{-\frac{2(\bar{\nu} - \bar{\nu}_2)^2}{(\omega_2)^2}} \quad (3-2)$$

A_2 is the relative area, ω_2 is the width, and $\bar{\nu}_2$ is the peak energy of the $S_0 \rightarrow S_2$ absorption band; corresponding variables are used for the S_1 peak. For S_1 , the width (ω_1) and center position ($\bar{\nu}_1$) were also allowed to vary in time exponentially. G_0 , the ground state lineshape is static. However, $G_0^*(t)$ starts at $\Delta t = 0$ red-shifted and broadened relative to G_0 , and shifts back to the G_0 values exponentially, with time constants of $\tau(\bar{\nu}_0^*)$ and $\tau(\omega_0^*)$.

The S_2 state was assigned a very short lifetime ($\tau_2 = 10$ fs), based upon the observation that TA dynamics have been found to be very similar regardless of whether the Soret or the Q-band state is initially excited. Given this, it was further assumed that the S_2 absorption does not contribute to the observed TA dynamics ($A_2 = 0$). The four orbital model of porphyrin UV/Vis absorption⁴²⁻⁴⁴ attributes the ground state spectrum (Soret and Q-band) to two pairs of transitions from the $a_{1u}(\pi)$ and $a_{2u}(\pi)$ occupied orbitals to a doubly degenerate $e_g(\pi^*)$ unoccupied orbital. Promotion of one electron should thus lead to an S_1 state with an excited state spectrum that has Soret and Q-band components, but shifted to the red as the overall bond order of the macrocycle has been reduced. Holten and coworkers found that the S_1 excited state absorption of a wide range of porphyrins is red-shifted, relative to the ground state absorption, and is most likely π - π^* in character⁴⁵⁻⁴⁷. A center position of 450 nm for the S_1 ‘‘Soret’’ absorption was found to be satisfactory. The lifetime of the S_1 state that best reproduced the TA data was found to

be sub-picosecond ($\tau_1 = 800$ fs), though values from 10 fs to 20 ps were tested. The contribution of S_1 transient absorption to the overall signal was also found to be very small; no evolution of the S_1 lineshape was required, so $\omega_l(t) = \omega_l(0) = \text{constant}$ and $\bar{\nu}_1(t) = \bar{\nu}_1(0) = \text{constant}$.

The evolution of the $S_0^*(t)$ species dominated the TA signals. The simulations and their comparison to the experimental data are presented in Figures 3-6, 3-7 and 3-8. A wide range of values of the adjustable parameters $\bar{\nu}_0^*(0)$, $\tau(\bar{\nu}_0)$, $\omega_0^*(0)$, $\tau(\omega_0^*)$ and A_0^* was tested, and the parameters that best reproduced the data are collected in Table 3-3.

	Lineshape Parameters ^a					Population Dynamics
	$\bar{\nu}(0) / \text{cm}^{-1}$	$\tau(\bar{\nu})$	$\omega(0) / \text{cm}^{-1}$	$\tau(\omega)$	A	τ
S_0^*	24500.0 ^b 23795.7	10 ps	1608 ^b 804	8 ps	1155 478	---
S_0	24200.0 23495.7	---	1340 670	---	1155 478	---
S_1	22225	---	3000	---	800	800 fs
S_2	---	---	---	---	0	10 fs

Table 3 - 3 Parameters used in TA simulations. ^aSee text for details of the equations used to simulate the TA data. ^bThe $\bar{\nu}(0)$ values for S_0^* are red-shifted 300 cm^{-1} relative to the values for the thermal S_0 ground state spectrum. The $\omega(0)$ values for S_0^* are 1.2 x the values for S_0 .

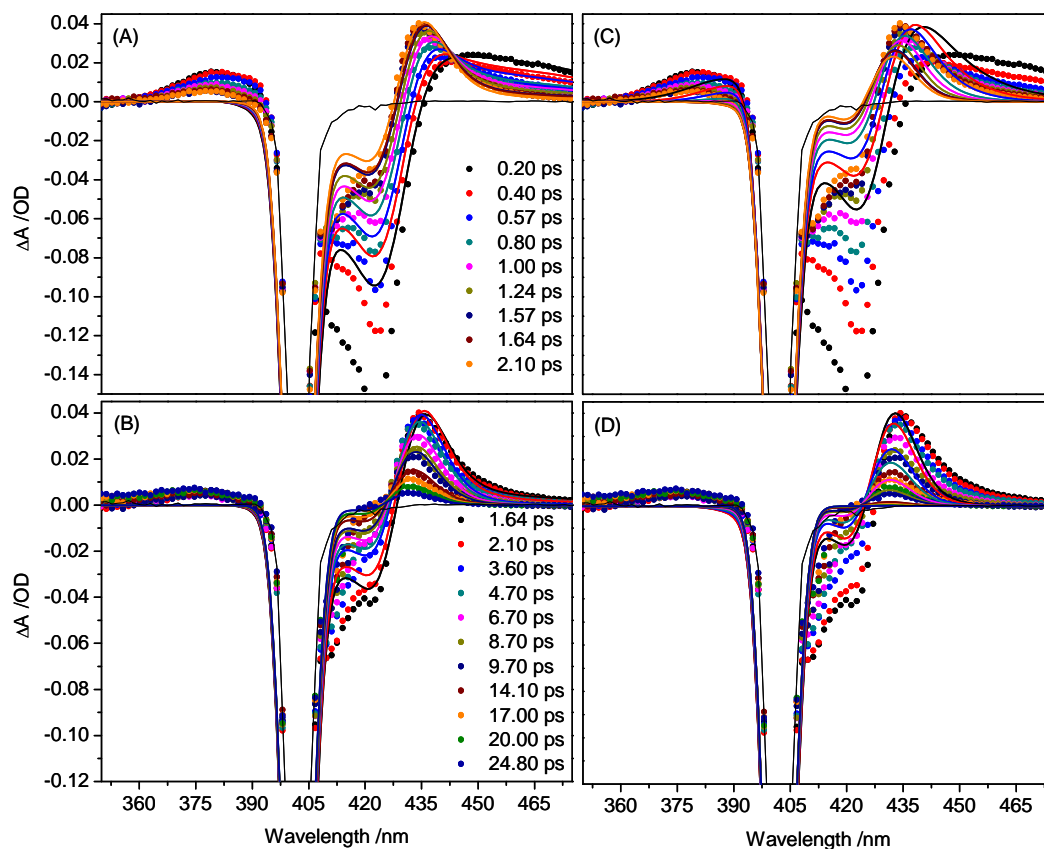


Figure 3 - 8 Transient absorption data (filled circles) and simulations (lines) for Fe^{II}OEP-2MeIm in CH₂Cl₂ using the vibrationally hot ground electronic state model. Pump = 402 nm, Probe = white light continuum (360-750 nm). The large dip in the spectra is a laser line artifact from the experiment (thin black line). Left panels are the first 2 ps (panel A) and 25 ps (panel B) with simulations using the parameters [S_2 : $\tau = 10$ fs, S_1 : $\tau = 800$ fs and S_0^* : $t(\nu) = 10$ ps, $t(\omega) = 8$ ps and the absorption of S_0^* was modeled as red-shifted by 300 cm⁻¹ and broadened by 20 % relative to S_0]. Right panels are the first 2 ps (panel C) and 25 ps (panel D) with simulations using the parameters from reference 30 [S_1 : $\tau = 50$ fs and S_0^* : $t(\nu) = 4$ ps, $t(\omega) = 400$ fs and the absorption of S_0^* was modeled as red-shifted by 200 cm⁻¹ and broadened by 150 % relative to S_0]

3.4 DISCUSSION

The electronic and vibrational dynamics of a symmetric, five-coordinate, high-spin, model heme complex, in an isotropic (to first order) solvent environment are presented. Complementary TA, TR³S and TRARRS experiments excite the blue side of the Soret (S₂) state and monitor the evolution of the heme in time. The observed dynamics contain contemporaneous contributions from rapid IC, IVR, and VER. Simulations of the evolving UV/Vis absorption line width and position of newly created ground state hemes reproduce most of the main features of both the TA spectra and the single-wavelength kinetic traces, and provide a framework within which to interpret the time-resolved resonance Raman findings.

The results presented here are consistent with a very rapid (sub 100fs) S₂ → S₁ transition, followed by a somewhat longer, but still sub-picosecond (800 fs) decay of S₁ to the ground electronic state. Given the rapidity of the IC processes, the amount of energy deposited in the vibrational manifold of the ground state heme is quite significant. The newly created S₀* absorption band appears to be broadened and shifted to lower energy. In our simulations, modest broadening of 20% and red-shifting of 300 cm⁻¹ in the absorption bands is sufficient to model the experimental data quite well. The narrowing and shifting to the room temperature, thermal line shape of S₀ occurs on an 8 – 10 ps timescale, and dominates the changes observed in the TA difference spectra. This process of shifting and narrowing reflects the vibrational relaxation of the heme, IVR and VER on the ground state surface. The TA experimental data, simulations and the kinetic data from TRARRS experiments lead to a simple model describing the dynamics of this simple heme compound as illustrated in Figure 3-9.

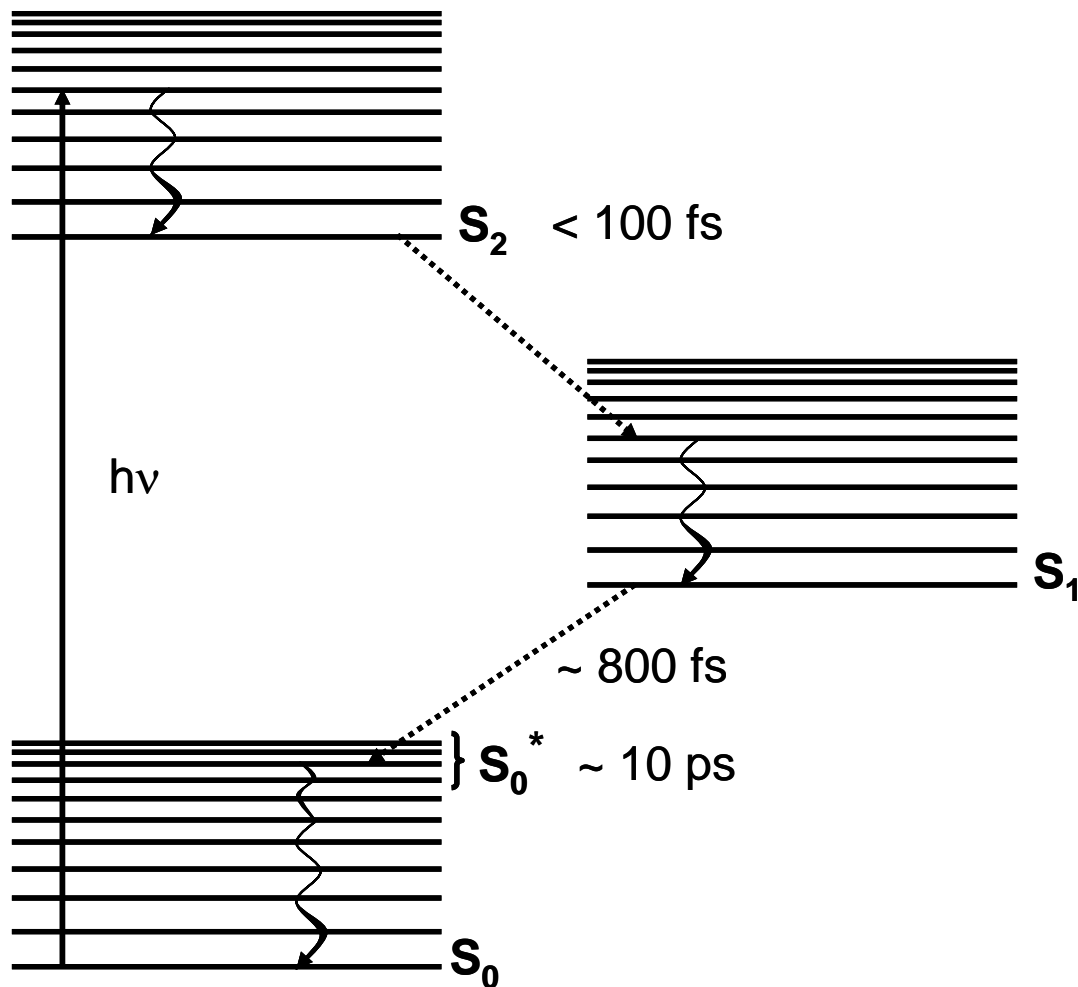


Figure 3 - 9 Simplified picture representing the events that follow electronic excitation in the Soret band of model heme Fe^{II}OEP-2MeIm in CH₂Cl₂, derived from the complimentary TA, simulations and TRARRS studies.

The time resolved Raman data are largely consistent with this picture as well. The anti-Stokes rise times are sub-picosecond (~700 fs), indicating the recovery of the ground electronic state. The anti-Stokes signals decay with time constants of 1.5 to 3 ps, significantly shorter than the vibrational dynamics evident in the TA spectra and simulations. The most likely explanation is that the anti-Stokes signals are largely reflecting mode-selective IVR processes that rapidly redistribute the excess energy in a

Boltzmann distribution, albeit at an elevated temperature. The anti-Stokes signals are quite weak, and it is likely that once the excess energy is distributed over the >100 degrees of freedom of the heme, the vibrational excitation in the high-frequency region is below the detection threshold of our experiments. The narrowing and shifting of the UV/Vis spectrum largely reflects the vibrational cooling of the heme to reach thermal equilibrium.

This interpretation of rapid (1-3 ps) IVR and slower (~10 ps) VER is consistent with previous nanosecond transient resonance Raman studies of five-coordinate, high-spin hemes in a variety of solvent environments^{18, 23, 36}. In these single-pulse studies, the anti-Stokes intensity is dependent upon the flux of the incident laser. As the flux increases, the heme is excited more often within a single pulse and a steady-state, non-Boltzmann distribution of vibrational energy associated with the ground electronic state is created and monitored with the transient anti-Stokes spectrum. One intriguing observation is that the distribution measured appears largely independent of the solvent. Very similar behavior is observed for the heme in Fe^{II}-deoxyhemoglobin in the protein, Fe^{II}-protoporphyrin IX in CTAB detergent micelles, and Fe^{II}OEP-2MeIm in CH₂Cl₂. It is reasonable, then, that the anti-Stokes signals reflect only intramolecular vibrational dynamics, and that these are largely independent of the solvent environment.

The data reported here are consistent with previously reported findings invoking a vibrationally hot ground electronic state model^{26, 30} but differ from the models invoking intermediate charge transfer electronic states^{17, 22, 25, 27, 48}. One of the earlier models proposed multiple electronic decay pathways that repopulated S₀ on ~300 fs and ~3 ps timescales^{17, 25, 48}. In the latest version of this model²⁷, the photoexcited heme decays

sequentially to an intermediate state called Hb_{I}^* through a metal-to-ring charge transfer event. The rapid back charge transfer leads to Hb_{II}^* , assigned to a vibrationally excited ground state macrocycle with a d-d* excited metal ion center. The decay of Hb_{II}^* back to the heme ground state then occurs on a 3 ps timescale. A two state evolution with time constants of 320 fs and 2.2 ps was proposed from time resolved absorption studies of the Q-band and band III regions. Both of these models were based upon global fitting of single-wavelength kinetic traces; no line shape evolution was included in the fitting procedure. The wavelength-dependence of the kinetic traces suggests that such global fitting may not be appropriate. The time constants can vary quite significantly across even relatively small regions of the UV/Vis spectrum (Table 3-2). Neither the time-resolved anti-Stokes nor the TA simulations presented here provide evidence for a 3 ps electronic state lifetime.

Actually, Holten and coworkers pointed out that the TA signatures of many metalloporphyrins are quite similar, with initially broad and red-shifted transient absorptions that relax on ~ 10 ps timescales⁴⁵⁻⁴⁷. The ubiquity of this behavior suggested to them that its origin could not be electronic, but was rather a hallmark of porphyrin vibrational dynamics. Our findings are entirely consistent with this interpretation.

A recent study by Champion and coworkers proposes even shorter IC in five-coordinate, high-spin hemes, with sub-50 fs IC back to the ground state^{29, 30}. They pump in the Q-band, and measure the TA in the Soret band region, and see most of the same features we observe. However, simulations of our data using their time constants did not yield satisfactory results (Figure 3-8, Panels (C) and (D)) for the dynamics of the red side of the Soret region at early or late times. In addition to the sub-100 fs decay of S_1 , they

propose a very broad S_0^* ($2.5 \times S_0$) that evolves in both peak position and width exponentially, with lifetimes of 4 ps and 400 fs, respectively. However, this led to relatively shallow bleaches and difference spectra that narrow too quickly, particularly evident in the 435 – 465 nm region. Slowing down the narrowing process while maintaining the very short S_1 lifetime did not correct the discrepancies. In our model, the longer lifetime of the S_1 state along with the slower line width and position changes fits this region of the TA difference spectra much better. Another TA study using ~ 70 fs pulses at 405 nm evaluated the Q-band and band III dynamics, and concluded that there were no electronic dynamics after ~ 500 fs subsequent to excitation²⁶. Vibrational dynamics associated with S_0^* occurred on 1 to 10's of picosecond timescales, and were modeled with an evolving line shape function as well. In contrast, we find that the ~ 800 fs S_1 lifetime is required to fit the earliest dynamics (< 2 ps, Figure 3-8, panel (A)). Extending the simulation and comparison to TA data to longer wavelengths may resolve this slight difference.

It is clear from Figure 3-8, however, that our model does not represent a complete picture of heme vibronic dynamics. In particular, Panels (A) and (B) show quite clearly that we do not adequately capture the behavior to the blue of the Soret band ($\sim 350 - 400$ nm). Ye et al.³⁰ model the dynamics of this region more accurately at earlier times because of the very broad line width used for S_0^* . At long times, though, there is clearly a persistent transient absorption intensity to the blue of the initial bleach that neither model picks up. Further study is clearly warranted to elucidate the origin of this transient difference signal.

Evaluation of the kinetic traces from the simulation, and comparison to the TA data provides strong evidence for the accuracy of the main features of the model (Figure 3-7, Table 3-2). The overall pattern of the traces is nearly identical, and the lifetimes are quite similar as well. For example, in the traces from 430 to 480 nm, the behavior of component 3 is virtually identical in the measurements and the simulation. The lifetime changes from about 12 – 14 ps at 430 nm to 2-3 ps at 480 nm. It should be pointed out that only the time-dependent difference spectra were evaluated in optimizing the parameters. That is, the parameters were not adjusted to improve the fit with the kinetic trace analyses.

There are potential complications from the concurrently changing transient absorption and resonance Raman spectra. The resonance cross section depends upon the absorption strength as well as the vibrational level population and cross section. If the UV/Vis spectrum is much broadened, the cross sections of both Stokes and anti-Stokes resonance Raman transitions may be lower than expected, depending upon the degree of broadening and the excitation wavelength. Re-absorption of the scattered light also will be affected by a changing absorption band, but in the opposite manner, so that some fortuitous cancellation will occur. Ye et al.³⁰ report a first-order attempt to examine the effect of the dynamical UV/Vis absorption spectrum upon anti-Stokes signals, using several approximations and the Kramers-Kronig transformation. A similar approach was proposed and tested by Kozich et al.⁴⁹ While the approximations like harmonic potential, Boltzmann distribution of vibrational energy even at very early Δt limit quantitative applicability of this treatment to systems in vibrational and electronic flux, the results indicate that the vibrational lifetimes measured may be significantly different from their

true values due to the evolving resonance conditions. At the moment, we attribute the anomalously long Stokes bleach recovery times to this effect, though this hypothesis remains to be tested. Currently, we are working on a way to more accurately probe these complicated, counteracting effects.

The working hypothesis behind these studies is that the initial distribution of excess vibrational energy deposited in the ground electronic state from a photoexcited (or intermediate excited) electronic state, and the subsequent redistribution and relaxation dynamics, depend strongly upon (1) the total amount of excitation energy in the system (2) the nature of the electronic excited state that couples to the ground state in the IC process, and (3) the intrinsic coupling of each mode to other molecular and solvent degrees of freedom. In practice, then, there is no single lifetime for a given vibrational mode.

The measured lifetime of a single mode reflects a complex set of dynamical processes. A fundamental, intrinsic $0 \leftarrow 1$ lifetime corresponds to the characteristic decay of the $v = 1$ vibrational level in the isolated, cold molecule. This τ_i^0 depends upon the intramolecular coupling of mode i to other molecular degrees of freedom, and is rather difficult to measure. In the molecule at room temperature in solution, the measured lifetime τ_i is almost certainly quite different from τ_i^0 . Intermolecular and intramolecular coupling to other motions will depend upon the excess energy in the system and the time-dependent populations of these other degrees of freedom, strongly affect the vibrational dynamics. The non-Boltzmann distributions that may persist in a photoexcited molecule for several picoseconds may dramatically affect the measured lifetime in ways that are difficult to predict.

In particular, these studies probe the dependence of heme vibrational dynamics upon the magnitude of the initial excess vibrational energy and the nature of the coupled excited state in IC. Comparisons of the TRARRS results to ps ligand-photolysis studies by Mizutani and Kitigawa provide insight into this fundamental issue. In those experiments, myoglobin with a CO ligand (Mb-CO) was photoexcited in the heme Q-band, and the resonance Raman Stokes and anti-Stokes spectra were measured as a function of time using $\lambda_{\text{probe}} = 435$ or 442 nm with ~ 2 - 2.3 ps pulses^{19, 20}. Some very interesting behavior of the newly photolyzed, five-coordinate transient Mb* species was seen. Examination of the modes that appear in the transient anti-Stokes spectrum and their decay kinetics is illuminating.

Photolysis of the CO from MbCO rapidly (< 1 ps) generated a vibrationally excited, five-coordinate, transient Mb* in its ground state but with significant population in ν_3 (1461 cm^{-1}), ν_4 (1360 cm^{-1}), ν_5 (1112 cm^{-1}) and ν_6 / ν_{32} (779 cm^{-1}). ν_7 (669 cm^{-1}) band was also observed in some spectra. In contrast, the early-time Fe^{II}OEP-2MeIm spectra exhibit significant intensity in ν_4 , ν_2 and the 1135 cm^{-1} band, but ν_3 and a transition at 1112 cm^{-1} assigned to ν_5 , and ν_6 / ν_{32} do not appear.

There are two possible sources for these differences. The spectra are measured at different positions within the UV/Visible Soret absorption band, so resonance effects may be important. More likely, though, is the interpretation that different subsets of modes are involved in IC for the two different processes. The coupling and accepting modes associated with IC lead to different initial vibrational energy distributions depending upon whether the excitation involves ligand photolysis or not. It is significant that the ν_4

transient is the most intense in both experiments. Clearly, this mode plays an important role in heme electronic dynamics.

The vibrational state lifetimes differ slightly in the two TRARRS studies. The ν_4 transient decayed with time constants of 1.9 ± 0.6 ps ($\lambda_{\text{probe}} = 436$ nm) and 1.1 ± 0.6 ps ($\lambda_{\text{probe}} = 442$ nm) with CO photolysis. Both of these lifetimes are somewhat shorter than the 2.6 ± 0.2 ps measured with photoexcitation of Fe^{II}OEP-2MeIm. Clearly, this intriguing difference needs to be revisited in parallel experiments under the same conditions. ν_7 decayed with 1.9 ± 0.6 ps kinetics in the photolysis experiments when $\lambda_{\text{probe}} = 442$ nm, but was not seen at 435 nm. We observed excitation in ν_7 as well, but it was considerably complicated by a solvent band; we were not confident in evaluating its kinetics unambiguously (not shown).

These differences are perhaps not surprising, as the two processes must necessarily participate in very different energy disposal processes. Mb-CO is a six-coordinate, low-spin heme in the ground state. Photoexcitation must ultimately result in the Fe ion becoming high-spin and moving out of the plane of the macrocycle. Photolysis also reduces the overall amount of energy that can wind up in the ground electronic state because some of the excitation energy is required to break the Fe-C bond, and some leaves with the newly photolyzed CO ligand. In the experiments by Mizutani and co-workers, this difference is compounded by their excitation in the lower energy Q-band in the first place.

In contrast, Fe^{II}OEP-2MeIm is already a five-coordinate, high-spin heme with a domed conformation in the ground state. In addition, all of the energy from the absorbed

photon is available to be deposited in the electronic ground state. The structural evolution of the two systems (e.g. the tuning modes) and the coupling of the excited states to the ground and any participating intermediate electronic states should differ, and be reflected in different initial vibrational excited state distributions observed upon IC to the ground electronic state. For example, Figure 3-3 indicates that ν_2 , a mode that does not even appear in the CO photolysis transients, rises and decays faster than the other two modes seen in the TRARRS studies of Fe^{II}OEP-2MeIm. This indicates that ν_2 may be a strong accepting mode for IC in the non-ligated heme, and that it decays rapidly intramolecularly to populate other heme degrees of freedom.

3.5 CONCLUSIONS:

The temporally overlapping, fast electronic and vibrational dynamics of the five-coordinate, high-spin heme has been studied with three complementary ultrafast techniques: transient absorption, time-resolved resonance Raman Stokes and time-resolved resonance Raman anti-Stokes spectroscopies. The data are largely consistent with a model in which the experimental observations are dominated by vibrational dynamics associated with an evolving ground state species. Excitation into the blue side of the Soret band led to very rapid $S_2 \rightarrow S_1$ decay (sub-100 fs), followed by somewhat slower (800 fs) $S_1 \rightarrow S_0^*$ nonradiative decay. The initial vibrationally excited, non-Boltzmann S_0^* state was modeled as shifted to lower energy by 300 cm^{-1} and broadened by 20%. On a ~ 10 ps timescale, the S_0^* state evolved into its room temperature, thermal distribution S_0 profile. Comparisons of anti-Stokes mode intensities and lifetimes from TRARRS studies in which the initial excited state was prepared by ligand photolysis begin to paint a map of the pathways of vibrational energy flow in the ground electronic

state and vibrational facilitation of the rapid IC processes in these heme systems. While TA studies appear to be relatively insensitive to initial preparation of the electronic excited state, the subsequent vibrational dynamics are not. Clearly, many more studies remain before we fully understand the photophysics and photochemistry in these systems. However, these TRARRS experiments have provided an important first step in unraveling the vibrational participation in IC in hemes, and the nature and pattern of heme vibrational dynamics established by photoexcitation.

3.6 REFERENCES

1. Miller, R. J. D., Vibrational energy relaxation and structural dynamics of heme proteins. *Annual Review of Physical Chemistry* 1991, 42, 581-614.
2. Miller, R. J. D., Energetics and Dynamics of Deterministic Protein Motion. *Accounts of Chemical Research* 1994, 27, (5), 145-50.
3. Miller, R. J. D., 2000 John C. Polanyi Award lecture mother nature and the molecular big bang. *Canadian Journal of Chemistry* 2002, 80, (1), 1-24.
4. Henry, E. R.; Levitt, M.; Eaton, W. A., Molecular dynamics simulation of photodissociation of carbon monoxide from hemoglobin. *Proceedings of the National Academy of Sciences of the United States of America* 1985, 82, (7), 2034-8.
5. Henry, E. R.; Eaton, W. A.; Hochstrasser, R. M., Molecular dynamics simulations of cooling in laser-excited heme proteins. *Proceedings of the National Academy of Sciences of the United States of America* 1986, 83, (23), 8982-6.
6. Straub, J. E.; Karplus, M., Molecular dynamics study of the photodissociation of carbon monoxide from myoglobin: ligand dynamics in the first 10 ps. *Chemical Physics* 1991, 158, (2-3), 221-48.

7. Li, P.; Champion, P. M., Investigations of the thermal response of laser-excited biomolecules. *Biophysical Journal* 1994, 66, (2, Pt. 1), 430-6.
8. Ma, J.; Huo, S.; Straub, J. E., Molecular Dynamics Simulation Study of the B-States of Solvated Carbon Monoxymyoglobin. *Journal of the American Chemical Society* 1997, 119, (10), 2541-2551.
9. Sagnella, D. E.; Straub, J. E., Directed Energy "Funneling" Mechanism for Heme Cooling Following Ligand Photolysis or Direct Excitation in Solvated Carbonmonoxy Myoglobin. *Journal of Physical Chemistry B* 2001, 105, (29), 7057-7063.
10. Okazaki, I.; Hara, Y.; Nagaoka, M., On vibrational cooling upon photodissociation of carbonmonoxymyoglobin and its microscopic mechanism from the viewpoint of vibrational modes of heme. *Chemical Physics Letters* 2001, 337, (1,2,3), 151-157.
11. Bu, L.; Straub, J. E., Vibrational energy relaxation of "tailored" hemes in myoglobin following ligand photolysis supports energy funneling mechanism of heme "cooling". *Journal of Physical Chemistry B* 2003, 107, (38), 10634-10639.
12. Lingle, R., Jr.; Xu, X.; Zhu, H.; Yu, S. C.; Hopkins, J. B., Picosecond Raman study of energy flow in a photoexcited heme protein. *Journal of Physical Chemistry* 1991, 95, (23), 9320-31.
13. Lingle, R., Jr.; Xu, X.; Zhu, H.; Yu, S. C.; Hopkins, J. B.; Straub, K. D., Direct observation of hot vibrations in photoexcited deoxyhemoglobin using picosecond Raman spectroscopy. *Journal of the American Chemical Society* 1991, 113, (10), 3992-4.
14. Alden, R. G.; Chavez, M. D.; Ondrias, M. R.; Courtney, S. H.; Friedman, J. M., Direct measurement of vibrational temperatures in photoexcited deoxyhemoglobin on

- picosecond time scales. *Journal of the American Chemical Society* 1990, 112, (8), 3241-2.
15. Alden, R. G.; Ondrias, M. R.; Courtney, S.; Findsen, E. W.; Friedman, J. M., Power-induced broadening of transient resonance Raman spectra of deoxyhemoglobin. *Journal of Physical Chemistry* 1990, 94, (1), 85-90.
16. Petrich, J. W.; Martin, J. L.; Houde, D.; Poyart, C.; Orszag, A., Time-resolved Raman spectroscopy with subpicosecond resolution: vibrational cooling and delocalization of strain energy in photodissociated (carbonmonoxy)hemoglobin. *Biochemistry* 1987, 26, (24), 7914-23.
17. Petrich, J. W.; Martin, J. L., Ultrafast absorption and Raman spectroscopy of heme proteins. *Chemical Physics* 1989, 131, (1), 31-47.
18. Simpson, M. C.; Peterson, E. S.; Shannon, C. F.; Eads, D. D.; Friedman, J. M.; Cheatum, C. M.; Ondrias, M. R., Transient Raman Observations of Heme Electronic and Vibrational Photodynamics in Deoxyhemoglobin. *Journal of the American Chemical Society* 1997, 119, (22), 5110-5117.
19. Mizutani, Y.; Kitagawa, T., Direct observation of cooling of heme upon photodissociation of carbonmonoxy myoglobin. *Science (Washington, D. C.)* 1997, 278, (5337), 443-446.
20. Mizutani, Y.; Kitagawa, T., Ultrafast dynamics of myoglobin probed by time-resolved resonance Raman spectroscopy. *Chemical Record* 2001, 1, (3), 258-275.
21. Li, P.; Sage, J. T.; Champion, P. M., Probing picosecond processes with nanosecond lasers: electronic and vibrational relaxation dynamics of heme proteins. *Journal of Chemical Physics* 1992, 97, (5), 3214-27.

22. Franzen, S.; Bohn, B.; Poyart, C.; Martin, J. L., Evidence for sub-picosecond heme doming in hemoglobin and myoglobin: a time-resolved resonance Raman comparison of carbonmonoxy and deoxy species. *Biochemistry* 1995, 34, (4), 1224-37.
23. Loparo, J. J.; Cheatum, C. M.; Ondrias, M. R.; Simpson, M. C., Transient Raman observations of heme vibrational dynamics in five-coordinate iron porphyrins. *Chemical Physics* 2003, 286, (2-3), 353-374.
24. Gao, Y.; Koyama, M.; El-Mashtoly, S. F.; Hayashi, T.; Harada, K.; Mizutani, Y.; Kitagawa, T., Time-resolved Raman evidence for energy 'funneling' through propionate side chains in heme 'cooling' upon photolysis of carbonmonoxy myoglobin. *Chemical Physics Letters* 2006, 429, (1-3), 239-243.
25. Petrich, J. W.; Poyart, C.; Martin, J. L., Photophysics and reactivity of heme proteins: a femtosecond absorption study of hemoglobin, myoglobin, and protoheme. *Biochemistry* 1988, 27, (11), 4049-60.
26. Kholodenko, Y.; Volk, M.; Gooding, E.; Hochstrasser, R. M., Energy dissipation and relaxation processes in deoxy myoglobin after photoexcitation in the Soret region. *Chemical Physics* 2000, 259, (1), 71-87.
27. Franzen, S.; Kiger, L.; Poyart, C.; Martin, J.-L., Heme photolysis occurs by ultrafast excited state metal-to-ring charge transfer. *Biophysical Journal* 2001, 80, (5), 2372-2385.
28. Ogilvie, J. P.; Plazenet, M.; Dadusc, G.; Miller, R. J. D., Dynamics of Ligand Escape in Myoglobin: Q-Band Transient Absorption and Four-Wave Mixing Studies. *Journal of Physical Chemistry B* 2002, 106, (40), 10460-10467.

29. Ye, X.; Demidov, A.; Champion, P. M., Measurements of the Photodissociation Quantum Yields of MbNO and MbO₂ and the Vibrational Relaxation of the Six-Coordinate Heme Species. *Journal of the American Chemical Society* 2002, 124, (20), 5914-5924.
30. Ye, X.; Demidov, A.; Rosca, F.; Wang, W.; Kumar, A.; Ionascu, D.; Zhu, L.; Barrick, D.; Wharton, D.; Champion, P. M., Investigations of Heme Protein Absorption Line Shapes, Vibrational Relaxation, and Resonance Raman Scattering on Ultrafast Time Scales. *Journal of Physical Chemistry A* 2003, 107, (40), 8156-8165.
31. Anfinrud, P. A.; Han, C.; Hochstrasser, R. M., Direct observations of ligand dynamics in hemoglobin by subpicosecond infrared spectroscopy. *Proceedings of the National Academy of Sciences of the United States of America* 1989, 86, (21), 8387-91.
32. Lian, T.; Locke, B.; Kholodenko, Y.; Hochstrasser, R. M., Energy Flow from Solute to Solvent Probed by Femtosecond IR Spectroscopy: Malachite Green and Heme Protein Solutions. *Journal of Physical Chemistry* 1994, 98, (45), 11648-56.
33. Lim, M.; Jackson, T. A.; Anfinrud, P. A., Femtosecond Near-IR Absorbance Study of Photoexcited Myoglobin: Dynamics of Electronic and Thermal Relaxation. *Journal of Physical Chemistry* 1996, 100, (29), 12043-12051.
34. Hu, C.; An, J.; Noll Bruce, C.; Schulz Charles, E.; Scheidt, W. R., Electronic configuration of high-spin imidazole-ligated iron(II) octaethylporphyrinates. *Inorg Chem FIELD Full Journal Title:Inorganic chemistry* 2006, 45, (10), 4177-85.
35. Alden, R. G.; Schneebeck, M. C.; Ondrias, M. R.; Courtney, S. H.; Friedman, J. M., Mode-specific relaxation dynamics of photoexcited iron(II) protoporphyrin IX in hemoglobin. *Journal of Raman Spectroscopy* 1992, 23, (10), 569-74.

36. Schneebeck, M. C.; Vigil, L. E.; Ondrias, M. R., Mode-selective energy localization during photoexcitation of deoxyhemoglobin and heme model complexes. *Chemical Physics Letters* 1993, 215, (1-3), 251-6.
37. Gunaratne Tissa, C.; Milliken, M.; Challa, J. R.; Simpson, M. C., Tunable ultrafast infrared/visible laser to probe vibrational dynamics. *Appl Opt FIELD Full Journal Title:Applied optics* 2006, 45, (3), 558-64.
38. Foggi, P.; Bussotti, L.; Neuwahl, F. V. R., Photophysical and photochemical applications of femtosecond time-resolved transient absorption spectroscopy. *International Journal of Photoenergy* 2001, 3, (2), 103-109.
39. Tsai, H.-H.; Simpson, M. C., Isolated Impact of Ruffling on the Vibrational Spectrum of Ni Porphyrins. Diagnosing Out-of-Plane Distortions. *Journal of Physical Chemistry A* 2004, 108, (7), 1224-1232.
40. Spiro, T. G.; Czernuszewicz, R. S.; Li, X. Y., Metalloporphyrin structure and dynamics from resonance Raman spectroscopy. *Coordination Chemistry Reviews* 1990, 100, 541-71.
41. Gunaratne, T.; Challa, J. R.; Simpson, M. C., Energy flow in push-pull chromophores: vibrational dynamics in para-nitroaniline. *ChemPhysChem* 2005, 6, (6), 1157-1163.
42. Gouterman, M., Effects of substitution on the absorption spectra of porphin. *Journal of Chemical Physics* 1959, 30, 1139-61.
43. Gouterman, M., Spectra of porphyrins. *Journal of Molecular Spectroscopy* 1961, 6, 138-63.

44. Gouterman, M. In *Optical spectra and electronic structure of porphyrins and related rings*, 1978; 1978; pp 1-165.
45. Rodriguez, J.; Holten, D., Ultrafast vibrational dynamics of a photoexcited metalloporphyrin. *Journal of Chemical Physics* 1989, 91, (6), 3525-31.
46. Rodriguez, J.; Kirmaier, C.; Holten, D., Optical properties of metalloporphyrin excited states. *Journal of the American Chemical Society* 1989, 111, (17), 6500-6.
47. Rodriguez, J.; Kirmaier, C.; Holten, D., Time-resolved and static optical properties of vibrationally excited porphyrins. *Journal of Chemical Physics* 1991, 94, (9), 6020-9.
48. Martin, J. L.; Migus, A.; Poyart, C.; Lecarpentier, Y.; Astier, R.; Antonetti, A., Femtosecond photolysis of carbon monoxide-ligated protoheme and hemoproteins: appearance of deoxy species with a 350-fsec time constant. *Proceedings of the National Academy of Sciences of the United States of America* 1983, 80, (1), 173-7.
49. Kozich, V.; Werncke, W., Influence of vibrational cooling on the time-dependence of stokes and anti-stokes resonance Raman scattering. *Journal of Molecular Structure* 2005, 735-736, 145-151.

CHAPTER 4

THE ELECTRONIC AND VIBRATIONAL DYNAMICS OF

$\text{Fe}^{\text{II}}\text{OEP}-(\text{Im})_2$ IN CH_2Cl_2

4.1 INTRODUCTION

Hemoglobin and myoglobin are respiratory proteins that serve an important function as the oxygen transport and storage agents respectively in mammals. Oxygen binds to the ferrous iron atom of the active site, an iron (II) protoporphyrin IX also known as protoheme, covalently bound to the protein through a single histidine (His93) protein residue. The heme group of these proteins can also reversibly bind diatomic ligands like CO and NO. In the bound state the iron atom is in the plane of the porphyrin macrocycle and has a low-spin ($S=0$) state. In the unligated state, the iron atom is displaced from the porphyrin plane by ~ 0.3 Å towards the histidine and has high-spin ($S=2$) state. Though these heme proteins are not directly involved in any photochemical transformations, it was shown that the $\pi-\pi^*$ electronic excitation of the heme group can lead to instantaneous ($<50\text{fs}$) photolysis of the bound diatomic ligand. The energy in excess of that required for breaking the iron to ligand bond is shared between the unligated heme and ligand. The events following photolysis include ligand escape, electronic and vibrational relaxation of the heme, Fe atom out of plane motion and spin state change, ligand rebinding (both geminate and bimolecular) and the associated protein structural and conformational relaxation. The usefulness of the transient spectral changes occurring as a result of these events in elucidating the protein structure function

relationships has led to an enormous amount of theoretical and experimental studies of these heme proteins.

Early flash photolysis studies¹⁻³ on heme proteins showed that the measured quantum yields for diatomic ligand photolysis varied in the order of $\text{CO} > \text{O}_2 > \text{NO}$. Various reasons for the difference in quantum yields have been proposed by different research groups such as different ligand dependent energy barriers for rebinding⁴, the formation of non-reactive states⁵, formation of short lived intermediate states⁶, different spin-orbit effects⁷, thermal barriers to rebinding evidenced by equal rates of combination of O_2 and CO at low temperature studies⁸, fast recombination of O_2 and NO compared to CO ⁹, with the primary assumption of an intrinsic quantum yield of 1 for all the ligands. However, a more recent study by Champion and coworkers has showed that the intrinsic quantum yield for photodissociation of O_2 and NO from myoglobin are 0.28 and 0.50 respectively based on a quantum yield of ~ 1 for dissociation of CO . The difference in measured quantum yields has been shown to be arising from difference in intrinsic quantum yields for different ligands¹⁰.

A few other ligands such as methyl, ethyl and tertiary butyl isocyanides and coordinating solvents^{11, 12} such as pyridine and piperidine apart from these three diatomic ligands are studied as well in case of nickel metalloporphyrins. In a more recent study¹³, photolysis of methionine axially bound to the ferrous iron atom of heme group in Cytochrome c using Soret band excitation and the five-coordinate photo product cooling dynamics are reported. The methionine ligand completely recombines with the photoproduct geminately with a time constant of 6.2 ps.

Regarding the relaxation of the heme group, the sub-nanosecond dynamics of the heme group following photolysis of the diatomic ligands in heme proteins as well as dynamics in the absence of photolysis using deoxy forms of the Hb and Mb are investigated using transient and time-resolved spectroscopies^{9, 10, 14-28}. The rapid internal conversion back to the ground state following π - π^* excitation is followed by rapid thermalization among the heme normal modes through intramolecular vibrational redistribution (IVR) and vibrational energy relaxation (VER) to the protein/solvent. Reported IVR rates vary from 1.5 to 10 ps^{14, 19-25, 28-31}, while the global lifetime associated with cooling is on the order of 5-40 ps^{17, 24, 31-34}.

Among the more interesting reports is the implication that mode-selective energy dissipation plays an important role in heme biochemical reactions³⁵⁻³⁸. Several other interesting results are obtained through molecular dynamics studies simulating the photoexcitation of heme proteins^{32, 34, 39, 40}. One of the earliest pioneering studies³² by Hochstrasser and coworkers indicated that the hemes excited by 353 or 530 nm photons, relaxed in a biphasic manner with roughly 50 % relaxing through a 1-4 ps fast process attributed to relaxation by heme collective modes and the remaining half relaxing through a 20-40 ps slow process attributed to thermal diffusion in the protein. Later simulation studies^{34, 39} by Straub and coworkers also showed a highly directed energy funneling between the heme group and the protein through isopropionate side chain interactions. Similar results are obtained by Okazaki et al⁴⁰ also through MD simulations. These are verified through direct time-resolved anti-Stokes Raman⁴¹ and less direct transient absorption experiments²⁵, where replacing the isopropionate side chains with methyl groups or H atoms resulted in slowing down of the cooling process.

In the present chapter, ultrafast spectroscopy experiments of the five-coordinate, high-spin model compound discussed in Chapter 3 are extended to include photolysis. Photolysis of an imidazole ligand from a model compound of the bound heme [$\text{Fe}^{\text{II}}\text{OEP}(\text{Im})_2$], never reported before, is presented. The polar isopropionate groups and the surrounding water molecules are absent and also the anisotropic protein environment. The subsequent electronic and vibrational energy relaxations of the photolysed heme observed with complimentary fs transient absorption and sub-ps time resolved Stokes resonance Raman studies are discussed and compared to the existing dynamics of the five-coordinate heme studies.

4.2 MATERIALS AND METHODS

Iron^{II} octaethyl porphyrin bis- imidazole [$\text{Fe}^{\text{II}}\text{OEP}(\text{Im})_2$] was prepared using a reported two phase method²⁷ as follows. All solutions were degassed several times and always kept under a slight overpressure of N_2 gas. Imidazole (Im; Aldrich) was recrystallized twice from benzene. $\text{Fe}^{\text{III}}\text{OEP}$ (Porphyrin Products; no further purification) was dissolved in CH_2Cl_2 (Fisher; spectroscopic grade) to a concentration of 0.5-1.0 mM. 10 ml of this solution was added to an equal volume of CH_2Cl_2 saturated with Im. A 1.0 M stock solution of $\text{Na}_2\text{S}_2\text{O}_4$ in deionised, distilled water (dd H_2O) saturated with 2MeIm was made. 10 ml of this stock was added to the $\text{Fe}^{\text{III}}\text{OEP}$ plus ligand solution under nitrogen pressure using an air-tight syringe (Hamilton). The solution was thoroughly mixed to get $\text{Fe}^{\text{II}}\text{OEP}(\text{Im})_2$ with a stable 2+ redox state in the organic layer. The top aqueous layer with excess ligand and reducing agent acts as a protective layer towards

oxidation of the sample $\text{Fe}^{\text{II}}\text{OEP}(\text{Im})_2$ in the organic layer. The sample was circulated through a 1 mm quartz flow cell using Teflon tubing and chemical resistant micropump under an over pressure of N_2 .

The femtosecond transient absorption experiments were performed at the Ohio Laboratory for Kinetic Spectrometry at Bowling Green State University. The details of the laser system and the experimental setup had been described in detail elsewhere⁴². Briefly, the output (800 nm, 100 fs and 1 kHz) from a Spectra-Physics Hurricane was used to generate pump pulses at 400 nm and white light continuum probe (360-750 nm) pulses using a 3 mm CaF_2 plate. The instrument response was 110 fs. The pump beam was chopped at a frequency of 100 Hz and was focused to a spot size of 2 mm at the sample before overlapping with the probe beam at the sample near collinear geometry ($\sim 5^\circ$). The relative polarizations of the pump and probe beams were at magic angle. Signals were collected by a 400 μm optical fiber connected to a CCD spectrograph (Ocean Optics, PC 2000). The optical chopper, delay time and the CCD spectrograph were computer controlled by LabView (National Instruments) programs (Ultrafast Systems, LLC). The sample was circulated under Ar gas pressure through a 1 mm flow cell using a micropump. The concentration of the sample was so that it has an optical density of ~ 0.5 per mm at the excitation wavelength of 402 nm. The final result was an average of three complete cycles of the transient data at all the time delay positions.

The details of the laser system used for time-resolved resonance Raman studies had been described elsewhere⁴³. Briefly, the output of a Ti:Sapphire based regenerative amplifier (785-835 nm, 80-100 fs, 650 ± 50 $\mu\text{J}/\text{pulse}$, 1 kHz; Clark MXR, Inc.) was frequency doubled in a long 30 mm KDP crystal to produce 410 or 413 nm pulses (500

fs, 60-70 $\mu\text{J}/\text{pulse}$). A 50-50 beam splitter produced the pump and probe beams, which were attenuated to 5.5 $\mu\text{J}/\text{pulse}$ and 2.5 $\mu\text{J}/\text{pulse}$, respectively, using neutral density filters. The probe beam, after passing through a motorized, calibrated translational stage (MM3000; Newport Inc.), was overlapped with the pump beam at the sample in a near collinear ($\sim 5^\circ$) geometry. Time-zero was estimated by mixing the residual 800 nm beams along the pump and probe beams and doubling them at the sample in a type II BBO crystal. The Transient signal is symmetric about the time-zero, weighted by the relative fluxes of the pump and probe pulses.

The Raman spectra were collected using a $\sim 135^\circ$ back-scattering geometry using a collection lens, f-matching lens and an angle tuned super-notch filter (center $\lambda = 415$ nm, Kaiser, Inc.). The Raman spectra were dispersed with a 0.5 meter imaging spectrograph (500 is, Chromex Inc.) and recorded with a thermoelectrically cooled, back-illuminated CCD camera (DU420 BV, Andor). The spectra were collected in random order; typical accumulation times were 25 s for each Raman spectrum. A reference spectrum at 64 ps was collected for each set of four Stokes Raman spectra. Transient spectra were then obtained by subtracting the reference spectrum from the corresponding set of pump-probe spectra. The full dynamics were measured multiple times.

The data was processed using Origin 7.5TM software. The kinetic traces were obtained by plotting the peak heights of the vibrational modes as a function of the time delay between the pump and probe beams. The decay portions of these kinetic traces are fit using a single exponential model.

4.3 RESULTS

The UV-vis absorption spectrum of the six-coordinate, low-spin heme model compound $\text{Fe}^{\text{II}}\text{OEP}-(\text{Im})_2$ in dichloromethane is shown in Figure 4-1. The most intense feature is the Soret (or B) band, which has a maximum at 412 nm. The two bands in the low energy region at 519 and 548 nm are due to the Q-band and are an order of magnitude weaker than the Soret band. The weaker band at high energy region is possibly an N-band. Generally three weaker bands known as the N, L and M bands are seen at high energy (~ 325 , ~ 275 and ~ 215 nm respectively) for metalloporphyrins. The M-band is only observed in gas phase, while the N and L bands can be seen in solution phase also.

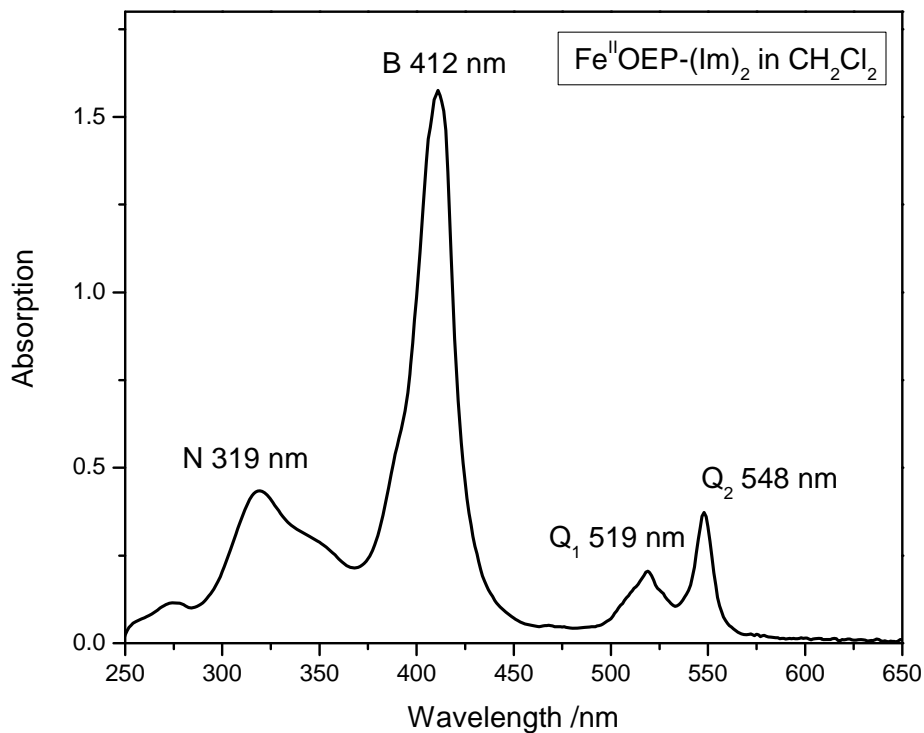


Figure 4 - 1 UV-vis absorption spectrum of $\text{Fe}^{\text{II}}\text{OEP}-(\text{Im})_2$ in CH_2Cl_2 .

Photoexcitation of this heme compound leads to photolysis of one of the imidazole ligands and the result is the formation of a high energy five-coordinate high-spin heme similar to deoxyheme. The excitation energy in excess of that required for the photolysis is shared between the imidazole ligand and the five-coordinate heme. The high energy five-coordinate heme undergoes vibrational relaxation processes before undergoing recombination with the photolysed ligand to return to the starting material. The ground state population depletion of the six-coordinate compound due to photoexcitation, the subsequent photoproduct formation and ligand recombination is studied using fs transient absorption measurements. The fs time-resolved absorption spectra of Fe^{II}OEP-(Im)₂ in CH₂Cl₂ obtained with a broad-band white light continuum probe following photoexcitation in the Soret band at 402 nm are presented in Figure 4-2.

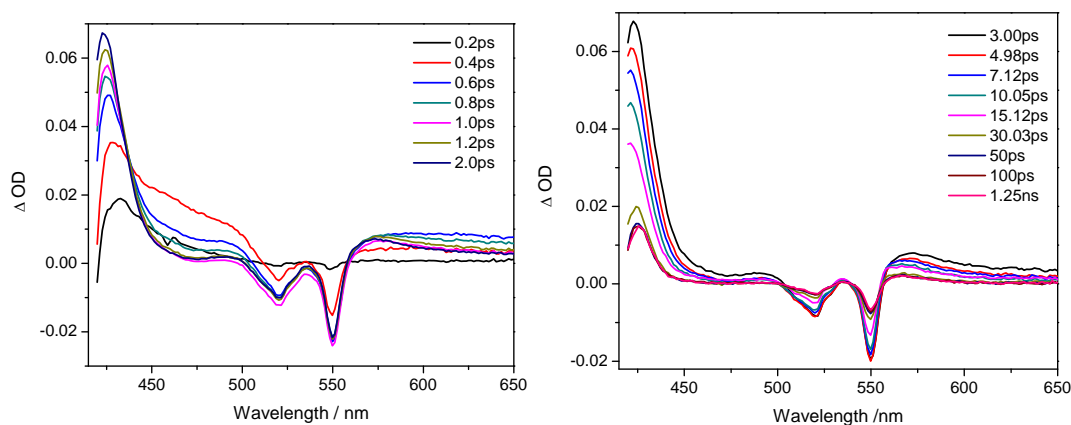


Figure 4 - 2 Femtosecond UV-vis transient absorption spectra of Fe^{II}OEP-(Im)₂ in CH₂Cl₂ using 402 nm excitation and broad-band white light continuum probe (360-700 nm). The instrument response is 110 fs. The optical density of the sample at excitation wavelength of 402 nm is ~ 0.5 per mm. Left panel shows the fast dynamics within the first 2 ps and right panel shows the slower dynamics up to 1.2 ns.

Within the instrument response, bleaching signals at the steady state Soret and Q-band positions corresponding to the ground electronic state depletion appear instantly. The Soret band bleach centered at 412 nm is complicated by the interference from the pump beam leakage to the detector and hence is not presented and will not be discussed further. Only the evolution of transient spectra to the red of excitation wavelength from 415 nm is presented. The Q-band bleach at 519 and 548 nm is clearly visible. However, the appearance of Q-band bleach is seen to be delayed compared to the Soret band signal due to the presence of positive chirp in the broad-band white light continuum probe pulse and the transient spectra are not corrected for the chirp. Initially broad and red-shifted transient absorption bands due to the photoproduct appear on the low energy side of the Soret and Q-bands, which spectrally narrow and blue-shift in time until about $\Delta t=2$ ps. After that a steady decrease in intensity and continued blue-shift is observed. This sort of spectral evolution is the hallmark of vibrational cooling. The fact that there is only a single transient absorption band in the Q-band region instead of two corresponding to the two Q-band bleaches confirms the absence of a hot six-coordinated compound. So the transients are safely assigned to the absorption of vibrationally hot ground electronic state of the five-coordinate photoproduct formed following the photolysis of one imidazole ligand. The spectral evolution and thermal equilibration of the five-coordinate heme is complete within 40 ps. Partial recovery of the Q-band bleach is observed within this time duration indicating the ligand recombination to form the six-coordinate heme has time scales overlapping with the vibrational cooling kinetics. The presence of residual bleach even after 1.0 ns suggests a second much slower phase of ligand recombination.

The kinetic traces are corrected for the chirp in white light continuum probe according to the procedure described in Chapter 3 ‘Materials and Methods’ section. Chirp corrected transient absorption kinetic traces at selected wavelengths of 425, 520, 550 and 570 nm are shown in Figure 4-3. The presence of significant transient absorption signal at all these wavelengths even after 1.0 ns is due to incomplete ligand recombination which suggests a much longer lifetime for the recombination process. All the kinetic traces are fit with a sum of exponentials of the form $y = y_0 + \sum_{i=1}^{i=n} A_i e^{-t/\tau_i}$; where t is the time delay, τ_i is the lifetime, y is the change in optical density [$\Delta OD(\lambda, t)$], y_0 is the residual optical density [$\Delta OD(\lambda, 1.2 \text{ ns})$] and n is the number of exponentials used for the best fit.

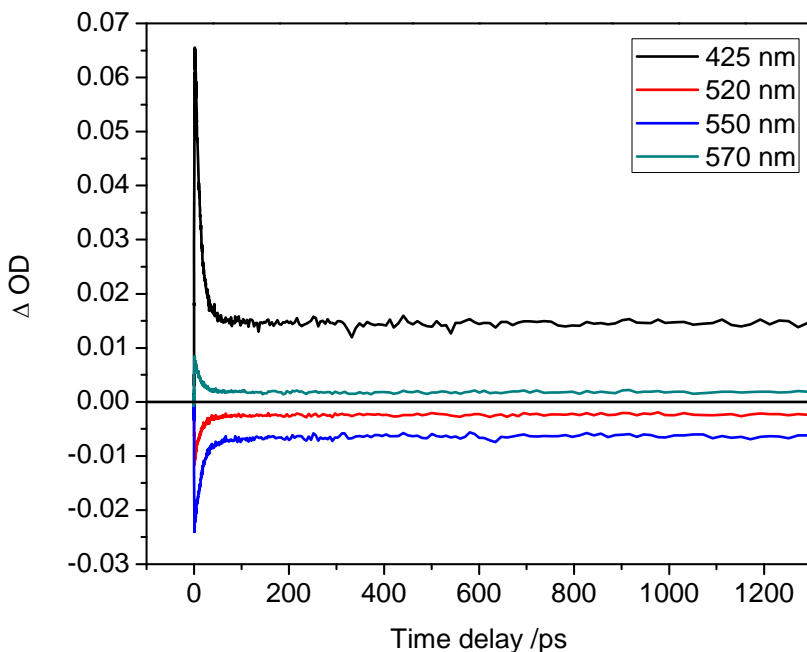


Figure 4 - 3 Chirp corrected kinetic traces of the TA signal of $\text{Fe}^{\text{II}}\text{OEP}-(\text{Im})_2$ in CH_2Cl_2 at the indicated wavelengths. Pump=402 nm, Probe=white light continuum. Instrument response=110 fs.

The exponential fitting parameters are listed in Table 4-1. At wavelengths with overlapping contributions from bleach and TA, both rise and decay were fit. At all other wavelengths, only the decay portions were fit. The parameter A_i represents the relative contribution of each component. Negative A_i implies rise and positive A_i means decay.

$\lambda(\text{nm})$	$A_1 (\%), t_1 (\text{fs})$	$A_2 (\%), t_2 (\text{ps})$	$A_3 (\%), t_3 (\text{ps})$	$A_4 (\%), t_4 (\text{fs})$
416	-39, 291±11	-30, 4.5±0.3	31, 11.7±0.5	
420	-51, 253±8	-20, 2.5±0.1	29, 12.2±0.2	
425	-57, 517±26		43, 11.0±0.3	
430	-55, 343±15		45, 9.3±0.2	
435	-53, 205±9		47, 8.5±0.2	
440	-57, 92±5		43, 7.1±0.1	
450			16, 7.5±0.2	84, 267±8
460			7, 9.2±0.6	93, 267±7
470			4, 7.2±0.9	96, 248±6
480			3, 8.9±1.5	97, 230±7
490			6, 10.2±1.0	94, 231±8
500			3, 5.2±1.5	97, 243±9
510			-22, 15.5±0.4	78, 228±8
520			-43, 15.7±0.5	57, 223±14
530			-34, 4.7±0.1	66, 194±10
540			-28, 6.3±0.3	72, 77±10
550			-40, 20.7±0.7	60, 121±12

Table 4 - 1 Exponential Fit parameters to Experimental TA Measurements of $\text{Fe}^{\text{II}}\text{OEP}(\text{Im})_2$ in CH_2Cl_2 using Soret band pump white light continuum probe. R^2 values in order from top: 0.99, 0.99, 0.99, 0.96, 0.97, 0.98, 0.99, 0.99, 0.99, 0.98, 0.98, 0.95, 0.95, 0.94, 0.98, 0.96, 0.97, 0.93, and 0.94.

The spectral dynamics are rather complex resulting in time constants that vary with wavelength due to the concurrent changes in spectral position and bandwidth on the time scale of the population changes. To gain insight into the overlapping dynamics and tease out the individual contributions, the Soret and Q-band transient absorption and the two Q-band bleaches are fit with Gaussian line shapes. Since the area under the curve is not sensitive to spectral evolution⁴⁴, this approach helps in isolating the spectral evolution dynamics that can be obtained from the analysis of the central peak position and band width changes in time from the population decay. The integrated intensity of the Soret and Q-band transient absorption bands obtained using this line shape analysis are plotted as a function of time delay and is shown in Figure 4-4. The Soret band transient absorption intensity grows exponentially at 1.3 ± 0.2 ps and decays at an exponential rate of 12.5 ± 1.4 ps. Q-band transient absorption was found to decay at an exponential rate of 9.2 ± 0.6 ps.

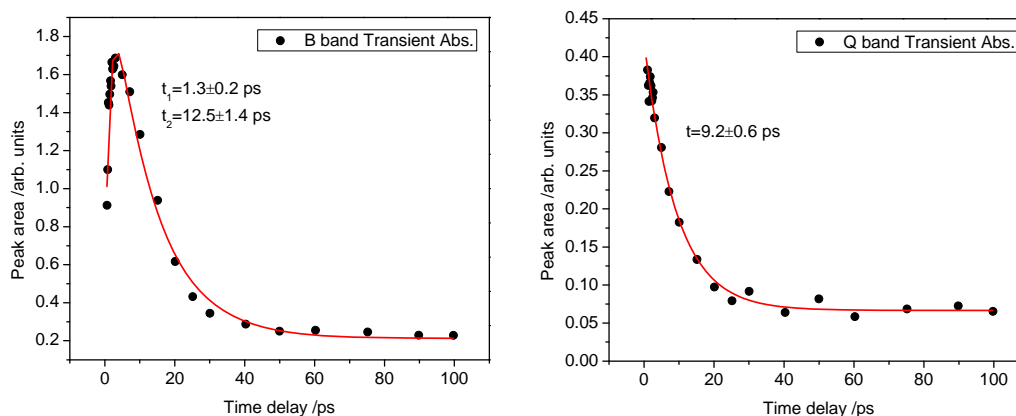


Figure 4 - 4 Time evolution of the integrated transient band intensity of Fe^{II}OEP-(Im)₂ in CH₂Cl₂. Left panel shows the rise and decay of the transient Soret band. The fast component contributes to 59%. Right panel shows the decay of the transient Q-band. Residual transient absorption is evident in both the traces even after 100 ps.

The integrated intensity of the two Q-band bleaches as a function of the time delay was plotted in Figure 4-5. They represent the six-coordinate ground electronic state population recovery following the photoexcitation at 402 nm. The Q₁ band at 519 nm recovers bi-exponentially at the rate of 451 ± 92 fs and 8.1 ± 0.8 ps. The Q₂ band shows a recovery time of 10.4 ± 0.7 ps.

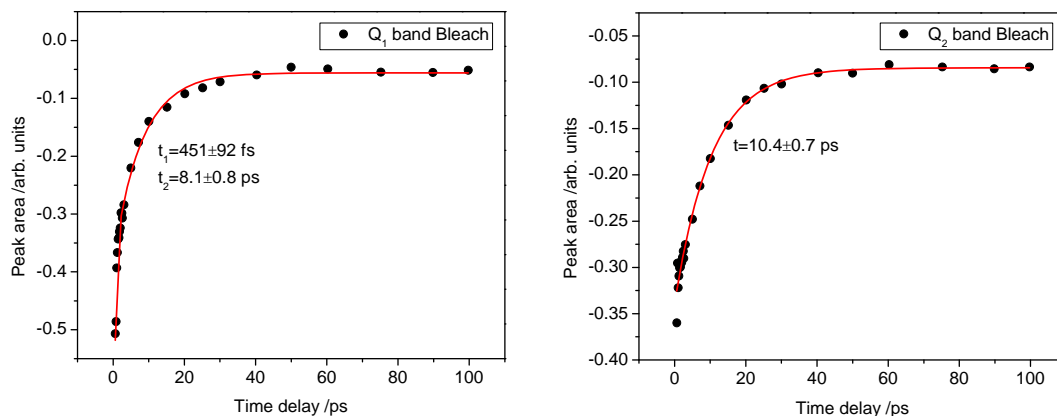


Figure 4 - 5 Time evolution of the integrated transient band intensity of Fe^{II}OEP-(Im)₂ in CH₂Cl₂. Left panel shows the bi-exponential recovery of the transient Q₁ band bleach centered at 519 nm. The fast component contributes to 65% of the decay. Right panel shows the recovery of the transient Q₂ band. Residual bleach is present even after 100 ps.

The central peak positions of the two Q-band bleaches, the Q-band transient absorption and the corresponding spectral widths as a function of the time delay are shown in Figure 4-6. The Q-band TA initially centered at 585 nm blue-shifts to reach an equilibrium value of 565 nm corresponding to the five-coordinate photoproduct absorption spectrum bi-exponentially with time constants of 613 ± 83 fs and 12.1 ± 2.8 ps. The TA band which is initially 30 nm broad also spectrally narrows at the same time with a time constant of 4.5 ± 0.4 ps. However, the central peak position and bandwidth of the two Q-band bleaches are not affected.

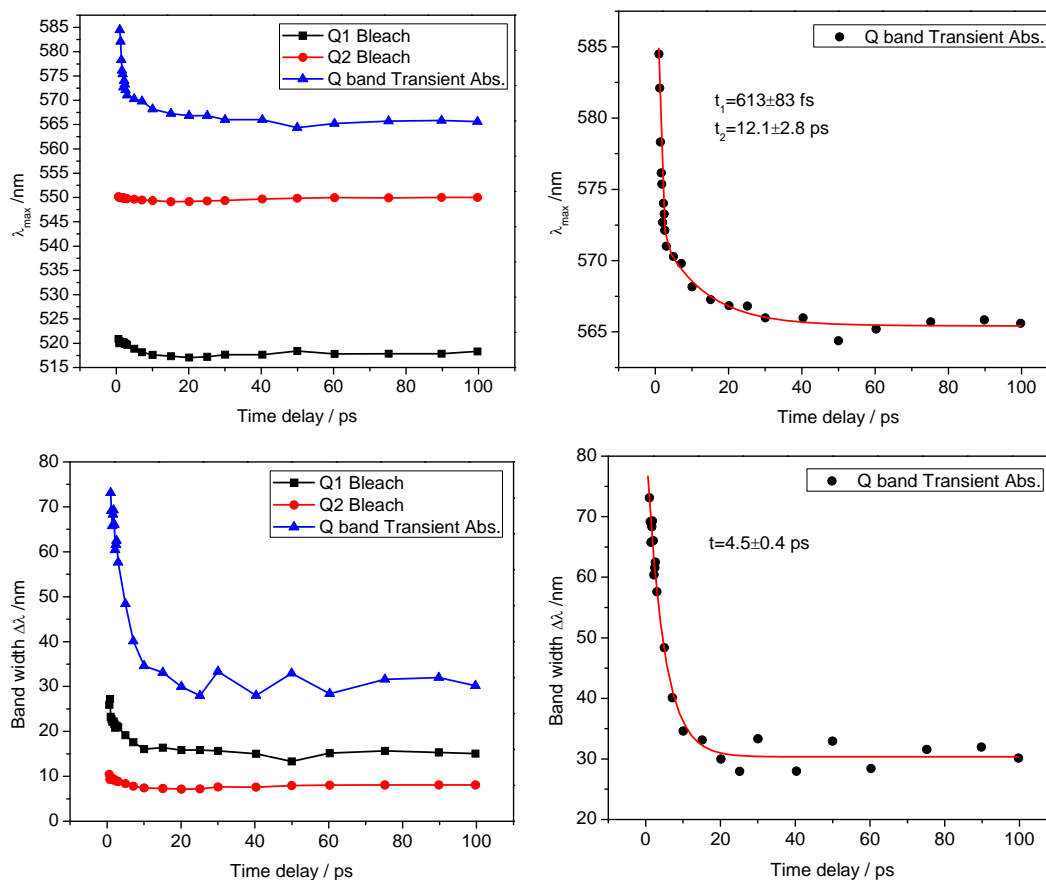


Figure 4 - 6 Spectral evolution of the transient spectra of $\text{Fe}^{\text{III}}\text{OEP}-(\text{Im})_2$ in CH_2Cl_2 . Left panel (top) shows the peak positions of the two Q-band bleaches and the Q-band transient absorption as a function of time delay. Right panel (top) shows the kinetic trace of the transient Q-band and the corresponding bi-exponential fit. The fast component contributes to 90%. Left panel (bottom) shows the spectral widths of the two Q-band bleaches and the Q-band transient absorption as a function of time delay. Right panel (bottom) shows the kinetic trace of the transient Q-band spectral width and the corresponding exponential fit. The peak position evolution has a fast component of about 600 fs and a slower component of about 12 ps. The spectral narrowing has a time constant of about 4.5 ps.

Complimentary time-resolved Stokes resonance Raman spectra of $\text{Fe}^{\text{III}}\text{OEP}-(\text{Im})_2$ in CH_2Cl_2 excited at 410 nm and probed at the same wavelength are presented in Figure 4-7. A steady state Stokes resonance Raman spectrum obtained with just the probe beam is also included for reference.

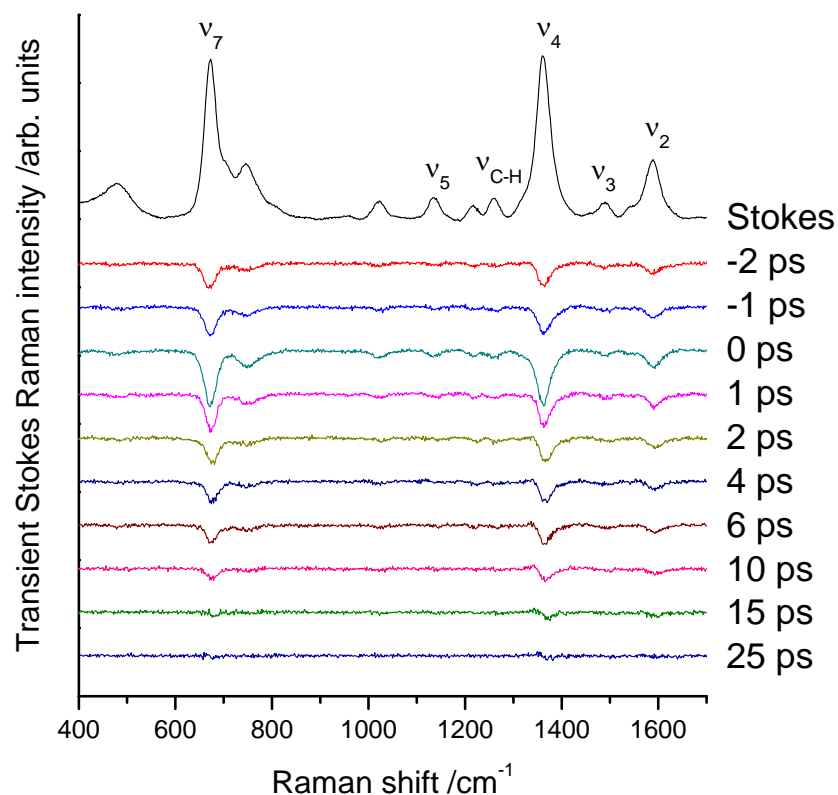


Figure 4 - 7 Time resolved Stokes resonance Raman spectra of Fe^{II}OEP-(Im)₂ in CH₂Cl₂ using 410 nm pump and 410 nm probe. Transients are obtained by subtracting the reference spectra at $\Delta t=64$ ps.

Because of the single color pump-probe approach, bleach signals can be seen even before zero time delay. The two strong features in the Stokes resonance Raman spectrum ν_4 and ν_7 at 672 and 1362 cm^{-1} due to totally symmetric porphyrin macrocycle vibrations suffer the maximum loss in intensity. The ν_2 vibration at 1593, assigned to an A_{1g} in-phase C_β - C_β stretch⁴⁵ and another mode at 746 cm^{-1} , possibly ν_6 ⁴¹ also show significant loss of intensity. A few other weaker modes ν_3 , ν_{CH} and ν_5 are also prominent. ν_3 has contributions from C_α - C_β stretching vibrations and is also a totally symmetric and macrocycle mode⁴⁶. ν_{CH} at 1260 cm^{-1} is due to symmetric CH_2 twist of the peripheral

ethyl substituents²⁷. ν_5 at 1135 cm^{-1} is due to the C_{β} -ethyl stretching vibrations^{27, 46}. Since these transient spectra are generated by subtracting a pump-probe spectrum at $\Delta t=64\text{ ps}$ from the pump-probe spectra at various time delays and the transient absorption spectra clearly show the presence of residual TA and bleach signals at this time delay, the slow phase of the ligand recombination is not monitored.

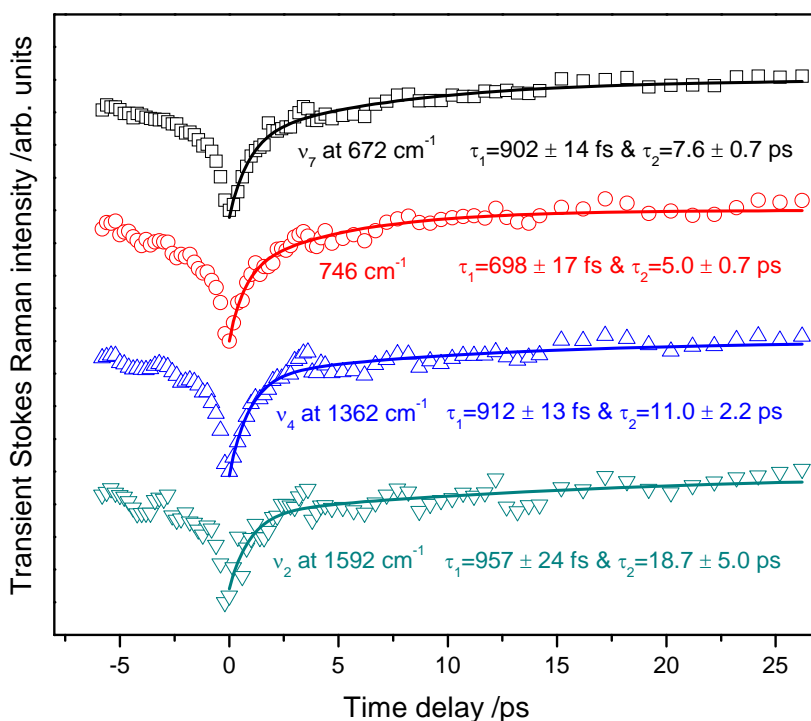


Figure 4 - 8 Vibrational mode population recovery kinetics on the ground electronic state of $\text{Fe}^{\text{II}}\text{OEP}-(\text{Im})_2$ using time-resolved Stokes resonance Raman spectroscopy. Pump=Probe=410 nm.

The transient Stokes Raman signal bleach recovery is monitored by plotting the average peak intensity as a function of time delay in Figure 4-8. All the vibrational modes monitored indicate a bi-exponential recovery of the ground state low spin six-coordinate heme with a fast lifetime component of about 700-950 fs and a slower component of 5-19

ps. The dynamics are due to vibrational relaxation on the ground electronic state overlapped with the fast phase ligand recombination similar to the case of geminate recombination of diatomic ligands observed in heme proteins. There is also a minor and much slower (\sim few ns) ligand recombination phase that is not monitored here.

4.4 DISCUSSION

Photoexcitation of the low-spin, six-coordinate heme in the Soret band leads to population in the excited electronic state of S_2 . Photolysis of one of the imidazole ligands is observed within the instrument response of 100 fs. Then based on the results presented here, the following questions need to be answered. Is the intrinsic photolysis quantum yield equal to one, i.e. does each molecule that absorbs a single photon of light undergo photolysis? If that is the case then the transient absorption bands should correspond only to the five-coordinate photoproduct and not the six-coordinate reactant. Even if we assume that a small fraction of the molecules undergo non-radiative decay directly to S_0 , then two transient absorption bands in the Q-band region should be observed corresponding to the two Q-band bleaches in the ground state spectrum. The results presented here clearly indicate the presence of only one red-shifted transient absorption band and the band widths and central peak positions of the Q-band bleaches are equivalent to those of the ground state six-coordinate absorption spectrum. So we conclude that there is no detectable or measurable formation of vibrationally hot-six coordinate ground state species following S_2 state photoexcitation. However, by a close monitoring of the two Q-band bleach positions and band widths (Figure 4-6), one will notice a slight red-shift and broadening especially in the Q_1 band at 520 nm. By considering the slight broadening and red-shift in Q_1 band also, we predict a quantum

yield of ~ 0.9 to 0.95 for the photolysis of an imidazole ligand in the reported heme model compound.

The second question that comes to mind is, “Does the photolysis occur directly from S_2 or does it happen from S_1 state following ultrafast internal conversion from $S_2 \rightarrow S_1$?” In order to answer this, two things need to be checked. One simple way of knowing if there is any population in the S_1 state is to monitor fluorescence from S_1 state, following excitation at the same wavelength used in these studies, but this approach is useful only if the radiative decay channel of S_1 state is active resulting in fluorescence. Another direct way of monitoring it will be to do parallel Q-band pump experiments under the same conditions and comparing the results obtained in the two experiments. At present, because of the lack of Q-band pump studies, we base our conclusions based on comparisons to the vast majority of existing literature in Q-band pump photolysis of CO, NO and O_2 from heme proteins.

Similar transient absorption results observed for heme proteins, with both Soret band excitation and Q-band excitation strongly indicate that the photolysis event occurs from the S_1 state rather than the S_2 state. Extremely fast photolysis events observed in these experiments then lead to the conclusion that $S_2 \rightarrow S_1$ state decay as well as the photolysis event together should occur in less than 100 to 300 fs.

The experimental results presented here are consistent with the observation of the photolysis of a single imidazole ligand with a quantum yield of near unity resulting in the formation of a vibrationally hot five-coordinate photoproduct similar to the one observed in photoexcitation of the five-coordinate heme model compound $Fe^{II}OEP-2MeIm$. The

transient absorption spectral features can be assigned to the difference in absorption of the hot five-coordinate, high spin photoproduct $[\text{Fe}^{\text{II}}\text{OEP-Im}]^*$ and the six-coordinate, low-spin $[\text{Fe}^{\text{II}}\text{OEP-(Im)}_2]$. The transient absorption bands spectrally narrow and blue-shift with time corresponding to intramolecular and intermolecular vibrational cooling of the five-coordinate photoproduct. Kinetic analysis of the spectral evolution in figure 4-6 indicated that 90% of the spectral shift occurred with a time constant of 613 ± 83 fs, while the remaining 10% recovers on a longer time scale of 12.1 ± 2.8 ps. The spectral narrowing occurred with a time constant of 4.5 ± 0.4 ps. We assign the 613 ± 83 and the 4.5 ± 0.6 ps lifetimes to the intramolecular vibrational relaxation (IVR) within the five-coordinate heme photoproduct and the longer lifetime of 12.1 ± 2.8 ps to intermolecular vibrational cooling process.

The simultaneous decay of both the transient bleaches and the transient absorption bands indicate the recombination of the imidazole ligand to the five-coordinate photoproduct resulting in the formation of the six-coordinate starting material. The band integral of the transient absorption band in the Q-band region is shown to decay with a life time of 9.2 ± 0.6 ps. The band integral of the Q₂ band bleach recovered with a lifetime of 10.4 ± 0.7 ps. This similar lifetime observed from the simultaneous decay of both the transient absorption and the transient bleach bands points out that it is due to the fast phase of ligand recombination. We assign this fast lifetime of ~ 10 ps to the geminate recombination of the imidazole ligand to the contemporaneously cooling five-coordinate heme photoproduct.

Analysis of the transient absorption band in the Soret band region should be treated with care, however, because only part of the TA band to the red of 415 nm could

be measured due to interference from the excitation laser at 402 nm and also the overlapping Soret band bleach could not be characterized. So we relied on the nonlinear Gaussian peak shape analysis instead and any predictions based on this are subject to the errors involved in the non linear fit analysis. Having said this, the band integral of the TA band in the Soret band region is noticed to rise and decay exponentially with time constants of 1.3 ± 0.2 and 12.5 ± 1.4 ps respectively. The Q_1 band bleach is also found to exhibit a bi-exponential decay of 451 ± 92 fs and 8.1 ± 0.8 ps, with the fast component comprising of 65%. The sub-ps and ps fast components from these two kinetic traces also reflect the vibrational cooling, while the longer time component is due to the geminate ligand recombination.

The same behavior is also evident from the individual kinetic traces and the single wave length kinetic traces at 520 and 550 nm correspond to exponential bleach recovery times of 15.7 ± 0.5 and 20.7 ± 0.7 ps respectively. These values are slightly more than the ones obtained from the band integral decay analysis and set a maximum for the geminate recombination lifetime. So we conclude that the imidazole ligand bigger in size compared to that of the diatomic ligands like CO, NO and O₂, can't diffuse further out into the solution from the photoproduct following photolysis and geminately recombines with a life time of 10 to 20 ps, competing with the intermolecular vibrational cooling dynamics.

The off-sets used in the single wavelength kinetic analysis as well as the band integral analysis, indicate the presence of a much slower phase of ligand recombination that is not complete even at 1.2 ns. The maximum signal observed at 425, 520 and 550 nm at earlier times correspond to optical density of 0.0657, 0.01054 and 0.0222 respectively. By 1.2 ns, the signals decayed to 0.0149, 0.0023 and 0.0064 respectively.

Based on this analysis, approximately 75 % of the photolysed ligand geminately recombines in the initial fast phase and the remaining 25 % of the ligands diffused away from the photoproduct into solution leading to recombination lifetimes on the order of a few ns or longer.

This behavior is also evident from the time resolved Stokes resonance Raman study. The transient resonance Raman spectra contained only features corresponding to the loss of intensity due to the depletion of six-coordinate compound and no positive Raman features corresponding to the five-coordinate photoproduct unlike what is reported in the literature for time resolved resonance Raman studies of carbonmonoxy myoglobin^{24, 28}. This could be due to the following reasons. Since the Raman probing wavelength was at 410 nm, close to the absorption maximum of the six-coordinate compound rather than the five-coordinate photoproduct (Abs. max of Fe^{II}OEP-2MeIm is 423 nm), and the fraction of molecules excited under the excitation conditions is less, the resonance enhancement for the six-coordinate starting material is much higher than that for the five-coordinate photoproduct.

All the vibrational modes exhibited a significant loss in intensity of their Stokes resonance Raman bands corresponding to excitation to S₂ state. ν_7 and ν_4 well coupled to the Soret transition suffered the maximum loss in intensity. The transient spectra obtained by subtracting the pump-probe spectrum at a time delay of 64 ps from the corresponding spectra recover to a flat featureless spectrum by 25 ps. By choosing the pump-probe spectrum at Δt of 64 ps to produce the transient spectra, the much slower ligand recombination phase is subtracted out from the measured kinetics. The choice of $\Delta t=64$ ps can be justified, by measuring the percentage of the ligand combined by that time

using the transient absorption data. By analyzing the transient absorption signal at 520 nm and 560 nm at 64 ps time delay, 99% of the geminate recombination phase is complete by then.

All the vibrational modes exhibited bi-exponential kinetics. The fast component ranged from 698 ± 17 to 957 ± 24 fs and the slower component ranged from 5.0 ± 0.7 to 18.7 ± 5.0 ps respectively. The fast component is mainly due to the intra molecular vibrational relaxation and the slow component has contributions from both intermolecular vibrational cooling as well as the fast geminate phase ligand recombination. The Core-size marker band ν_2 at 1593 cm^{-1} should be more sensitive to the geminate phase ligand recombination as the ligand recombination leads to movement of the Fe (II) atom back into the plane of the porphyrin and change in the core size of the porphyrin macrocycle. This can be seen from the huge Raman frequency shift of the ν_2 band in going from 5-coordinate to 6-coordinate compound in steady state resonance Raman spectra. It can be assumed that the Stokes Raman bleach recovery time scale of this band should be very similar to the ligand recombination time.

Complimentary time-resolved anti-Stokes resonance Raman experiments are not available at present to be compared to the present data.

4.5 CONCLUSIONS

The photolysis of an imidazole ligand from a six-coordinate bound heme model compound, the intra and intermolecular vibrational cooling of the five-coordinate photo product and the ligand recombination events are studied in the absence of the protein. The initial results of the imidazole ligand photolysis studied for the first time are

compared to the vastly studied diatomic ligand photolysis of bound heme proteins and a more recent study involving the photolysis of methionine from Cytochrome *c*. No detectable vibrationally hot six-coordinate ground state heme is observed, indicating the intrinsic quantum yield of the photolysis to be close to unity. Comparisons to the heme protein studies tentatively assign the photolysis to be occurring from the S_1 state rather than the S_2 state, though this needs to be verified in parallel Q-band pump experiments under the same conditions. The intramolecular vibrational relaxation is the major contribution to the photoproduct cooling on the order of 0.6 to 4.5 ps time scale. The intermolecular vibrational cooling has a lifetime of approximately 10 ps. On average 75% of the photolysed ligand geminately recombines on the time scale of 10-20 ps strongly overlapping with the vibrational cooling dynamics. Complimentary time resolved Stokes resonance Raman experiments support these observations as well.

4.6 REFERENCES

1. Bucher, T.; Kaspers, J., Photochemical cleavage of carbon monoxide-myoglobin by ultraviolet radiation (activity of the protein component of the pigment for absorbed quanta). *Biochimica et Biophysica Acta* **1947**, 1, 21-34.
2. Gibson, Q. H.; Ainsworth, S., Photosensitivity of hem compounds. *Nature (London, United Kingdom)* **1957**, 180, 1416-17.
3. Brunori, M.; Giacometti, G. M., Photochemistry of hemoproteins. *Methods in Enzymology* **1981**, 76, (Hemoglobins), 582-95.
4. Austin, R. H.; Beeson, K. W.; Eisenstein, L.; Frauenfelder, H.; Gunsalus, I. C., Dynamics of ligand binding to myoglobin. *Biochemistry* **1975**, 14, (24), 5355-73.

5. Chernoff, D. A.; Hochstrasser, R. M.; Steele, A. W., Geminate recombination of oxygen and hemoglobin. *Proceedings of the National Academy of Sciences of the United States of America* **1980**, 77, (10), 5606-10.
6. Reynolds, A. H.; Rand, S. D.; Rentzepis, P. M., Mechanisms for excited state relaxation and dissociation of oxymyoglobin and carboxymyoglobin. *Proceedings of the National Academy of Sciences of the United States of America* **1981**, 78, (4), 2292-6.
7. Cornelius, P. A.; Hochstrasser, R. M.; Steele, A. W., Ultrafast relaxation in picosecond photolysis of nitrosylhemoglobin. *Journal of Molecular Biology* **1983**, 163, (1), 119-28.
8. Frauenfelder, H.; Wolynes, P. G., Rate theories and puzzles of heme protein kinetics. *Science (Washington, DC, United States)* **1985**, 229, (4711), 337-45.
9. Petrich, J. W.; Poyart, C.; Martin, J. L., Photophysics and reactivity of heme proteins: a femtosecond absorption study of hemoglobin, myoglobin, and protoheme. *Biochemistry* **1988**, 27, (11), 4049-60.
10. Ye, X.; Demidov, A.; Champion, P. M., Measurements of the Photodissociation Quantum Yields of MbNO and MbO₂ and the Vibrational Relaxation of the Six-Coordinate Heme Species. *Journal of the American Chemical Society* **2002**, 124, (20), 5914-5924.
11. Kim, D.; Holten, D., Picosecond measurements on the binding and release of basic ligands by excited states of nickel(II) porphyrins. *Chemical Physics Letters* **1983**, 98, (6), 584-9.

12. Kim, D.; Kirmaier, C.; Holten, D., Nickel porphyrin photophysics and photochemistry. A picosecond investigation of ligand binding and release in the excited state. *Chemical Physics* **1983**, 75, (3), 305-22.
13. Wang, W.; Ye, X.; Demidov, A. A.; Rosca, F.; Sjodin, T.; Cao, W.; Sheeran, M.; Champion, P. M., Femtosecond Multicolor Pump-Probe Spectroscopy of Ferrous Cytochrome c. *Journal of Physical Chemistry B* **2000**, 104, (46), 10789-10801.
14. Li, P.; Sage, J. T.; Champion, P. M., Probing picosecond processes with nanosecond lasers: electronic and vibrational relaxation dynamics of heme proteins. *Journal of Chemical Physics* **1992**, 97, (5), 3214-27.
15. Petrich, J. W.; Martin, J. L., Ultrafast absorption and Raman spectroscopy of hemeproteins. *Chemical Physics* **1989**, 131, (1), 31-47.
16. Franzen, S.; Bohn, B.; Poyart, C.; Martin, J. L., Evidence for sub-picosecond heme doming in hemoglobin and myoglobin: a time-resolved resonance Raman comparison of carbonmonoxy and deoxy species. *Biochemistry* **1995**, 34, (4), 1224-37.
17. Lim, M.; Jackson, T. A.; Anfinrud, P. A., Femtosecond Near-IR Absorbance Study of Photoexcited Myoglobin: Dynamics of Electronic and Thermal Relaxation. *Journal of Physical Chemistry* **1996**, 100, (29), 12043-12051.
18. Kholodenko, Y.; Volk, M.; Gooding, E.; Hochstrasser, R. M., Energy dissipation and relaxation processes in deoxy myoglobin after photoexcitation in the Soret region. *Chemical Physics* **2000**, 259, (1), 71-87.
19. Schneebeck, M. C.; Vigil, L. E.; Ondrias, M. R., Mode-selective energy localization during photoexcitation of deoxyhemoglobin and heme model complexes. *Chemical Physics Letters* **1993**, 215, (1-3), 251-6.

20. Simpson, M. C.; Peterson, E. S.; Shannon, C. F.; Eads, D. D.; Friedman, J. M.; Cheatum, C. M.; Ondrias, M. R., Transient Raman Observations of Heme Electronic and Vibrational Photodynamics in Deoxyhemoglobin. *Journal of the American Chemical Society* **1997**, 119, (22), 5110-5117.
21. Alden, R. G.; Chavez, M. D.; Ondrias, M. R.; Courtney, S. H.; Friedman, J. M., Direct measurement of vibrational temperatures in photoexcited deoxyhemoglobin on picosecond time scales. *Journal of the American Chemical Society* **1990**, 112, (8), 3241-2.
22. Lingle, R., Jr.; Xu, X.; Zhu, H.; Yu, S. C.; Hopkins, J. B., Picosecond Raman study of energy flow in a photoexcited heme protein. *Journal of Physical Chemistry* **1991**, 95, (23), 9320-31.
23. Lingle, R., Jr.; Xu, X.; Zhu, H.; Yu, S. C.; Hopkins, J. B.; Straub, K. D., Direct observation of hot vibrations in photoexcited deoxyhemoglobin using picosecond Raman spectroscopy. *Journal of the American Chemical Society* **1991**, 113, (10), 3992-4.
24. Mizutani, Y.; Kitagawa, T., Direct observation of cooling of heme upon photodissociation of carbonmonoxy myoglobin. *Science (Washington, D. C.)* **1997**, 278, (5337), 443-446.
25. Ye, X.; Demidov, A.; Rosca, F.; Wang, W.; Kumar, A.; Ionascu, D.; Zhu, L.; Barrick, D.; Wharton, D.; Champion, P. M., Investigations of Heme Protein Absorption Line Shapes, Vibrational Relaxation, and Resonance Raman Scattering on Ultrafast Time Scales. *Journal of Physical Chemistry A* **2003**, 107, (40), 8156-8165.

26. Franzen, S.; Kiger, L.; Poyart, C.; Martin, J.-L., Heme photolysis occurs by ultrafast excited state metal-to-ring charge transfer. *Biophysical Journal* **2001**, 80, (5), 2372-2385.
27. Loparo, J. J.; Cheatum, C. M.; Ondrias, M. R.; Simpson, M. C., Transient Raman observations of heme vibrational dynamics in five-coordinate iron porphyrins. *Chemical Physics* **2003**, 286, (2-3), 353-374.
28. Mizutani, Y.; Kitagawa, T., Ultrafast dynamics of myoglobin probed by time-resolved resonance Raman spectroscopy. *Chemical Record* **2001**, 1, (3), 258-275.
29. Alden, R. G.; Ondrias, M. R.; Courtney, S.; Findsen, E. W.; Friedman, J. M., Power-induced broadening of transient resonance Raman spectra of deoxyhemoglobin. *Journal of Physical Chemistry* **1990**, 94, (1), 85-90.
30. Alden, R. G.; Schneebeck, M. C.; Ondrias, M. R.; Courtney, S. H.; Friedman, J. M., Mode-specific relaxation dynamics of photoexcited iron(II) protoporphyrin IX in hemoglobin. *Journal of Raman Spectroscopy* **1992**, 23, (10), 569-74.
31. Challa, J. R.; Gunaratne Tissa, C.; Simpson, M. C., State preparation and excited electronic and vibrational behavior in hemes. *J Phys Chem B* **2006**, 110, (40), 19956-65.
32. Henry, E. R.; Eaton, W. A.; Hochstrasser, R. M., Molecular dynamics simulations of cooling in laser-excited heme proteins. *Proceedings of the National Academy of Sciences of the United States of America* **1986**, 83, (23), 8982-6.
33. Genberg, L.; Heisel, F.; McLendon, G.; Miller, R. J. D., Vibrational energy relaxation processes in heme proteins: model systems of vibrational energy dispersion in disordered systems. *Journal of Physical Chemistry* **1987**, 91, (22), 5521-4.

34. Bu, L.; Straub, J. E., Vibrational energy relaxation of "tailored" hemes in myoglobin following ligand photolysis supports energy funneling mechanism of heme "cooling". *Journal of Physical Chemistry B* **2003**, 107, (38), 10634-10639.
35. Ansari, A.; Berendzen, J.; Bowne, S. F.; Frauenfelder, H.; Iben, I. E. T.; Sauke, T. B.; Shyamsunder, E.; Young, R. D., Protein states and proteinquakes. *Proceedings of the National Academy of Sciences of the United States of America* **1985**, 82, (15), 5000-4.
36. Elber, R.; Karplus, M., Multiple conformational states of proteins: a molecular dynamics analysis of myoglobin. *Science (Washington, DC, United States)* **1987**, 235, (4786), 318-21.
37. Miller, R. J. D., Vibrational energy relaxation and structural dynamics of heme proteins. *Annual Review of Physical Chemistry* **1991**, 42, 581-614.
38. Gu, Y.; Li, P.; Sage, J. T.; Champion, P. M., Photoreduction of heme proteins: spectroscopic studies and cross-section measurements. *Journal of the American Chemical Society* **1993**, 115, (12), 4993-5004.
39. Sagnella, D. E.; Straub, J. E., Directed Energy "Funneling" Mechanism for Heme Cooling Following Ligand Photolysis or Direct Excitation in Solvated Carbonmonoxy Myoglobin. *Journal of Physical Chemistry B* **2001**, 105, (29), 7057-7063.
40. Okazaki, I.; Hara, Y.; Nagaoka, M., On vibrational cooling upon photodissociation of carbonmonoxymyoglobin and its microscopic mechanism from the viewpoint of vibrational modes of heme. *Chemical Physics Letters* **2001**, 337, (1,2,3), 151-157.
41. Gao, Y.; Koyama, M.; El-Mashtoly, S. F.; Hayashi, T.; Harada, K.; Mizutani, Y.; Kitagawa, T., Time-resolved Raman evidence for energy 'funneling' through propionate

side chains in heme 'cooling' upon photolysis of carbonmonoxy myoglobin. *Chemical Physics Letters* **2006**, 429, (1-3), 239-243.

42. Foggi, P.; Bussotti, L.; Neuwahl, F. V. R., Photophysical and photochemical applications of femtosecond time-resolved transient absorption spectroscopy. *International Journal of Photoenergy* **2001**, 3, (2), 103-109.

43. Gunaratne Tissa, C.; Milliken, M.; Challa, J. R.; Simpson, M. C., Tunable ultrafast infrared/visible laser to probe vibrational dynamics. *Appl Opt FIELD Full Journal Title:Applied optics* **2006**, 45, (3), 558-64.

44. Kovalenko, S. A.; Schanz, R.; Hennig, H.; Ernsting, N. P., Cooling dynamics of an optically excited molecular probe in solution from femtosecond broadband transient absorption spectroscopy. *Journal of Chemical Physics* **2001**, 115, (7), 3256-3273.

45. Tsai, H.-H.; Simpson, M. C., Isolated Impact of Ruffling on the Vibrational Spectrum of Ni Porphyrins. Diagnosing Out-of-Plane Distortions. *Journal of Physical Chemistry A* **2004**, 108, (7), 1224-1232.

46. Spiro, T. G.; Czernuszewicz, R. S.; Li, X. Y., Metalloporphyrin structure and dynamics from resonance Raman spectroscopy. *Coordination Chemistry Reviews* **1990**, 100, 541-71.

CHAPTER 5

THE ELECTRONIC DYNAMICS OF $\text{Fe}^{\text{II}}\text{OEP-2MeIm}$ AND $\text{Fe}^{\text{II}}\text{OEP-(Im)}_2$ IN CH_2Cl_2 FOLLOWING Q-BAND EXCITATION

5.1 INTRODUCTION

Petrich et al.¹ in 1988 gave a detailed description of the electronic dynamics of the heme proteins unligated and ligated with diatomic ligands CO, NO and O₂ as well as that of a protoheme in the absence of the protein ligated with CO and NO. Single wavelength kinetics are measured following photo excitation in the Q-band (S₁). Photolysis was reported to occur in all the compounds with or without the presence of protein in less than 50 fs leading to the formation of two intermediate electronic states Hb_I* and Hb_{II}* each having a lifetime of 300 fs and 2.5 ps (3.2 ps in case of deoxy Mb) respectively. The absorption maxima for these two intermediate electronic states were assigned to 470 and 455 nm based on kinetic evidence, but no spectral information of the two states has been reported by them or by anyone in the following years.

The parallel intermediate electronic state decay model was modified in 2001 by Franzen et al.² to sequential relaxation pathway (Q₁-Hb_I*-Hb_{II}*-Hb) through the same intermediate electronic states. Again, both the ligated and unligated heme proteins were studied following electronic excitation in the Q-band (S₁). The intermediate electronic state Hb_I* was proposed to form via ultrafast iron-to-porphyrin ring charges transfer and then Hb_{II}* due to porphyrin ring-to-iron back charge transfer process. The absorption maxima were assigned at 450 and 478 nm respectively for Hb_I* and Hb_{II}* again based on

kinetic evidence. Both these studies and the interpretations are based on single wavelength kinetics or global fitting of the kinetics at several wavelengths and ignored the effect of absorption spectral evolution such as narrowing and blue-shifting as the molecule vibrationally cools to return to thermal equilibrium.

Exactly a year before the above study by Franzen et al was published; Kholodenko et al.³ reported transient absorption study of deoxy Mb (unligated) in the Q-band and band III (a weak absorption band centered at 630 nm) regions using Soret band excitation (S_2). Two electronic relaxation processes, one less than 100 fs and another of a few 100 fs were reported and based on the anisotropy decay values, it was concluded that there were no electronic relaxation components present after ~ 600 fs, in contrast to the predictions by Petrich and Franzen et al. The transient spectral features were successfully simulated to represent the difference spectra of vibrationally hot and cold ground state Mb molecules and the ground state vibrational relaxation was shown to bi-exponential involving a major fast (1.5 to 4 ps) and a slow (~ 15 ps) component.

More recent studies by Ye et al.^{4,5} in 2002 and 2003 confirmed this vibrationally hot ground electronic state model using Q-band excitation experiments of both ligated (MbCO, MbNO and met Mb) and deoxy Mb. The electronic relaxation of the S_2 state is not present in these studies and the vibrationally hot ground electronic state of the five-coordinate heme was found to form in less than 30 fs and the vibrational cooling features were successfully simulated with lifetimes of 0.4 and 4 ps.

The electronic and vibrational dynamics of a simple five-coordinate, high-spin model compound of the heme group in deoxyMb, Fe^{II}OEP-2MeIm in CH₂Cl₂ following

excitation in the Soret band region (S_2) were reported⁶ by us in 2006 and presented in Chapter 3 of this thesis. The observed dynamics were consistent with the vibrationally hot ground electronic state model of Kholodenko and Ye et al. The observed transient features were simulated with 10 fs S_2 state decay, 800 fs S_1 state decay and 8-10 ps spectral evolution lifetimes corresponding to vibrational cooling on the ground electronic state. Complimentary time-resolved anti-Stokes resonance Raman spectral (TRARRS) studies reported rise times (~ 750 fs) equivalent to S_1 state decay and mode-specific vibrational relaxation times of 1.6 ± 0.2 , 2.7 ± 0.2 , 2.8 ± 0.2 ps for ν_2 , ν_4 and ν_5 vibrational modes respectively.

The electronic dynamics of a simple six-coordinate, low-spin model compound of the bound heme, $\text{Fe}^{\text{II}}\text{OEP}(\text{Im})_2$ in CH_2Cl_2 following excitation in the Soret band region (S_2) were presented in Chapter 4 of this thesis. Near unity quantum yield for the photolysis of a single imidazole ligand, formation of a vibrationally hot five-coordinate photoproduct similar to the case of diatomic ligand bound heme proteins and no detectable hot six-coordinate starting material were reported. Vibrational cooling of the five-coordinate photoproduct was shown to involve a major 0.6 to 4.5 ps process assigned to IVR and a minor 10 ps process associated with VER. Most (75%) of the dissociated imidazole ligands were found to recombine geminately on the time scale of 10-20 ps and the rest of them didn't undergo any recombination even at 1.2 ns. It was pointed out that parallel Q-band pump experiments are needed to find out if the photolysis occurred directly from S_2 or from S_1 following $S_2 \rightarrow S_1$ ultrafast decay.

For an easy comparison to the vast majority of experimental results of heme proteins involving Q-band pump studies and to establish the exact photolysis reaction

channel, Q-band (S_1) pump experiments were performed on the two five- and six-coordinate model compounds and the preliminary results are presented in this chapter.

5.2 MATERIALS AND METHODS

The five-coordinate and six-coordinate heme model compounds, iron^{II} octaethyl porphyrin 2-methyl imidazole [$\text{Fe}^{\text{II}}\text{OEP-2meIm}$] and iron^{II} octaethyl porphyrin bis-imidazole [$\text{Fe}^{\text{II}}\text{OEP}-(\text{Im})_2$] are prepared according to the two phase method described elsewhere⁷ and also in the previous Chapters 3 and 4. The final product is a dichloromethane solution of the compound protected towards oxidation by an aqueous layer containing 1.0 M $\text{Na}_2\text{S}_2\text{O}_4$ solution above. Typical volume of the solutions is 50 ml. The concentrations of the samples are adjusted to have an optical density of 0.5 at the excitation wavelength of 541 nm. All solutions are degassed and kept under an overpressure of dry N_2 or Ar gas during the sample making process as well as the experimental interrogation. The sample is circulated through a 1 mm quartz flow cell using Teflon tubing and a chemical resistant micropump under an overpressure of Ar gas. While circulating the sample during experiments, extreme care is taken to flow only the denser porphyrin containing dichloromethane layer.

The femtosecond transient absorption experiments were performed at the Ohio State University Center for Chemical and Biophysical Dynamics (CCBD). The details of the laser system and the experimental setup had been described in detail elsewhere⁸. Briefly, the low energy 30 fs laser pulses at 800 nm from an oscillator (Mira, Coherent) are amplified in a regenerative amplifier (Legend, Coherent/Positive Light) to generate 2.5 mJ output (800 nm, 40 fs and 1 kHz). The fs output at 800 nm is used to generate pump pulses at 541 nm with the help of an OPA coupled with an SFG module (OPerA,

Coherent) and white light continuum probe pulses (320-700 nm) with the help of a 1 mm thick rotating CaF₂ plate. The instrument response is approximately 300 fs. The white light continuum is split into two parts of nearly equal energy, to generate probe and reference beams. The reference beam is used to minimize the noise due to fluctuations in the continuum intensity. Both the probe and reference beams separated vertically in space by a few mm go through the sample and are detected simultaneously using an imaging spectrograph (TRIAX 550, Jobin Yvon) coupled with a thermoelectrically cooled, back-illuminated CCD camera (Symphony, Jobin Yvon). The pump beam is overlapped with the probe beam spot in the sample at an angle of 5° and is blocked after the sample from entering the spectrometer using a beam block. The relative polarizations of the pump and probe beams are set to magic angle of 54.7°. In spite of the pump beam being blocked, considerable amount of the scattered pump beam enters the spectrometer and interferes with the detected transient signal. A dual notch filter that selectively cuts-off 543 and 647 nm light is used at the entrance of the spectrometer slit is used. Hence the Q-band bleach signals could not be measured. And also unfortunately transmission of light below 420 nm through the filter steeply decreased making it extremely difficult to characterize the Soret band bleach.

The pump and probe beams are chopped at a frequency of 25 and 12.5 Hz respectively to create pump ON and pump OFF conditions in the sample using two synchronized optical choppers. The CCD camera acquisition is also referenced to the choppers to increase the signal to noise ratio. At a given pump-probe delay, 250 acquisitions each of 20 ms integration are used with every other acquisition being with

the pump ON condition. Then the transient absorption signal is obtained using the following equation.

$$\Delta OD = -\log_{10} \left\{ \frac{\left[\frac{I_{probe}}{I_{reference}} \right]_{Pump\ ON}}{\left[\frac{I_{probe}}{I_{reference}} \right]_{Pump\ OFF}} \right\}$$

The data accumulation, optical delay stage, choppers and the CaF₂ crystal rotation are controlled using a home-developed software programs written using Labview 7. The final result is an average of 3 complete cycles of the data collected at the entire set of pump-probe delay positions. The resulting transient absorption spectra are corrected for chirp due to group velocity dispersion in the white light continuum probe pulse using procedures already incorporated into the data collection software. The data was processed using Origin 7.5TM software.

5.3 RESULTS AND DISCUSSION

As described in the methods section, the Soret and Q-band bleaches could not be characterized due to the notch filter that is used in the experiments to block the scattered pump laser beam entering the sample and hence the preliminary results of only the transient absorption signals in the Soret band region of the two model compounds are presented here.

Figure 5-1 shows the transient absorption spectra of Fe^{II}OEP-2MeIm in CH₂Cl₂ corresponding to the rapid formation of vibrationally hot ground electronic state species within the instrument response following photoexcitation to S1 state. The transient absorption features are extremely broad and red-shifted at early times, which spectrally

narrow and blue-shift approaching the equilibrium ground state absorption spectral shape of the five-coordinate heme. This spectral evolution as well as the excited electronic state (S_1) decay results in an increase in the absorption signal at wavelength (424 nm) corresponding to the equilibrium absorption maximum and reaches a maximum at about 2.5 ps after the excitation.

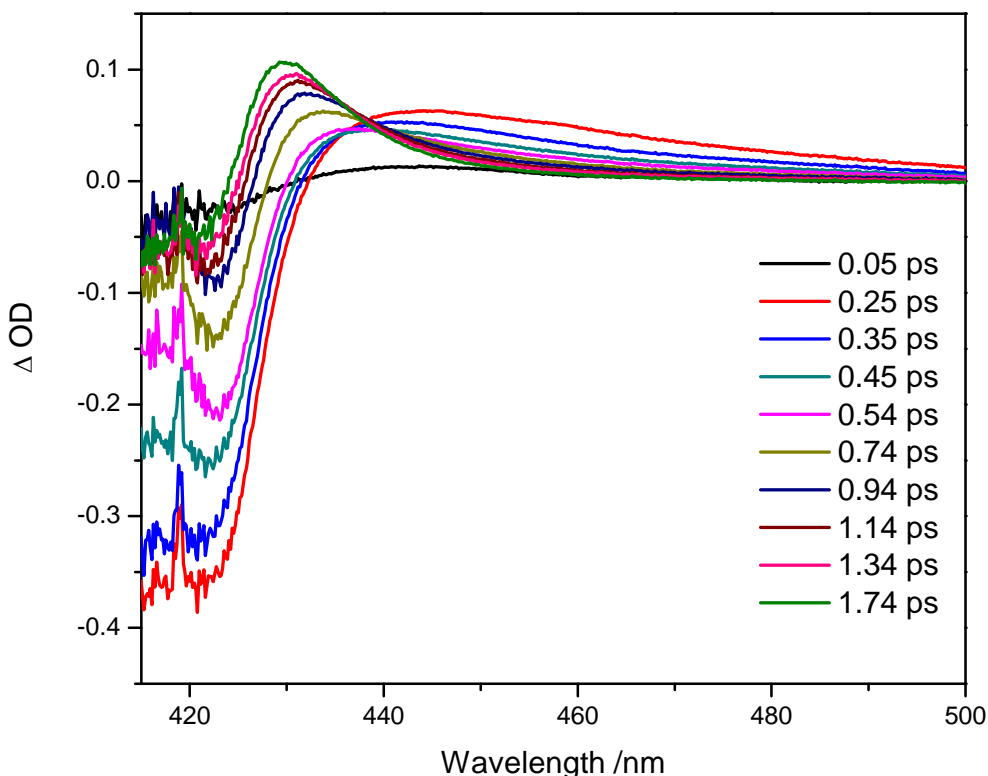


Figure 5 - 1 A representative set of Transient absorption experimental data showing the fast dynamics associated with the first 2.0 ps for $\text{Fe}^{\text{II}}\text{OEP-2MeIm}$ in CH_2Cl_2 . Pump=541 nm, Probe=white light continuum generated in CaF_2 , Instrument response=300 fs.

The slower phase of the spectral evolution is presented in Figure 5-2. The spectral shift after 2.5 ps slows down and a continued narrowing is observed. The vibrational

cooling and thermal equilibration on the ground electronic state is complete by about 30 ps.

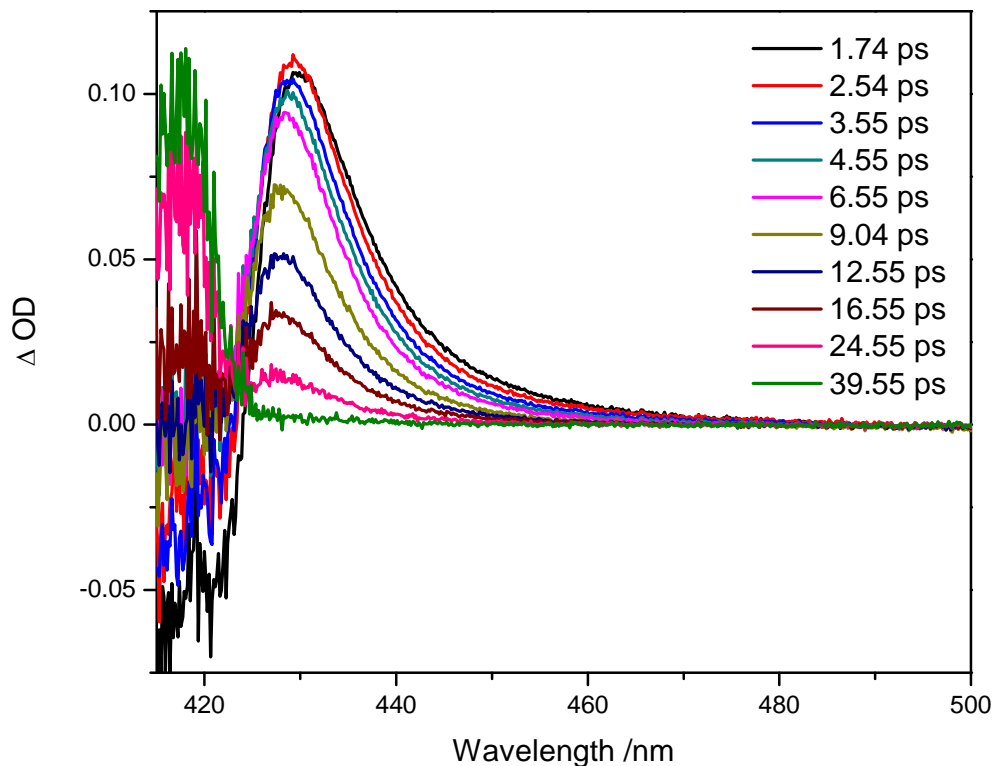


Figure 5 - 2 A representative set of transient absorption experimental data showing the slow dynamics from 2 to 40 ps for Fe^{II}OEP-2MeIm in CH₂Cl₂. Pump=541 nm, Probe=white light continuum generated in CaF₂, Instrument response=300 fs.

Kinetic traces of the transient absorption signal in the Soret band region at selected set of wavelengths and the corresponding exponential fits are presented in Figure 5-3 and the results are tabulated in Table 5-1. At longer wavelengths, the kinetics are faster compared to those at shorter wavelengths. Essentially, three different components are present, one on the order of a few hundred fs, a second one on the order of 3 ps and a third component of approximately 6-10 ps.

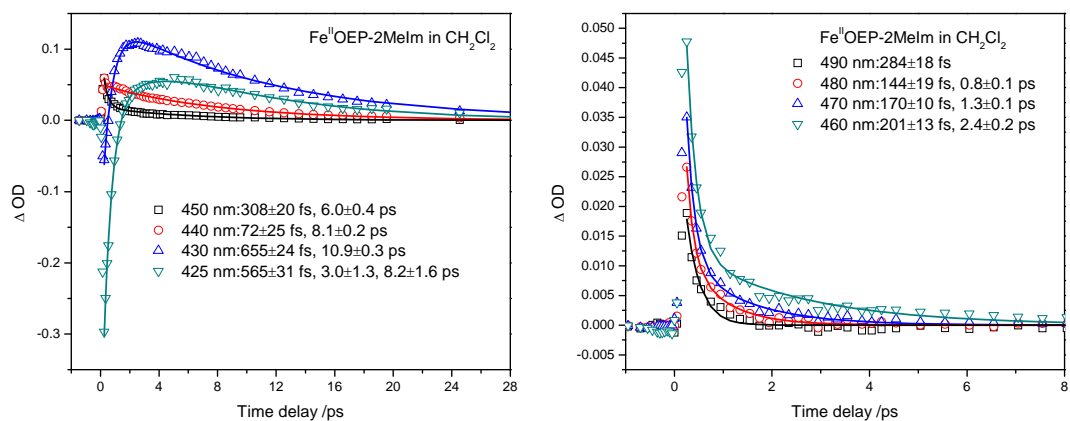


Figure 5 - 3 Kinetic traces of the transient absorption data for Fe^{II}OEP-2MeIm in CH₂Cl₂ at the wavelengths indicated and the associated exponential fits.

λ (nm)	A ₁ (%), t ₁ (fs)	A ₂ (%), t ₂ (ps)	A ₃ (%), t ₃ (ps)	R ²
425	-64, 565±31	-17, 3.0±1.3	19, 8.2±1.6	0.998
430	-67, 655±24		33, 10.9±0.3	0.993
440	87, 72±25		13, 8.1±0.2	0.994
450	83, 308±20		17, 6.0±0.4	0.992
460	90, 201±13	10, 2.4±0.2		0.992
470	89, 170±10	11, 1.3±0.1		0.996
480	86, 144±19	14, 0.8±0.1		0.993
490	100, 284±18			0.966
500	100, 257±23			0.937

Table 5 - 1 Exponential Fits to Experimental TA Measurements of Fe^{II}OEP-2MeIm in CH₂Cl₂ following excitation at 541 nm.

The kinetic trace at 425 nm corresponding to the equilibrium absorption spectral maximum represents all the three components; the first two can be assigned to IVR and

the longer component is due to VER on the ground electronic state. The similarity of the initial fast phase transient absorption spectra of $\text{Fe}^{\text{II}}\text{OEP}-(\text{Im})_2$ in CH_2Cl_2 following Q-band excitation at 541 nm to that of the five-coordinate compound indicate the formation of a vibrationally hot five-coordinate photoproduct.

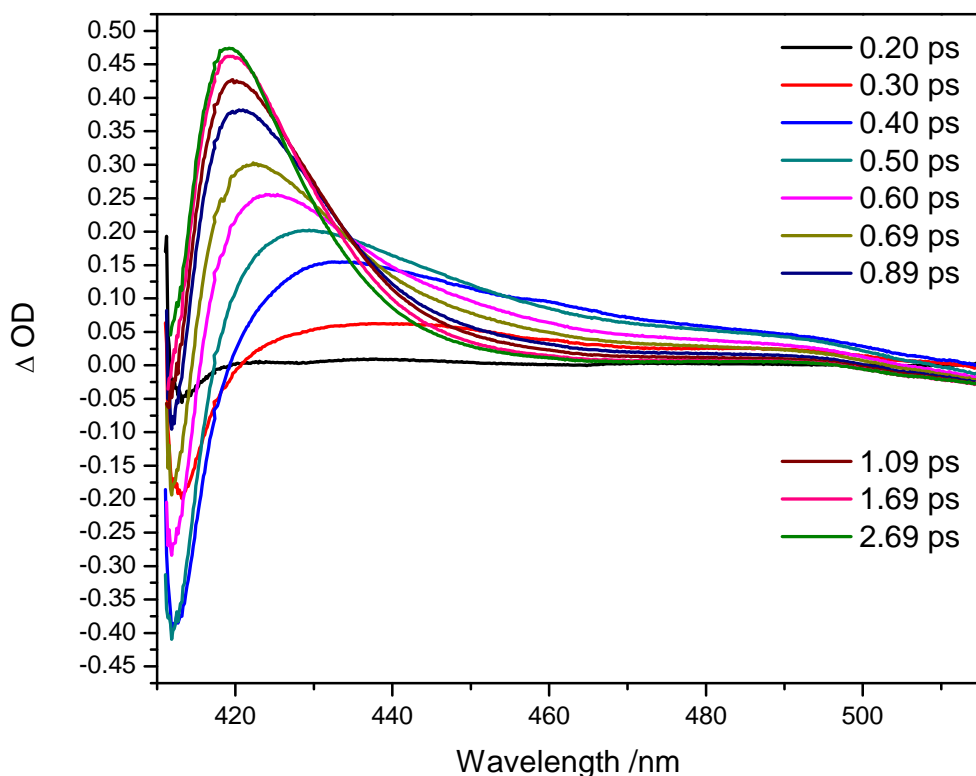


Figure 5 - 4 A representative set of transient absorption experimental data showing the fast dynamics associated with the first 2.7 ps for $\text{Fe}^{\text{II}}\text{OEP}-(\text{Im})_2$ in CH_2Cl_2 . Pump=541 nm, Probe=white light continuum generated in CaF_2 , Instrument response=300 fs.

Spectral evolution leads to increase in the signal approximately at 425 nm corresponding to the five-coordinate compound absorption position and reaches maximum at 2.69 ps, delayed by ~ 150 fs compared to $\text{Fe}^{\text{II}}\text{OEP}-2\text{MeIm}$. The Figure 5-5

shows the decay of transient signal and continues spectral evolution after 2.7 ps up to 2.0 ns. The transient signal decay saturates at about 50 ps and further decay becomes extremely slow.

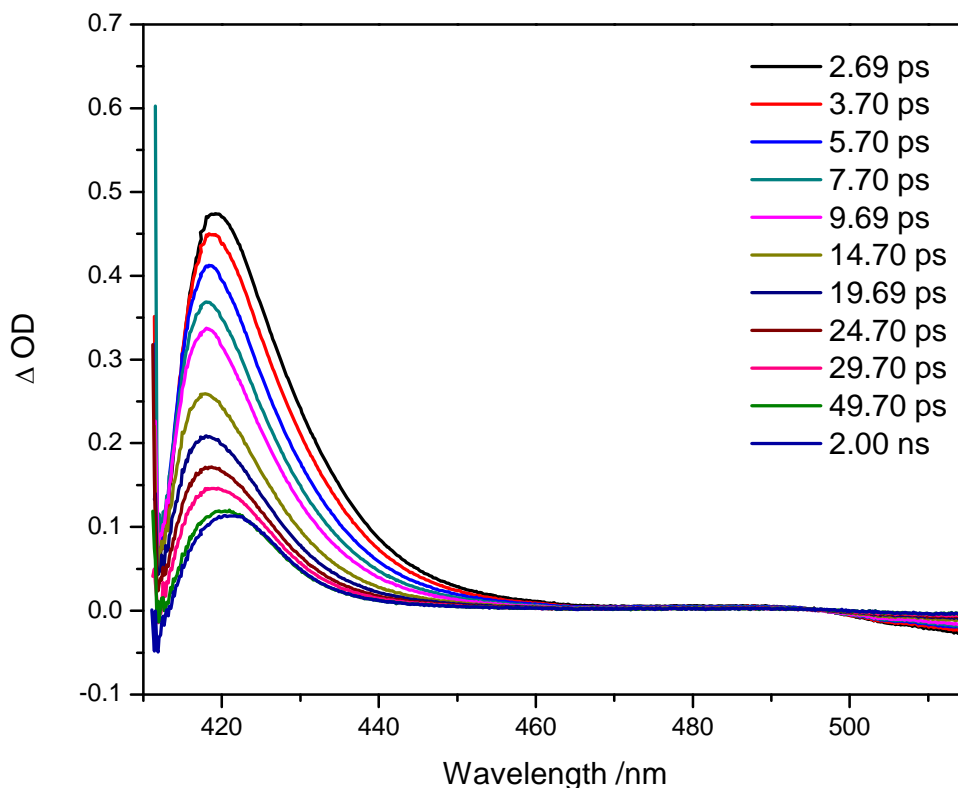


Figure 5 - 5 Transient absorption experimental data showing the slow dynamics from 2.7 ps to 2.0 ns for Fe^{II}OEP-(Im)₂ in CH₂Cl₂. Pump=541 nm, Probe=white light continuum generated in CaF₂, Instrument response=300 fs.

The kinetic traces of the transient absorption signal as a function of the time delay and the corresponding exponential fits after photoexcitation are presented in Figure 5-6. The rise of the signal at all the wavelengths measured is instrument limited and only an

estimate of approximately 140 fs can be reported based on the rise of signal at 425 nm. Mainly two components are observed, one corresponding to 270-350 fs and a longer component in the range of 7 to 16 ps. This longer component is mainly due to the fast geminate ligand recombination and the minor intermolecular vibrational cooling dynamics.

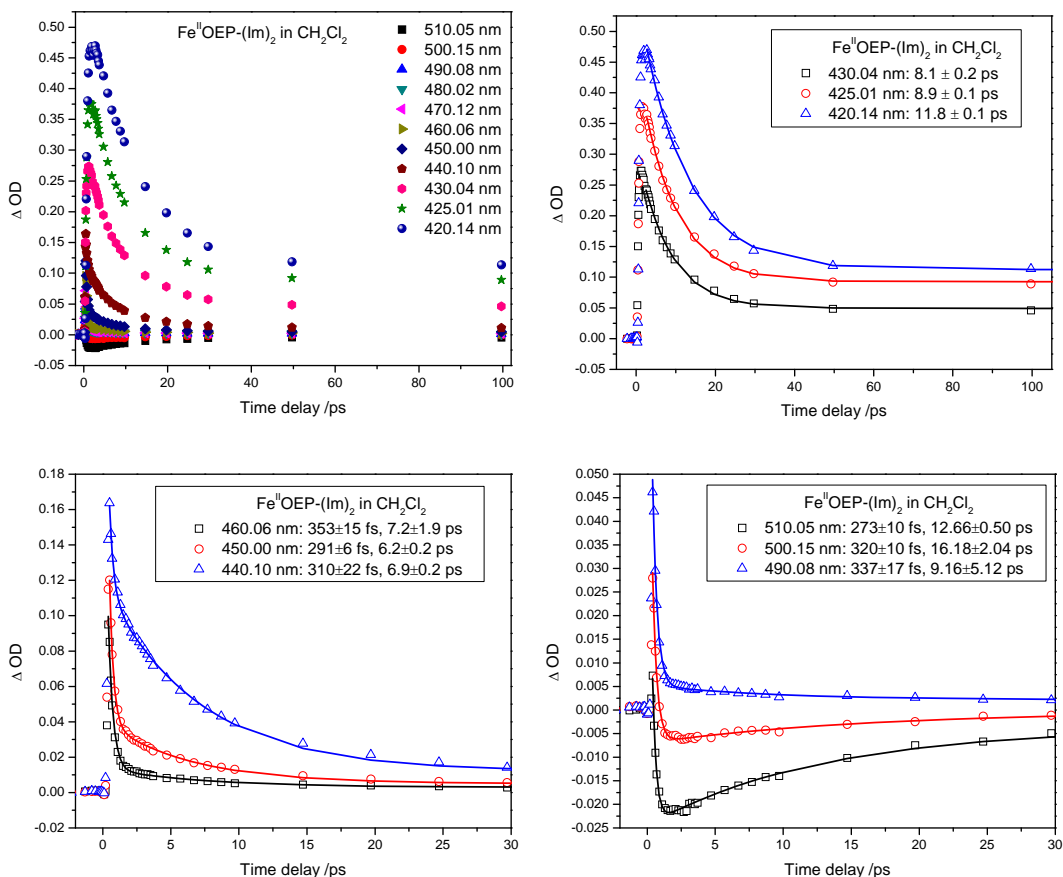


Figure 5 - 6 Kinetic traces of the transient absorption data for $\text{Fe}^{\text{II}}\text{OEP}-(\text{Im})_2$ in CH_2Cl_2 at the wavelengths indicated and the associated exponential fits.

$\lambda(\text{nm})$	$A_1 (\%), t_1 (\text{fs})$	$A_2 (\%), t_2 (\text{ps})$	off-set	r^2
420		100, 11.8±0.1	0.1124	0.999
425		100, 8.9±0.1	0.0925	0.999
430		100, 8.1±0.2	0.0492	0.999
440	71, 309±22	29, 6.9±0.2	0.0121	0.999
450	93, 291±6	7, 6.2±0.2	0.0051	0.995
460	96, 353±15	4, 7.2±1.9	0.0029	0.995
470	98, 344±15	2, 8.7±5.7	0.0024	0.994
480	98, 347±17	2, 11.1±6.7	0.0024	0.991
490	98, 337±17	2, 9.2±5.1	0.0022	0.991
500	95, 320±10	-5, 16.2±2.0	-0.0002	0.995
510	86, 273±10	-14, 12.7±0.5	-0.0037	0.996

Table 5 - 2 Exponential Fits to Experimental TA Measurements of Fe^{II}OEP-(Im)₂ in CH₂Cl₂ following excitation at 541 nm.

Based on the maximum (0.377838) and residual (0.09249) intensity of the transient signal at 425 nm, corresponding to equilibrium absorption spectral position of Fe^{II}OEP-2MeIm in CH₂Cl₂, 76 % of the photolysed imidazole ligands geminately recombine well below 100 ps. Since both the Soret and Q-band bleaches could not be characterized in these studies, an accurate time constant for ligand recombination is not obtained. The longer life time component of 7-16 ps obtained from the single wavelength measurements contain both the vibrational cooling and geminate recombination kinetics

Because of the problems due to the notch filter employed in these studies, the ground state depletion and reformation of the six-coordinate compound could not be monitored. And also we could not determine if there is any hot six-coordinate compound

being formed. These experiments certainly need to be repeated with better notch or short pass filters in order to fully characterize whether the photolysis is occurring from S_1 or S_2 excited electronic states. Nevertheless, the preliminary results and the similarity of the transient spectral features to that of the Soret band pump studies imply that there is only very little or negligible formation of the hot six-coordinate species.

5.4 CONCLUSIONS

The preliminary results of the Q-band excitation studies of the two model compounds $\text{Fe}^{\text{II}}\text{OEP-2MeIm}$ and $\text{Fe}^{\text{II}}\text{OEP-(Im)}_2$ in CH_2Cl_2 are presented as a comparison the Soret band excitation studies presented in the previous two chapters. Based on the single wavelength kinetic traces, the five-coordinate compound undergoes intramolecular vibrational relaxation on the time scale of 0.6 to 3.0 ps and intermolecular vibrational cooling on the time scale of 6-10 ps. The IVR and VER time scales are equivalent to those observed in the Soret band excitation studies implying that the hot ground state is formed via $S_1 \rightarrow S_0$ nonradiative decay channel rather than the direct $S_2 \rightarrow S_0$ channel. The photochemical reaction channel involving the photolysis of imidazole needs to be characterized further to make reliable predictions. Single wavelength kinetic analysis of the six-coordinated compound implied a fast geminate recombination occurring on the time scale of vibrational cooling. However, in the light of these interpretations being based on the single wavelength kinetics that are extremely sensitive to dominant spectral evolution in the transient features, the importance for repeating these experiments to characterize the transient bleach is stressed. Parallel time-resolved Raman studies using Q-band excitation will lead to deep insight into the mode-specific non-equilibrium

vibrational dynamics and to characterize the effect of excited electronic state preparation and the protein.

5.5 REFERENCES

1. Petrich, J. W.; Poyart, C.; Martin, J. L., Photophysics and reactivity of heme proteins: a femtosecond absorption study of hemoglobin, myoglobin, and protoheme. *Biochemistry* 1988, 27, (11), 4049-60.
2. Franzen, S.; Kiger, L.; Poyart, C.; Martin, J.-L., Heme photolysis occurs by ultrafast excited state metal-to-ring charge transfer. *Biophysical Journal* 2001, 80, (5), 2372-2385.
3. Kholodenko, Y.; Volk, M.; Gooding, E.; Hochstrasser, R. M., Energy dissipation and relaxation processes in deoxy myoglobin after photoexcitation in the Soret region. *Chemical Physics* 2000, 259, (1), 71-87.
4. Ye, X.; Demidov, A.; Champion, P. M., Measurements of the Photodissociation Quantum Yields of MbNO and MbO₂ and the Vibrational Relaxation of the Six-Coordinate Heme Species. *Journal of the American Chemical Society* 2002, 124, (20), 5914-5924.
5. Ye, X.; Demidov, A.; Rosca, F.; Wang, W.; Kumar, A.; Ionascu, D.; Zhu, L.; Barrick, D.; Wharton, D.; Champion, P. M., Investigations of Heme Protein Absorption Line Shapes, Vibrational Relaxation, and Resonance Raman Scattering on Ultrafast Time Scales. *Journal of Physical Chemistry A* 2003, 107, (40), 8156-8165.
6. Challa, J. R.; Gunaratne Tissa, C.; Simpson, M. C., State preparation and excited electronic and vibrational behavior in hemes. *J Phys Chem B* 2006, 110, (40), 19956-65.

7. Loparo, J. J.; Cheatum, C. M.; Ondrias, M. R.; Simpson, M. C., Transient Raman observations of heme vibrational dynamics in five-coordinate iron porphyrins. *Chemical Physics* 2003, 286, (2-3), 353-374.
8. Burdzinski, G.; Hackett, J. C.; Wang, J.; Gustafson, T. L.; Hadad, C. M.; Platz, M. S., Early Events in the Photochemistry of Aryl Azides from Femtosecond UV/Vis Spectroscopy and Quantum Chemical Calculations. *Journal of the American Chemical Society* 2006, 128, (41), 13402-13411.

CHAPTER 6

EFFECT OF METHYL GROUPS ON THE VIBRATIONAL DYNAMICS OF *PARA*-NITROANILINE

6.1 INTRODUCTION

Para-nitroaniline (PNA) which has an electron donating group (-NH₂) and an electron withdrawing group (-NO₂) connected via a conjugated linker (benzene ring) serves as a simple prototypical model compound for 'push-pull' chromophores. The huge change in dipole moment in the presence of an external electric field parallel to the transition dipole¹ gives rise to large molecular hyper-polarizability which in turn leads to bulk nonlinear optical susceptibilities essential for nonlinear optical activity. For example, the ground electronic state of PNA has a dipole moment of ~ 6 D. Upon photoexcitation, charge transfer from the NH₂ to NO₂ group increases the dipole moment up to ~ 14 D in the excited electronic state. Reports by Davydov et al.² that there is a strong correlation between the charge transfer in organic materials with donor and acceptor groups connected by benzene ring and second harmonic generation (SHG) efficiency made PNA and its derivatives promising for nonlinear optical applications, in particular for second order nonlinear optical processes such as SHG. Besides the NLO activity, the charge transfer nature of the electronic excitation makes it a good solvation probe and also serves as a model compound for electron transfer studies. Hence the photophysical properties of this simple push-pull compound *para*-nitroaniline (PNA) and its N-alkyl derivatives have been the subject of extensive theoretical³⁻⁷ and experimental studies⁸⁻¹⁸.

The linear and nonlinear optical properties of push-pull chromophores strongly depend on the surrounding solvent properties like polarity and hydrogen bonding ability. For example, PNA has a strong UV-vis absorption spectrum whose absorption maximum exhibits a huge solvatochromic red-shift of 5350 cm^{-1} in going from nonpolar cyclohexane ($\lambda_{\text{max}}=322\text{ nm}$) to highly polar dimethylsulfoxide ($\lambda_{\text{max}}=389\text{ nm}$). This is often qualitatively explained using two-state models which treat the ground and the lowest excited electronic state as linear combinations of two basis states corresponding to the neutral and zwitterionic resonance structures of the chromophore. With increase in solvent polarity, the relative energy of the ionic form decreases and the amount of zwitterionic character in the ground electronic state increases resulting in a red-shift of the charge transfer absorption band. The increased mixing of the ionic nature in the ground electronic state also affects the equilibrium geometries and vibrational frequencies of the push-pull chromophores. Push-pull molecules such as PNA¹⁸, N, N-dimethyl-4-nitroaniline (NNDMPNA)^{18, 19} and phenol blue²⁰⁻²² have been shown to have solvent state selective excitation of the solute molecules leading to wavelength dependent Stokes shift in resonance Raman spectra.

Resonance Raman spectral analysis of PNA in various solvents by Moran et al.¹³ showed that the excited electronic state is the one which is more affected by the solvent, questioning the validity of two-state models for organic push-pull chromophores which are successfully applied in predicting the solvation effects on the linear and nonlinear optical properties of linear push-pull polyenes and some inorganic charge transfer complexes^{23, 24}. In spite of these being not quantitatively ideal, modified self-consistent

two-state models incorporating electron-phonon coupling and solvent contributions still provide deep insight into the qualitative behavior of these systems²⁵⁻²⁸.

The time-resolved spectroscopic properties of PNA were also found to be sensitive to the solvent properties like polarity. Time-resolved microwave conductivity measurements of PNA suggested an intersystem crossing quantum yield of ~ 1 in nonpolar benzene and ~ 0.5 in more polar dioxane⁹. Ultrafast charge transfer dynamics of PNA in water and dioxane reported by Thomsen et al.¹¹ using transient absorption spectroscopy showed that the relaxation on excited singlet state surface of PNA including the $S_1 \rightarrow S_0$ internal conversion is extremely rapid (~ 300 fs) and that the quantum yield for intersystem crossing is ~ 0.4 in dioxane and only ~ 0.03 in more polar water. It follows from these two studies that the quantum yield for intersystem crossing in PNA is strongly dependent on solvent polarity and it is very little or negligible in highly polar solvents.

Kovalenko et al.¹² classified the relaxation events observed in transient absorption studies following photoexcitation of PNA into solvation (<100 fs), intramolecular charge transfer (120-140 fs), internal conversion (250-400 fs) governed by twisting of the NO_2 group and vibrational cooling (1-3 ps) on the ground electronic state as shown in Figure 6-1. A rapid vibrational cooling time of 1 ps was predicted based on the spectral evolution of the transient absorption peaks between 1 and 10 ps after photoexcitation. Transient stimulated emission was also observed for the first time from S_1 state of PNA.

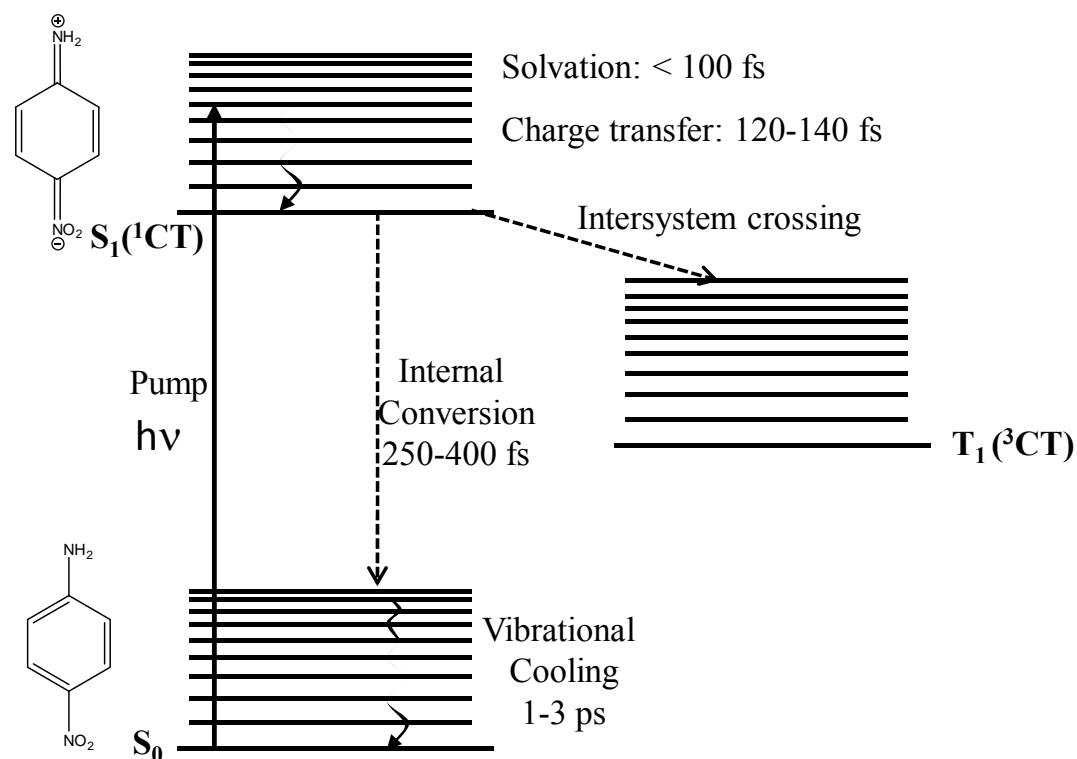


Figure 6 - 1 The events following photoexcitation of PNA forming the charge transfer excited electronic state. Figure based on the results of Kovalenko et al. PNA undergoes rapid internal conversion to the ground state or intersystem crossing to the lowest triplet state. The branching ratio and the individual relaxation rates are strongly dependent on the solvent polarity.

The idea of internal conversion (IC) through a conical intersection involving the NO_2 twisting coordinate was introduced in order to explain the ultrafast internal conversion process based on semi-empirical ab-initio method calculations (SAM1)^{12, 29}. Twisted intramolecular charge transfer model³⁰ was used in explaining the excited state geometry. Equilibrium geometry on the excited state surface corresponds to NO_2 twist angle of 75° and NH_2 wagging angle of 0° . The system evolves along the NO_2 twisting coordinate until it meets an isoenergetic point of S_1 and S_0 at NO_2 twist angle of 60° , at which point the vibronic factors lead to effective coupling of the two states leading to ultrafast internal conversion. Comparisons to N, N-dimethyl benzonitrile (DMABN) are

drawn where twisting of the alkyl substituted amino group plays an important role instead of the acceptor group^{31, 32}.

Kozich et al.^{15, 33} evaluated the vibrational energy redistribution of PNA in the ground electronic state after internal conversion following photoexcitation to the charge transfer state using time resolved resonance Raman spectroscopy. The idea of conical intersections in PNA internal conversion was adopted in explaining the mechanistic aspects of the internal conversion process leading to nonequilibrium vibrational energy distribution in coupling and accepting modes in a manner contrary to the rapid thermalization and vibrational cooling on the ground state proposed by Ernsting et al.^{12, 29, 34} A weakly Raman active mode at 1510 cm^{-1} , assigned to an overtone or combination band of $-\text{NO}_2$ out of plane motion, was reported to show fastest rise time comparable to the IC rate and pronounced excess population representing the main accepting mode. Intense high frequency modes with large Franck-Condon factors gain excited state population mainly by IVR and relax considerably slowly (6-7 ps) via IVR to low frequency motions and simultaneous cooling to solvent degrees of freedom. The vibrational cooling life times are significantly slower than the reported values from less direct transient absorption studies.

SAMI calculations^{12, 29, 34} showed that the PNA absorption spectral shape is conformationally broadened due to a distribution of NO_2 twist angles. The ground electronic state is flat as a function of the NO_2 twisting coordinate, but the charge transfer state is composed of various NO_2 twist angles and hence NO_2 twisting plays an important role in relaxation of PNA on S_1 surface. Gunaratne et al.¹⁷ used narrow bandwidth pumping at three different wavelengths on the low energy side of the PNA absorption

spectrum, thus exciting the subpopulations involving different NO₂ twist angles, and probed the vibrational dynamics on S₀ following S₀←S₁ internal conversion. No excitation wavelength dependence of the vibrational dynamics was observed and hence it was concluded that the IC occurs from a relaxed S₁ state or from the same crossing point on S₁ regardless of the nature of the initially excited conformation. The phenyl breathing mode at 860 cm⁻¹ and the symmetric NO₂ stretch at 1310 cm⁻¹ were shown to exhibit vibrational lifetimes in S₀ of 8.1±0.6 ps and 5.2±0.6 ps respectively; the corresponding peak shift lifetimes are 3.2±0.4 ps and 4.6±0.7 ps respectively. The significant difference in lifetimes obtained from the peak shift evolution and integrated intensity decay profile of the phenyl breathing mode at 860 cm⁻¹ was suggested to be primarily due to at least two processes operating on competitive timescales in the relaxation process following internal conversion. The intramolecular vibrational energy redistribution on S₀ was proposed to occur on 2-5 ps time scales and the subsequent vibrational cooling to bath degrees of freedom was proposed to happen on 5-10 ps time scales.

The transient absorption and time-resolved Raman studies suggest that the main relaxation pathway of para-nitroaniline in polar solvents following photoexcitation is via ultrafast nonradiative decay resulting in large excess of energy in the ground state molecular vibrations. The relaxation of the resulting hot solute molecules created on femtosecond time scale to the surrounding solvent molecules is an important process in understanding molecular scale heat flow. An understanding of the role of molecular vibrations in effectively dissipating the excess energy in the form of heat to the surrounding solvent molecules can be used to effectively direct or funnel the thermal energy for possible applications such as photo thermal therapy.

In order to better understand the mode-specific vibrational dynamics and exert more control over the energy relaxation pathways in PNA molecule, the effect of structure on the underlying vibrational energy relaxation need to studied in detail. To better improve the directional energy flow, various substituent groups such as $-CH_3$, $-OH$, $-COOH$, $-CN$, $-CF_3$, $-Cl$ and so on can be tested and classified as efficient microscopic thermal conductors and isolators. By selective substitution of the molecular conductors and isolators, the excess vibrational energy following photoexcitation can be efficiently funneled towards a cancer tumor or any other target for photothermal therapy (PTT)³⁵⁻⁴³ applications making them good photothermal sensitizers. The primary goal of the experiments discussed in this chapter is to probe the effect of methyl groups on the mode-specific vibrational energy dynamics of PNA dissolved in DMSO.

The single color time resolved resonance Raman spectroscopic studies of PNA in DMSO reported by us elsewhere¹⁷ are extended here to include the effect of simple methyl group substitution on the dynamics. The molecular structures of the three different methyl group derivatives of PNA are shown in Figure 6-2. The energy relaxation dynamics of 2-methyl and 2, 6-dimethyl substituted PNA compounds are not available, but the N, N-dimethyl substituted PNA in acetonitrile has been shown to exhibit longer cooling times compared to that of PNA in water, the difference being assigned to reduced hydrogen bonding ability of NNDMPNA as the hydrogen atoms of the amino group are replaced by methyl groups³⁴. No triplet state was observed in the case of NNDMPNA in acetonitrile also similar to that of PNA in water.

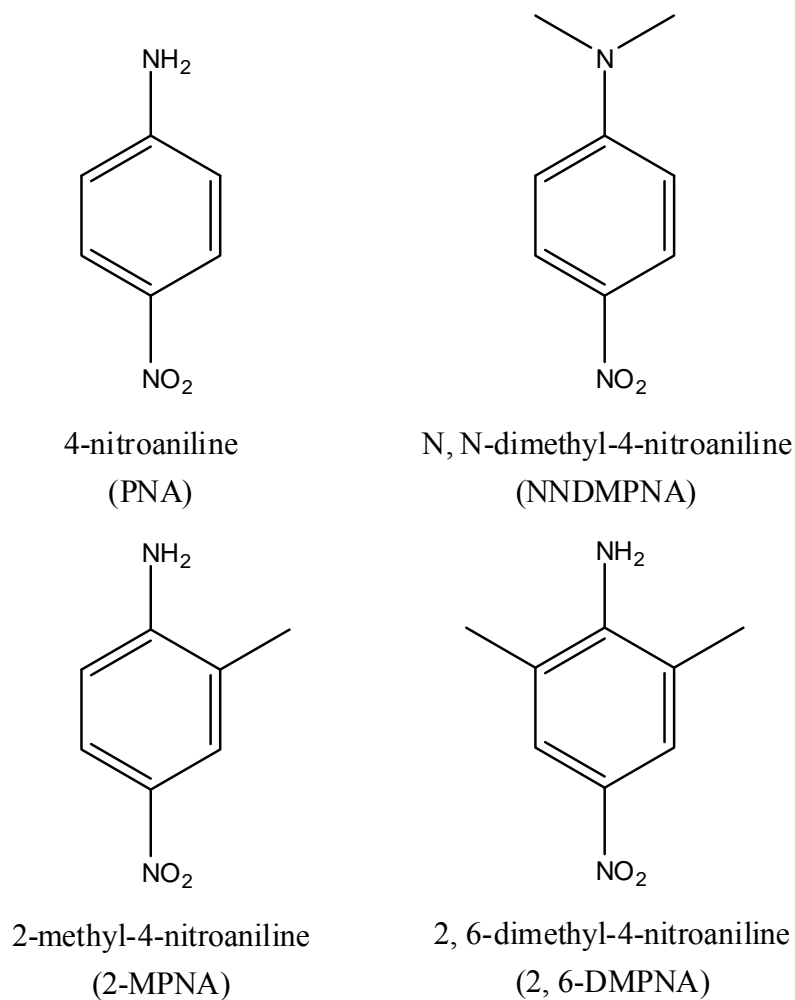


Figure 6 - 2 The chemical structures of 4-nitroaniline (PNA) and its methyl derivatives 2-methyl-4-nitroaniline (2-MPNA), 2, 6-dimethyl-4-nitroaniline (2, 6-DMPNA) and N, N-dimethyl-4-nitroaniline (NNDMPNA).

NNDMPNA has been shown to undergo demethylation upon photoexcitation in the presence of external acceptors such as nitrobenzene in benzene or methoxide ion in methanol⁴⁴. The mechanism of demethylation is proposed to be initiated by photoinduced electron transfer to the lowest triplet state. Photochemical studies of NNDMPNA as initiator of lauryl acrylate polymerization using laser irradiation at 337 nm also proposed the involvement of a triplet state with lifetime less than 30 ns^{45, 46}. These findings suggest the possibility of triplet state, radical formation and radiative emissions from the singlet

and triplet excited states of N-alkyl derivatives of PNA in nonpolar solvents, with fluorescence being the only radiative process in polar solvents. However, no significant triplet state absorption or emission was observed in transient absorption experiments of NNDMPNA³⁴ or N-benzyl-2-MPNA⁴⁷.

6.2 MATERIALS AND METHODS

PNA (Alfa Aesar, 99%), 2-MPNA (Aldrich, 97%), 2, 6-DMPNA (Sigma-Aldrich) and NNDMPNA (TCI America, 98%) were used as purchased without further purification. Typically 50 ml solutions were prepared by dissolving the compounds in dimethylsulfoxide (DMSO, Fisher Scientific, ACS Certified 99.9%, used without further purification) to get a concentration of 3-4 mM. All experiments were performed at room temperature. The solution was flowed rapidly through a 1 mm quartz flow cell using a chemically resistant peristaltic pump to prevent degradation of the sample in the excitation volume.

A single color pump probe setup using the fs pulses from Clark-MXR CPA-100 system, as described in Chapter 2, was used for sub-ps time-resolved resonance Raman studies. Briefly, a Ti: Sapphire regenerative amplifier seeded by femtosecond pulses from a mode-locked Ti: Sapphire oscillator provided 100-150 fs pulse train of 1 kHz repetition rate tunable within a small wavelength range of 780-840 nm. Approximately 300 μ J of the fs output was frequency-doubled in a 30 mm KDP crystal to produce \sim 0.8 ps pulses with 50-60 μ J per pulse. The spectral full width at half maximum intensity (FWHM) of the pulse was 17-25 cm^{-1} ; this corresponds to a (Gaussian) transform-limited temporal FWHM of 588 – 865 fs. A 50:50 beam splitter produced the pump and probe beams which were attenuated to approximately 5 and 2 μ J/pulse, respectively, using Schott glass

neutral density filters. Time resolution was obtained by passing the probe beam through a motorized, calibrated delay stage (MM3000, Newport Inc). The two beams were overlapped at the sample in a nearly collinear geometry ($\sim 5^\circ$).

Time-zero was estimated by allowing the residual 800 nm in each beam to travel the beam paths and doubling in a BBO crystal at the sample position. As these experiments are one-color, pump-probe experiments, the transient signal is symmetric about time-zero, weighted by the relative energies of the pump and probe pulses. Refinement of the assignment of time-zero was thus provided by the signal itself⁴⁸.

A $\sim 135^\circ$ back-scattering geometry was used to collect spectra. The collection assembly consisted of a collection lens, f-matching lens, and depolarizer. Rayleigh scattering was rejected with an angle-tuned holographic super notch filter (Kaiser, Inc.). The time-resolved anti-Stokes Raman spectra were recorded with a thermoelectrically-cooled, back-illuminated CCD camera (DU-420 BV, Andor) using a 0.5 meter imaging spectrograph (500is, Chromex, Inc.). Typical accumulation time for each spectrum was 60 seconds. At each temporal delay, pump-only and probe-only control spectra were acquired under the same conditions as the pump-probe data.

The data was processed using Origin 7.5TM software. After removing the artifacts due to cosmic radiation in all the Raman spectra, the pump-probe spectrum obtained at a longer time delay (reference) was subtracted from the corresponding pump-probe spectrum to remove the pump only and probe only contributions. The pump-probe reference spectra for 2-MPNA, 2,6-DMPNA and NNDMPNA are collected at time delays of 60, 64 and -103 ps respectively. The background was then manually subtracted

using the Origin baseline subtraction routine to generate transient spectra. Transient features were characterized with Lorentzian line shapes using non-linear least squares fitting, where possible. Kinetic traces were derived from the integrated areas of the transient spectra, and the decay portions were fit using an exponential model. Peak positions also were fit to exponential functions.

Computations were performed to determine the theoretical vibrational frequencies and the normal mode characterizations. Unconstrained geometry optimization and vibrational calculation were done using Gaussian 03, at the density functional theory level with B3LYP functional and 6-31+G(2d, p) basis set. A scaling factor of 0.98 was applied to the DFT calculated vibrational frequencies for comparison to the experimental values.

6.3 RESULTS

The single color time-resolved anti-Stokes resonance Raman spectroscopy results of all the three methyl derivatives of PNA are first presented individually. They are then compared to one another in the Discussion section. Figure 6-3 shows the UV-vis absorption spectra of PNA, 2-MPNA, 2, 6-DMPNA and NNDMPNA dissolved in DMSO. The absorption maxima of these compounds in DMSO correspond to 389, 393, 396 and 407 nm respectively with no significant change in bandwidth. The observed red-shift on methyl substitution is due to increased electron density in the molecule because of the positive inductive effect of methyl groups. The red-shift is more pronounced in case of N-methyl substituted PNA compared to that of phenyl ring substituted (*ortho* position to the amino group) PNA compounds 2-MPNA and 2, 6-DMPNA.

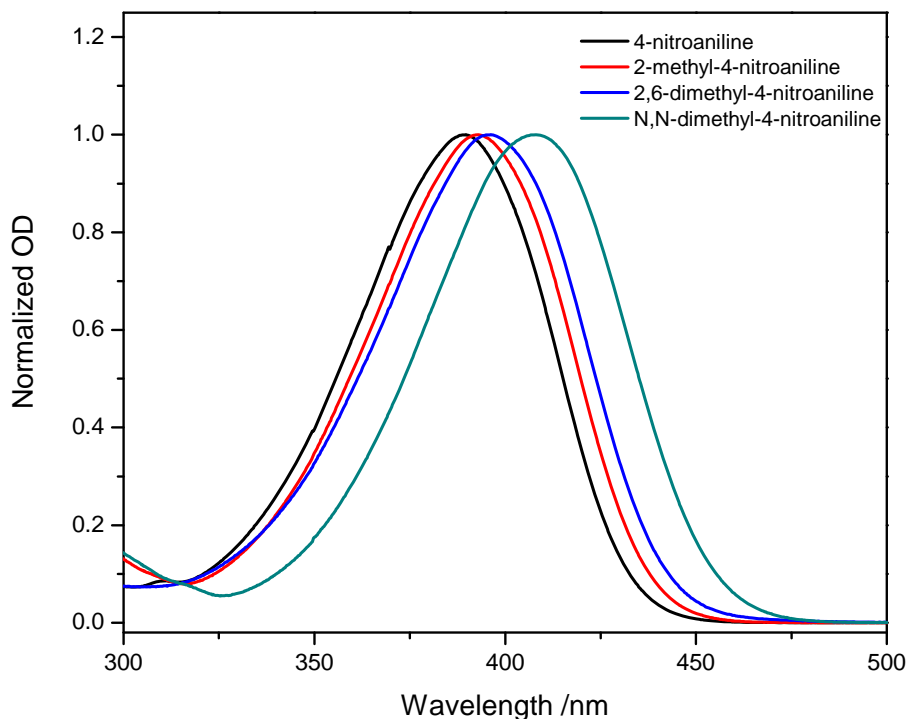


Figure 6 - 3 UV-visible absorption spectra of 4-nitroaniline, 2-methyl-4-nitroaniline, 2, 6-dimethyl-4-nitroaniline and N, N-dimethyl-4-nitroaniline dissolved in dimethylsulfoxide.

Figure 6-4 shows the Stokes resonance Raman spectra of PNA, 2-MPNA, 2, 6-DMPNA and NNDMPNA dissolved in DMSO, obtained with 403, 410.5, 410.35 and 403.5 nm laser excitation and normalized to the intense NO_2 symmetric stretching vibration at about 1310 cm^{-1} . The solvent vibrational bands at 676 cm^{-1} and 706 cm^{-1} are marked with *. The Raman vibrational features upon N-methyl substitution did not change except for a very small shift in some of the Raman peaks; the Raman spectra of PNA and NNDMPNA look very similar to each other. Methylation of the phenyl ring introduces some changes to the Raman spectrum. The ν_{19} (Ph-1) vibration seen at 860 cm^{-1} in PNA is shifted to 934 and 947 cm^{-1} respectively in 2-MPNA and 2, 6-DMPNA.

Two additional low frequency vibrations appear upon methyl substitution on the phenyl ring at 771 and 815 cm^{-1} for 2-MPNA and at 736 and 808 cm^{-1} for 2, 6-DMPNA. The NO_2 symmetric stretching vibration seen at 1310 cm^{-1} in PNA, has a shoulder on the low frequency side in case of 2-MPNA and 2,6-DMPNA.

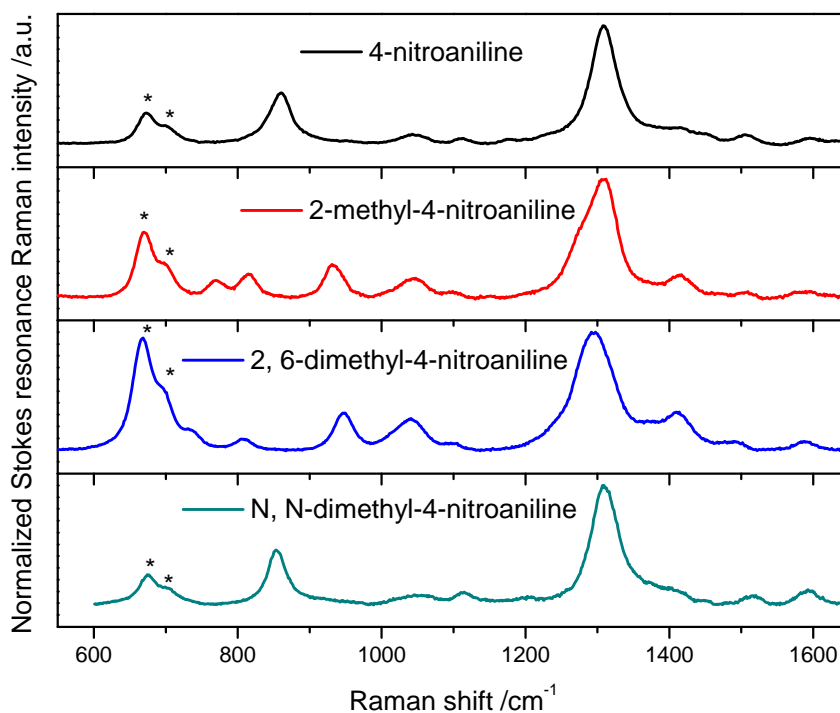


Figure 6 - 4 Stokes Resonance Raman spectra 4-nitroaniline, 2-methyl-4-nitroaniline , 2, 6-dimethyl-4-nitroaniline and N, N-dimethyl-4-nitroaniline in DMSO, obtained with 403, 410.5, 410.35 and 403.5 nm excitation respectively, normalized to the intense NO_2 symmetric stretching vibration at about 1310 cm^{-1} . The DMSO solvent bands are marked with *.

A few selected vibrational modes from the resonance Raman spectra or compared to the computational results along with an approximate normal mode description is presented in Table 6-1.

Compound	Experiment ^a	Calculation ^b B3LYP 6-31G (2d, p)	Assignment & Approximate description ^c
2-MPNA	771	762	ν_{18}
	-	766	ν_{19} , NO ₂ wagging
	815	811	ν_{20}
	934	929	ν_{23} , Ph-1, Ph-NO ₂ , δ_s (NO ₂), Ph-CH ₃ ,
	1280	1300	ν_{32} , Ph-NH ₂
	1310	1339	ν_{33} , Ph-NO ₂ , ν_s (NO ₂)
	1507	1501	ν_{39} , Ph-19a
	-	1534	ν_{40} , ν_{as} (NO ₂)
2, 6 – DMPNA	743	728	ν_{20}
	-	765	ν_{22} , NO ₂ wagging
	808	805	ν_{23} ,
	947	947	ν_{27} , Ph-1, Ph-NO ₂ , δ_s (NO ₂)
	1284	1300	ν_{36} , Ph-NH ₂
	1307	1334	ν_{37} , Ph-NO ₂ , ν_s (NO ₂)
	1492	1487	ν_{46} , Ph-19a
	-	1534	ν_{47} , ν_{as} (NO ₂)
NNDMPNA	-	765	ν_{20} , NO ₂ wagging
	855	849	ν_{23} , Ph-1, Ph-NO ₂ , δ_s (NO ₂)
	1310	1330	ν_{37} , Ph-NO ₂ , Ph-N(CH ₃) ₂ , ν_s (NO ₂)
	1516	1497	ν_{46} , Ph-19a
	-	1520	ν_{47} , ν_{as} (NO ₂)
PNA	-	765	ν_{15} , NO ₂ wagging
	860	857	ν_{19} , Ph-1, Ph-NO ₂ , δ_s (NO ₂)
	-	1301	ν_{27} , Ph-NH ₂
	1310	1342	ν_{29} , Ph-NO ₂ , ν_s (NO ₂)
	1512	1506	ν_{32} , Ph-19a
	-	1532	ν_{33} , ν_{as} (NO ₂)

Table 6 - 1 Selected experimental and calculated vibrational frequencies (in cm⁻¹).

^aExperimental data in DMSO obtained with 403 nm (PNA), 403.5 nm (NNDMPNA), 410.5 nm (2-MPNA), 410.35 nm (2, 6-DMPNA).

^bScaling factor 0.98; ^cAssignment and Mode descriptions according to Varsanyi⁴⁹ and Kozich *et al*¹⁵,

³³.

An out of plane motion assigned to NO₂ wagging is present in all the three compounds including PNA at 765 cm⁻¹. A mode due to NO₂ in plane deformation, Ph-

NO₂ stretch and due to the phenyl ring motion is present at about 855 cm⁻¹ both in PNA and NNDMPNA, and is shifted to 929 cm⁻¹ in 2-MPNA and 947 cm⁻¹ in 2, 6-DMPNA. A mode primarily due to NO₂ symmetric stretch and Ph-NO₂ stretch is present at 1342, 1330, 1339 and 1334 cm⁻¹ and the corresponding NO₂ asymmetric stretch motion is found at 1532, 1520, 1534 and 1534 cm⁻¹ in PNA, NNDMPNA, 2-MPNA and 2, 6-DMPNA respectively. A vibrational mode primarily due to the phenyl ring motion is present at about 1487-1506 in all the compounds. Two new vibrations, at 762 and 811 cm⁻¹ for 2-MPNA and 728 and 805 cm⁻¹ for 2, 6-DMPNA are also due to phenyl ring motion.

N, N-dimethyl-4-nitroaniline (NNDMPNA):

Typical time resolved anti-Stokes resonance Raman spectra (single color 403.5 nm pump-probe) of NNDMPNA in DMSO are presented in Figure 6-5. The time resolved spectra at different time delays between the pump and probe beams are obtained by subtracting the pump only and probe only contributions from the pump-probe spectra at the respective time delays, so they represent the spectral features of the transient excited species only. At zero time delay corresponding to the photoexcitation event, the transient Raman spectrum is flat with no detectable vibrational signatures. With increase in time delay between the photoexcitation and probe, two strong vibrational bands around 1300 cm⁻¹ and 850 cm⁻¹ and a weak band at about 1490 cm⁻¹ appear that grow and decay in intensity resulting in a flat featureless transient spectrum by 30 ps. The 855 cm⁻¹ band is more intense than that at 1307 cm⁻¹ in the anti-Stokes transient spectrum, in contrast to the relative intensities in the Stokes spectrum. The transient vibrational bands at earlier

times are broad and red-shifted relative to the corresponding Stokes Raman bands and evolve in time eventually to approach the steady state ground vibrational state values.

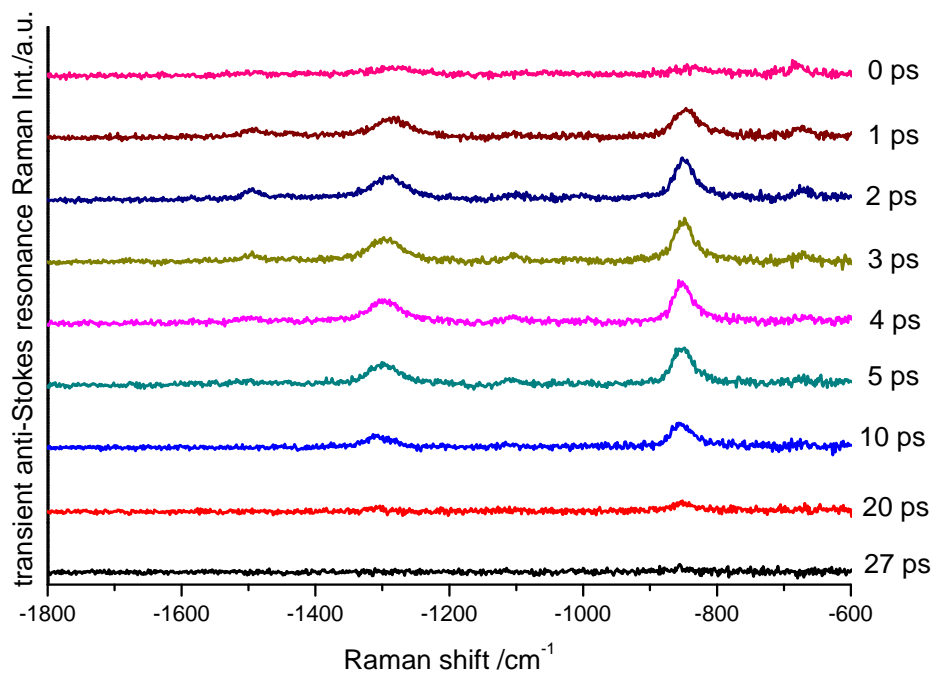


Figure 6 - 5 Representative set of time-resolved anti-Stokes resonance Raman spectra of NNDMPNA in DMSO obtained using pump and probe beams at 403.5 nm. Transient spectra were generated by subtracting the pump-probe spectrum at $\Delta t = -103$ ps from the pump-probe spectra at each time delay. The background in the transient Raman spectra was removed using Origin 7.5 TM baseline routine.

The transient spectra are fit with Lorentzian peak shapes to generate kinetic information of the integrated intensity and the corresponding kinetic traces are shown in Figure 6-6.

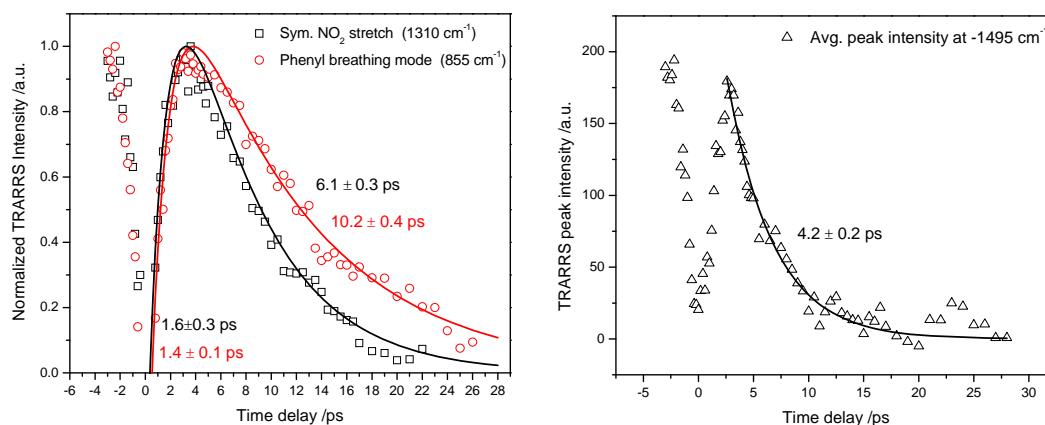


Figure 6 - 6 Kinetic analysis of time-resolved anti-Stokes resonance Raman spectra of NNDMPNA dissolved in DMSO. Squares and circles represent the experimental integrated intensity, triangles represent the average peak intensity at -1495 cm^{-1} and lines represent the exponential curve-fits at positive time delay. The decay only portion of the 1495 cm^{-1} band is fit using $A_1 \exp^{-t/\tau_1}$; the rise and decay kinetics of 1310 and 855 cm^{-1} bands are fit using $A_1 \exp^{-t/\tau_1} + A_2 \exp^{-t/\tau_2}$.

The results of fitting these integrated intensity vs time data after $\Delta t=0$ ps to a bi-exponential function are also presented in Figure 6-6. Within the nonlinear fit error, both the bands exhibit a similar rise time of ~ 1.5 ps. The rate of decay of the 862 cm^{-1} mode is significantly slower than that of the 1310 cm^{-1} band. Accurate Lorentzian peak fits of the weak transient Raman band at $\sim 1500\text{ cm}^{-1}$ were not available; hence the integrated intensity and spectral evolution kinetics are not presented. Instead, the average peak intensity at the peak maximum of 1495 cm^{-1} is plotted as a function of time delay. The transient peak intensity vs time data after $\Delta t=0$ ps was fit to a single exponential decay function of 4.2 ± 0.2 ps time constant.

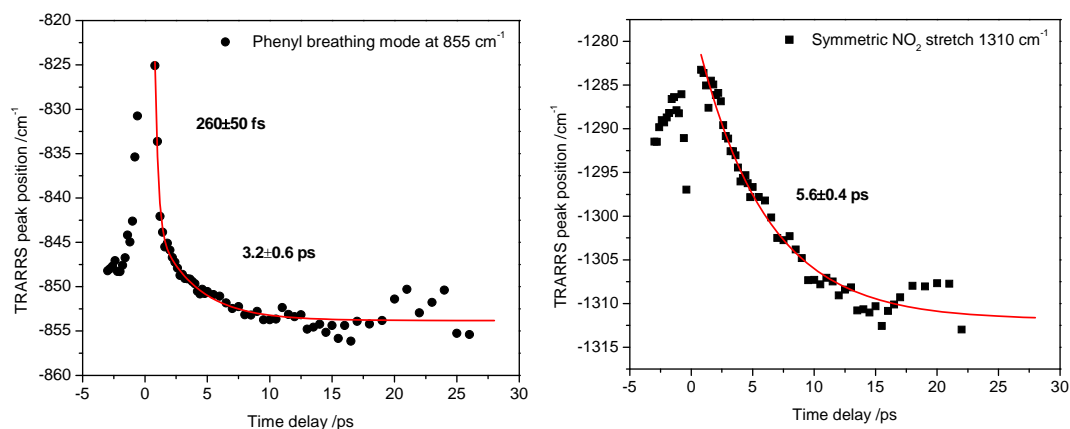


Figure 6 - 7 Kinetic analysis of the peak position shifts of anti-Stokes Raman transients subsequent to photoexcitation at 403.5 nm of NNDMPNA in DMSO. Peak positions were determined by nonlinear fitting of the transients with Lorentzian peak shapes. The lines represent the exponential fits to the peak-position data at positive time delay. The 855 cm^{-1} band is fit using a function of the form $y=y_0+A_1 \exp^{-t/\tau_1}+A_2 \exp^{-t/\tau_2}$; $y_0=-853.82\pm 0.28 \text{ cm}^{-1}$. The 1310 cm^{-1} band is fit using a function of the form $y=y_0+A_1 \exp^{-t/\tau_1}$; $y_0=-1311.85\pm 0.67 \text{ cm}^{-1}$. The value of y_0 corresponds to the equilibrium vibrational frequency of the corresponding mode.

Analysis of the time-dependent peak position shifts is presented in Figure 6-7. The peak position shift of the 855 cm^{-1} band is well fit by a bi-exponential decay function with time constants of $0.3 \pm 0.1 \text{ ps}$ and $3.2 \pm 0.6 \text{ ps}$. The 1310 cm^{-1} band peak position shift is fit using a single exponential decay function of time constant $5.6 \pm 0.4 \text{ ps}$. The lifetime of 855 cm^{-1} band obtained from peak-shift kinetics is significantly smaller than the one obtained from the intensity decay kinetics similar to the case of PNA.

2-methyl-4-nitro aniline (2-MPNA):

Typical time resolved anti-Stokes resonance Raman spectra (single color 410.5 nm pump-probe) of 2-MPNA in DMSO obtained by subtracting the pump only and probe only contributions from the pump-probe spectra are presented in Figure 6-8.

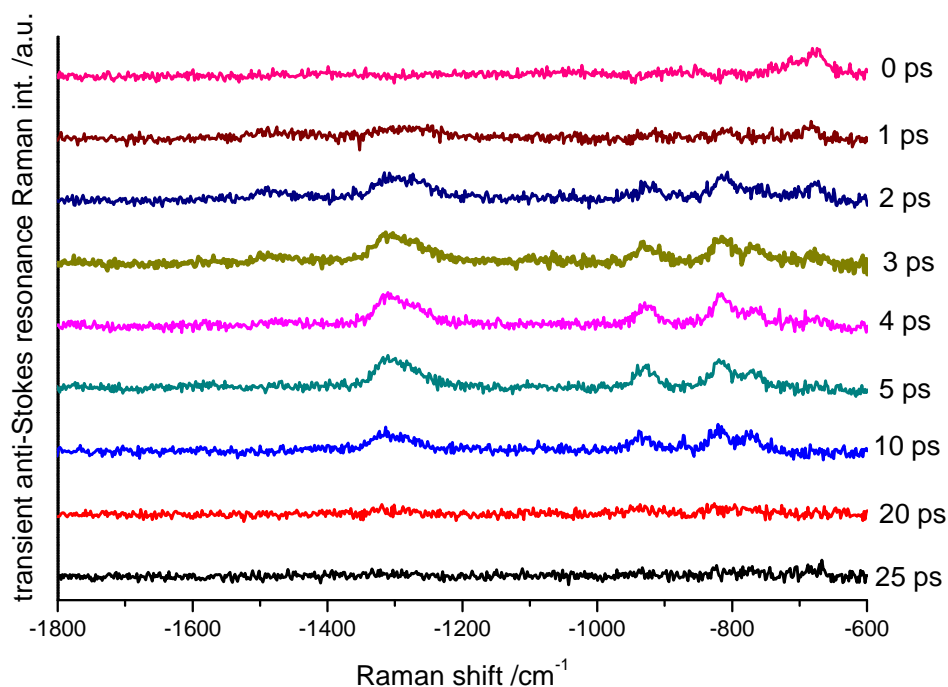


Figure 6 - 8 Representative set of time-resolved anti-Stokes resonance Raman spectra of 2-MPNA in DMSO obtained using pump and probe beams at 410.5 nm. Transient spectra were generated by subtracting the pump-probe spectrum at $\Delta t = 60$ ps from the pump-probe spectra at each time delay. The background in the transient Raman spectra was removed using Origin 7.5 TM baseline routine.

Similar to NNDMPNA, the transient spectra are flat and featureless at $\Delta t = 0$ ps, transient anti-Stokes vibrational bands grow and decay in intensity as time progresses eventually leading to a flat transient spectrum by 25 ps. The intensity of other bands is relatively weak compared to that of 1310 cm^{-1} band. The band observed at about 860 cm^{-1} in the case of PNA and NNDMPNA is shifted to 933 cm^{-1} , transient feature at about 1500 cm^{-1} is only weakly visible and two new transient bands at 815 cm^{-1} and 768 cm^{-1} are observed. The central peak positions are initially broad and red-shifted and approach the steady state Stokes spectral values as time progresses. All the bands grow and decay

in intensity within 25 ps of photoexcitation by the pump pulse. The transient spectrum at zero time delay shows some intensity in the solvent band.

The transient spectra are fit with Lorentzian peak shapes. However, only the intense 1300 band resulted in good fits with high accuracy. The kinetics of the integrated peak intensity and central peak position of this vibrational mode are presented in Figure 6-8. It exhibits a rise time of 1.5 ± 0.2 ps similar to NNDMPNA, but the lifetime is significantly longer (9.3 ± 0.6 ps) compared to that of PNA (5.2 ps) or NNDMPNA (6.1 ps). The central peak position evolves exponentially with a time constant of 2.9 ± 0.4 ps.

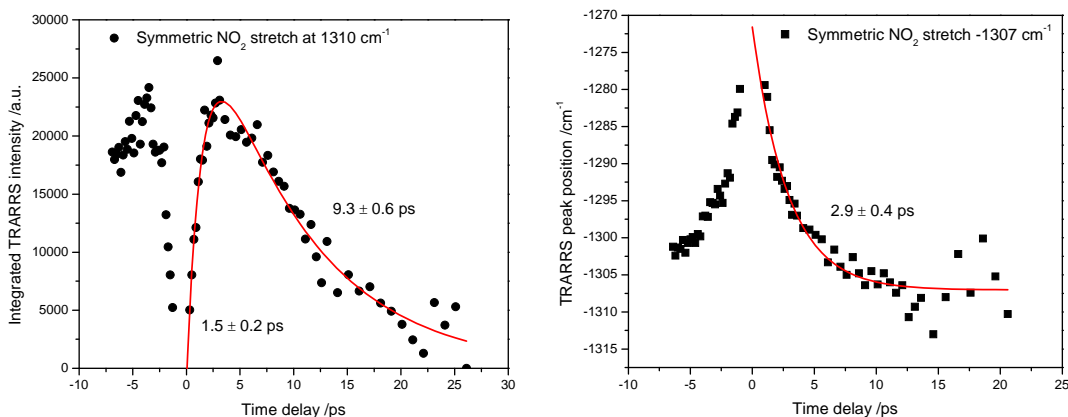


Figure 6 - 9 Kinetic analysis of the transient anti-Stokes Raman mode of 2-MPNA in DMSO at 1307 cm^{-1} . Circles represent the experimental integrated intensity, squares represent the central peak position and lines represent the exponential curve-fits at positive time delay. The rise and decay kinetics of 1310 cm^{-1} band intensity is fit using $A_1 \exp^{-t/\tau_1} + A_2 \exp^{-t/\tau_2}$. The peak position shift is fit using a function of the form $y = y_0 + A_1 \exp^{-t/\tau}$; $y_0 = -1307.04 \pm 0.66 \text{ cm}^{-1}$. The value of y_0 corresponds to the equilibrium vibrational frequency of the corresponding mode.

The rise and decay kinetics of the rest of the anti-Stokes bands are obtained by plotting the average peak intensity as a function of time delay as shown in the Figure 6-10. The kinetics of the 1310 cm^{-1} band obtained using this method is also included for an

easy comparison of the errors involved in the two different approaches. The integrated peak intensity is insensitive to spectral evolution resulting from red-shifting and spectral narrowing of the individual vibrational bands, whereas spectral evolution dynamics are convolved in the kinetic information obtained from average peak intensity. All the vibrational modes exhibit similar rise and decay kinetics with approximately 3 ps rise time and 9 ps decay time.

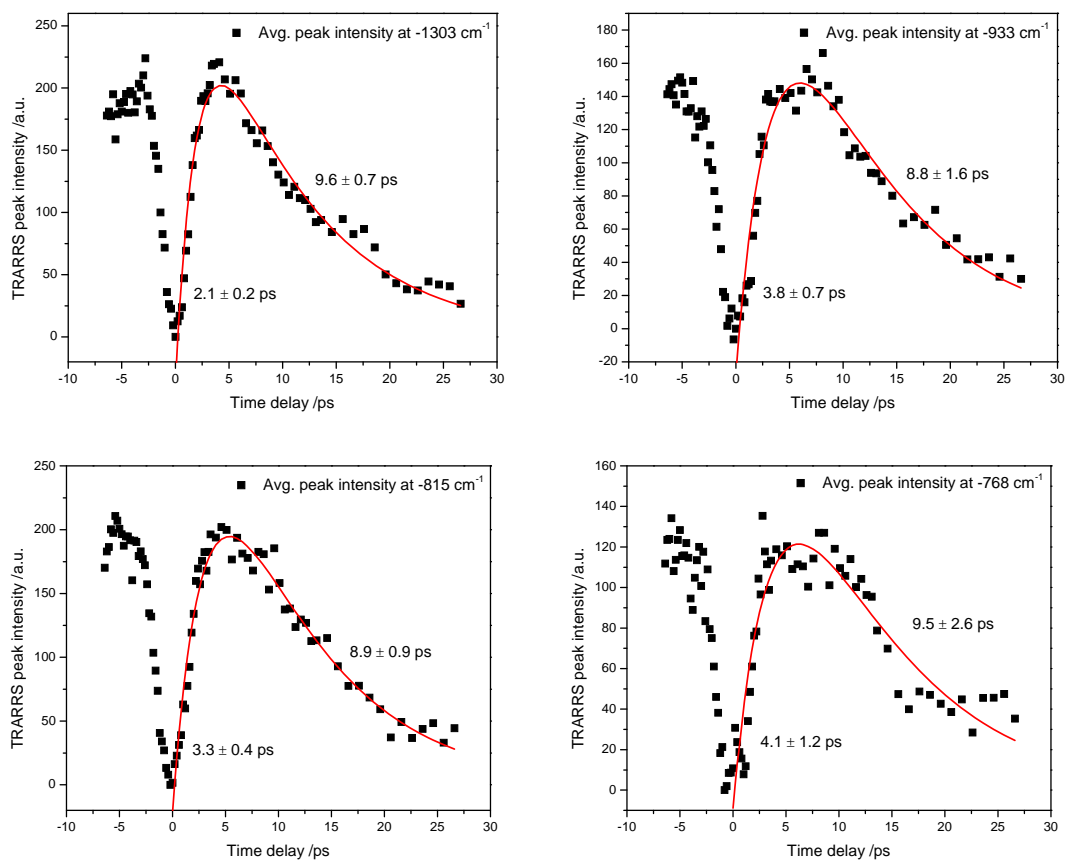


Figure 6 - 10 Kinetic analysis of time-resolved anti-Stokes resonance Raman spectra of 2-MPNA dissolved in DMSO. Symbols represent the average peak intensity of the individual vibrational modes seen in the transient spectra and lines represent the exponential curve-fits at positive time delay. The average peak intensity at 1303 cm^{-1} was obtained by averaging the intensity at $1301, 1302, 1303, 1304$ and 1305 cm^{-1} . The average intensity of other modes was also obtained similarly. The rise

and decay kinetics at average peak positions of 1303, 933, 815 and 768 cm^{-1} are fit using a biexponential function of the form $A_1 \exp^{-t/\tau_1} + A_2 \exp^{-t/\tau_2}$.

2, 6-dimethyl-4-nitroaniline (2, 6-DMPNA):

Transient anti-Stokes resonance Raman spectra of 2, 6-DMPNA dissolved in DMSO obtained with 410.35 nm pump-probe method are shown in the Figure 6-11. Five different vibrational modes at 1492, 1307, 947, 808 and 743 cm^{-1} are seen to gain intensity upon internal conversion and decay via vibrational relaxation resulting in a flat featureless transient Raman spectrum by 20 ps after photoexcitation event. The intensity of the 808 and 743 cm^{-1} bands are significantly lower than that of the other three modes. The transient spectrum at zero time delay shows some intensity in the solvent band.

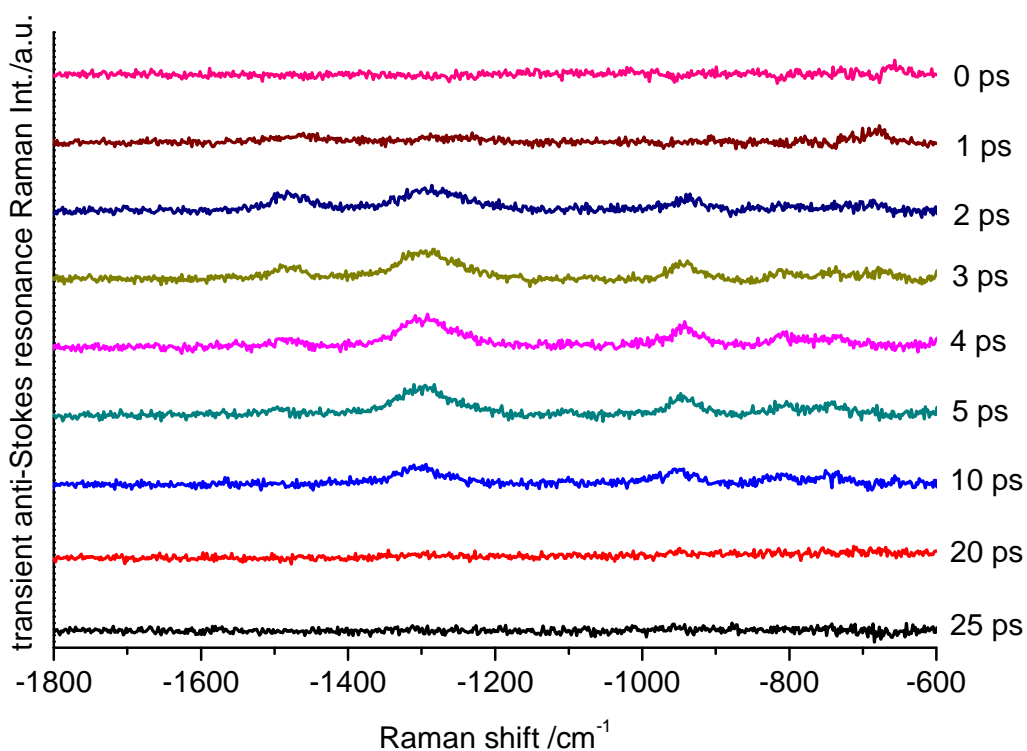


Figure 6 - 11 Representative set of time-resolved anti-Stokes resonance Raman spectra of 2, 6-DMPNA in DMSO obtained using pump and probe beams at 410.35 nm. Transient spectra were

generated by subtracting the pump-probe spectrum at $\Delta t = 64$ ps from the pump-probe spectra at each time delay. The background in the transient Raman spectra was removed using Origin 7.5 TM baseline routine.

The transient spectra are fit with Lorentzian peak shapes, but only the 1307 cm^{-1} band gave reliable fits with high accuracy. The integrated intensity and the central peak position are plotted as a function of the time delay between the pump and probe pulses to get the kinetic information as shown in Figure 6-12. The kinetic profile of the integrated intensity was fit to a bi-exponential function comprising of an exponential rise (1.9 ± 0.2 ps) and an exponential decay (5.7 ± 0.5 ps). The kinetic profile of the peak position shift was fit to a bi-exponential decay function of time constants, 0.3 ± 0.1 ps and 3.6 ± 0.5 ps. The peak shift kinetics are quite fast compared to the integrated intensity decay lifetime.

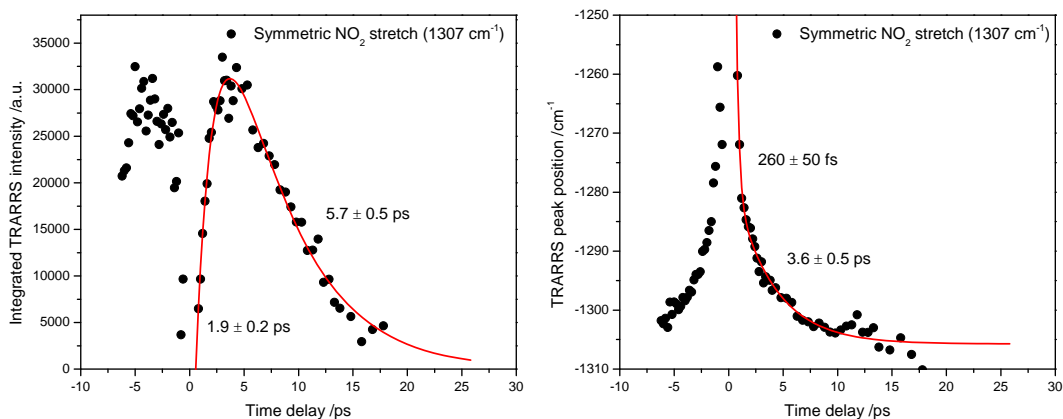


Figure 6 - 12 Kinetic analysis of the transient anti-Stokes Raman mode of 2, 6-DMPNA in DMSO at 1307 cm^{-1} . Symbols represent the experimental integrated intensity and central peak position and lines represent the corresponding exponential curve-fits at positive time delay. The rise and decay kinetics of 1310 cm^{-1} band intensity is fit using $A_1 \exp^{-t/\tau_1} + A_2 \exp^{-t/\tau_2}$. The peak position shift is fit using a function of the form $y = y_0 + A_1 \exp^{-t/\tau_1}$; $y_0 = -1305.7 \pm 0.7\text{ cm}^{-1}$. The value of y_0 corresponds to the equilibrium vibrational frequency of the corresponding mode.

The average peak intensity is plotted as a function of time delay for all the other modes including the 1300 band for comparison in Figure 6-13. The 1480 band exhibits the fastest rise and decay kinetics among all the transient vibrational modes populated during internal conversion. The rise time of 0.3 ps is comparable to the internal conversion lifetimes reported for PNA and NNDMPNA. All the other modes exhibit similar rise time of approximately 2 ps. The decay of 945 cm^{-1} mode is slower than the 810 cm^{-1} mode by one ps. The lifetime of the 1300 mode obtained from the average peak intensity is comparable to that obtained from the integrated intensity.

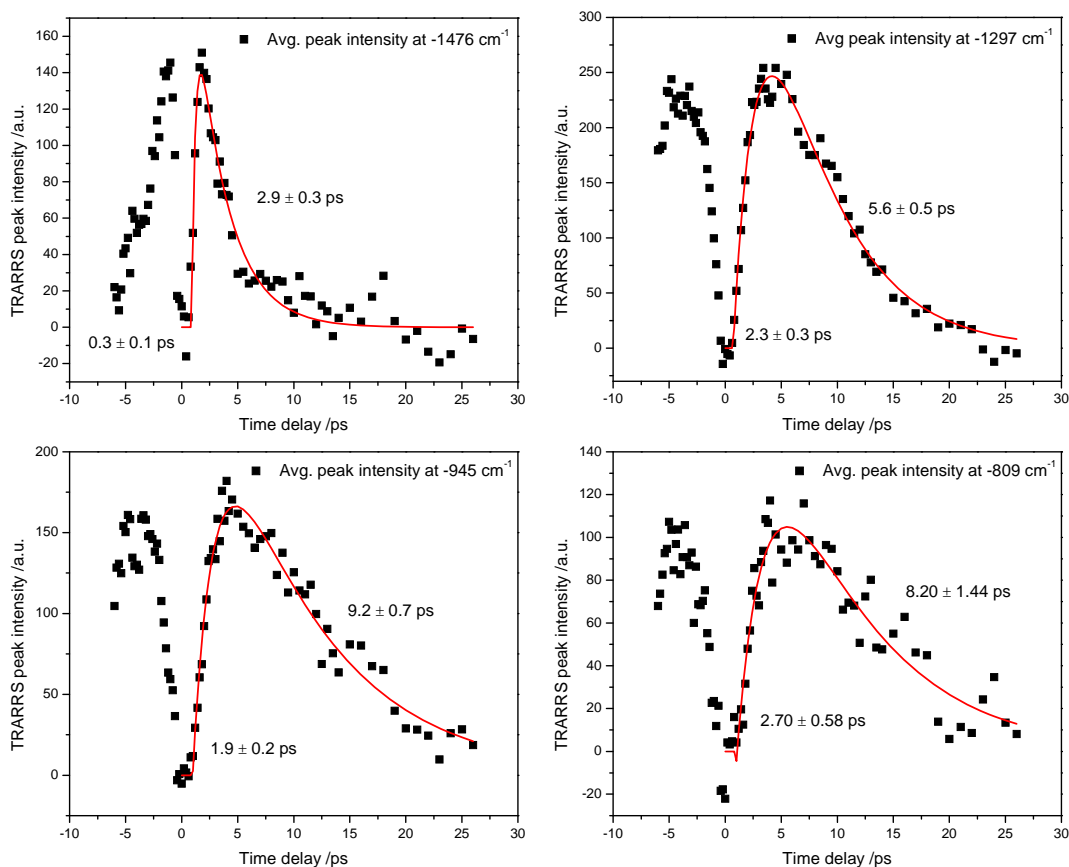


Figure 6 - 13 Kinetic analysis of time-resolved anti-Stokes resonance Raman spectra of 2-MPNA dissolved in DMSO. Symbols represent the average peak intensity of the individual vibrational modes seen in the transient spectra and lines represent the exponential curve-fits at positive time

delay. The average peak intensity at 1476 cm^{-1} was obtained by averaging the intensity at 1474, 1475, 1476, 1477 and 1478 cm^{-1} . The average intensity of other modes was also obtained in the same way. The rise and decay kinetics at average peak positions of 1476, 1297, 945 and 809 cm^{-1} are fit using a bi-exponential function of the form $A_1 \exp^{-t/\tau_1} + A_2 \exp^{-t/\tau_2}$.

6.4 DISCUSSION

Photoexcitation of a solute molecule present in a solvent pool generates a nonthermal vibrational energy distribution on the excited electronic state that is determined, to first order, by the Franck-Condon factors for the various vibrational degrees of freedom. This initial distribution evolves rapidly due to dephasing, intramolecular and intermolecular vibrational relaxation (IVR and VER) and conformational relaxation of both the molecule and the surrounding solvent. The excited electronic state relaxes further either by radiatively emitting the excess energy as fluorescence or phosphorescence or by nonradiative processes such as internal conversion and intersystem crossing. The charge transfer excited electronic state (S_1) of PNA is extremely short lived with little or no fluorescence as indicated by the fs time-resolved absorption experiments. The S_1 state relaxes on a time scale competitive to the dynamic processes occurring on S_1 surface via IC or ISC, depending on the solvent polarity. The efficiency of ISC is negligibly small compared to that of IC in polar solvents suggesting that IC is the only relaxation channel from S_1 state of PNA in polar solvents.

Similar to the photoexcitation event, the IC process also deposits an excess of energy in the molecular degrees of freedom on the ground electronic state, the specifics of which also may not be mode-neutral. It is often assumed that the vibrational degrees of freedom with large Franck-Condon factors which couple the two electronic states through

vibronic coupling will be the main accepting modes of this excess energy⁵⁰. However, in PNA with IC rates competing with the dynamic processes on the excited S₁ surface, a conical intersection^{51, 52} between S₁ and S₀ states is highly possible. In such a scenario, the vibrational modes that tune the relaxation of the molecule (also known as the tuning modes) towards the conical intersection, the location of which may or may not be in the Franck-Condon region, determine the initial mode-specific or mode-selective vibrational energy distribution on the ground electronic state. Then the vibrational modes of appropriate symmetry act as the coupling and primary accepting modes of the excess energy in internal conversion¹⁵.

Semi-empirical ab-initio calculations (SAM1) by Kovalenko et al.^{12, 29} confirmed the presence of a conical intersection between S₁ and S₀ states of PNA corresponding to an NO₂ group twist angle of 60° of the excited electronic state geometry. Kozich et al.^{15, 33} showed that a vibrational mode at 1510 cm⁻¹, assigned to an overtone or combination band of an out of plane vibration, acts as the main accepting mode following internal conversion of PNA dissolved in DMSO. The totally symmetric modes with high Franck-Condon factors act as the secondary accepting modes gaining energy via IVR.

Based on the three NNDMPNA, 2-MPNA and 2, 6-DMPNA molecules studied here, methyl group substitution on amino nitrogen increases the lifetimes of the individual vibrational modes without significantly affecting the overall vibrational dynamics, i.e. the overtone band of the NO₂ wagging mode is always the primary accepting mode and the remaining vibrational modes gain intensity at slightly delayed times acting as the secondary accepting modes, just like in PNA. Methyl group substitution on the phenyl ring at *ortho* position to the amino group opens up new

channels of energy relaxation through two phenyl modes. The experimental lifetimes are summarized in Tables 6-2 and 6-3.

Vibration	PNA ^a		NNDMPNA		2-MPNA		2, 6-DMPNA	
	v/ cm ⁻¹	τ/ ps	v/ cm ⁻¹	τ/ ps	v/ cm ⁻¹	τ/ ps	v/ cm ⁻¹	τ/ ps
Sym NO ₂ stretch	1310	5.2±0.6	1310	6.1±0.3	1310	9.3±0.6	1307	5.7±0.5
Phenyl breathing Ph-1	860	8.1±0.6	855	10.2±0.4	934	8.8±1.6	947	9.2±0.7
NO ₂ wagging overtone	1512	fast, weak	1516	4.2±0.2	1507	fast, weak	1492	2.9±0.3
Unassigned Phenyl ring vibration	-	-	-	-	815	8.9±0.9	808	8.2±1.4
Unassigned Phenyl ring vibration	-	-	-	-	768	9.5±2.6	743	weak

Table 6 - 2 Effect of methyl group substitution on the vibrational energy relaxation lifetimes of PNA^a

^aLifetimes obtained by plotting the transient integrated or average peak intensity as a function of time delay. ^bLifetimes of PNA obtained from Gunaratne et al. *ChemPhysChem* 2005, 6, 1157-63.

Vibration	PNA ^b		NNDMPNA		2-MPNA		2, 6-DMPNA	
	v/ cm ⁻¹	τ/ ps	v/ cm ⁻¹	τ/ ps	v/ cm ⁻¹	τ/ ps	v/ cm ⁻¹	τ/ ps
Sym NO ₂ stretch	1310	4.6±0.7	1310	5.6±0.4	1310	2.9±0.4	1307	0.3±0.1 3.6±0.5
Phenyl breathing Ph-1	860	3.2±0.5 ^b	855	0.3±0.1 3.2±0.6	934	8.8±1.6	947	9.2±0.7

Table 6 - 3 Effect of methyl group substitution on the vibrational energy relaxation lifetimes of PNA^a

^aLifetimes obtained using change in vibrational frequency as a function of the time delay. ^bLifetimes of PNA obtained from Gunaratne et al. *ChemPhysChem* 2005, 6, 1157-63.

The vibrational band that appears at 1512 cm^{-1} for PNA in DMSO, assigned to an overtone of NO_2 wagging mode (ν_{15}), or a combination band of the NO_2 wagging with ν_{14} or a phenyl vibrational mode (ν_{32}) by Kozich et al. , shows up at 1516, 1507 and 1492 cm^{-1} for NNDMPNA, 2-MPNA and 2, 6-DMPNA respectively. In all the three compounds, this vibrational mode exhibits the fastest rise and decay times among all the vibrations that gain intensity during IC from the S_1 state. Only the decay profile of the integrated intensity was fit for NNDMPNA which resulted in a decay life time of 4.2 ± 0.2 ps. In case of 2-MPNA, this mode could not be characterized even using the average peak intensity because of the weak signal and fast kinetics. In case of 2, 6-DMPNA, it has fast rise and decay times of 0.3 ± 0.1 and 2.9 ± 0.3 ps respectively. Methyl substitution does not affect the role of this vibrational motion as the primary accepting mode during IC. The accuracy in assigning this band needs to be improved possibly using isotopic substitution studies. Given the importance of NO_2 group out of plane motion in PNA IC, this is most probably the overtone band of NO_2 wagging or this could as well be due to the NO_2 asymmetric stretching vibration (ν_{33} in case of PNA).

The vibrational frequency of the intense band at 1310 cm^{-1} due to NO_2 symmetric stretch and Ph- NO_2 stretch is not affected upon methyl substitution, but the lifetimes are. The vibrational mode in case of 2-MPNA has a longer intensity decay lifetime of 9.3 ± 0.6 ps compared to that of 6.1 ± 0.3 ps in NNDMPNA and 5.7 ± 0.5 ps in 2, 6-DMPNA. Just like PNA, the lifetime obtained using the vibrational frequency evolution (6.7 ± 0.4 ps) in NNDMPNA, is comparable to that from the intensity kinetics for this mode. But 2-MPNA and 2, 6-DMPNA exhibit complex spectral evolution kinetics different from those obtained using the intensity data. The transient vibrational frequency of the 1310 cm^{-1}

mode approaches the equilibrium value significantly faster (2.9 ± 0.4 ps) than the decay of its intensity (9.3 ± 0.3 ps) in 2-MPNA. The vibrational frequency of this mode in 2, 6-DMPNA exhibits a bi-exponential life time of 0.3 ± 0.1 ps and 3.6 ± 0.5 ps.

The peak shift relaxes faster than the anti-Stokes Raman intensity. This difference can be explained as follows using the analysis by Schrader et al.¹⁶ and Gunaratne et al. For a given vibrational mode, the anti-Stokes Raman signal results only from population in the excited vibrational states and its intensity scales as the vibrational quantum number. As the excited vibrational levels relax, the intensity decreases going to zero finally as all the molecules in that particular mode return to the ground vibrational state. With increase in vibrational quantum number, the vibrational frequency decreases due to diagonal anharmonicity as well as due to anharmonic coupling to other populated vibrational degrees of freedom. So for a vibrational mode well coupled to other degrees of freedom, the two time dependencies differ from each other. If the peak shift results only from diagonal anharmonicity then the two time dependencies will be similar. Since the diagonal anharmonicities are usually smaller than the off-diagonal anharmonicities, the peak shift relaxation is a good indicator of vibrational coupling to other populated modes. Hence, it follows that the methyl substitution on phenyl ring results in population of new modes that couple to the NO₂ symmetric stretching mode contrary to that on the amino nitrogen.

The vibrational band observed at 860 cm^{-1} in steady state Resonance Raman spectra of PNA in DMSO is assigned to a phenyl breathing vibration (ν_{19} in PNA) with contributions from Ph-NO₂ and Ph-NH₂ stretching motions. The vibrational frequency of this mode is shifted to 855 cm^{-1} in NNDMPNA, 934 cm^{-1} in 2-MPNA and 947 cm^{-1} in

2, 6-DMPNA. This is the most intense transient anti-Stokes Raman band in the case of NNDMPNA similar to PNA. The decay lifetime of this phenyl breathing mode observed at 860 cm^{-1} in PNA ($\sim 8.1\text{ ps}$) is similar in all the three compounds with $10.2 \pm 0.4\text{ ps}$ in NNDMPNA, $8.8 \pm 1.6\text{ ps}$ in 2-MPNA and $9.2 \pm 0.7\text{ ps}$ in 2, 6-DMPNA. The peak shift relaxes faster at a bi-exponential rate with lifetimes of 0.3 ± 0.1 and $3.2 \pm 0.7\text{ ps}$ in NNDMPNA. The peak shift evolution could not be characterized for 2-MPNA and 2, 6-DMPNA. The difference in the two time dependencies of NNDMPNA implies that this mode relaxes via coupling to other degrees of freedom.

The transient anti-Stokes Raman spectra of 2-MPNA and 2, 6-DMPNA in DMSO feature population in new vibrational modes at 815 and 771 cm^{-1} in 2-MPNA, and 808 and 743 cm^{-1} in 2,6-DMPNA not present in the case of PNA or NNDMPNA. The lifetime of the first mode is similar in the compounds, $8.9 \pm 0.9\text{ ps}$ and $8.2 \pm 1.4\text{ ps}$ in 2-MPNA and 2, 6-DMPNA respectively. We were able to characterize the second mode only in 2-MPNA with a life time of $9.5 \pm 2.6\text{ ps}$.

6.5 CONCLUSIONS

Ultrafast time-resolved anti-Stokes resonance Raman studies of 2-MPNA, 2, 6-DMPNA and N, N-DMPNA in DMSO have been reported with main focus on the effect of methyl groups on the vibrational dynamics of 4-nitroaniline (PNA). Similar to the case of PNA, a vibrational mode at about 1495 cm^{-1} , most probably due to an out of plane vibrational motion involving NO_2 group acts as the coupling and primary accepting mode during internal conversion of all the three compounds following photoexcitation. This mode exhibits the fastest rise times comparable to the excited electronic state decay time

and decays faster than the other modes observed in the resonance Raman studies. Based on the kinetics of the NO₂ wagging overtone band at about $\sim 1495\text{ cm}^{-1}$, no significant impact of methyl group substitution was observed on the electronic dynamics, but the vibrational dynamics are affected to a large extent. The N-methyl substitution was found to increase the cooling lifetimes of the vibrations possibly due to reduced H-bonding ability. Methyl-group substitution on the phenyl ring at *ortho* position to the amino group resulted in population of two new low frequency vibrational modes. Peak-shift and intensity decay kinetics resulted in different lifetimes for the 1310 cm^{-1} band due to symmetric NO₂ stretching in 2-MPNA and 2, 6-DMPNA indicating the dominant off-diagonal coupling of this mode to other populated low frequency motions. It is interesting to note that in case of PNA and NNDMPNA the difference in lifetimes is more prominent for the mode at about 860 cm^{-1} due to phenyl breathing motion and not for the symmetric NO₂ stretching band. These studies again confirm the importance of NO₂ group motion, and the role of its coupling to the phenyl ring vibrations in the vibrational dynamics of para-nitroaniline and its derivatives.

6.6 REFERENCES

1. Wortmann, R.; Kraemer, P.; Glania, C.; Lebus, S.; Detzer, N., Deviations from Kleinman symmetry of the second-order polarizability tensor in molecules with low-lying perpendicular electronic bands. *Chemical Physics* 1993, 173, (1), 99-108.
2. Davydov, B. L.; Derkacheva, L. D.; Dunina, V. V.; Zhabotinskii, M. E.; Zolin, V. F.; Koreneva, L. G.; Samokhina, M. A., Correlation of charge transfer to laser second harmonics generation. *Pis'ma v Zhurnal Eksperimental'noi i Teoreticheskoi Fiziki* 1970, 12, (1), 24-6.

3. Hiberty, P. C.; Ohanessian, G., Valence-bond description of conjugated molecules. 3. The through-resonance concept in para-substituted nitrobenzenes. *Journal of the American Chemical Society* 1984, 106, (23), 6963-8.
4. Karna, S. P.; Prasad, P. N.; Dupuis, M., Nonlinear optical properties of p-nitroaniline: An ab initio time-dependent coupled perturbed Hartree-Fock study. *Journal of Chemical Physics* 1991, 94, (2), 1171-81.
5. Mikkelsen, K.; Luo, Y.; Agren, H.; Joergensen, P., Solvent induced polarizabilities and hyperpolarizabilities of para-nitroaniline studied by reaction field linear response theory. *Journal of Chemical Physics* 1994, 100, (11), 8240-50.
6. Champagne, B., Vibrational polarizability and hyperpolarizability of p-nitroaniline. *Chemical Physics Letters* 1996, 261, (1,2), 57-65.
7. Moran, A. M.; Myers Kelley, A.; Tretiak, S., Excited state molecular dynamics simulations of nonlinear push-pull chromophores. *Chemical Physics Letters* 2002, 367, (3,4), 293-307.
8. Schmid, E. D.; Moschallski, M.; Peticolas, W. L., Solvent effects on the absorption and Raman spectra of aromatic nitrocompounds. Part 1. Calculation of preresonance Raman intensities. *Journal of Physical Chemistry* 1986, 90, (11), 2340-6.
9. Schuddeboom, W.; Warman, J. M.; Biemans, H. A. M.; Meijer, E. W., Dipolar Triplet States of p-Nitroaniline and N-Alkyl Derivatives with One-, Two-, and Three-Fold Symmetry. *Journal of Physical Chemistry* 1996, 100, (30), 12369-12373.
10. Mohanalingam, K.; Hamaguchi, H.-o., Raman spectroscopic study on the two distinct solvated structures of p-nitroaniline in acetonitrile. *Chemistry Letters* 1997, (6), 537-538.

11. Thomsen, C. L.; Thogersen, J.; Keiding, S. R., Ultrafast Charge-Transfer Dynamics: Studies of p-Nitroaniline in Water and Dioxane. *Journal of Physical Chemistry A* 1998, 102, (7), 1062-1067.
12. Kovalenko, S. A.; Schanz, R.; Farztdinov, V. M.; Hennig, H.; Ernsting, N. P., Femtosecond relaxation of photoexcited para-nitroaniline: solvation, charge transfer, internal conversion and cooling. *Chemical Physics Letters* 2000, 323, (3,4), 312-322.
13. Moran, A. M.; Kelley, A. M., Solvent effects on ground and excited electronic state structures of p-nitroaniline. *Journal of Chemical Physics* 2001, 115, (2), 912-924.
14. An, Q.; Gilch, P., Cooling of hot para-nitroaniline probed by non-resonant Raman scattering. *Chemical Physics Letters* 2002, 363, (3,4), 397-403.
15. Kozich, V.; Werncke, W.; Vodchits, A. I.; Dreyer, J., Ultrafast excitation of out-of-plane vibrations and vibrational energy redistribution after internal conversion of 4-nitroaniline. *Journal of Chemical Physics* 2003, 118, (4), 1808-1814.
16. Schrader, T.; Sieg, A.; Koller, F.; Schreier, W.; An, Q.; Zinth, W.; Gilch, P., Vibrational relaxation following ultrafast internal conversion: comparing IR and Raman probing. *Chemical Physics Letters* 2004, 392, (4-6), 358-364.
17. Gunaratne, T.; Challa, J. R.; Simpson, M. C., Energy flow in push-pull chromophores: Vibrational dynamics in para-Nitroaniline. *ChemPhysChem* 2005, 6, (6), 1157-1163.
18. Kimura, Y.; Fukuda, M.; Kajimoto, O.; Terazima, M., Study on the vibrational energy relaxation of p-nitroaniline, N,N-dimethyl-p-nitroaniline, and azulene by the transient grating method. *Journal of Chemical Physics* 2006, 125, (19), 194516/1-194516/12.

19. Fujisawa, T.; Terazima, M.; Kimura, Y., Excitation wavelength dependence of the Raman-Stokes shift of N,N-dimethyl-p-nitroaniline. *Journal of Chemical Physics* 2006, 124, (18), 184503/1-184503/9.
20. Yamaguchi, T.; Kimura, Y.; Hirota, N., Solvent and solvent density effects on the spectral shifts and the bandwidths of the absorption and the resonance Raman spectra of phenol blue. *Journal of Physical Chemistry A* 1997, 101, (48), 9050-9060.
21. Yamaguchi, T.; Kimura, Y.; Hirota, N., The excitation energy dependence of the Raman-Stokes shift: The resonance Raman spectra of phenol blue in methanol. *Journal of Chemical Physics* 1997, 107, (11), 4436-4438.
22. Yamaguchi, T.; Kimura, Y.; Hirota, N., Solvation state selective excitation in resonance Raman spectroscopy. I. Experimental study on the C:N and the C:O stretching modes of phenol blue. *Journal of Chemical Physics* 1998, 109, (20), 9075-9083.
23. Gould, I. R.; Young, R. H.; Mueller, L. J.; Albrecht, A. C.; Farid, S., Electronic Structures of Exciplexes and Excited Charge-Transfer Complexes. *Journal of the American Chemical Society* 1994, 116, (18), 8188-99.
24. Gould, I. R.; Young, R. H.; Mueller, L. J.; Albrecht, A. C.; Farid, S., Electronic Coupling Matrix Elements in Acceptor-Donor Excited States and the Effect of Charge-Transfer Character on Their Radiative Rate Constants. *Journal of the American Chemical Society* 1994, 116, (7), 3147-8.
25. Painelli, A., Vibronic contribution to static NLO properties: exact results for the DA dimer. *Chemical Physics Letters* 1998, 285, (5,6), 352-358.
26. Painelli, A., Amplification of NLO responses: vibronic and solvent effects in push-pull polyenes. *Chemical Physics* 1999, 245, (1-3), 185-197.

27. Painelli, A.; Terenziani, F., A non-perturbative approach to solvatochromic shifts of push-pull chromophores. *Chemical Physics Letters* 1999, 312, (2-4), 211-220.
28. Painelli, A.; Terenziani, F., Optical Spectra of Push-Pull Chromophores in Solution: A Simple Model. *Journal of Physical Chemistry A* 2000, 104, (47), 11041-11048.
29. Farztdinov, V. M.; Schanz, R.; Kovalenko, S. A.; Ernsting, N. P., Relaxation of Optically Excited p-Nitroaniline: Semiempirical Quantum-Chemical Calculations Compared to Femtosecond Experimental Results. *Journal of Physical Chemistry A* 2000, 104, (49), 11486-11496.
30. Grabowski, Z. R.; Dobkowski, J., Twisted intramolecular charge transfer (TICT) excited states: energy and molecular structure. *Pure and Applied Chemistry* 1983, 55, (2), 245-52.
31. Jamorski Jodicke, C.; Luthi Hans, P., Time-dependent density functional theory (TDDFT) study of the excited charge-transfer state formation of a series of aromatic donor-acceptor systems. *Journal of the American Chemical Society* 2003, 125, (1), 252-64.
32. Jamorski, C. J.; Luthi, H.-P., Rational classification of a series of aromatic donor-acceptor systems within the twisting intramolecular charge transfer model, a time-dependent density-functional theory investigation. *Journal of Chemical Physics* 2003, 119, (24), 12852-12865.
33. Kozich, V.; Werncke, W.; Dreyer, J.; Brzezinka, K. W.; Rini, M.; Kummrow, A.; Elsaesser, T., Vibrational excitation and energy redistribution after ultrafast internal conversion in 4-nitroaniline. *Journal of Chemical Physics* 2002, 117, (2), 719-726.

34. Kovalenko, S. A.; Schanz, R.; Hennig, H.; Ernsting, N. P., Cooling dynamics of an optically excited molecular probe in solution from femtosecond broadband transient absorption spectroscopy. *Journal of Chemical Physics* 2001, 115, (7), 3256-3273.
35. Gunaratne, T. C.; Simpson, M. C. In *Electronic and vibronic energy flow in molecular assemblies: Current research and future directions utilizing transient absorption and transient Raman spectroscopic methods*, 2005; 2005; pp AEI-142.
36. Camerin, M.; Rello, S.; Villanueva, A.; Ping, X.; Kenney, M. E.; Rodgers, M. A. J.; Jori, G., Photothermal sensitisation as a novel therapeutic approach for tumours: Studies at the cellular and animal level. *European Journal of Cancer* 2005, 41, (8), 1203-1212.
37. Camerin, M.; Rodgers, M. A. J.; Kenney, M. E.; Jori, G., Photothermal sensitisation: evidence for the lack of oxygen effect on the photosensitising activity. *Photochemical & Photobiological Sciences* 2005, 4, (3), 251-253.
38. Busetti, A.; Soncin, M.; Reddi, E.; Rodgers, M. A. J.; Kenney, M. E.; Jori, G., Photothermal sensitization of amelanotic melanoma cells by Ni(II)-octabutoxy-naphthalocyanine. *Journal of Photochemistry and Photobiology, B: Biology* 1999, 53, (1-3), 103-109.
39. Jori, G.; Spikes, J. D., Photothermal sensitizers: possible use in tumor therapy. *Journal of Photochemistry and Photobiology, B: Biology* 1990, 6, (1-2), 93-101.
40. Vietri, F.; Guglielmi, R.; Belbusti, M.; Crispino, M.; Tombolini, P.; Jori, G., Photothermal sensibilization. *Laser & Technology* 1992, 2, (1), 21-5.

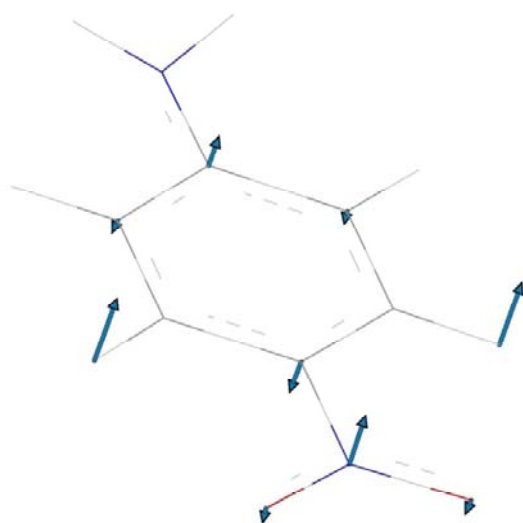
41. Gu, Y.; Chen Wei, R.; Xia, M.; Jeong Sang, W.; Liu, H., Effect of photothermal therapy on breast tumor vascular contents: noninvasive monitoring by near-infrared spectroscopy. *Photochemistry and photobiology* 2005, 81, (4), 1002-9.
42. Huang, X.; El-Sayed, I. H.; Qian, W.; El-Sayed, M. A., Cancer Cell Imaging and Photothermal Therapy in the Near-Infrared Region by Using Gold Nanorods. *Journal of the American Chemical Society* 2006, 128, (6), 2115-2120.
43. El-Sayed, I. H.; Huang, X.; El-Sayed, M. A., Selective laser photo-thermal therapy of epithelial carcinoma using anti-EGFR antibody conjugated gold nanoparticles. *Cancer Letters (Amsterdam, Netherlands)* 2006, 239, (1), 129-135.
44. Goerner, H.; Doepp, D., Photoinduced demethylation of 4-nitro-N,N-dimethylaniline. *Photochemical & Photobiological Sciences* 2002, 1, (4), 270-277.
45. Costela, A.; Garcia-Moreno, I.; Garcia, O.; Sastre, R., Laser-assisted photochemistry of N,N-dimethyl-4-nitroaniline initiator of polymerization. *Chemical Physics Letters* 2001, 347, (1,2,3), 115-120.
46. Costela, A.; Garcia-Moreno, I.; Garcia, O.; Sastre, R., Photosensitization of N,N-dimethylaniline by N,N-dimethyl-4-nitroaniline as a new bimolecular photoinitiation system for polymerization. *Macromolecular Chemistry and Physics* 2001, 202, (11), 2253-2261.
47. Sugita, A.; Yanagi, K.; Kuroyanagi, K.; Takahashi, H.; Aoshima, S.; Tsuchiya, Y.; Tasaka, S.; Hashimoto, H., Photo-excited state of N-benzyl MNA studied by femtosecond time-resolved absorption spectroscopy. *Chemical Physics Letters* 2003, 382, (5,6), 693-698.

48. Gunaratne Tissa, C.; Milliken, M.; Challa, J. R.; Simpson, M. C., Tunable ultrafast infrared/visible laser to probe vibrational dynamics. *Applied optics* 2006, 45, (3), 558-64.
49. Varsanyi, G., *Vibrational Spectra of Benzene derivatives*. 1969.
50. Englman, R.; Jortner, J., Energy gap law for radiationless transitions in large molecules. *Molecular Physics* 1970, 18, (2), 145-64.
51. Klessinger, M., Conical intersections and the mechanism of singlet photoreactions. *Angewandte Chemie, International Edition in English* 1995, 34, (5), 549-51.
52. Domcke, W.; Stock, G., Theory of ultrafast nonadiabatic excited-state processes and their spectroscopic detection in real time. *Advances in Chemical Physics* 1997, 100, 1-169.

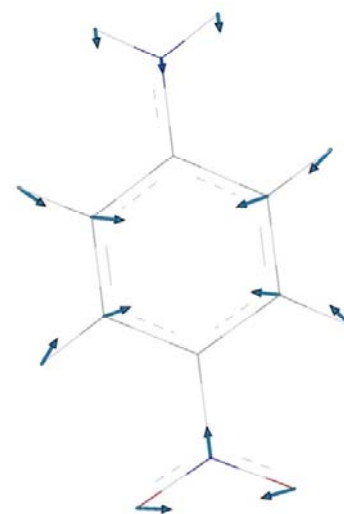
APPENDIX 6-1

The Normal mode displacement vectors of the selected vibrational modes of 4-nitroaniline (PNA), 2-methyl-4-nitroaniline (2-MPNA), 2, 6-dimethyl-4-nitroaniline (2, 6-DMPNA) and N, N-dimethyl-4-nitroaniline (NNDMPNA) obtained from Gaussian 03 calculations at the density functional theory level with B3LYP functional and 6-31+G (2d, p) basis set are presented as follows. The normal mode displacement vectors are plotted using GaussView 3.0.

PNA:

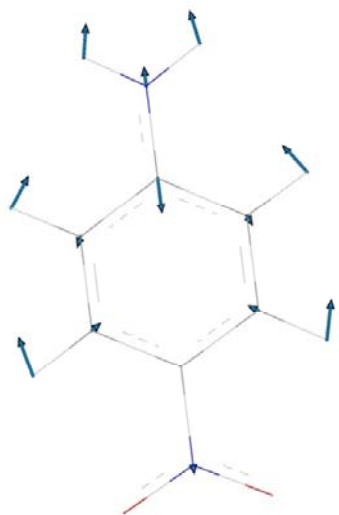


PNA: ν_{15} at 765 cm^{-1}

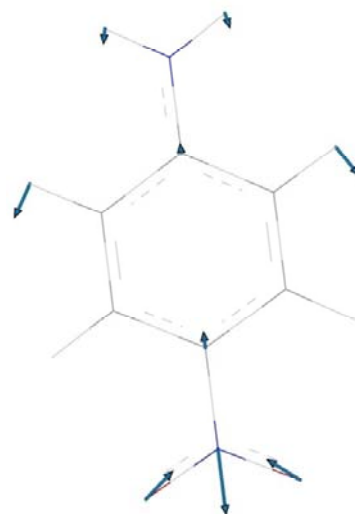


PNA: ν_{19} at 857 cm^{-1}

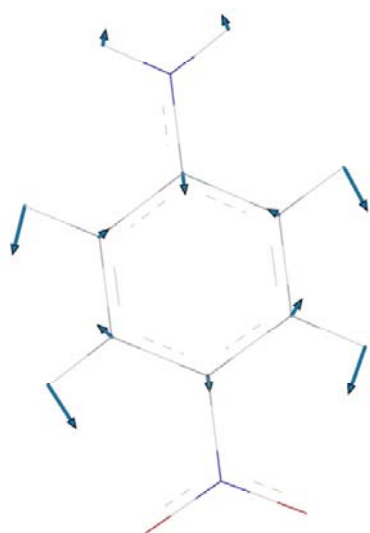
Figure A6 - 1 The Normal mode displacement vector images of PNA vibrations ν_{15} and ν_{19} at 765 and 857 cm^{-1} respectively.



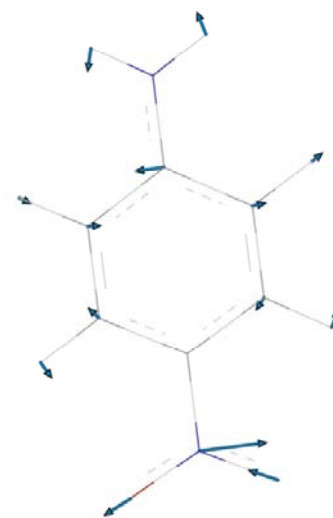
PNA: ν_{27} at 1301 cm^{-1}



PNA: ν_{29} at 1342 cm^{-1}



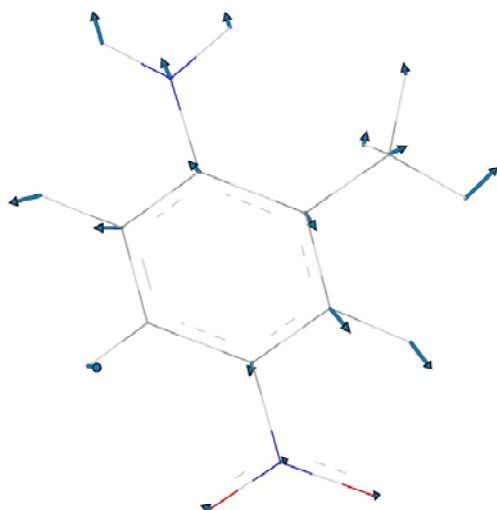
PNA: ν_{32} at 1506 cm^{-1}



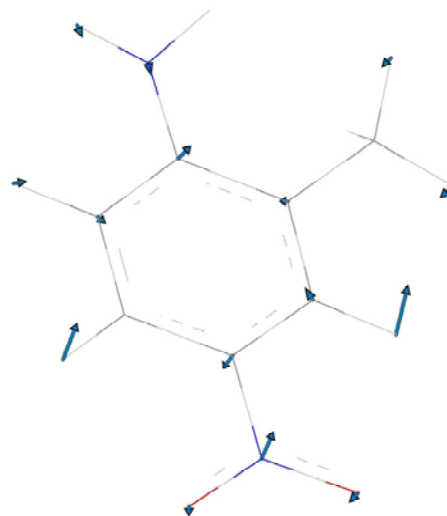
PNA: ν_{33} at 1532 cm^{-1}

Figure A6 - 2 The Normal mode displacement vector images of PNA vibrations ν_{27} , ν_{29} , ν_{32} and ν_{33} at 1301 , 1342 , 1506 and 1532 cm^{-1} respectively.

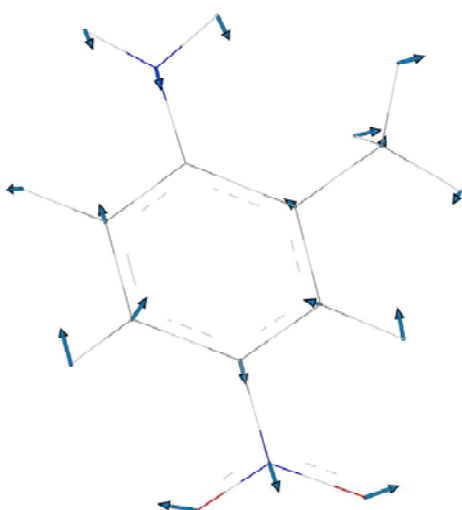
2-MPNA:



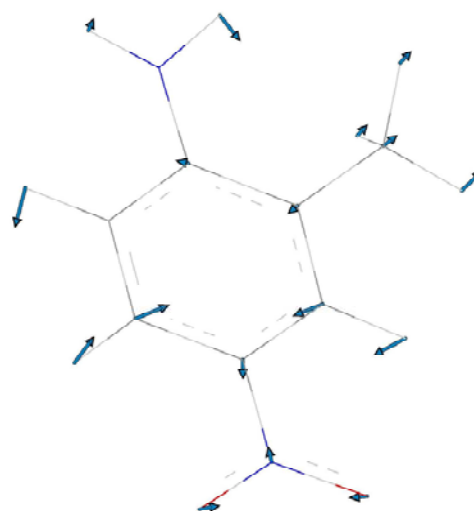
2-MPNA: ν_{18} at 762 cm^{-1}



2-MPNA: ν_{19} at 766 cm^{-1}

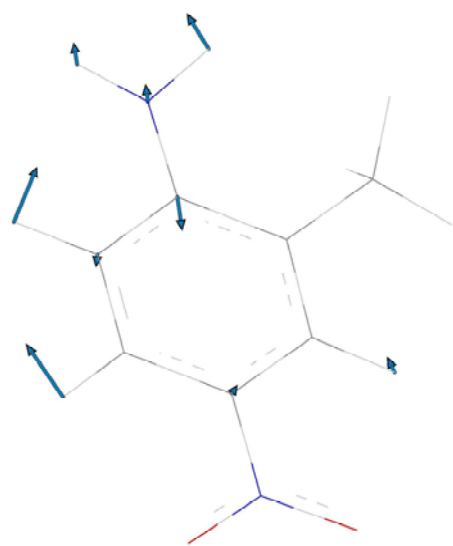


2-MPNA: ν_{20} at 811 cm^{-1}

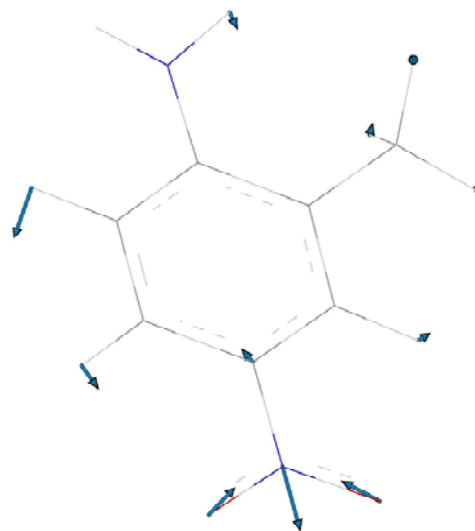


2-MPNA: ν_{23} at 929 cm^{-1}

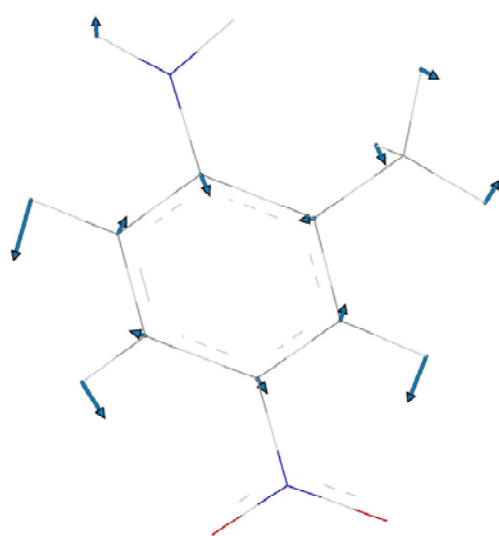
Figure A6 - 3 The Normal mode displacement vector images of 2-MPNA vibrations ν_{18} , ν_{19} , ν_{20} and ν_{23} at 762 , 766 , 811 and 929 cm^{-1} respectively.



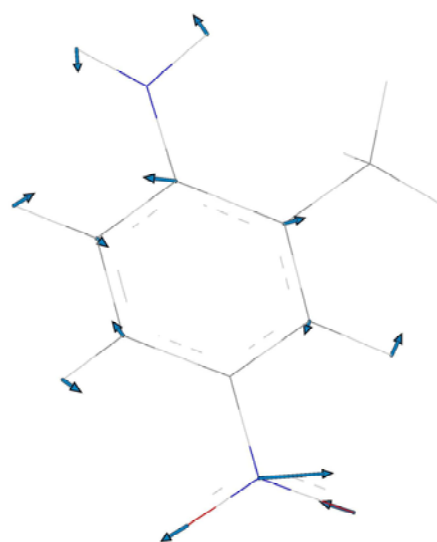
2-MPNA: ν_{32} at 1300 cm^{-1}



2-MPNA: ν_{33} at 1339 cm^{-1}



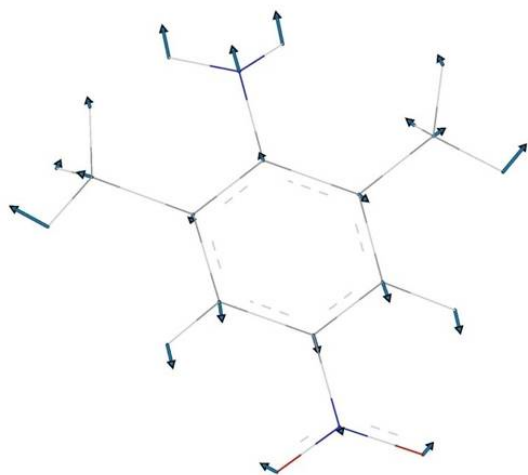
2-MPNA: ν_{39} at 1501 cm^{-1}



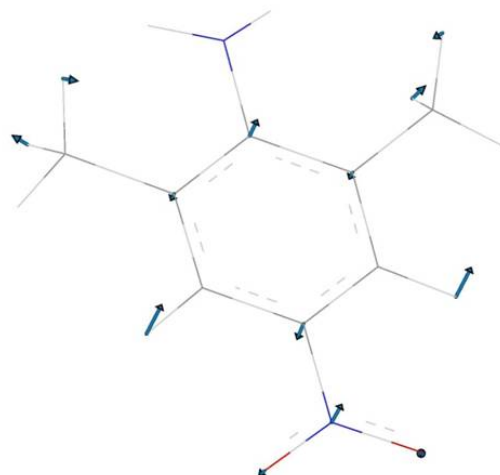
2-MPNA: ν_{40} at 1534 cm^{-1}

Figure A6 - 4 The Normal mode displacement vector images of 2-MPNA vibrations ν_{32} , ν_{33} , ν_{39} and ν_{40} at 1300 , 1339 , 1501 and 1534 cm^{-1} respectively.

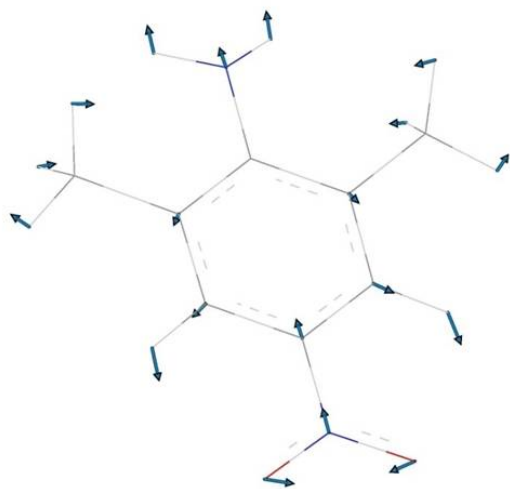
2, 6-DMPNA:



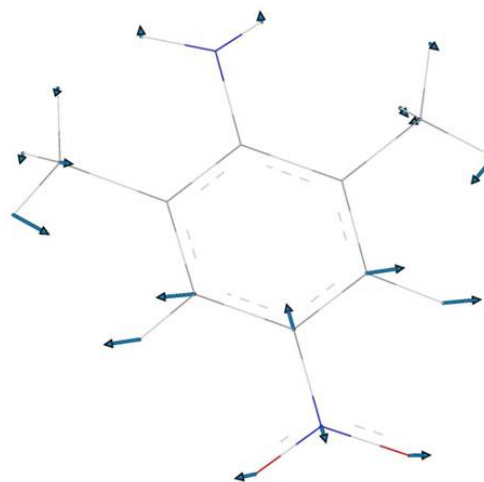
2, 6-DMPNA: ν_{20} at 728 cm^{-1}



2, 6-DMPNA: ν_{22} at 765 cm^{-1}

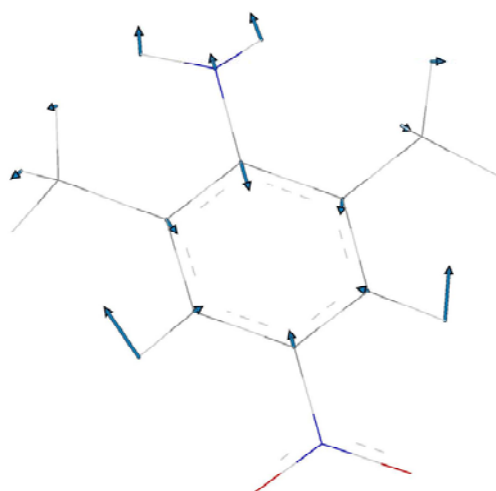


2, 6-DMPNA: ν_{23} at 805 cm^{-1}

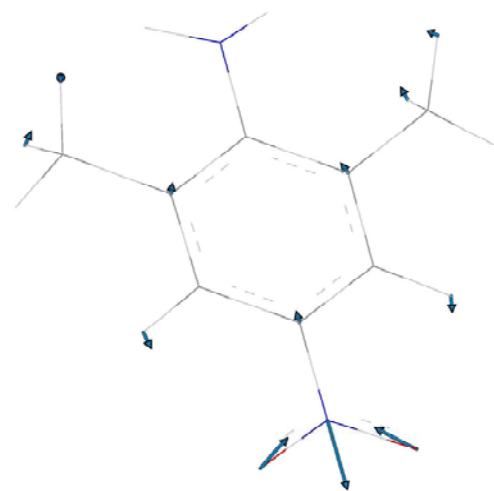


2, 6-DMPNA: ν_{27} at 947 cm^{-1}

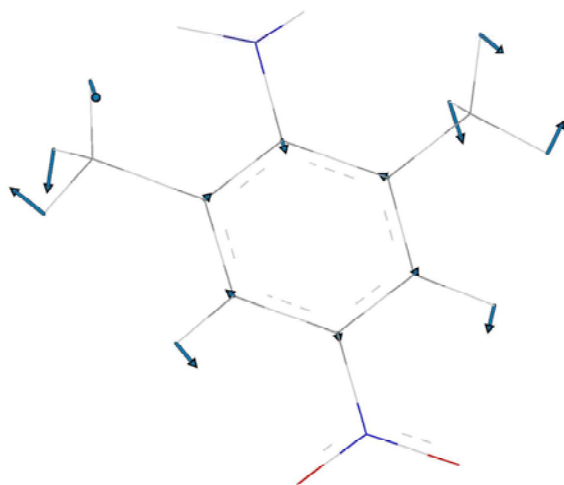
Figure A6 - 5 The Normal mode displacement vector images of 2, 6-DMPNA vibrations ν_{20} , ν_{22} , ν_{23} and ν_{27} at 728 , 765 , 805 and 947 cm^{-1} respectively.



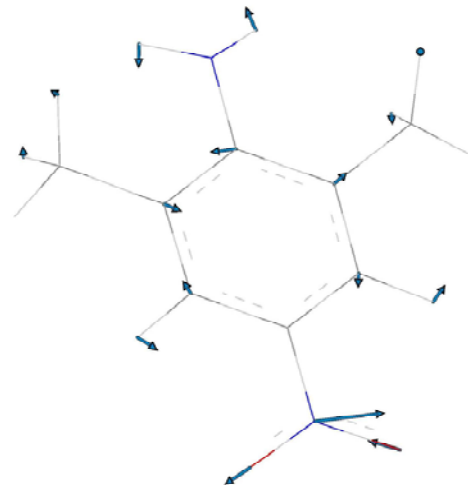
2, 6-DMPNA: ν_{36} at 1300 cm^{-1}



2, 6-DMPNA: ν_{37} at 1334 cm^{-1}



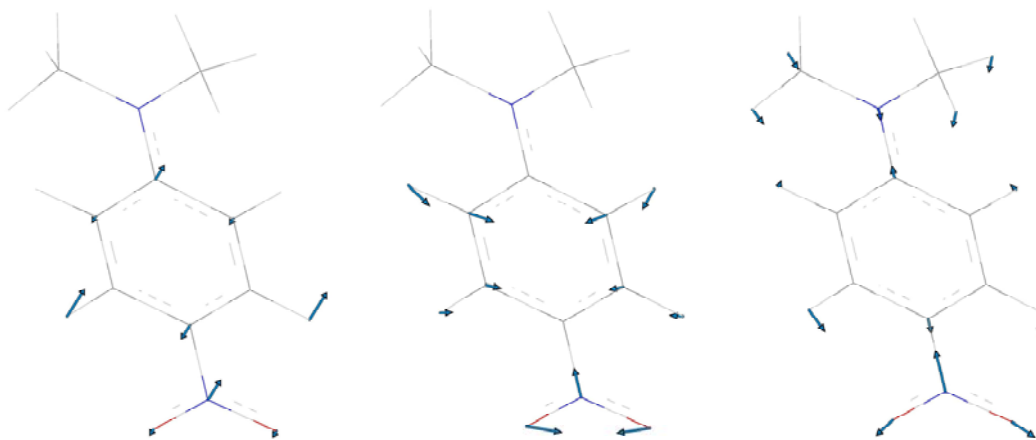
2, 6-DMPNA: ν_{46} at 1497 cm^{-1}



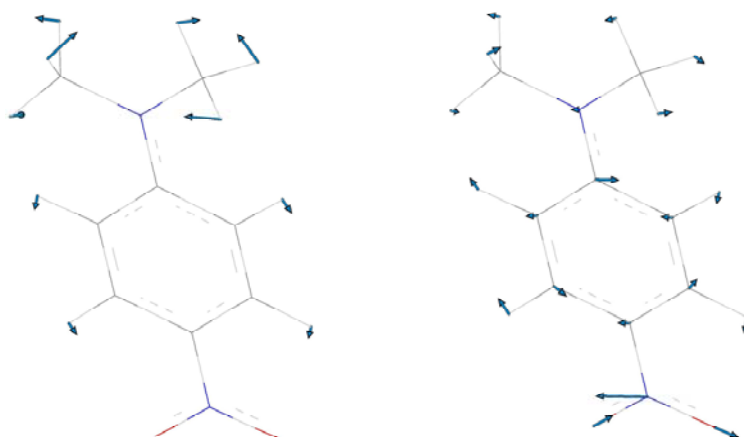
2, 6-DMPNA: ν_{47} at 1520 cm^{-1}

Figure A6 - 6 The Normal mode displacement vector images of 2, 6-DMPNA vibrations ν_{36} , ν_{37} , ν_{46} and ν_{47} at 1300, 1334, 1497 and 1520 cm^{-1} respectively.

N, N-DMPNA:



N, N-DMPNA: ν_{20} at 765 cm⁻¹ N, N-DMPNA: ν_{23} at 849 cm⁻¹ N, N-DMPNA: ν_{37} at 1330 cm⁻¹



N, N-DMPNA: ν_{46} at 1497 cm⁻¹

N, N-DMPNA: ν_{47} at 1520 cm⁻¹

Figure A6 - 7 The Normal mode displacement vector images of N, N-DMPNA vibrations ν_{20} , ν_{23} , ν_{37} , ν_{46} and ν_{47} at 765, 849, 1330, 1497 and 1520 cm⁻¹ respectively.

BIBLIOGRAPHY

Alden, R. G.; Chavez, M. D.; Ondrias, M. R.; Courtney, S. H.; Friedman, J. M., Direct measurement of vibrational temperatures in photoexcited deoxyhemoglobin on picosecond time scales. *Journal of the American Chemical Society* **1990**, 112, (8), 3241-2.

Alden, R. G.; Ondrias, M. R.; Courtney, S.; Findsen, E. W.; Friedman, J. M., Power-induced broadening of transient resonance Raman spectra of deoxyhemoglobin. *Journal of Physical Chemistry* **1990**, 94, (1), 85-90.

Alden, R. G.; Schneebeck, M. C.; Ondrias, M. R.; Courtney, S. H.; Friedman, J. M., Mode-specific relaxation dynamics of photoexcited iron(II) protoporphyrin IX in hemoglobin. *Journal of Raman Spectroscopy* **1992**, 23, (10), 569-74.

Alfano, R. R., The super continuum laser source. **1989**.

An, Q.; Gilch, P., Cooling of hot para-nitroaniline probed by non-resonant Raman scattering. *Chemical Physics Letters* **2002**, 363, (3,4), 397-403.

Anfinrud, P. A.; Han, C.; Hochstrasser, R. M., Direct observations of ligand dynamics in hemoglobin by subpicosecond infrared spectroscopy. *Proceedings of the National Academy of Sciences of the United States of America* **1989**, 86, (21), 8387-91.

Ansari, A.; Berendzen, J.; Bowne, S. F.; Frauenfelder, H.; Iben, I. E. T.; Sauke, T. B.; Shyamsunder, E.; Young, R. D., Protein states and proteinquakes. *Proceedings of the National Academy of Sciences of the United States of America* **1985**, 82, (15), 5000-4.

Assmann, J.; Kling, M.; Abel, B., Watching photoinduced chemistry and molecular energy flow in solution in real time. *Angewandte Chemie, International Edition* **2003**, 42, (20), 2226-2246.

Austin, R. H.; Beeson, K. W.; Eisenstein, L.; Frauenfelder, H.; Gunsalus, I. C., Dynamics of ligand binding to myoglobin. *Biochemistry* **1975**, 14, (24), 5355-73.

Backus, S.; Durfee, C. G., III; Murnane, M. M.; Kapteyn, H. C., High power ultrafast lasers. *Review of Scientific Instruments* **1998**, 69, (3), 1207-1223.

Bakker, H. J., Effect of intermolecular interactions on vibrational-energy transfer in the liquid phase. *Journal of Chemical Physics* **1993**, 98, (11), 8496-506.

Barzoukas, M.; Runser, C.; Fort, A.; Blanchard-Desce, M., A two-state description of (hyper)polarizabilities of push-pull molecules based on a two-form model. *Chemical Physics Letters* **1996**, 257, (5,6), 531-537.

Bettati, S.; Mozzarelli, A.; Perutz, M. F., Allosteric mechanism of haemoglobin: rupture of salt-bridges raises the oxygen affinity of the T-structure. *Journal of molecular biology* **1998**, 281, (4), 581-5.

Bhattacharjee, Y., Measuring the immeasurable. *Nature (London, United Kingdom)* **2001**, 412, (6846), 474-476.

Bloembergen, N., From nanosecond to femtosecond science. *Reviews of Modern Physics* **1999**, 71, (2), S283-S287.

Bluhm, M. M.; Bodo, G.; Dintzis, H. M.; Kendrew, J. C., The crystal structure of myoglobin. IV. A Fourier projection of sperm-whale myoglobin by the method of isomorphous replacement. *Proc. Roy. Soc. (London)* **1958**, A246, 369-89.

Borbulevych, O. Y.; Clark, R. D.; Romero, A.; Tan, L.; Antipin, M. Y.; Nesterov, V. N.; Cardelino, B. H.; Moore, C. E.; Sanghadasa, M.; Timofeeva, T. V., Experimental and theoretical study of the structure of N,N-dimethyl-4-nitroaniline derivatives as model compounds for non-linear optical organic materials. *Journal of Molecular Structure* **2002**, 604, (1), 73-86.

Brunori, M.; Giacometti, G. M., Photochemistry of hemoproteins. *Methods in Enzymology* **1981**, 76, (Hemoglobins), 582-95.

Bu, L.; Straub, J. E., Vibrational energy relaxation of \"tailored\" hemes in myoglobin following ligand photolysis supports energy funneling mechanism of heme \"cooling\". *Journal of Physical Chemistry B* **2003**, 107, (38), 10634-10639.

Bucher, T.; Kaspers, J., Photochemical cleavage of carbon monoxide-myoglobin by ultraviolet radiation (activity of the protein component of the pigment for absorbed quanta). *Biochimica et Biophysica Acta* **1947**, 1, 21-34.

Burdzinski, G.; Hackett, J. C.; Wang, J.; Gustafson, T. L.; Hadad, C. M.; Platz, M. S., Early Events in the Photochemistry of Aryl Azides from Femtosecond UV/Vis Spectroscopy and Quantum Chemical Calculations. *Journal of the American Chemical Society* **2006**, 128, (41), 13402-13411.

Busetti, A.; Soncin, M.; Reddi, E.; Rodgers, M. A. J.; Kenney, M. E.; Jori, G., Photothermal sensitization of amelanotic melanoma cells by Ni(II)-octabutoxy-naphthalocyanine. *Journal of Photochemistry and Photobiology, B: Biology* 1999, 53, (1-3), 103-109.

Camerin, M.; Rello, S.; Villanueva, A.; Ping, X.; Kenney, M. E.; Rodgers, M. A. J.; Jori, G., Photothermal sensitisation as a novel therapeutic approach for tumours: Studies at the cellular and animal level. *European Journal of Cancer* 2005, 41, (8), 1203-1212.

Camerin, M.; Rodgers, M. A. J.; Kenney, M. E.; Jori, G., Photothermal sensitisation: evidence for the lack of oxygen effect on the photosensitising activity. *Photochemical & Photobiological Sciences* 2005, 4, (3), 251-253.

Causgrove, T. P.; Dyer, R. B., Picosecond structural dynamics of myoglobin following photolysis of carbon monoxide. *Journal of Physical Chemistry* **1996**, 100, (8), 3273-7.

Challa, J. R.; Gunaratne Tissa, C.; Simpson, M. C., State preparation and excited electronic and vibrational behavior in hemes. *J Phys Chem B* **2006**, 110, (40), 19956-65.

Champagne, B., Vibrational polarizability and hyperpolarizability of p-nitroaniline. *Chemical Physics Letters* **1996**, 261, (1,2), 57-65.

Champion, P. M.; Lange, R., On the quantitation of light emission from cytochrome c in the low quantum yield limit. *Journal of Chemical Physics* **1980**, 73, (12), 5947-57.

Cheriaux, G.; Chambaret, J.-P., Ultra-short high-intensity laser pulse generation and amplification. *Measurement Science and Technology* **2001**, 12, (11), 1769-1776.

Chernoff, D. A.; Hochstrasser, R. M.; Steele, A. W., Geminate recombination of oxygen and hemoglobin. *Proceedings of the National Academy of Sciences of the United States of America* **1980**, 77, (10), 5606-10.

Cho, M., Ultrafast vibrational spectroscopy in condensed phases. *PhysChemComm* **2002**, 5, 40-58.

Cornelius, P. A.; Hochstrasser, R. M.; Steele, A. W., Ultrafast relaxation in picosecond photolysis of nitrosylhemoglobin. *Journal of Molecular Biology* **1983**, 163, (1), 119-28.

Costela, A.; Garcia-Moreno, I.; Garcia, O.; Sastre, R., Laser-assisted photochemistry of N,N-dimethyl-4-nitroaniline initiator of polymerization. *Chemical Physics Letters* **2001**, 347, (1,2,3), 115-120.

Costela, A.; Garcia-Moreno, I.; Garcia, O.; Sastre, R., Photosensitization of N,N-dimethylaniline by N,N-dimethyl-4-nitroaniline as a new bimolecular photoinitiation system for polymerization. *Macromolecular Chemistry and Physics* **2001**, 202, (11), 2253-2261.

Cupane, A.; Leone, M.; Vitano, E.; Cordone, L., Structural and dynamic properties of the heme pocket in myoglobin probed by optical spectroscopy. *Biopolymers* **1988**, 27, (12), 1977-97.

Davis, D.; Sreekumar, K.; Sajeev, Y.; Pal, S., Optimization of Nonlinear Optical Properties by Substituent Position, Geometry and Symmetry of the Molecule: An ab Initio Study. *Journal of Physical Chemistry B* **2005**, 109, (29), 14093-14101.

Davydov, B. L.; Derkacheva, L. D.; Dunina, V. V.; Zhabotinskii, M. E.; Zolin, V. F.; Koreneva, L. G.; Samokhina, M. A., Correlation of charge transfer to laser second harmonics generation. *Pis'ma v Zhurnal Eksperimental'noi i Teoreticheskoi Fiziki* **1970**, 12, (1), 24-6.

Deak, J. C.; Iwaki, L. K.; Dlott, D. D., Vibrational energy redistribution in polyatomic liquids: ultrafast IR-Raman spectroscopy of acetonitrile. *Journal of Physical Chemistry A* **1998**, 102, (42), 8193-8201.

Deak, J. C.; Iwaki, L. K.; Dlott, D. D., Vibrational Energy Redistribution in Polyatomic Liquids: Ultrafast IR-Raman Spectroscopy of Nitromethane. *Journal of Physical Chemistry A* **1999**, 103, (8), 971-979.

Deak, J. C.; Iwaki, L. K.; Rhea, S. T.; Dlott, D. D., Ultrafast infrared-Raman studies of vibrational energy redistribution in polyatomic liquids. *Journal of Raman Spectroscopy* **2000**, 31, (4), 263-274.

Deak, J. C.; Pang, Y.; Sechler, T. D.; Wang, Z.; Dlott, D. D., Vibrational Energy Transfer Across a Reverse Micelle Surfactant Layer. *Science (Washington, DC, United States)* **2004**, 306, (5695), 473-476.

Dlott, D. D., Vibrational energy redistribution in polyatomic liquids: 3D infrared-Raman spectroscopy. *Chemical Physics* **2001**, 266, (2-3), 149-166.

Domcke, W.; Stock, G., Theory of ultrafast nonadiabatic excited-state processes and their spectroscopic detection in real time. *Advances in Chemical Physics* **1997**, 100, 1-169.

Elber, R.; Karplus, M., Multiple conformational states of proteins: a molecular dynamics analysis of myoglobin. *Science (Washington, DC, United States)* **1987**, 235, (4786), 318-21.

El-Sayed, I. H.; Huang, X.; El-Sayed, M. A., Selective laser photo-thermal therapy of epithelial carcinoma using anti-EGFR antibody conjugated gold nanoparticles. *Cancer Letters (Amsterdam, Netherlands)* 2006, 239, (1), 129-135.

Englman, R.; Jortner, J., Energy gap law for radiationless transitions in large molecules. *Molecular Physics* **1970**, 18, (2), 145-64.

Farztdinov, V. M.; Schanz, R.; Kovalenko, S. A.; Ernsting, N. P., Relaxation of Optically Excited p-Nitroaniline: Semiempirical Quantum-Chemical Calculations Compared to Femtosecond Experimental Results. *Journal of Physical Chemistry A* **2000**, 104, (49), 11486-11496.

Fermi, G.; Perutz, M. F.; Shulman, R. G., Iron distances in hemoglobin: comparison of x-ray crystallographic and extended x-ray absorption fine structure studies. *Proceedings of the National Academy of Sciences of the United States of America* **1987**, 84, (17), 6167-8.

Foggi, P.; Bussotti, L.; Neuwahl, F. V. R., Photophysical and photochemical applications of femtosecond time-resolved transient absorption spectroscopy. *International Journal of Photoenergy* **2001**, 3, (2), 103-109.

Franzen, S.; Bohn, B.; Poyart, C.; Martin, J. L., Evidence for sub-picosecond heme doming in hemoglobin and myoglobin: a time-resolved resonance Raman comparison of carbonmonoxy and deoxy species. *Biochemistry* **1995**, 34, (4), 1224-37.

Franzen, S.; Kiger, L.; Poyart, C.; Martin, J.-L., Heme photolysis occurs by ultrafast excited state metal-to-ring charge transfer. *Biophysical Journal* **2001**, 80, (5), 2372-2385.

Frauenfelder, H.; Wolynes, P. G., Rate theories and puzzles of hemeprotein kinetics. *Science (Washington, DC, United States)* **1985**, 229, (4711), 337-45.

Fujisawa, T.; Terazima, M.; Kimura, Y., Excitation wavelength dependence of the Raman-Stokes shift of N,N-dimethyl-p-nitroaniline. *Journal of Chemical Physics* **2006**, 124, (18), 184503/1-184503/9.

Gao, Y.; Koyama, M.; El-Mashtoly, S. F.; Hayashi, T.; Harada, K.; Mizutani, Y.; Kitagawa, T., Time-resolved Raman evidence for energy 'funneling' through propionate side chains in heme 'cooling' upon photolysis of carbonmonoxy myoglobin. *Chemical Physics Letters* **2006**, 429, (1-3), 239-243.

Genberg, L.; Heisel, F.; McLendon, G.; Miller, R. J. D., Vibrational energy relaxation processes in heme proteins: model systems of vibrational energy dispersion in disordered systems. *Journal of Physical Chemistry* **1987**, 91, (22), 5521-4.

Gibson, Q. H.; Ainsworth, S., Photosensitivity of hem compounds. *Nature (London, United Kingdom)* **1957**, 180, 1416-17.

Goerner, H.; Doepp, D., Photoinduced demethylation of 4-nitro-N,N-dimethylaniline. *Photochemical & Photobiological Sciences* **2002**, 1, (4), 270-277.

Goodno, G. D.; Miller, R. J. D., Femtosecond Heterodyne-Detected Four-Wave-Mixing Studies of Deterministic Protein Motions. 1. Theory and Experimental Technique of Diffractive Optics-Based Spectroscopy. *Journal of Physical Chemistry A* **1999**, 103, (49), 10619-10629.

Gould, I. R.; Young, R. H.; Mueller, L. J.; Albrecht, A. C.; Farid, S., Electronic Structures of Exciplexes and Excited Charge-Transfer Complexes. *Journal of the American Chemical Society* **1994**, 116, (18), 8188-99.

Gould, I. R.; Young, R. H.; Mueller, L. J.; Albrecht, A. C.; Farid, S., Electronic Coupling Matrix Elements in Acceptor-Donor Excited States and the Effect of Charge-Transfer Character on Their Radiative Rate Constants. *Journal of the American Chemical Society* **1994**, 116, (7), 3147-8.

Gouterman, M., Effects of substitution on the absorption spectra of porphin. *Journal of Chemical Physics* **1959**, 30, 1139-61.

Gouterman, M., Spectra of porphyrins. *Journal of Molecular Spectroscopy* **1961**, 6, 138-63.

Gouterman, M. In *Optical spectra and electronic structure of porphyrins and related rings*, 1978; 1978; pp 1-165.

Grabowski, Z. R.; Dobkowski, J., Twisted intramolecular charge transfer (TICT) excited states: energy and molecular structure. *Pure and Applied Chemistry* **1983**, 55, (2), 245-52.

Graener, H.; Laubereau, A., New results on vibrational population decay in simple liquids. *Applied Physics B: Photophysics and Laser Chemistry* **1982**, B29, (3), 213-18.

Graener, H.; Seifert, G., Vibrational and orientational relaxation of monomeric water molecules in liquids. *Journal of Chemical Physics* **1993**, 98, (1), 36-45.

Gu, Y.; Li, P.; Sage, J. T.; Champion, P. M., Photoreduction of heme proteins: spectroscopic studies and cross-section measurements. *Journal of the American Chemical Society* **1993**, 115, (12), 4993-5004.

Gu, Y.; Chen Wei, R.; Xia, M.; Jeong Sang, W.; Liu, H., Effect of photothermal therapy on breast tumor vascular contents: noninvasive monitoring by near-infrared spectroscopy. *Photochemistry and photobiology* 2005, 81, (4), 1002-9.

Gunaratne, T.; Challa, J. R.; Simpson, M. C., Energy flow in push-pull chromophores: vibrational dynamics in para-nitroaniline. *ChemPhysChem* 2005, 6, (6), 1157-1163.

Gunaratne, T. C.; Simpson, M. C. In *Electronic and vibronic energy flow in molecular assemblies: Current research and future directions utilizing transient absorption and transient Raman spectroscopic methods*, 2005; 2005; pp AEI-142.

Gunaratne Tissa, C.; Milliken, M.; Challa, J. R.; Simpson, M. C., Tunable ultrafast infrared/visible laser to probe vibrational dynamics. *Applied optics* 2006, 45, (3), 558-64.

Hamm, P.; Lim, M.; Hochstrasser, R. M., Vibrational energy relaxation of the cyanide ion in water. *Journal of Chemical Physics* 1997, 107, (24), 10523-10531.

Hamm, P.; Ohline, S. M.; Zinth, W., Vibrational cooling after ultrafast photoisomerization of azobenzene measured by femtosecond infrared spectroscopy. *Journal of Chemical Physics* 1997, 106, (2), 519-529.

Hamm, P.; Wiemann, S.; Zurek, M.; Zinth, W., Highly sensitive multichannel spectrometer for subpicosecond spectroscopy in the mid-infrared. *Optics Letters* **1994**, 19, (20), 1642-4.

Heilweil, E. J.; Casassa, M. P.; Cavanagh, R. R.; Stephenson, J. C., Population lifetimes of hydroxyl($v = 1$) and hydroxyl-d($v = 1$) stretching vibrations of alcohols and silanols in dilute solution. *Journal of Chemical Physics* **1986**, 85, (9), 5004-18.

Henry, E. R.; Eaton, W. A.; Hochstrasser, R. M., Molecular dynamics simulations of cooling in laser-excited heme proteins. *Proceedings of the National Academy of Sciences of the United States of America* **1986**, 83, (23), 8982-6.

Henry, E. R.; Levitt, M.; Eaton, W. A., Molecular dynamics simulation of photodissociation of carbon monoxide from hemoglobin. *Proceedings of the National Academy of Sciences of the United States of America* **1985**, 82, (7), 2034-8.

Hiberty, P. C.; Ohanessian, G., Valence-bond description of conjugated molecules. 3. The through-resonance concept in para-substituted nitrobenzenes. *Journal of the American Chemical Society* **1984**, 106, (23), 6963-8.

Hu, C.; An, J.; Noll Bruce, C.; Schulz Charles, E.; Scheidt, W. R., Electronic configuration of high-spin imidazole-ligated iron(II) octaethylporphyrinates. *Inorganic chemistry* **2006**, 45, (10), 4177-85.

Huang, X.; El-Sayed, I. H.; Qian, W.; El-Sayed, M. A., Cancer Cell Imaging and Photothermal Therapy in the Near-Infrared Region by Using Gold Nanorods. *Journal of the American Chemical Society* 2006, 128, (6), 2115-2120.

Jamorski, C. J.; Luthi, H.-P., Rational classification of a series of aromatic donor-acceptor systems within the twisting intramolecular charge transfer model, a time-dependent density-functional theory investigation. *Journal of Chemical Physics* **2003**, 119, (24), 12852-12865.

Jamorski Jodicke, C.; Luthi Hans, P., Time-dependent density functional theory (TDDFT) study of the excited charge-transfer state formation of a series of aromatic donor-acceptor systems. *Journal of the American Chemical Society* **2003**, 125, (1), 252-64.

Jori, G.; Spikes, J. D., Photothermal sensitizers: possible use in tumor therapy. *Journal of Photochemistry and Photobiology, B: Biology* 1990, 6, (1-2), 93-101.

Karna, S. P.; Prasad, P. N.; Dupuis, M., Nonlinear optical properties of p-nitroaniline: An ab initio time-dependent coupled perturbed Hartree-Fock study. *Journal of Chemical Physics* **1991**, 94, (2), 1171-81.

Keller, U., Recent developments in compact ultrafast lasers. *Nature (London, United Kingdom)* **2003**, 424, (6950), 831-838.

Kendrew, J. C.; Bodo, G.; Dintzis, H. M.; Parrish, R. G.; Wyckoff, H.; Phillips, D. C., A three-dimensional model of the myoglobin molecule obtained by x-ray analysis. *Nature* **1958**, 181, (4610), 662-6.

Kholodenko, Y.; Volk, M.; Gooding, E.; Hochstrasser, R. M., Energy dissipation and relaxation processes in deoxy myoglobin after photoexcitation in the Soret region. *Chemical Physics* **2000**, 259, (1), 71-87.

Kim, D.; Holten, D., Picosecond measurements on the binding and release of basic ligands by excited states of nickel(II) porphyrins. *Chemical Physics Letters* **1983**, 98, (6), 584-9.

Kim, D.; Kirmaier, C.; Holten, D., Nickel porphyrin photophysics and photochemistry. A picosecond investigation of ligand binding and release in the excited state. *Chemical Physics* **1983**, 75, (3), 305-22.

Kimura, Y.; Fukuda, M.; Kajimoto, O.; Terazima, M., Study on the vibrational energy relaxation of p-nitroaniline, N,N-dimethyl-p-nitroaniline, and azulene by the transient grating method. *Journal of Chemical Physics* **2006**, 125, (19), 194516/1-194516/12.

Klessinger, M., Conical intersections and the mechanism of singlet photoreactions. *Angewandte Chemie, International Edition in English* **1995**, 34, (5), 549-51.

Kovalenko, S. A.; Schanz, R.; Farztdinov, V. M.; Hennig, H.; Ernsting, N. P., Femtosecond relaxation of photoexcited para-nitroaniline: solvation, charge transfer, internal conversion and cooling. *Chemical Physics Letters* **2000**, 323, (3,4), 312-322.

Kovalenko, S. A.; Schanz, R.; Hennig, H.; Ernsting, N. P., Cooling dynamics of an optically excited molecular probe in solution from femtosecond broadband transient absorption spectroscopy. *Journal of Chemical Physics* **2001**, 115, (7), 3256-3273.

Kozich, V.; Dreyer, J.; Ashihara, S.; Werncke, W.; Elsaesser, T., Mode-selective O-H stretching relaxation in a hydrogen bond studied by ultrafast vibrational spectroscopy. *Journal of Chemical Physics* **2006**, 125, (7), 074504/1-074504/9.

Kozich, V.; Werncke, W., Influence of vibrational cooling on the time-dependence of Stokes and anti-Stokes resonance Raman scattering. *Journal of Molecular Structure* **2005**, 735-736, 145-151.

Kozich, V.; Werncke, W.; Dreyer, J.; Brzezinka, K. W.; Rini, M.; Kummrow, A.; Elsaesser, T., Vibrational excitation and energy redistribution after ultrafast internal conversion in 4-nitroaniline. *Journal of Chemical Physics* **2002**, 117, (2), 719-726.

Kozich, V.; Werncke, W.; Vodchits, A. I.; Dreyer, J., Ultrafast excitation of out-of-plane vibrations and vibrational energy redistribution after internal conversion of 4-nitroaniline. *Journal of Chemical Physics* **2003**, 118, (4), 1808-1814.

Lange, C.; Hunte, C., Crystal structure of the yeast cytochrome bc₁ complex with its bound substrate cytochrome c. *Proceedings of the National Academy of Sciences of the United States of America* **2002**, 99, (5), 2800-2805.

Laubereau, A.; Kaiser, W., Vibrational dynamics of liquids and solids investigated by picosecond light pulses. *Reviews of Modern Physics* **1978**, 50, (3), 607-65.

Lawrence, C. P.; Skinner, J. L., Vibrational spectroscopy of HOD in liquid D₂O. VI. Intramolecular and intermolecular vibrational energy flow. *Journal of Chemical Physics* **2003**, 119, (3), 1623-1633.

Lehmann, K. K.; Pate, B. H.; Scoles, G. In *Intramolecular vibrational energy relaxation (IVR) in large molecules: homogeneous IVR lifetimes and the mechanism of energy relaxation*, 1992; 1992; pp 53-65.

Lenchenkov, V.; She, C.; Lian, T., Vibrational Relaxation of CN Stretch of Pseudo-Halide Anions (OCN⁻, SCN⁻, and SeCN⁻) in Polar Solvents. *Journal of Physical Chemistry B* **2006**, 110, (40), 19990-19997.

Li, P.; Champion, P. M., Investigations of the thermal response of laser-excited biomolecules. *Biophysical Journal* **1994**, 66, (2, Pt. 1), 430-6.

Li, P.; Sage, J. T.; Champion, P. M., Probing picosecond processes with nanosecond lasers: electronic and vibrational relaxation dynamics of heme proteins. *Journal of Chemical Physics* **1992**, 97, (5), 3214-27.

Li, X. Y.; Czernuszewicz, R. S.; Kincaid, J. R.; Stein, P.; Spiro, T. G., Consistent porphyrin force field. 2. Nickel octaethylporphyrin skeletal and substituent mode assignments from nitrogen-15, meso-d4, and methylene-d16 Raman and infrared isotope shifts. *Journal of Physical Chemistry* **1990**, 94, (1), 47-61.

Lian, T.; Locke, B.; Kholodenko, Y.; Hochstrasser, R. M., Energy Flow from Solute to Solvent Probed by Femtosecond IR Spectroscopy: Malachite Green and Heme Protein Solutions. *Journal of Physical Chemistry* **1994**, 98, (45), 11648-56.

Lim, M.; Jackson, T. A.; Anfinrud, P. A., Femtosecond Near-IR Absorbance Study of Photoexcited Myoglobin: Dynamics of Electronic and Thermal Relaxation. *Journal of Physical Chemistry* **1996**, 100, (29), 12043-12051.

Lingle, R., Jr.; Xu, X.; Zhu, H.; Yu, S. C.; Hopkins, J. B., Picosecond Raman study of energy flow in a photoexcited heme protein. *Journal of Physical Chemistry* **1991**, 95, (23), 9320-31.

Lingle, R., Jr.; Xu, X.; Zhu, H.; Yu, S. C.; Hopkins, J. B.; Straub, K. D., Direct observation of hot vibrations in photoexcited deoxyhemoglobin using picosecond Raman spectroscopy. *Journal of the American Chemical Society* **1991**, 113, (10), 3992-4.

Loparo, J. J.; Cheatum, C. M.; Ondrias, M. R.; Simpson, M. C., Transient Raman observations of heme vibrational dynamics in five-coordinate iron porphyrins. *Chemical Physics* **2003**, 286, (2-3), 353-374.

Lu, D.; Chen, G.; Perry, J. W.; Goddard, W. A., III, Valence-Bond Charge-Transfer Model for Nonlinear Optical Properties of Charge-Transfer Organic Molecules. *Journal of the American Chemical Society* **1994**, 116, (23), 10679-85.

Ma, J.; Huo, S.; Straub, J. E., Molecular Dynamics Simulation Study of the B-States of Solvated Carbon Monoxymyoglobin. *Journal of the American Chemical Society* **1997**, 119, (10), 2541-2551.

Maine, P.; Strickland, D.; Bado, P.; Pessot, M.; Mourou, G., Generation of ultrahigh peak power pulses by chirped pulse amplification. *IEEE Journal of Quantum Electronics* **1988**, QE-24, (2), 398-403.

Martin, J. L.; Migus, A.; Poyart, C.; Lecarpentier, Y.; Astier, R.; Antonetti, A., Femtosecond photolysis of carbon monoxide-ligated protoheme and hemoproteins:

appearance of deoxy species with a 350-fsec time constant. *Proceedings of the National Academy of Sciences of the United States of America* **1983**, 80, (1), 173-7.

Martinez, O. E., *IEEE Journal of Quantum Electronics* **1987**, QE-23, (1), 59-64.

McCamant, D. W.; Kukura, P.; Yoon, S.; Mathies, R. A., Femtosecond broadband stimulated Raman spectroscopy: Apparatus and methods. *Review of Scientific Instruments* **2004**, 75, (11), 4971-4980.

Mikkelsen, K.; Luo, Y.; Agren, H.; Joergensen, P., Solvent induced polarizabilities and hyperpolarizabilities of para-nitroaniline studied by reaction field linear response theory. *Journal of Chemical Physics* **1994**, 100, (11), 8240-50.

Miller, R. J. D., Vibrational energy relaxation and structural dynamics of heme proteins. *Annual Review of Physical Chemistry* **1991**, 42, 581-614.

Miller, R. J. D., Energetics and Dynamics of Deterministic Protein Motion. *Accounts of Chemical Research* **1994**, 27, (5), 145-50.

Miller, R. J. D., 2000 John C. Polanyi Award lecture mother nature and the molecular big bang. *Canadian Journal of Chemistry* **2002**, 80, (1), 1-24.

Mizutani, Y.; Kitagawa, T., Direct observation of cooling of heme upon photodissociation of carbonmonoxy myoglobin. *Science (Washington, D. C.)* **1997**, 278, (5337), 443-446.

Mizutani, Y.; Kitagawa, T., Ultrafast dynamics of myoglobin probed by time-resolved resonance Raman spectroscopy. *Chemical Record* **2001**, 1, (3), 258-275.

Mohanalingam, K.; Hamaguchi, H.-o., Raman spectroscopic study on the two distinct solvated structures of p-nitroaniline in acetonitrile. *Chemistry Letters* **1997**, (6), 537-538.

Moran, A. M.; Kelley, A. M., Solvent effects on ground and excited electronic state structures of p-nitroaniline. *Journal of Chemical Physics* **2001**, 115, (2), 912-924.

Moran, A. M.; Myers Kelley, A.; Tretiak, S., Excited state molecular dynamics simulations of nonlinear push-pull chromophores. *Chemical Physics Letters* **2002**, 367, (3,4), 293-307.

Moulton, P. F., Spectroscopic and laser characteristics of titanium-doped aluminum oxide. *Journal of the Optical Society of America B: Optical Physics* **1986**, 3, (1), 125-33.

Mourou, G., The ultrahigh-peak-power laser. Present and future. *Applied Physics B: Lasers and Optics* **1997**, 65, (2), 205-211.

Nagai, K.; Kitagawa, T., Differences in iron(II)-Ne(His-F8) stretching frequencies between deoxyhemoglobins in the two alternative quaternary structures. *Proceedings of the National Academy of Sciences of the United States of America* **1980**, 77, (4), 2033-7.

Ogilvie, J. P.; Plazanet, M.; Dadusc, G.; Miller, R. J. D., Dynamics of Ligand Escape in Myoglobin: Q-Band Transient Absorption and Four-Wave Mixing Studies. *Journal of Physical Chemistry B* **2002**, 106, (40), 10460-10467.

Okamoto, H., High-sensitivity measurement of ultrafast transient infrared spectra based on optically heterodyned detection of absorption anisotropy. *Chemical Physics Letters* **1998**, 283, (1,2), 33-38.

Okamoto, H.; Tasumi, M., Picosecond transient infrared spectroscopy of electronically excited 4-dimethylamino-4'-nitrostilbene in the fingerprint region (1640-940 cm^{-1}). *Chemical Physics Letters* **1996**, 256, (4,5), 502-508.

Okazaki, I.; Hara, Y.; Nagaoka, M., On vibrational cooling upon photodissociation of carbonmonoxymyoglobin and its microscopic mechanism from the viewpoint of vibrational modes of heme. *Chemical Physics Letters* **2001**, 337, (1,2,3), 151-157.

Owrutsky, J. C.; Li, M.; Locke, B.; Hochstrasser, R. M., Vibrational Relaxation of the CO Stretch Vibration in Hemoglobin-CO, Myoglobin-CO, and Protoheme-CO. *Journal of Physical Chemistry* **1995**, 99, (13), 4842-6.

Painelli, A., Vibronic contribution to static NLO properties: exact results for the DA dimer. *Chemical Physics Letters* **1998**, 285, (5,6), 352-358.

Painelli, A., Amplification of NLO responses: vibronic and solvent effects in push-pull polyenes. *Chemical Physics* **1999**, 245, (1-3), 185-197.

Painelli, A.; Terenziani, F., A non-perturbative approach to solvatochromic shifts of push-pull chromophores. *Chemical Physics Letters* **1999**, 312, (2-4), 211-220.

Painelli, A.; Terenziani, F., Optical Spectra of Push-Pull Chromophores in Solution: A Simple Model. *Journal of Physical Chemistry A* **2000**, 104, (47), 11041-11048.

Perutz, M. F.; Fermi, G.; Luisi, B.; Shaanan, B.; Liddington, R. C., Stereochemistry of cooperative mechanisms in hemoglobin. *Accounts of Chemical Research* **1987**, 20, (9), 309-21.

Pessot, M.; Maine, P.; Mourou, G., 1000 Times expansion/compression of optical pulses for chirped pulse amplification. *Optics Communications* **1987**, 62, (6), 419-21.

Pessot, M.; Squier, J.; Mourou, G.; Harter, D. J., Chirped-pulse amplification of 100-fsec pulses. *Optics Letters* **1989**, 14, (15), 797-9.

Petrich, J. W.; Martin, J. L., Ultrafast absorption and Raman spectroscopy of hemeproteins. *Chemical Physics* **1989**, 131, (1), 31-47.

Petrich, J. W.; Martin, J. L.; Houde, D.; Poyart, C.; Orszag, A., Time-resolved Raman spectroscopy with subpicosecond resolution: vibrational cooling and delocalization of strain energy in photodissociated (carbonmonoxy)hemoglobin. *Biochemistry* **1987**, 26, (24), 7914-23.

Petrich, J. W.; Poyart, C.; Martin, J. L., Photophysics and reactivity of heme proteins: a femtosecond absorption study of hemoglobin, myoglobin, and protoheme. *Biochemistry* **1988**, 27, (11), 4049-60.

Raman, C. V.; Krishnan, K. S., A new type of secondary radiation. *Nature (London, United Kingdom)* **1928**, 121, 501-2.

Reid, G. D.; Wynne, K., Ultrafast laser technology and spectroscopy. *Encyclopedia of Analytical Chemistry* **2000**, 13644-13670.

Reynolds, A. H.; Rand, S. D.; Rentzepis, P. M., Mechanisms for excited state relaxation and dissociation of oxymyoglobin and carboxymyoglobin. *Proceedings of the National Academy of Sciences of the United States of America* **1981**, 78, (4), 2292-6.

Rodriguez, J.; Holten, D., Ultrafast vibrational dynamics of a photoexcited metalloporphyrin. *Journal of Chemical Physics* **1989**, 91, (6), 3525-31.

Rodriguez, J.; Kirmaier, C.; Holten, D., Optical properties of metalloporphyrin excited states. *Journal of the American Chemical Society* **1989**, 111, (17), 6500-6.

Rodriguez, J.; Kirmaier, C.; Holten, D., Time-resolved and static optical properties of vibrationally excited porphyrins. *Journal of Chemical Physics* **1991**, 94, (9), 6020-9.

Sagnella, D. E.; Straub, J. E., Directed Energy "Funneling" Mechanism for Heme Cooling Following Ligand Photolysis or Direct Excitation in Solvated Carbonmonoxy Myoglobin. *Journal of Physical Chemistry B* **2001**, 105, (29), 7057-7063.

Schmid, E. D.; Moschallski, M.; Peticolas, W. L., Solvent effects on the absorption and Raman spectra of aromatic nitrocompounds. Part 1. Calculation of preresonance Raman intensities. *Journal of Physical Chemistry* **1986**, 90, (11), 2340-6.

Schneebeck, M. C.; Vigil, L. E.; Ondrias, M. R., Mode-selective energy localization during photoexcitation of deoxyhemoglobin and heme model complexes. *Chemical Physics Letters* **1993**, 215, (1-3), 251-6.

Schrader, T.; Sieg, A.; Koller, F.; Schreier, W.; An, Q.; Zinth, W.; Gilch, P., Vibrational relaxation following ultrafast internal conversion: comparing IR and Raman probing. *Chemical Physics Letters* **2004**, 392, (4-6), 358-364.

Schuddeboom, W.; Warman, J. M.; Biemans, H. A. M.; Meijer, E. W., Dipolar Triplet States of p-Nitroaniline and N-Alkyl Derivatives with One-, Two-, and Three-Fold Symmetry. *Journal of Physical Chemistry* **1996**, 100, (30), 12369-12373.

Schweitzer-Stenner, R., Structure and dynamics of biomolecules probed by Raman spectroscopy. *Journal of Raman Spectroscopy* **2005**, 36, (4), 276-278.

Shimajima, A.; Tahara, T., Picosecond Time-Resolved Resonance Raman Study of the Photoisomerization of Retinal. *Journal of Physical Chemistry B* **2000**, 104, (39), 9288-9300.

Simpson, M. C.; Peterson, E. S.; Shannon, C. F.; Eads, D. D.; Friedman, J. M.; Cheatum, C. M.; Ondrias, M. R., Transient Raman Observations of Heme Electronic and Vibrational Photodynamics in Deoxyhemoglobin. *Journal of the American Chemical Society* **1997**, 119, (22), 5110-5117.

Spence, D. E.; Kean, P. N.; Sibbett, W., 60-Femtosecond pulse generation from a self-mode-locked titanium-doped sapphire laser. *Optics Letters* **1991**, 16, (1), 42-4.

Spiro, T. G.; Czernuszewicz, R. S.; Li, X. Y., Metalloporphyrin structure and dynamics from resonance Raman spectroscopy. *Coordination Chemistry Reviews* **1990**, 100, 541-71.

Straub, J. E.; Karplus, M., Molecular dynamics study of the photodissociation of carbon monoxide from myoglobin: ligand dynamics in the first 10 ps. *Chemical Physics* **1991**, 158, (2-3), 221-48.

Strickland, D.; Mourou, G., Compression of amplified chirped optical pulses. *Optics Communications* **1985**, 55, (6), 447-9.

Sugita, A.; Yanagi, K.; Kuroyanagi, K.; Takahashi, H.; Aoshima, S.; Tsuchiya, Y.; Tasaka, S.; Hashimoto, H., Photo-excited state of N-benzyl MNA studied by femtosecond time-resolved absorption spectroscopy. *Chemical Physics Letters* **2003**, 382, (5,6), 693-698.

Swanson, R.; Trus, B. L.; Mandel, N.; Mandel, G.; Kallai, O. B.; Dickerson, R. E., Tuna cytochrome c at 2.0 Å resolution. I. Ferricytochrome structure analysis. *Journal of Biological Chemistry* **1977**, 252, (2), 759-75.

Takano, T.; Dickerson, R. E., Conformation change of cytochrome c. I. Ferrocycytochrome c structure refined at 1.5 Å resolution. *Journal of Molecular Biology* **1981**, 153, (1), 79-94.

Thompson, W. H.; Blanchard-Desce, M.; Hynes, J. T., Two Valence Bond State Model for Molecular Nonlinear Optical Properties. Nonequilibrium Solvation Formulation. *Journal of Physical Chemistry A* **1998**, 102, (39), 7712-7722.

Thomsen, C. L.; Thogersen, J.; Keiding, S. R., Ultrafast Charge-Transfer Dynamics: Studies of p-Nitroaniline in Water and Dioxane. *Journal of Physical Chemistry A* **1998**, 102, (7), 1062-1067.

Tokmakoff, A.; Sauter, B.; Kwok, A. S.; Fayer, M. D., Phonon-induced scattering between vibrations and multiphoton vibrational up-pumping in liquid solution. *Chemical Physics Letters* **1994**, 221, (5-6), 412-18.

Tokmakoff, A.; Urdahl, R. S.; Zimdars, D.; Francis, R. S.; Kwok, A. S.; Fayer, M. D., Vibrational spectral diffusion and population dynamics in a glass-forming liquid: variable bandwidth picosecond infrared spectroscopy. *Journal of Chemical Physics* **1995**, 102, (10), 3919-31.

Treacy, E. B., Optical pulse compression with diffraction gratings. *IEEE Journal of Quantum Electronics* **1969**, QE-5, 454-58.

Trebino, R.; DeLong, K. W.; Fittinghoff, D. N.; Sweetser, J. N.; Krumbugel, M. A.; Richman, B. A.; Kane, D. J., Measuring ultrashort laser pulses in the time-frequency

domain using frequency-resolved optical gating. *Review of Scientific Instruments* **1997**, 68, (9), 3277-3295.

Trebino, R.; Editor, *Frequency-Resolved Optical Gating: The Measurement of Ultrashort Laser Pulses*. 2002; p 456 pp.

Trebino, R.; Kane, D. J., Using phase retrieval to measure the intensity and phase of ultrashort pulses: frequency-resolved optical gating. *Journal of Optical Society of America A* **1993**, 10, (5), 1101-1110.

Trebino, R.; O'Shea, P.; Kimmel, M.; Gu, X., Measuring ultrashort laser pulses just got a lot easier! *Optics & Photonics News* **2001**, 12, (6), 22-25.

Tsai, H.-H.; Simpson, M. C., Isolated Impact of Ruffling on the Vibrational Spectrum of Ni Porphyrins. Diagnosing Out-of-Plane Distortions. *Journal of Physical Chemistry A* **2004**, 108, (7), 1224-1232.

Varsanyi, G., *Vibrational Spectra of Benzene derivatives*. 1969.

Vietri, F.; Guglielmi, R.; Belbusti, M.; Crispino, M.; Tombolini, P.; Jori, G., Photothermal sensitization. *Laser & Technology* 1992, 2, (1), 21-5.

Wang, W.; Ye, X.; Demidov, A. A.; Rosca, F.; Sjodin, T.; Cao, W.; Sheeran, M.; Champion, P. M., Femtosecond Multicolor Pump-Probe Spectroscopy of Ferrous Cytochrome c. *Journal of Physical Chemistry B* **2000**, 104, (46), 10789-10801.

Wang, Z.; Pang, Y.; Dlott Dana, D., The vibrational Stokes shift of water (HOD in D2O). *The Journal of chemical physics* **2004**, 120, (18), 8345-8.

Wilbrandt, R.; Jensen, N. H., Time-resolved resonance Raman spectroscopy: the triplet state of all-trans-retinal. *Journal of the American Chemical Society* **1981**, 103, (5), 1036-41.

Wortmann, R.; Kraemer, P.; Glania, C.; Lebus, S.; Detzer, N., Deviations from Kleinman symmetry of the second-order polarizability tensor in molecules with low-lying perpendicular electronic bands. *Chemical Physics* **1993**, 173, (1), 99-108.

Wylie, I. W.; Koningstein, J. A., Photoisomerization and time-resolved Raman studies of 15-15'-cis-b-carotene and 15-15'-trans-b-carotene. *Journal of Physical Chemistry* **1984**, 88, (14), 2950-3.

Yamaguchi, T.; Kimura, Y.; Hirota, N., Solvent and solvent density effects on the spectral shifts and the bandwidths of the absorption and the resonance Raman spectra of phenol blue. *Journal of Physical Chemistry A* **1997**, 101, (48), 9050-9060.

Yamaguchi, T.; Kimura, Y.; Hirota, N., The excitation energy dependence of the Raman-Stokes shift: The resonance Raman spectra of phenol blue in methanol. *Journal of Chemical Physics* **1997**, 107, (11), 4436-4438.

Yamaguchi, T.; Kimura, Y.; Hirota, N., Solvation state selective excitation in resonance Raman spectroscopy. I. Experimental study on the C:N and the C:O stretching modes of phenol blue. *Journal of Chemical Physics* **1998**, 109, (20), 9075-9083.

Ye, X.; Demidov, A.; Champion, P. M., Measurements of the Photodissociation Quantum Yields of MbNO and MbO₂ and the Vibrational Relaxation of the Six-Coordinate Heme Species. *Journal of the American Chemical Society* **2002**, 124, (20), 5914-5924.

Ye, X.; Demidov, A.; Rosca, F.; Wang, W.; Kumar, A.; Ionascu, D.; Zhu, L.; Barrick, D.; Wharton, D.; Champion, P. M., Investigations of Heme Protein Absorption Line Shapes, Vibrational Relaxation, and Resonance Raman Scattering on Ultrafast Time Scales. *Journal of Physical Chemistry A* **2003**, 107, (40), 8156-8165.

Zewail, A. H., Femtochemistry. Past, present, and future. *Pure and Applied Chemistry* **2000**, 72, (12), 2219-2231.

Zewail, A. H., Femtochemistry: Atomic-Scale Dynamics of the Chemical Bond. *Journal of Physical Chemistry A* **2000**, 104, (24), 5660-5694.

Zeylikovich, I.; Alfano, R. R., Coherence properties of the supercontinuum source. *Applied Physics B: Lasers and Optics* **2003**, 77, (2-3), 265-268.

Zijlstra, W. G.; Buursma, A.; Meeuwssen-van der Roest, W. P., Absorption spectra of human fetal and adult oxyhemoglobin, de-oxyhemoglobin, carboxyhemoglobin, and methemoglobin. *Clinical chemistry* **1991**, 37, (9), 1633-8.

Zinth, W.; Kolmeder, C.; Benna, B.; Irgens-Defregger, A.; Fischer, S. F.; Kaiser, W., Fast and exceptionally slow vibrational energy transfer in acetylene and phenylacetylene in solution. *Journal of Chemical Physics* **1983**, 78, (6, Pt. 2), 3916-21.